Sede Amministrativa: Università degli Studi di Padova
Dipartimento di Fisica e Astronomia “G. Galilei”

Corso di Dottorato di Ricerca in Astronomia
Ciclo XXX

OPEN CLUSTERS IN GAIA ERA

Coordinatore: Ch.mo Prof. Giampaolo Piotto
Supervisore: Dr.ssa Antonella Vallenari

Dottorando: Francesco Pensabene

Abstract

Context. Open clusters (OCs) are optimal tracers of the Milky Way disc. They are observed at every distance from the Galactic center and their ages cover the entire lifespan of the disc. The actual OC census contain more than 3000 objects, but suffers of incompleteness out of the solar neighborhood and of large inhomogeneity in the parameter determinations present in literature.
Both these aspects will be improved by the on-going space mission *Gaia* . In the next years *Gaia* will produce the most precise three-dimensional map of the Milky Way by surveying other than 1 billion of stars. For those stars *Gaia* will provide extremely precise measurement of proper motions, parallaxes and brightness.

Aims. In this framework we plan to take advantage of the first *Gaia* data release, while preparing for the coming ones, to: *i)* move the first steps towards building a homogeneous data base of OCs with the high quality *Gaia* astrometry and photometry; *ii)* build, improve and test tools for the analysis of large sample of OCs; *iii)* use the OCs to explore the properties of the disc in the solar neighborhood.

Methods and Data. Using ESO archive data, we analyze the photometry and derive physical parameters, comparing data with synthetic populations and luminosity functions, of three clusters namely NGC 2225, NGC 6134 and NGC 2243. These clusters are interesting since we use the parameters determination of this study to test the reliability of BASE-9, a free available automated Bayesian analysis tool for parameters determination of stellar clusters, re-analyzing the clusters with this tool and comparing the results with the ones obtained from photometric analysis.
Then we made use of the *Gaia* first data release parallaxes and proper motions (TGAS) complemented by the UCAC4 proper motions in region where TGAS data quality was not sufficient, to study a sample of OCs, whose stars are brighter than G=12. Furthermore we

made use of the HSOY proper motions catalog on a sample of fainter clusters. In both cases we employed the free available automated UPMASK method for membership selection. This procedure use Principal Component Analysis and k-means clustering to select stars having similar properties on the photometric planes. This procedure was adapted to select cluster members using also proper motions and parallaxes. Using BASE-9 we derive the physical parameters of OCs, such as age, distance, metallicity and extinction. Finally using *galpy*, a Python package for galactic dynamics calculations, we calculate the orbits for the clusters with available literature values of the radial velocities.

Results. We develop and validate an automated pipeline that can be used on the astrometric and photometric data of the second *Gaia* data release and more in general on large samples of data. We estimate in a homogeneous way: *i)* proper motions and parallaxes of 147 OCs; *ii)* age, distance moduli and extinction of 42 OCs; *iii)* metallicities of 37 OCs; *iv)* 3D orbits of 36 OCs. For NGC 2225, NGC 6134 and NGC 2243 we perform a detailed photometric analysis estimating also the number of cluster stars, the binary fraction and the radial extension.

Introduction

During the centuries the new physical theories and the technological development have enlarged widely our comprehension about both the world of the phenomenon and of the noumenon. Despite this, the knowledge of the position and in particular of the distance and motion of the stars in the sky remains a crucial aspect of astronomical research, today as much as two thousands years ago.

In this field one of the most ambitious mission of the European Space Agency (ESA) has being carried out, the *Gaia* mission. Launched on 19 December 2013 with the aim to produce the most complete and precise three dimensional map of our Galaxy, *Gaia* will provide ultra-accurate measurements of positions, parallaxes, proper motions and brightness of more than 1 billion of stars. The results of *Gaia* will give an important contribution to our understanding of many different astronomical fields from stellar structure and evolution to cosmology.

In this Thesis we focus on Open Clusters (OCs). These objects are groups of stars, from few dozens to several thousands, gravitationally bounded. They are born in the same event of stars formation, a gravitational collapse of a giant molecular cloud. OCs are then groups of coeval stars that share the same chemical composition. Photometric data permits to derive the physical parameters of OCs, such as age and extinction, with a higher accuracy in comparison to other astronomical objects. Astrometric data provide membership and distances. OCs lie on the Galaxy disc and are observed at every distance from the center, from 4 kpc up to more than 20 kpc. Furthermore they cover the entire lifespan of the disc, with age than

vary from a few Myr to 9 Gyr. Then OCs trace naturally the morphology, and the evolution of the disc. Young clusters are optimal tracers of the spiral arms of the Galaxy, where it is thought that the star formation events occur. One of the main problems related to OCs study is the large inhomogeneity of their parameter determinations in literature, due to the different methods of analysis adopted over the years by the many astronomers that have worked in this field. This can hamper the definition of the disk properties from OCs.

The main goal is to derive a homogeneous Catalog of OC properties, using Gaia high quality data. Here we make use of the first Gaia data release, with the goal of paving the way to the scientific exploitation of the second and upcoming data releases. We study a sample of about 150 OCs, while validating the tools we will use in the future. In this framework, the main aspects the work presented in these pages are the following:

- deriving the properties of a sample of OCs from photometry and astrometry in order to derive the age, the extinction, the distance, the metallicity, the proper motions and the membership probability of their stars.
- Building and combining tools for OCs analysis. In this work we present and use `FILLTHETEMPO`, a software that creates synthetic stellar populations from isochrones and compares them with observational data, and two variants of the literature tool UPMASK (Krone-Martins & Moitinho, 2014), meant to work with astrometric data of TGAS and with proper motions of HSOY and with 2MASS photometry. The aim is to built a pipeline, as automated as possible, able to perform parameter determinations on a large sample of OCs.
- Exploring the properties of the disc in the solar neighborhood using OCs. This work focuses on two of the main topic in OCs field: *i)* the slope of the Galactocentric metallicity gradient as derived from photometric metallicity; *ii)* the relation between age and OCs scaleheight on the disc plane. Particular attention is given to the third Galactic quadrant, a region of the disc with peculiar features still not well understood.

Concerning the data, we adopt three photometric data sets, namely the data from ESO archive for three OCs; the first *Gaia* Data Release (DR1) and the 2 Micron All Sky Survey (2MASS). The astrometric data are taken from the *Tycho-Gaia* astrometric solution (TGAS) and from the Hot Stuff for One Year catalog (HSOY). The outline of this Thesis is as follows. In Chapter 1 we summarize the current state of knowledge on open clusters. Chapter 2 offers

an overview on the on going *Gaia* mission. In Chapter 1 we present the study of three OCs, namely NGC 2225, NGC 6134 and NGC 2243 using data from ESO archive, and the related methods and tools. In Chapter 4 we derive the properties of a sample of about 134 OCs using 2MASS photometry and TGAS astrometry. In Chapter 5 we determine the properties of about 13 OCs on the basis of 2MASS photometry and HSOY proper motions. Finally, in Chapter 6 we draw the main conclusions.

Contents

List of acronyms and abbreviations

2MASS Two Micron All Sky Survey
AF Astrometric field
AGIS Astrometric Global Iterative Solution (Lindegren et al. (2012) and Lindegren et al. (2016a))
BASE-9 Bayesian Analysis for Stellar Evolution with Nine Parameters (von Hippel et al., 2006)
BP *Gaia* Blue Photometer
CCD Charge-Coupled Device
CMD Colour-Magnitude Diagram
DAML02 The catalog of open clusters by Dias et al. (2002)
DAML14 Expansion of DAML02 Dias et al. (2014)
DM Distance Modulus
DPAC *Gaia* Data Processing and Analysis Consortium **DR** Differential Reddening
DR1 first *Gaia* Data Release
ESA European Space Agency
ESO European Southern Observatory
FoV Field of View
GC Globular Cluster
GMC Giant Molecular Cloud
H-R Hertzsprung–Russell
HSOY Hot Stuff for One Year
ISM Interstellar Medium

IMF Initial mass function

LBC Large Binocular Camera

LBT Large Binocular Telescope

LF Luminosity Function

MCMC Markov Chain Monte Carlo

MS Main Sequence

MW Milky Way

MWSC Milky Way Star Clusters catalog (Kharchenko et al., 2013)

OC Open Cluster

RC Red Clump

RP *Gaia* Red Photometer

RVS Radial-Velocity Spectrometer

SM Sky Mapper

TGAS *Tycho-Gaia* Astrometric Solution

TO Tunr-Off

UCAC4 The fourth U.S. Naval Observatory CCD Astrograph Catalog (Zacharias et al., 2013)

UPMASK Unsupervised Membership Assignment Method (Krone-Martins & Moitinho, 2014)

VVV VISTA Variables in the Vía Láctea survey (Borissova et al., 2014)

WFI Wide Field Imager

1 Open clusters

Est enim Galaxia nihil aliud, quam innumerarum stellarum coacervatim consitarum congeries.

Galileo Galilei, *Sidereus Nuncius (1610)*

Our Galaxy is a complex system in which visible mass is formed principally by stars and gas. The formation of a star is not an isolated event in the majority of cases but rather it's located in the context of a star cluster formation (Baumgardt & Kroupa, 2007). Star clusters are groups of stars bond together by mutual gravitational attraction. Star clusters are objects which differ from each other in several aspects, like for example number of stars that varies from a few tens up to 10^6 members or age, that cover a large range, from a few million years up to several Gyr.
In the work presented in these pages, the attention is focused on a specific kind of star clusters, the open clusters (OCs). This chapter summarize our present knowledge about what OCs are and how to use them to study the structure and the evolution of our Galaxy.

1.1 Historical observations

Since the dawn of Human Kind, the prominent OCs were recognized as groups of stars. For example, tracks of Pleiades observations are present in many ancient cultures all around the world, from Homer in Greece, to Maori people in New Zeland or to Sioux in North America.

Also the Hyades are well known by the Greeks since 1000 b.C., and probably even before, which identified them as the *head* of Taurus constellation.

Apart from these two, other OCs were known by early astronomers but only as fuzzy patches of light in the night sky. Some examples can be found in ancient Greek and Roman astronomy. Hipparchus, a Greek astronomer, described the Double Cluster (NGC 869 and NGC 884) as a patch of light in Perseus, while Ptolemy, in the same period, identified M7 (also known as Ptolemy cluster for good reasons) as a bright nebula. Other examples can be found among asian astronomers. One for all, Abd al-Rahman al-Sufi, a persian astronomer who in his *Book of Fixed Stars* cataloged the Omicron Velorum cluster IC 2391 as a *nebulous star*.

To resolve these nebulae into their constituent stars we had to wait until 1609. When Galileo Galilei turned the telescope that he built to the night sky discovering, among other things, that the light patches were composed by dozens of different stars very close to each other. In 1654 the Sicilian astronomer Giovanni Hodierna was the first to use the telescope specifically to investigate the real nature of the undefined bright nebulae. To him is attributed the identification of M 41, M 47, NGC 2362 and NGC 2451.

The first to realise that these stars were physically related, was the English naturalist Reverend John Michell. He pointed out that the probability to see from Earth a single group of stars as the result of a fortuitous alignment on our line of sigh was 1 on 496000.

The first extended study of nebulous celestial objects was performed in the 1790s by the English astronomer William Herschel. Since then the census of star clusters continue to increase under the efforts of astronomers. Nowadays, the study and the research of star clusters is still a very active field of research, with the growth of stars census continuously fed by the implementation of observational equipment, and many catalogs of these objects were created. The first widely used of these catalogs was the 1180 objects catalog produced by Lynga (1981), updated and published in 1987 as the Lund Catalog of Open Cluster Data, CDS, Strasbourg (Lynga, 1987).

The next considerable step arrived in the mid-90's with the work of J.-C. Mermiliod at the Lausanne Observatory. He develop a web-based database for galactic open cluster called WEBDA (Mermilliod, 1995)[1], based on catalogs of Lauberts (1982) and Lynga (1987). In addition to photometry in the many photometric systems in which the cluster stars had been observed, the dataset contains spectral classifications, radial and rotational velocities, as-

[1] http://webda.physics.muni.cz

trometric data, with membership probabilities, positions and a complete bibliography of published data and a thorough cross-identification between different studies.
In the late 1990's the data of HIPPARCOS mission permitted to widely improve our knowledge of OCs, measuring the absolute parallax with milli-arcsecond accuracy of as many as 117 955 objects (ESA, 1997). Using these data Dias et al. (2002) (DAML02) produced a catalogue of 1700 objects. The catalog did not apply any selection criterion on data and contains all cluster that had been identified as candidate. DAML02 provide information about clusters position and kinematic and also about distance, reddening, age and metallicity. In the current version the catalog is expanded to 2174 OCs, Dias et al. (2014) (hereafter DAML14).
A further increase of clusters census arrive from infrared observations, able to identify clusters in regions obscured by interstellar medium (ISM) in optical band, e.g. inner regions of Galaxy and star forming regions. In this context the main contribution arrive from the 2 Micron All Sky Survey (2MASS[2]), Skrutskie et al. (2006). Using 2MASS Froebrich, Scholz and Raftery (FSR, Froebrich et al. (2007)) obtained a sample of star clusters within 20° of the galactic plane. Of these, 681 are previously known OCs and 86 globular clusters, while the remaining 1021 are new cluster candidates, with an estimated contamination rate of 50%.
Using 2MASS photometry the number of known OCs has been further increased by surveys like the Milky Way Star Cluster (MWSC, Kharchenko et al. (2013)) in which were studied 3784 objects identifying 2808 of them as OCs or the VISTA Variables in the Vía Láctea (VVV, Borissova et al. (2014)) that taken advantage of near infrared photometry to search clusters in the direction of the inner Galactic disc and bulge, see Sect. 1.4.

1.2 Definition

The OCs are groups of stars that were born in the same event of gravitational collapse of a giant molecular cloud. This implies that the stars belonging to the same cluster share roughly the same age and also the same chemical composition, because they are sons of the same mother cloud.
Is not simple to give a strict definition of OCs. Originally the OCs were identified as clusters

[2]http://www.ipac.caltech.edu/2mass/

that do not shown the classical features typical of globular clusters (GCs). Indeed GCs are spherically shaped high density agglomerates of a huge amount of stars, whereas the OCs are: *sparsely populated, loosely concentrated, barely gravitationally bound systems of a few tens or hundreds of stars, (Friel, 1995).*

The OCs are located in the Galactic disc, where stellar formation has continued over time, while GCs are tipically located in the Galactic halo and bulge. Indeed another aspect that discriminates between OCs and GCs is that the former are also much younger that the latter. Indeed the Galactic GCs have the same age as the Galaxy ($\sim 10^{10}$ yrs) whereas the bulk of OCs have age < 1 Gyr. This age difference produces as a consequence also a difference in metallicity. The GCs were formed in the primordial environment of the Galaxy and then are composed by metal poor stars, instead the OCs were formed in an environment already metal enriched by the products of atomic nucleosynthesis of the first massive stars of the Galaxy. Then the OCs are significantly more metal rich respect to GCs.

In the last decades the increasing quality of modern instruments led to the discovery of the presence of multiple stellar populations in most, if not all, GCs (see e.g. Piotto et al. (2005)). A very impressive manifestation of this feature is the presence of split or broadened sequences, e.g. Main Sequence or Red Giant Branch. There is a debate on-going on the kind of the stars which polluted the second generation altering their light elements abundances; however, this is not part of the Thesis and will not be discussed here. But a particular aspect of multiple stellar populations is useful to discern between GCs and OCs. Indeed the presence of the Na-O anticorrelation seems to be a peculiar feature of GCs, see Carretta et al. (2010), whereas every OC that was observed seems to be chemically homogeneous.

Also at low-mass can be defined a lower limit for OCs. Lada & Lada (2003), pointed out that a group of stars to be considered an OC need to be *"stable against tidal disruption"*. Indeed the star clusters are bound together by reciprocal gravitational attraction and the passage near to another cluster or to a giant molecular cloud and the effect of the galactic tidal field could partially or totally destroy the cluster. This aspect is discussed in more detail in the next section, for now is important to stress out that a group of gravitational bounded stars in order to survive at least 10^8 yrs must have a minimum of $\sim$35 members. Less rich star aggregations are not considered cluster, but rather are classified as stellar associations.

1.3 Cluster formation and evolution

Both clusters and single stars are formed from the gravitational collapse of a giant molecular cloud (GMC). These clouds, made mainly of molecular hydrogen plus dust, have typically a filamentary structure with an extension of $10 - 100$ pc, a temperature of $10 - 100$ K, a mass $\geqslant 10^4 M_{\odot}$ and a density ranging from ≈ 10 to $\approx 10^2$ particles/cm^3, see Kennicutt & Evans (2012). The physical process involved in the mechanisms of formation and accretion of GMC is still an open issue. What we know is that if the mass of the cloud or of a region of the cloud exceeds a certain mass limit (the Jeans mass), the gravitational collapse occur, see Jeans (1902). On a global scale the GMCs are stabilized against this mechanism by internal turbulent pressure. But the collapse between turbulent flows can produce dense cores that are gravitationally unstable, and the collapse can be triggered locally, see Klessen et al. (2000). During the cloud collapse, due to efficiency of cooling process, the value of Jeans mass can decrease. This fact combined with the inhomogeneities of the cloud can produce the split of the initial collapsing core into sub-cores that continue separately to each other the collapse, in a process called fragmentation (see e.g. Salaris & Cassisi (2005)). In this way a GMCs can originate a group of stars with different masses.

Obviously the star-formation efficiency (SFE) of the process, i.e. the fraction of gas turned into stars, is not 100%. Then during the early phase of its life a cluster is composed by both stars and gas, these clusters are called *embedded*. The young stars of an embedded cluster are totally obscured in visual bands and can be observed only at infrared wavelength. Infrared observations show that initially the stars of the clusters as not concentrated in a central system, but instead they follow the filamentary structure of the progenitor GMCs. From this phase the star may gravitationally bound each other forming a stellar system, or they may disperse.

Bastian (2011) offers a review of how these two scenarios may occur. The crucial passage that discerns between the two cases is the gas removal due to stellar feedback, that come mainly from the winds and photoionisation of massive stars. If the embedded cluster is supposed to be in virial equilibrium when the gas loss occurs the system will pass in a super-virial state, decreasing the gas contribution to the gravitational potential. In order to find a new equilibrium the system will expand its radius, and in this process the cluster or part of it may be disrupted, see Hills (1980). The occurrence or not of this process derives from the ratio between the mass of the stars and the total mass, i.e. from SFE. If this value falls below 33% the cluster will be victim of infant mortality, see Bastian & Goodwin

(2006). This lower limit is however strongly linked to the definition of SFE and of embedded cluster. Indeed the fact that many stars can be formed in the same GMC collapse event, does not imply that these stars must be considered a cluster. Furthermore the GMCs are not homogeneous spherical clouds, but clumpy filamentary-shaped sub-structured objects. These sub-structures play a prominent role in the formation of the star system and can produce a local SFE much higher with respect to the global one, see Goodwin (2009). In this case the cluster is born in a sub-virial state, which largely limits the effect of gas expulsion in stars loss (Smith et al., 2011).
Another important process that occurs in the first millions of years of life of clusters is mass segregation. It is a dynamical phenomenon due to gravitational interaction between stars with different masses that produce a greater centralization of massive stars with respect to the least massive ones (Spitzer, 1969). The effect of mass segregation is observed in OCs, where the red-giant stars are tipically more concentrated near the center of the cluster with respect to the less massive Main Sequence stars. Furthermore studies of near OCs, where is possible to reach lower masses, highlight a lack of low mass stars (as the Pleiades (Moraux et al., 2004), Praesepe (Kraus & Hillenbrand, 2007) and Hyades (Bouvier et al., 2008)), i.e. a number of low mass stars in disagreement with that predicted by the cluster's mass functions. This lack is the result of the gradual evaporation of low mass stars that are pushed in the outer part of their cluster for mass segregation effect and then are the first that leave the cluster and enrich the field stars population.

All the process described above finally create star cluster, which life can be characterized by three dynamical time scales, see Meylan (2000). *i) Crossing time* t_{cr}, the time necessary to a star to move across the system; *ii) Relaxation time* t_{rlx}, the time needed by two-body encounter between stars to redistribute energies; *iii) evolution time* t_{ev}, the time scale of energy-changing mechanisms. The t_{rlx} is related to the number of cluster members and vary from a value very similar to the t_{cr} (few Myr), for cluster with few dozen members, to an order of magnitude higher, for cluster with several hundred or thousand members. Spitzer & Harm (1958) pointed out that the timescale of cluster evaporation, due to tidal field, for an isolated cluster is about ~ 100 times the t_{rlx}. This estimation sets an upper limit for clusters lifetime, from several hundreds of Myr for clusters with few members, to some Gyr for the more populous.
However the OCs are not isolated object and events like encounters with GMCs or tidal forces have also a prominent role in dictating their lifetime, Spitzer (1958). Furthermore

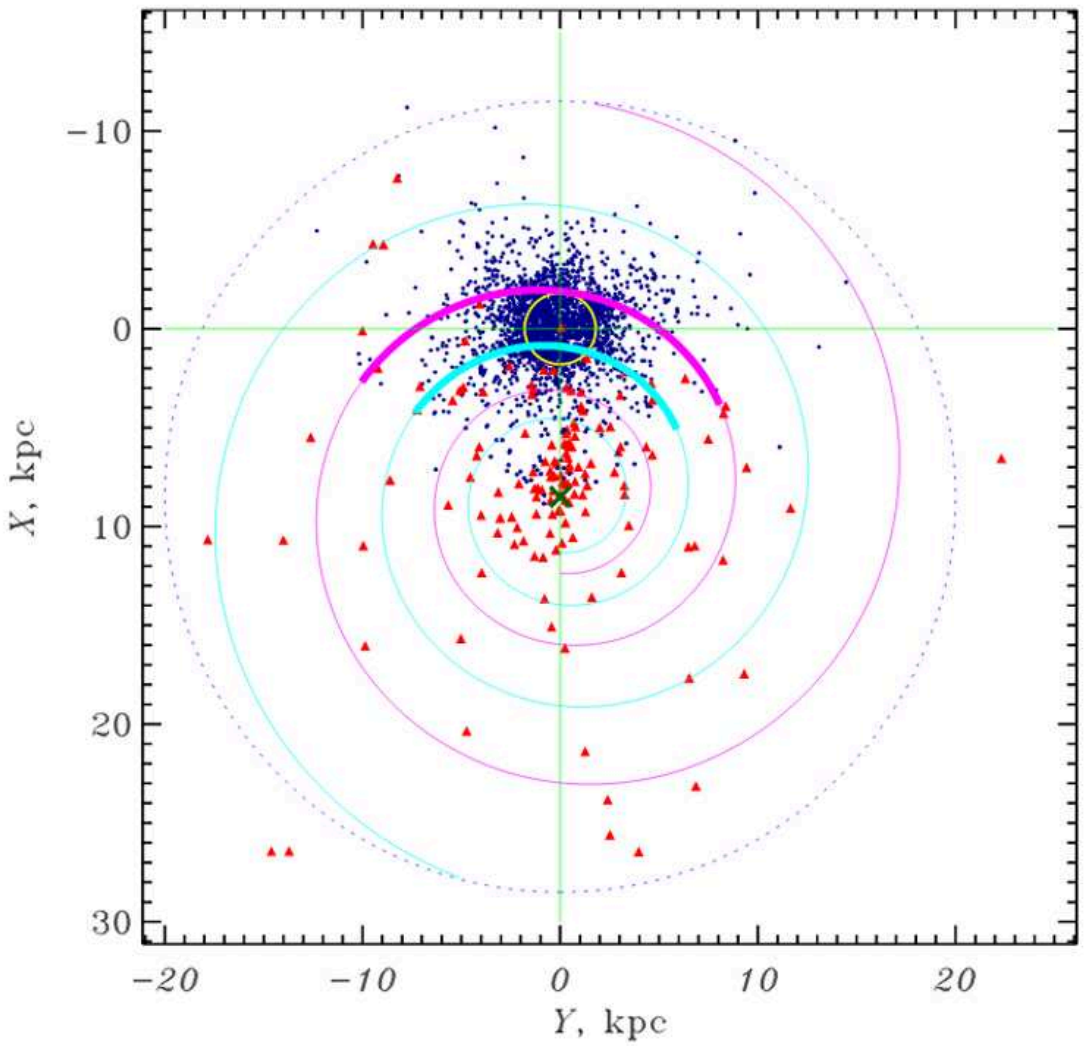

Figure 1.1: MWCS OCs distribution projected onto the Galactic XY-plane (Kharchenko et al., 2013). Blue dots are open clusters and associations, red triangles mark globular clusters. An approximate diameter of Galactic disc is defined by the dotted circle (radius $\sim$ 20 kpc). The yellow circle with radius of 1.8 kpc is centered on the Sun. The galactic center coordinates are $(X, Y) = (8.5, 0)$. The local spiral arms are represented by the cyan and magenta thick sections of spirals (Piskunov et al., 2006). Image from Kharchenko et al. (2013).

numerical simulation (Portegies Zwart et al., 2004) have showed how the t_{rlx} evolve during the clusters life, implying that present day estimation may not reflect the dynamical age of the cluster.

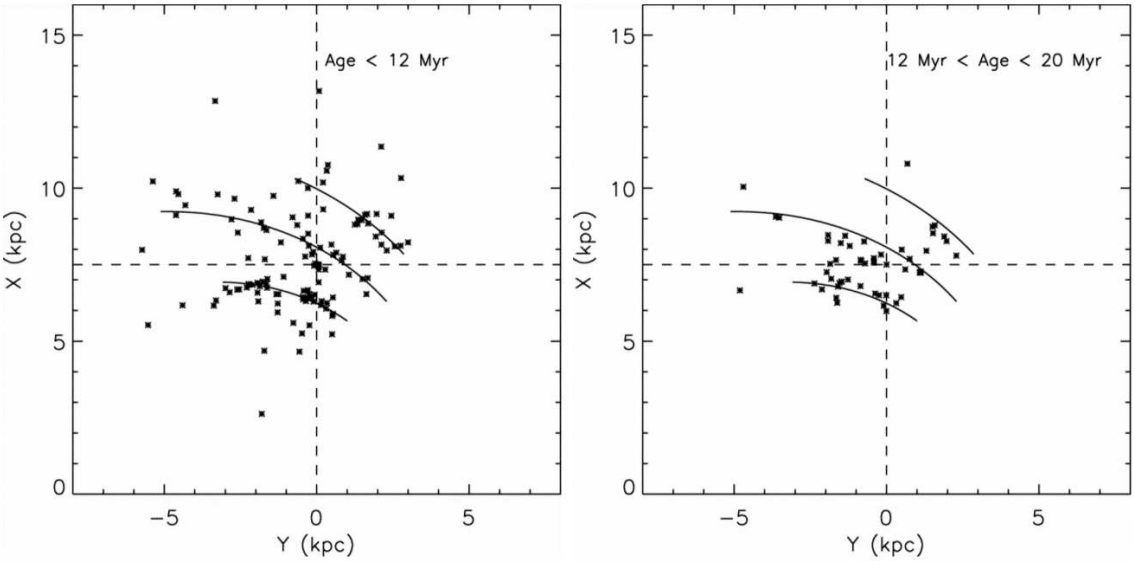

Figure 1.2: Dias & Lépine (2005) sample of cluster projected onto the Galactic XY-plane selected in two range of ages: *left* OCs with age < 12 Myr, *right* OCs with age between 12 and 20 Myr. The solid line represent approximately the present day position of the arms. The Sun position is fixed at $(X, Y) = (7.5, 0)$.

1.4 Properties

Spatial distribution

The current view is that OCs formation occurs only (or almost only) in the spiral arms of the Galaxy and that the gravitational collapse mechanism of the GMCs is triggered by density waves, see e.g. Roberts (1969), Shu et al. (1972) or more recently Cedrés et al. (2013). This vision is supported by the fact that OCs are concentrated in the the Galaxy disc, see Fig. 1.1 and Fig. 1.3. We can see how the distribution of OCs follows the Galactic plane at all Galactocentric radii.

Furthermore Dias & Lépine (2005) showed that younger OCs are young the more they are

constrained to the spiral arms, see Fig. 1.2. The explanation is that encounter with GMC and interaction with non-axisymmetric features of the disc, make the clusters motion not in-built to disc rotation and then during their life OCs leave their initial position. In this context also the irregularities of gravitational potential of the disc contribute to increase the OCs random motion.

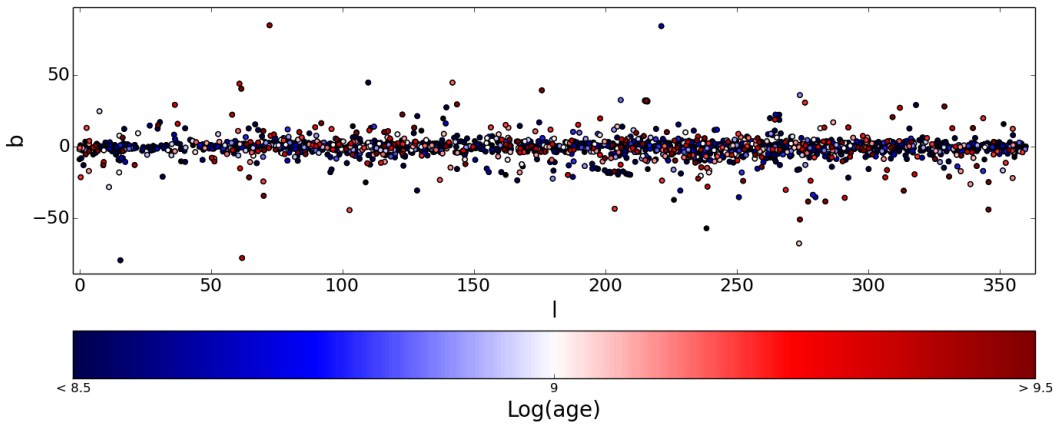

Figure 1.3: Sky position of all the 2174 OCs of the DAML14 catalogue, in galactic coordinates. The black dots represent OCs for which no age estimation is available. The colored dots follow a dichotomic color-scheme based on their age, centered at 1 Gyr, that highlights the position in b of OCs as a function of their age.

This feature is also clearly observable in the direction perpendicular to the galactic plane, see Fig. 1.3. Also here it can be seen how young clusters have latitude dispersion very lower compared to that of the older ones. Buckner & Froebrich (2014), using homogeneous subsample of MWCS, DAML14 and WEBDA, find a substantial difference in scaleheight of the cluster older and younger than 1 Gyr. Indeed until the first gigayear of life OCs scaleheight increase from few pc up to ≈ 100 pc. From 1 Gyr of age the scaleheight increases faster, see Fig. 1.4. This is likely due to the fact that the old OCs population is dominated by objects that have experienced strong scatter process. Clusters that do not undergo such an event will remain close to the Galactic plane and that increases their probability of disruption. As mentioned in the previous section during their life OCs increase their radii and then they became more and more subject to star loss until total dissipation.
A similar explanation can be used to understand the lack of old clusters in the inner region of the Galactic disc. OCs distribution indeed exhibits a radial gradient in age. In Fig. 1.5 one

can see a clear lack of old clusters toward the center of the Galaxy. Also here the tendency to increase the radius with age cause an increase of tidal disruption probability toward the center of the Galaxy, where the stars density increase and the perturbations caused by the bulge are stronger. Furthermore there is also an observational bias linked to the density increase. Indeed in a crowed background is difficult to identify clusters as overdense region of the field and it is harder to observe faint red stars of an old cluster, than bluer and brighter stars of a younger one.

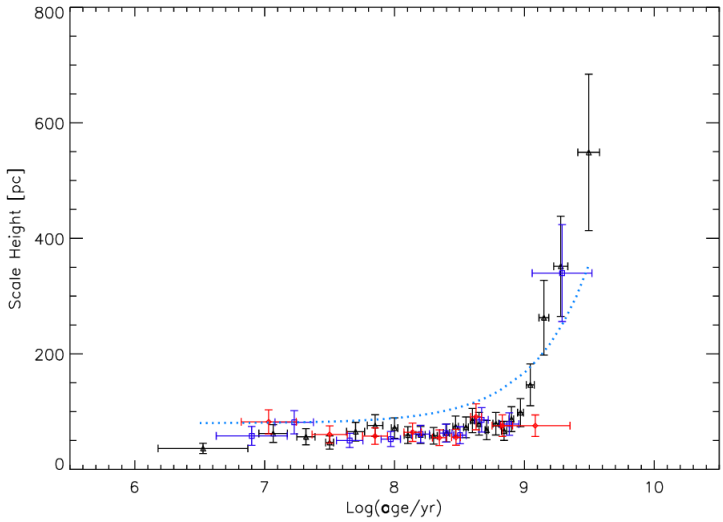

Figure 1.4: Evolution of the clusters scaleheight h_0. Black triangles indicate MWSC sample, blue squares DAML02 sample and red diamonds OCs from WEBDA. The dashed line is the approximate scaleheight–age relation for field stars, see Buckner & Froebrich (2014).

Age

OCs cover the entire lifespan of the disc, and as already mentioned they appear to continue forming in the spiral arms. Then the ages of OCs span a wide range, from young cluster observed in stars forming regions, (e.g. NGC 2024, IC 348, NGC 2264, NGC 2362 have all an age < 10 Myr, see Haisch et al. (2001)), to old cluster survived several Gyr. Be 17, Be 39 and NGC 6791 are the oldest known OCs with an age of respectively 8-9 Gyr (Bragaglia et al., 2006), 6.5 Gyr (Bragaglia et al., 2012) and 8.3 Gyr (Brogaard et al., 2012).
We have seen in the previous section that both an angular and radial age gradient is observed in the OCs, but these are likely the results of biases in observation or disruption successive to the formation. Any star formation gradient seems to affect the OCs spatial distribution.

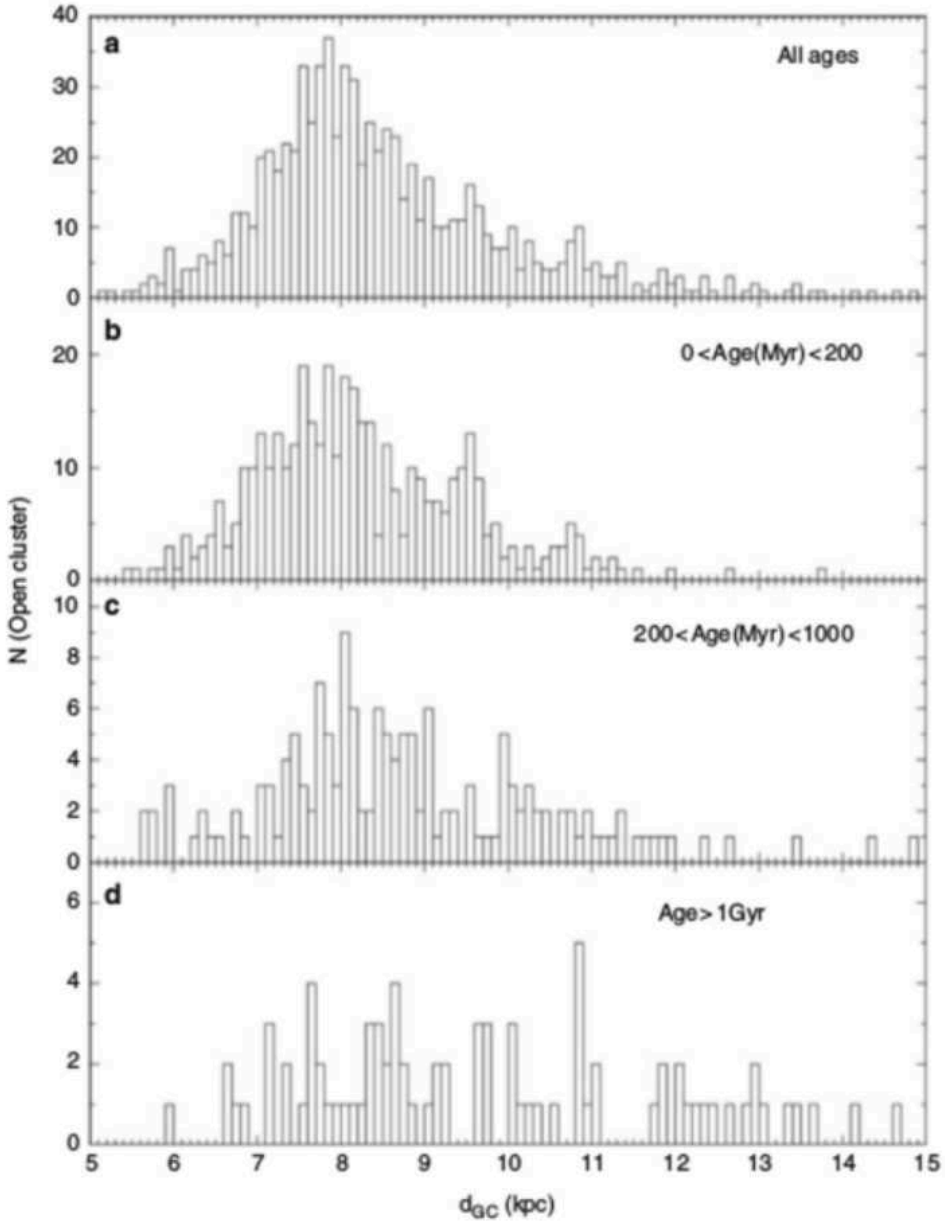

Figure 1.5: Friel (2013). OCs distribution as a function of distance from galactic center (sample from WEBDA). OCs are grouped by age as indicated.

Furthermore many studies were performed to investigate about the presence of an age-metallicity relation, see Bragaglia & Tosi (2006), Carraro et al. (2007), Friel & Janes (1993), Friel et al. (2002), Pancino et al. (2010) and Netopil et al. (2016). But a clear relation between these two cluster's proprieties was not found in any region of the disc sampled by OCs, see Fig. 1.6. This result indicates that if an enrichment of the disc occurs it was oc-

curred in the very early phases of disc lifetime, or that the disc was locally not well mixed or finally that migration play a role. Examples are some old cluster with solar metallicity, like NGC 188 with an age of 6-7 Gyr, or even with super-solar metallicity, like the 8-9 Gyr old cluster NGC 6791 with a metallicity from high resolution spectra of [Fe/H] $= +0.47$ (Gratton et al., 2006).

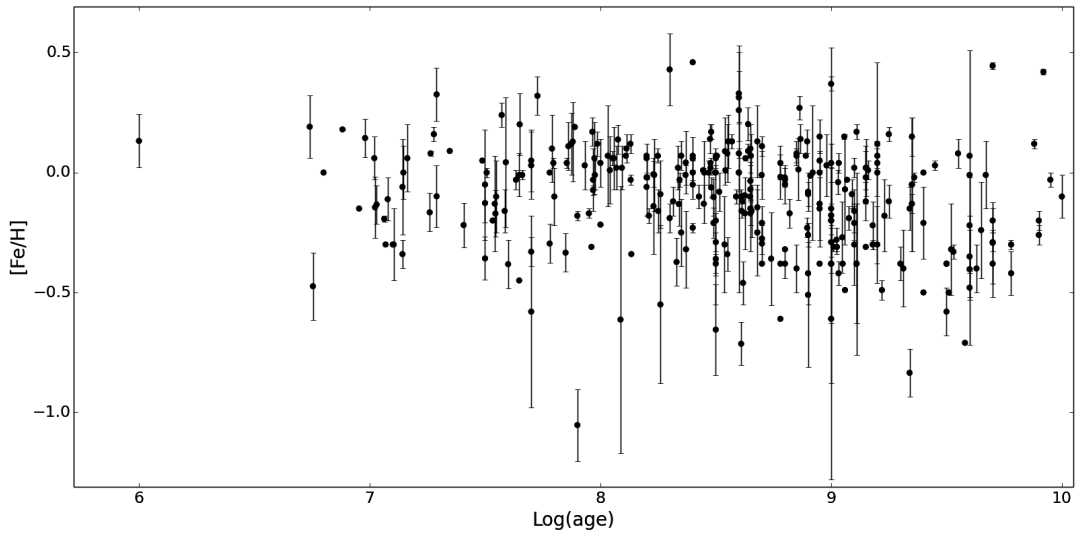

Figure 1.6: Age-metallicity relation from DAML14 clusters.

1.4.1 Chemical composition

As already shown in Fig. 1.6 the typical metallicity of the OCs is in the range $-1 \leqslant$ [Fe/H] $\leqslant 0.5$ dex, with the vast majority of OCs within $\pm$0.3 dex from solar. Many studies pointed out that the metallicity distribution of OCs seems to follow a radial gradient, or at least to show lower values farther from the Galactic center.

The metallicity radial distribution of OCs has been a lively field of research for the last forty years. For example Twarog et al. (1997), analysing a sample of 76 OCs, found that the Galactic metallicity gradient can be described in terms of two flat distributions, an inner solar one ([Fe/H]$= 0$) and an outer sub-solar one ([FE/H]$= -0.3$), with a sharp discontinuity at $R_{GC} \sim 10$ kpc. A more recent study performed by Lépine et al. (2011) attributed this feature to corotation of the gas that naturally produce a separation between an inner region and an outer region of the disc. However no chemical evolution model is able to reproduce this feature. Instead Friel et al. (2002) pointed out a metallicity abundance gradient of -0.06

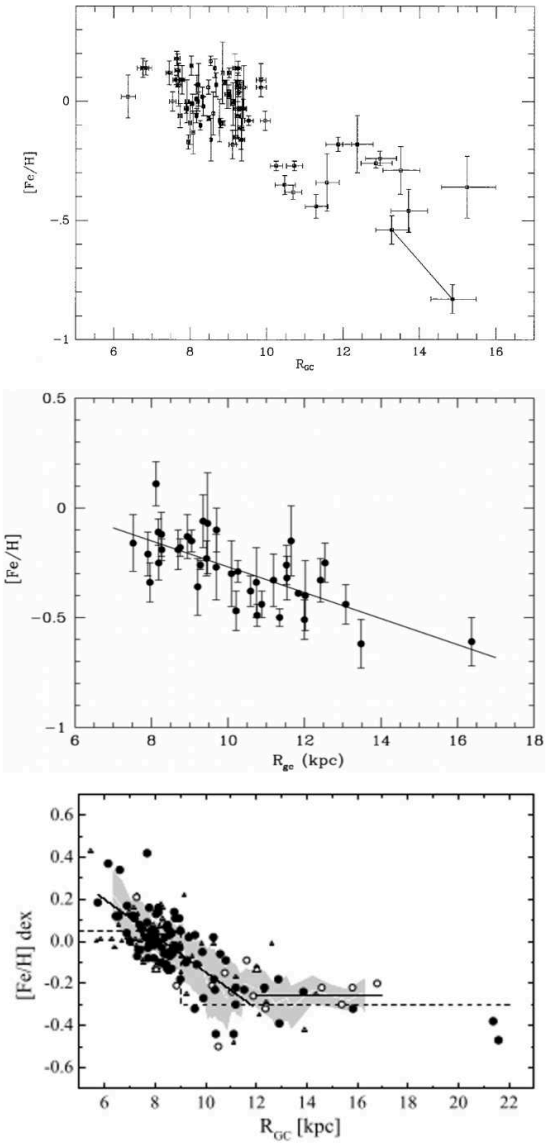

Figure 1.7: Radial metallicity distribution through years. *Upper panel:* Twarog et al. (1997) found two flat distributions, 76 OCs used (from photometry and low-resolution spectra). *Middle panel:* Friel et al. (2002) found unique distribution, 39 old OCs used (from low-resolution spectra). *Lower panel:* Netopil et al. (2016) found two negative slope distributions (solid lines). The circles represent spectroscopic data (high-resolution in black). Photometric metallicities are shown with triangles. The dashed line shows the metallicity plateaus and the step-like discontinuity found by Lépine et al. (2011). The grey area is the mean errors range.

dex kpc^{-1} over a range in R_{GC} of 7 to 16 kpc. The current interpretation of the radial metallicity distribution of the Milky Way disc from OCs suggests an inner steeper gradient (from -0.05 to -0.09 dex kpc^{-1}) and an outer shallower (or even flat) one, with the transition occurring somewhere between R_{GC} $\sim$10-12 kpc (e.g. Carraro et al. (2004), Sestito et al. (2008), Andreuzzi et al. (2011), Yong et al. (2012), Frinchaboy et al. (2013), Heiter et al. (2014) Magrini et al. (2015), Jacobson et al. (2016), Cantat-Gaudin et al. (2016)). Recently Netopil et al. (2016) derived the metallicities for 172 OCs from both spectroscopy and photometry, creating the larger sample, at the present day, of homogenized OCs metallicities. They used the spectroscopic data of 100 objects for a study of the radial metallicity distribution, deriving a gradient of about -0.07 dex kpc^{-1} out to R$_{GC}$ $\sim$ 12 kpc and one of about -0.016 dex kpc^{-1} for R_{GC} > 12 kpc. However it is important to note that the small number of known OCs in the outer disc and the large uncertainties on their parameters estimation make difficult to understand if the outer radial metallicity gradient follow a flat or slightly negative slope and if a time evolution occurs. In Fig. 1.7 we show some examples of the different interpretations of the radial metallicity distribution.
In Fig. 1.8 it is plotted the OCs count as a function of [Fe/H]. The set used is the fraction of DAML14 clusters for which a metallicity determination is available ($\sim$ 14.5%). The histogram shows a marked peak in the solar metallicity neighborhood. This feature simply reflect the fact that the majority of clusters with a known metallicity are close to the Sun.

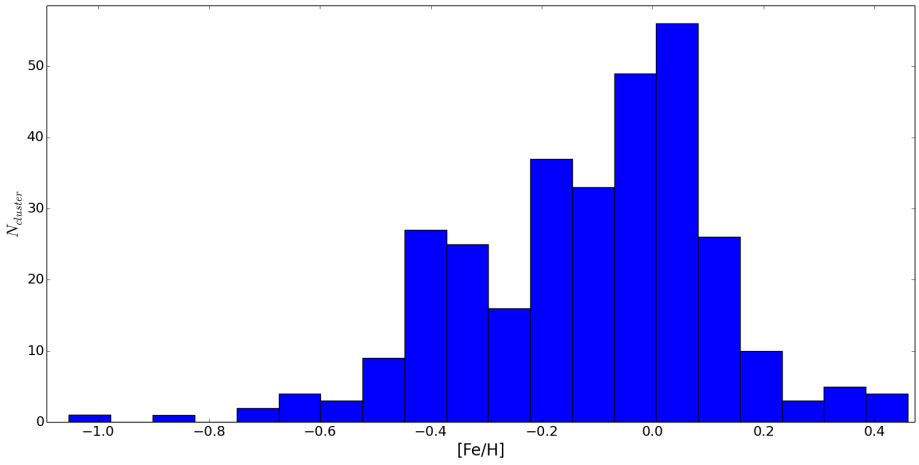

Figure 1.8: Metallicity distribution of OCs in the DAML14 catalogue.

Spectroscopic analysis of clusters single stars permit both an individual chemical element analysis and a star-to-star analysis. Whit this kind of investigation was pointed out in the

last decades that globular cluster present chemical inhomogeneities in Na, O, Mg, Al, or Si abundances, e.g. Gratton et al. (2012). The most evident of these star-to-star elemental abundance variation in globular cluster are the Na-O anti-correlation and the Mg-Al anti-correlation, see Gratton et al. (2001). Instead as already mentioned in section 1.2 no anti-correlation evidence was found in OCs, that show an homogeneous chemical composition. This feature of OCs distinguish sharply OCs from globular clusters.

1.5 OCs as stellar laboratories and galactic tracers

OCs are interesting object in the context of Galaxy disc study. They can be used for studying a vast array of astrophysical phenomena at various scale, from stellar structure and evolution to global analysis of Galaxy. The OCs have two principal features which make them powerful tools for the analysis of the Galaxy disc: *(i)* they are groups of stars with different masses born in the same event of star formation; *(ii)* they occupy a well defined region of our Galaxy, the disc.

The first point permits a determination of fundamental cluster properties such as age, metallicty, distance and reddening via color-magnitude diagrams (CMDs) and color-color diagrams with higher accuracy with respect to the field stars. Furthermore the advantage to be a group of coeval stars with a common chemical composition is useful also in the single member analysis. Indeed, as long as membership is well defined, we can determine the physical parameters, useful to study stellar structure, such as mass, evolutionary stage and luminosity, with greater reliability compared to isolated stars of disc population.

The possibility to have a group of stars at the same distance and with same age and metallicity make OCs also an ideal laboratory to test stellar structure and evolution models. GCs have the advantage to have a larger number of members, but they cover a range of age narrower respect to OCs and are also generally metal-poor, see Fig. 1.9. This means that the evolutionary phases of GCs are better defined on the CMDs, but can be used to test the models in a different parameters space compared to OCs. The two kinds of clusters cover indeed complementary parts of the metallicity-age (i.e. stellar mass) plane, making comparison to stellar evolutionary models more complete. The discrepancy between observed clusters and theoretical models has often led to a better comprehension of stellar structure mechanisms. For example the presence of a gap along the MS found in some OCs has led to reconsider the theories of stellar surface convection in stars less massive that the Sun, we

return in detail on this point in Sect. 3.4.1.

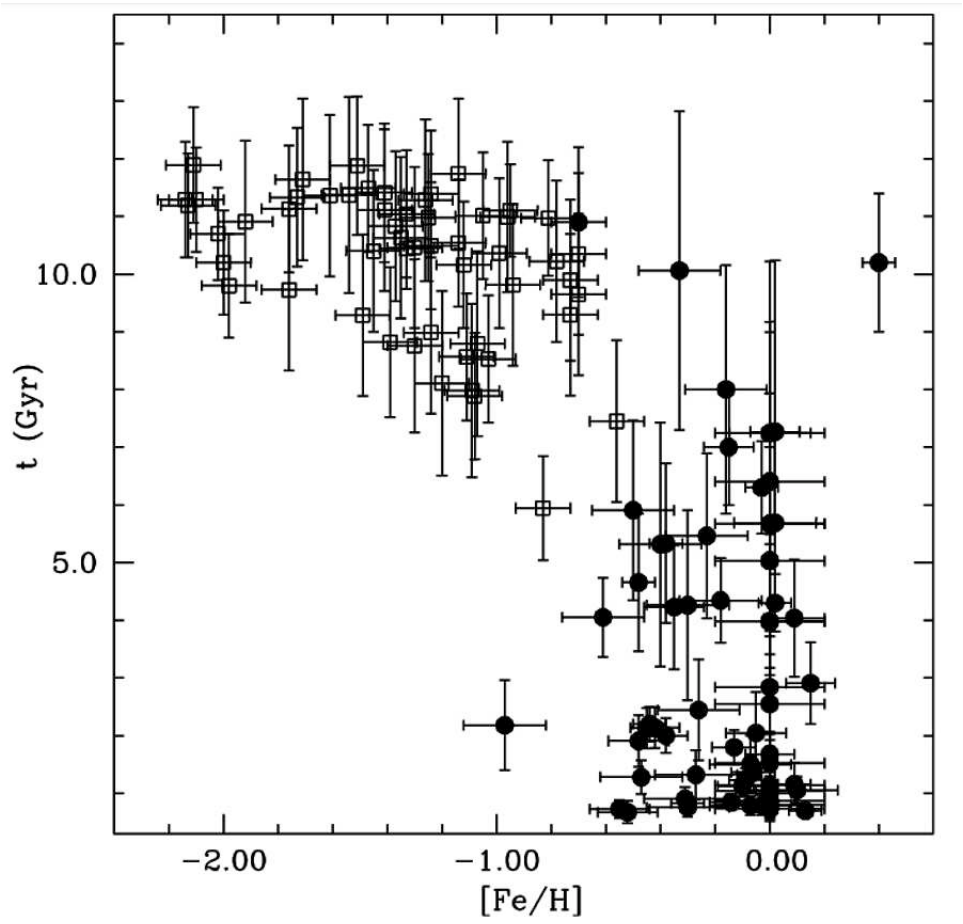

Figure 1.9: Salaris et al. (2004). Age-metallicity distribution for the OCs (filled circles) and the GCs studied by Salaris & Weiss (2002) (open squares).

The relative small number of cluster members in OCs makes them also ideal subjects for N-body simulations, that are able to reproduce the entire life of a cluster given the initial condition. The possibility to perform a realistic analysis of the dynamical evolution of a single OC, permits to explore the role played by effects like variation in the initial mass function (IMF), mass loss from stellar evolution, binary encounters, tidal perturbation from the smooth galactic field and shocks from spiral arm passages or encounters with molecular clouds of different masses, densities, and spatial distributions (see e.g. Terlevich (1987), de La Fuente Marcos (1997), Hurley et al. (2005), Lamers & Gieles (2006)).
As mentioned at the beginning of this chapter another important aspect of OCs is their spa-

tial distribution. OCs are born in the spiral arms and during their life they leave their initial position to spread all over the disc, see section 1.4. This means that young cluster can be used as tracers of the spiral structure of the Galaxy, see e.g. Becker & Fenkart (1970) or Moitinho et al. (2006).
As already pointed out OCs are observed at every R_{GC}, this is an important feature because allows both a morphological and physical study of the entire disc. Indeed the accurate determination of distance, reddening, age and metallicity of the OCs, combined both to the wide range of these parameters that they cover and to their spatial distribution, permits to investigate the evolution of the dynamics and physics of the disc. Understand how OCs properties and position vary with time gives hints about how the Galaxy disc evolve during its life. One of the most prominent example of this is the study of mechanisms that produced the galactocentric metallicity gradient of OCs, section 1.4.1.

1.5.1 Reliability of open cluster parameters

One of the main problem related to use OCs as Galaxy disc tracers is the significantly inhomogeneities on their parameters determination. During the years several studies on single or small sample of OCs have been performed with different methods. Eye-fit with isochrones on the clusters CMDs is the method tipically used to derive age, distance, and reddening. Also the metallicity can be derived in this way but spectroscopic analysis produce more reliable results. Spatial distribution and astrometric data can be used to define a membership probability of the clusters members in order to better separate them to the field population. Different methods lead to different results. In particular the choice of the model to reproduce the observed data have a great influence on the OCs parameters determination.
In the last decades, several photometric surveys or catalogs, as the already mentioned 2MASS, DAML14, MWSC or VVV, significantly increased both the amount of available data and the number of OCs (or candidates) in the Milky Way. In order to efficiently handle those large amount of data many semiautomatic tools was developed. These kind of tools have the aim to perform a parameters determination on a large sample of OCs minimizing the human interaction needed. They are based on different conceptual approaches and work both referring to different theoretical models and using different kinds of data (visual photometry, near infrared photometry, spectroscopy, astrometry, etc.). The homogeneous compilations of OCs parameters obtained in this way are very powerful tools to study the Galaxy disc

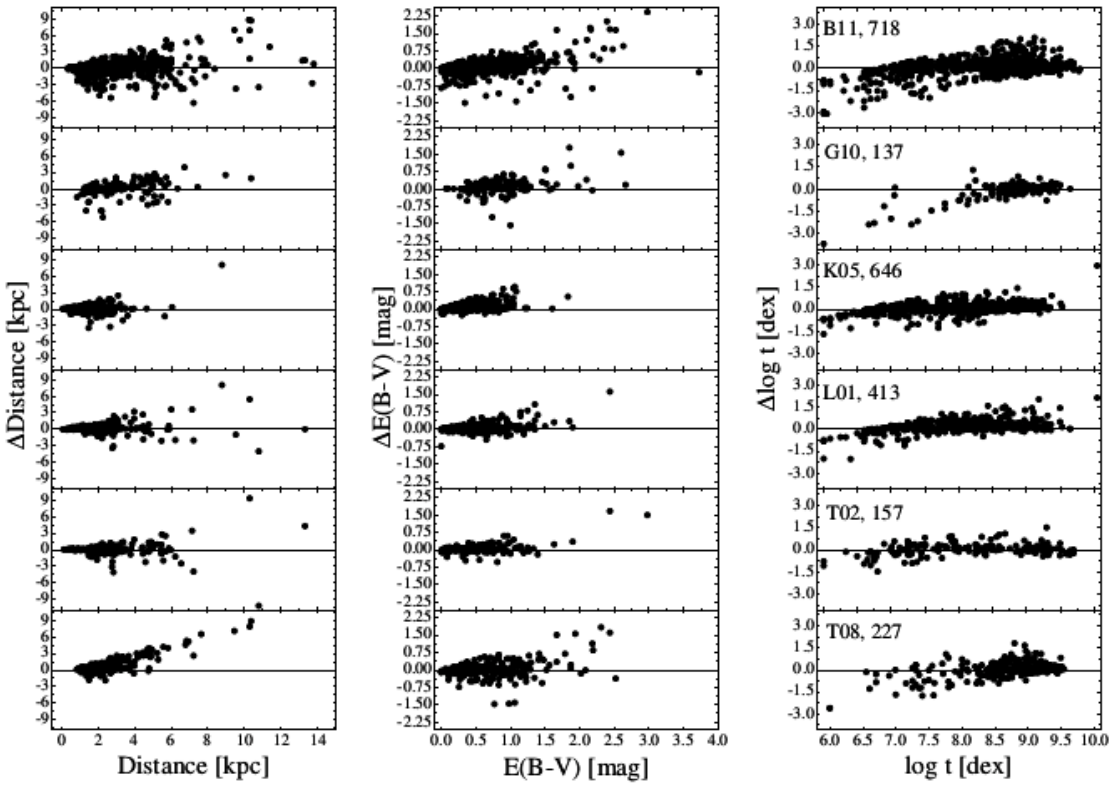

Figure 1.10: Netopil et al. (2015). Comparison between OCs parameters listed in MWSC and the ones derived, for the objects in common, in different studies. The considered studies are: B11) Bukowiecki et al. (2011), based on 2MASS JHK_S photometry and Girardi et al. (2002) isochrones; G10) Glushkova et al. (2010) and Koposov et al. (2008), based on 2MASS JHK_S photometry and Girardi et al. (2002) isochrones; K05) Kharchenko et al. (2005a) and Kharchenko et al. (2005b), based on Jhonson BV photometry and Girardi et al. (2002) isochrones; L01) Loktin et al. (2001), based on several photometric systems and Bressan et al. (1993) isochrones; T02) Tadross (2001), based on Jhonson UBV photometry and Meynet et al. (1993) isochrones; T08) The extensive series of papers by the working group of A.L.Tadross (Tadross (2008a), Tadross (2008b), Tadross (2009a), Tadross (2009b), Tadross (2011), Tadross (2012), Tadross & Nasser (2010), Tadross et al. (2012)), based on 2MASS JHK_S photometry and Marigo et al. (2008) isochrones. The number of clusters in common are listed near to the reference name.

properties, however the problem of inferring different results using different methods still remains.

An analysis of this problem was recently performed by Netopil et al. (2015). They com-

pare the OCs parameters listed in six different extensive photometric study with the results of MWSC for clusters in common. The results and the details of the study are shown in Fig. 1.10. The mean standard deviation for the distance, age, and reddening amounts to 1.2 kpc, 0.5 dex, and 0.27 mag, respectively. However for the most distant objects the differences can reach 8 kpc and for the younger the results differ even by 3 dex for log t. These inconsistencies in the results are unexpected for OCs, for which it is relatively easy to derive accurate parameters. The problem is that OCs parameters are strongly coupled in the isochrone fitting procedure and then a wrong choice of one parameter affects all others as well. Detailed studies performed on single clusters suffer less of this problem with respect to methods that analyze them automatically.

Over the years these semiautomatic tools have become more and more sophisticated and able to combine information inferred by different kind of data. An example is the UPMASK method (Krone-Martins & Moitinho (2014), see Sect. 4.4 for a description), largely employed in this work. The improvement of both tools and the data quality will increase the reliability of open cluster parameters determination.

2 Gaia mission

Gaia is one of the most ambitious and important scientific mission currently on progress in the field of astronomy. *Gaia* will provide the most precise three-dimensional map of our Galaxy by surveying up to 1 billion stars, which correspond to 1% of the total Galaxy's star population.
In this chapter we give an overview about the *Gaia* satellite and its characteristics, focusing on the data of the first data release used in this work.

2.1 Overview

The main task of *Gaia* is to provide astrometric measurements of stars of magnitude down to 20.7 mag in *Gaia* G band ($\sim$ 1 billion stars). Astrometry is the oldest branch of astronomy Perryman (2012) and it concerns the study of the positions of celestial objects. The study of the stars position in the sky and their changes leads to important discoveries like the trigonometric stellar parallax (Bessel 1838, Henderson 1840, von Struve 1840). However, the accuracy of the parallax measurements performed from the ground is heavily affected by the Earth's atmosphere. This strongly limited the number of measurements to few thousands (Finch & Zacharias (2016)) before the launch of the HIPPARCOS satellite of the European Space Agency (ESA) in 1997. HIPPARCOS collected the parallax of 117955 objects (ESA, 1997) with milli-arcsecond accuracy. Those data gave a great impulse to many area of astronomical research, such as stellar structure and evolution, kinematics of stellar groups and structure of the MW (see the review by Perryman (2009)).
The on going *Gaia* mission can be considered as the successor of HIPPARCOS. *Gaia* was

first proposed by Lennart Lindegren and Michael Perryman in 1993 (Høg & Knude, 2014). At that time the name of the project was *GAIA*, for Global Astrometric Interferometer for Astrophysics and it was born as optical interferometry space mission. The project was afterward modified, when some studies showed that interferometry was not the best choice for astrometric purposes. *Gaia* was selected as ESA cornerstone mission in 2000 and the implementation phase started in 2006 Gaia Collaboration et al. (2016b). The satellite was launched on 19 December 2013. Few weeks later *Gaia* arrived at its operating point, the second Lagrange point of the Sun-Earth-Moon system (see Fig. 2.1), chosen in order to have uninterrupted eclipse-free observations. *Gaia* moves around L_2 in a Lissajous-type orbit with a period of $\sim$180 days. The five-year nominal science operations phase started in the summer of 2014, after six months of commissioning and performance verification.
The nominal lifetime of the mission is 5 years. At the end of this time we will obtain the three dimensional space position of the stars (G < 20.7 mag) and their tangential velocities on the celestial sphere. Besides, for a brighter subset of those stars (see next section) we will derive further quantities such as radial-velocity, metallicities, stellar chemical abundances and interstellar extinctions.
Gaia, similarly to HIPPARCOS (Perryman et al., 1989), is a slowly spinning satellite that measures the crossing times of targets transiting the focal plane, see Lindegren & Bastian (2011). The observation times then indicate the position of the sources, in the along-scan direction, of the source respect to the instrument axes. The astrometric catalogue is built up from several of those observation by AGIS (Astrometric Global iterative Solution, Lindegren et al. (2012) and Lindegren et al. (2016a)). Simultaneously AGIS uses a subset of well-behaved sources (bright, stable and point-like) to continuously calibrate the instrument pointing (attitude) as a function of time and the geometric calibration. This feature of AGIS makes *Gaia* a self-calibrating mission.
A pan-European collaboration composed of several hundred astronomers and software specialists (the Data Processing and Analysis Consortium, DPAC) takes care of the data processing and analysis.

2.1.1 Scientific apparatus

Gaia is equipped with two three-mirror anastigmatic (TMA) telescopes, with apertures of 1.45 m $\times$ 0.50 m, which illuminate a shared focal plane. Following the same scan mech-

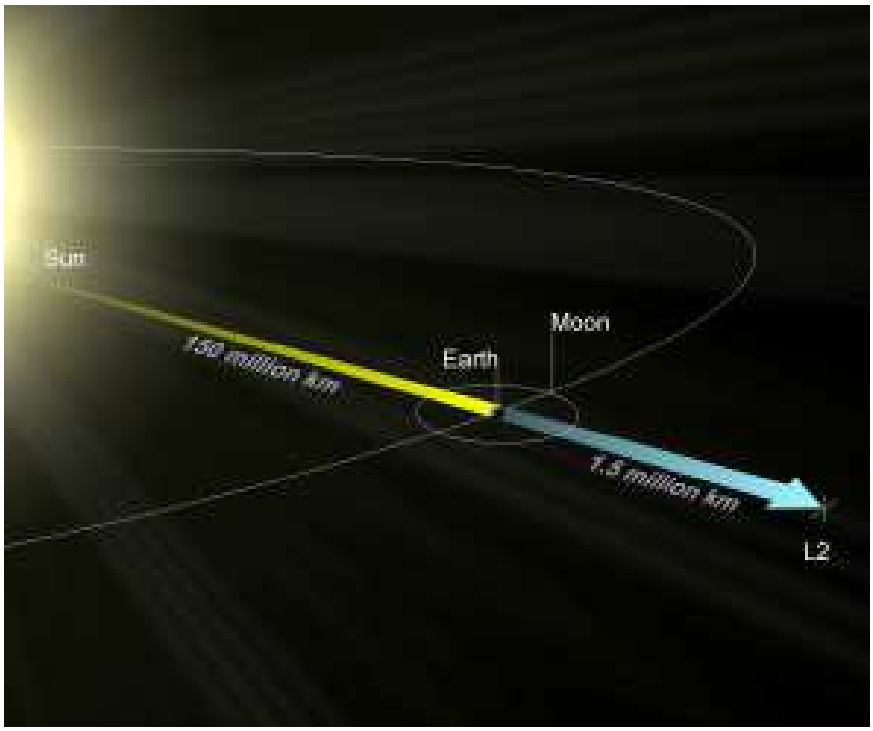

Figure 2.1: *Gaia* position with respect to the Earth's orbit (from www.http://sci.esa.int/gaia).

anism employed in HIPPARCOS (Perryman et al., 1989), *Gaia* scans the sky, spinning uniformly around an axis that forms an angle ξ = 45° from the Sun direction with a spin rate of $\omega_z = 60'' \; s^{-1}$. This scanning law maximizes the uniformity of sky coverage and ensures the highest possible astrometric accuracy.
The inclination to the Sun has been chosen in order to obtain the maximum parallax sensitivity.

The telescopes point to different directions forming the basic angle $\Gamma = 106^{\circ}.5$. The basic angle is an essential aspect of *Gaia* measurement principle, because it permits to derive absolute parallaxes from the relative ones. Indeed, this large angle allows us to measure the relative parallactic displacements between stars that have a substantially different parallax factor, for details see Gaia Collaboration et al. (2016b).
The focal plane carries 106 CCD detectors, arranged in a mosaic of 7 across-scan rows and 17 along-scan strips, for a total of 938 million of pixels. It plays a major role with important tasks such as: (i) adaptive optics and basic angle monitoring; (ii) object detection in the sky mapper (SM); (iii) astrometry in the astrometric field (AF); (iv) photometry and

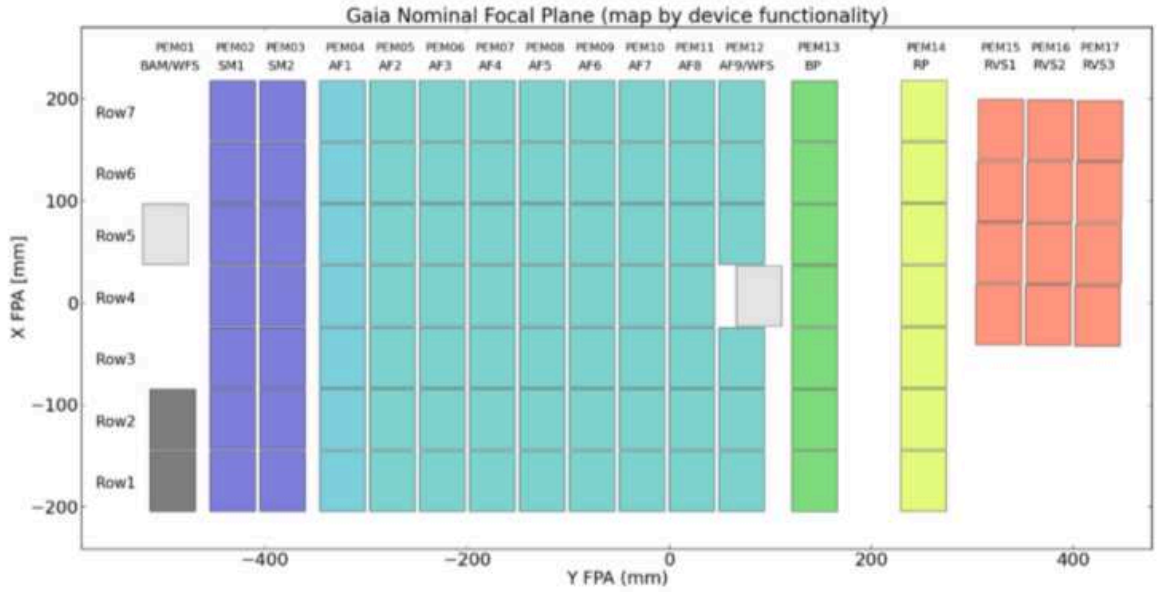

Figure 2.2: The *Gaia* focal plane. The 106 CCD are color-coded according to their different function. The light grey squares represent the wave-front sensors while the dark grey are the basic angle monitors. The two column of CCD designated for sky mapping are in violet. The AF is light blue and the BP and RP are respectively green and yellow. Finally the red CCD indicate the RVS. (Picture from Crowley et al. (2016)).

spectroscopy using two different photometer, a red one (RP) and a blue one (BP); (v) spectroscopy using the radial-velocity spectrometer (RVS). In Fig. 2.2 we report a schematic picture of the *Gaia's* focal plane, for further details see Kohley et al. (2012) and Crowley et al. (2016).

The BP works at 330-680 nm while the RP at 640-1050 nm. The photometers permit to characterize which type of object is observed, such as stars or quasar, and to derive their physical parameters, such as interstellar reddening, surface gravities, metallicities, and effective temperatures for stars, photometric redshifts for quasars, etc. Furthermore photometry can be used to estimate and correct the chromatic shifts due to optical aberration, see Carrasco et al. (2017) for details about *Gaia* photometry.
The RVS covers the wavelength range of 845-872 nm. This region hosts strong lines such as the CaII triplet and the hydrogen Paschen series which permit robust radial velocity determinations. We also find a diffuse interstellar band located at 862 nm (Munari et al., 2008). The RVS will survey the whole sky at a rate of about 100 spectra per second, producing

about 15 billion spectra over the mission time for stars brighter than $G_{GRS} \sim 16$ ($\sim$ 150 million stars), see Recio-Blanco et al. (2016).

2.2 Scientific goal

Gaia 's main scientific goal is to locate the stars into the six-dimensional phase-space. Besides, *Gaia* will provide astrophysical properties, such as surface gravity, effective temperature, and metallicity of those stars.
The space environment and the *Gaia* design permit to reach accuracy, sensitivity, dynamic range, and sky coverage not achievable from ground-based surveys. In particular, astrometric data of *Gaia* are unique because global and because the micro-arcsecond astrometry precision is possible only from space.
The availability of such a homogeneous large data catalog permits investigations on various and very different topics, such as structure, dynamics, and evolution of the Galaxy, stellar physics, multiple star systems, stellar variability, unresolved galaxy and Quasars, exoplanets detection and fundamental physics. Gaia Collaboration et al. (2016b) offer a detailed review of *Gaia* 's scientific goals.

2.3 Gaia Data Release 1

As already mentioned a source is on average observed 70 times by *Gaia* during the 5 years of nominal lifetime of the mission. Then in order to have the ultimate catalog with all the sources at the highest accuracy achievable we have to wait the end of the mission and of the post-operational phase. The *Gaia* DPAC (Gaia Collaboration et al., 2016b) expects to release the final catalog for 2022-2023. For this reason, a series of intermediate release will be delivered during this period in order to allow the astronomical community to access to *Gaia* data earlier than the end of the mission, even if not at the maximum of their precision. At the moment only the first of those catalog was released, in the *Gaia* Data Release 1 (*Gaia* DR1), based on the data collected during the first 14 months of the mission.

2.3.1 Contents of *Gaia* DR1

The DR1 contain a total of 1 142 679 769 sources, including astrometry and G band photometry. The 97.725% of those sources are brighter than G$\sim$20.7, the 50% brighter than G$\sim$19, and the 2.275% brighter than G$\sim$14.5. The presence of a small subset of sources fainter of G = 21 mag is probably due to erroneous determination of the G-band flux that have however passed the quality preselection of the data, see Sect. 2.3.2. The typical uncertainties quoted on the mean value of G vary from 0.03 mag at the faint limit of the survey to 0.001 mag or better for bright stars (G $\lesssim$ 13).
The astrometric data is divided in two data sets:

1. *TGAS*: The *Tycho-Gaia* astrometric solution (TGAS) (Michalik et al., 2015), is a subset of 2 057 050 stars obtained combining the 93 635 stars in common with HIPPARCOS (ESA (1997), van Leeuwen (2007)) and the 1 963 415 stars in common with Tycho-2 (Høg et al., 2000) in order to provide a complete astrometric single-star solution. On average the uncertainty for the positions is about 0.3 mas. The same value is obtained for parallax uncertainty. The parallaxes are also affected by a systematic of 0.3 mas on the zero point (see Sect. 2.3.3). For the proper motion the mean uncertainty is about 1 mas yr^{-1} for the stars in common with Tycho-2 and 0.06 mas yr^{-1} for the stars in common with HIPPARCOS.
   In Fig. 2.3 it is shown the distribution of the sources in magnitude.

2. *Secondary data set*: The secondary data set contains the remaining sources (1 140 622 719), for which, with 14 month of observation, it was only possible to provide positions with a typical uncertainty of about 10 mas.

The reference frame of positions and proper motions is aligned with the International Celestial Reference Frame (ICRF) referring to the epoch J2015.0, with a precision of 0.1 mas, and non-rotating with respect to ICRF to within 0.03 mas yr^{-1}.
Furthermore the DR1 contains the light curves for 3194 variable stars, of which 599 are Cepheid (43 newly discovered) and 2595 RR Lyrae (343 new).

2.3.2 Data validation

Before the release of *Gaia* DR1 catalog the DPAC paid particular attention to the validation of the *Gaia* DR1 data. The first step was an internal control of the data quality performed on

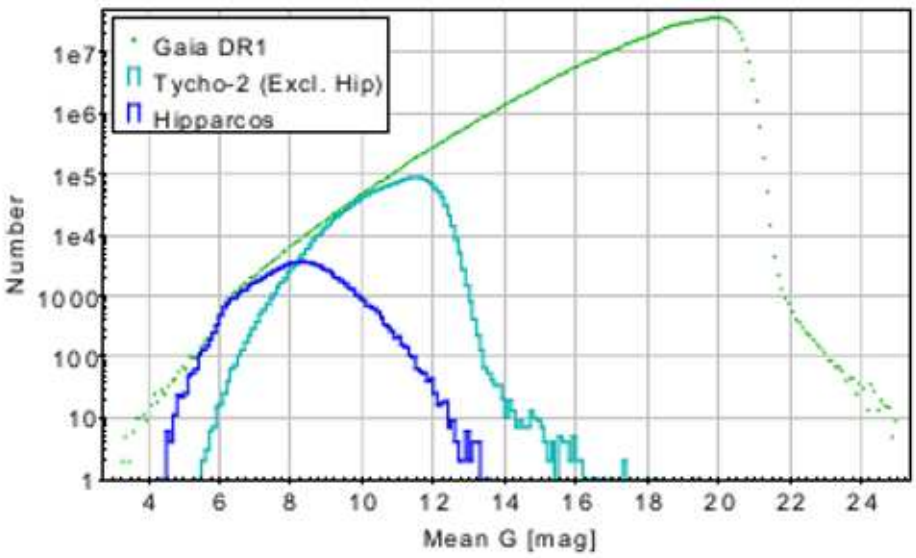

Figure 2.3: Distribution of the mean values of G for all Gaia DR1 sources shown as histograms with 0.1 mag wide bins. Image from Gaia Collaboration et al. (2016a).

astrometric data (see Lindegren et al. (2016a)), on photometric data (see Eyer et al. (2017)) and on variable stars (see Evans et al. (2017)).
A second quality check was then performed on the whole DR1 data considered together. Arenou et al. (2017) describe this validation performed on all the catalog. They found a series of minor problems that was overtaken by filtering the data before they are incorporated into the data release, or by addressing them as know limitations of *Gaia* DR1. Several filters were applied to the data, see Gaia Collaboration et al. (2016a) for details.

2.3.3 Limitations of *Gaia* DR1

The incomplete nature of *Gaia* DR1 summed with the validation step discussed in the previous Sect. create a series of weakness, listed below, in the final catalog.

1. DR1 contains solutions obtained in less than a quarter of the nominal lifetime of the mission. TGAS for its full astrometric solution uses less than 1% of the data volume expected for the final astrometric solution.

2. The use of Hipparcos and Tycho-2 sources as prior data for TGAS imposes to it the brightness limit of those catalog, V $\lesssim$ 11.5 mag.

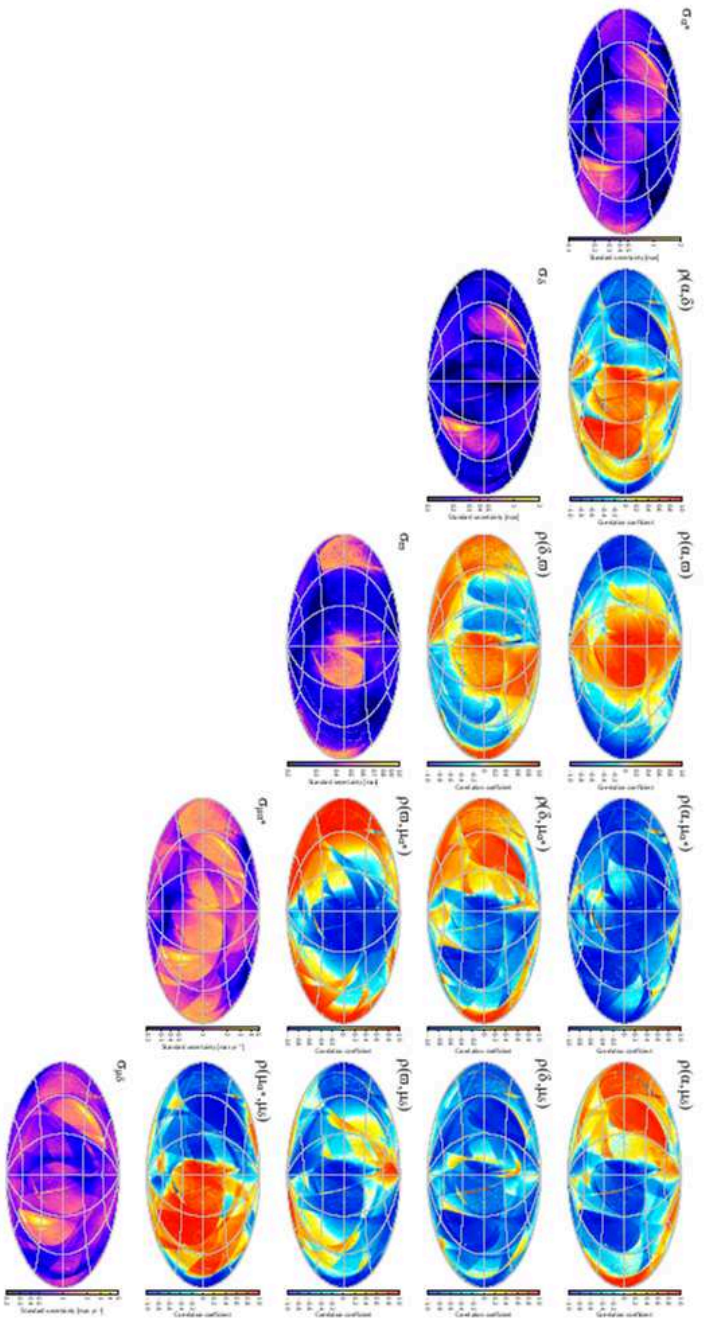

Figure 2.4: Statistic uncertainties for TGAS dataset. The standard uncertainties in α, δ, $\mu_{\alpha*}$, μ_δ and ϖ are shown on the main diagonal. Off-diagonal, the correlation coefficients are plotted between the corresponding parameters on the main diagonal (in the range [-1,1]). All maps use an Aitoff projection in equatorial (ICRS) coordinates, with origin $\alpha = \delta = 0$ at the center and α increasing from right to left. figure from Lindegren et al. (2016b).

3. The astrometric solution, including the calibration refinement of line-spread function (LSF) and point-spread function (PSF), is a part of a processing loop. The present solution suffers largely both of chromaticity effect and of uncalibrated variations of the LSF and PSF, see Lindegren et al. (2016a) for details.

4. Many stars brighter than G $\sim$ 7 are heavily saturated and the instrument configuration is difficult to calibrate due to their sparsity. This involves a lack for those objects in *Gaia* DR1, see Gaia Collaboration et al. (2016a).

5. The filters applied during the validation stage affect the completeness of Gaia. Furthermore in very crowded area ($\sim$ 400 000 stars per square degree) the effective magnitude limit of *Gaia* may be brighter by more than 2 mag, see Arenou et al. (2017) for details.

6. The different number of observation for different regions of the sky, due to the limited fraction of the *Gaia* scanning program contained in DR1, produces inhomogeneities on proper motions errors around the whole sky, see Chapter 4.

7. The astrometric error distributions can not be described separately. Correlations between astrometric parameters are given in dimensionless units (values in the range [-1,1]), see Fig. 2.4.

8. All sources are considered single stars, and the radial component of their motions is ignored. Then, all the proper motion variations caused by orbital motion in binaries or perspective effects are neglected.

2.3.4 Parallax zero-point uncertainty

Another important aspect of the *Gaia* DR1 are local systematic biases up to $\pm$0.3 mas affecting the TGAS parallaxes. Those biases was studied by Arenou et al. (2017) in the astrometric validation of GDR1. They consider 135000 quasars. The parallax of a quasar is considered null, then the study of their parallaxes gives direct information about parallax errors and their properties. They select sky regions of 2°, with at least 20 quasar, computing the mean parallax value for each region, see Fig 2.5. This method have the disadvantage of not mapping all the sky and in particular the Galactic plane, because of the lack of those objects present on it. They detect systematics with an average value of 0.3 mas amplitude, with local variations.

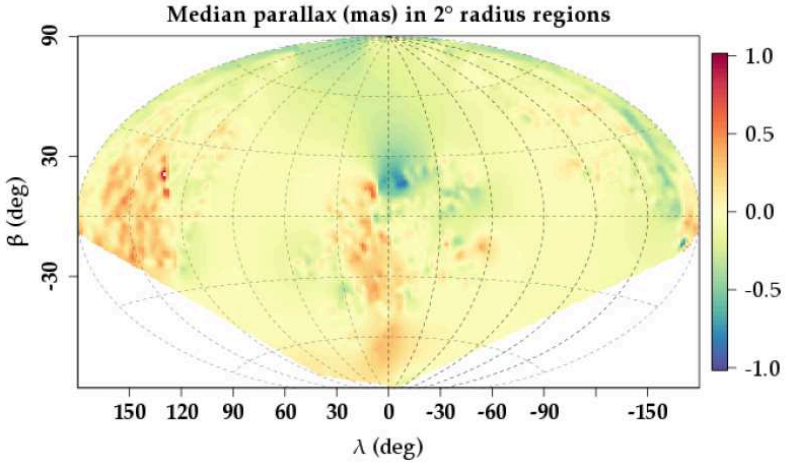

Figure 2.5: Map of mean parallax values for quasars in sky regions of 2°, ecliptic coordinates.

3 Photometric study of three open clusters

In this Chapter we rely on the photometric data to study the properties of three open clusters, NGC 2225, NGC 2243, NGC 6134. Two of them are located in the anti-center direction, while the other is in the inner disk. Both regions are specially interesting. In comparison with previous studies, here we take advantage of a larger field of view (FoV) which permits to analyse the external regions of the clusters, while allowing for a better field contamination correction. These objects will be used to validate the Bayesian analysis tool BASE-9 (see Chapter 4). The structure of the Chapter is as follows: in Sect. 3.1 first we present the selected cluster; in Sect. 3.2 we describe the data and the data reduction; in Sect. 3.3 we describe the methods, and the stellar models we use to analyze the data; in Sect. 3.4 we present the results. Finally in Sect. 3.5 we use the data to validate our Bayesian classification method.

3.1 The selected clusters

In this section we present the main properties of the three selected clusters as defined in literature.

3.1.1 NGC 2225

NGC 2225 is an OC located in the direction of MW's anti-center in the third quadrant (l $= 218°.78$; b $= -9°.86$). The third quadrant is a very interesting region, where young OCs can trace structure of the spiral arms , and the can be used to define the Galactic disc radial

abundance gradient outside the solar circle (see, e.g., Vázquez et al. 2008, see Moitinho et al. 2006).

In addition, the outer disc of the Milky Way is an important stellar repository reflecting the history of any migration that may have occurred in our Galaxy. Previous study of NGC 2225 is done by Carraro et al. (2005) (hereafter Car05). They obtained BVI photometry with the CCD camera on the 1.0-m telescope at Cerro Tololo Interamerican Observatory (CTIO, Chile), on a field of view (FoV) of about 4×4.1 arcmin^2. They found an age of 1 Gyr, a metallicity of $Z = 0.008$, and a reddening and distance modulus of $E(B-V) = 0.35$ mag and $(m-M) = 13.6$ mag.

3.1.2 NGC 6134

NGC 6134 is an OC located in the fourth quadrant (l $= 334^{\circ}.92$; b $= -0^{\circ}.20$). This cluster is a very interesting object. The latest studies indicated an age around 1 Gyr. As mentioned in Sect. 1.4, there are very few the OCs older than 1 Gyr in the inner part of the galaxy disc, in particular near the disc plane.

NGC 6134 is a well-studied OC. The first photometric study was carried out by Lindoff (1972) who derived, by means of UBV photometry, a color excess $E(B-V) = 0.45$ mag, a distance of ~ 700 pc and an age of about 0.7 Gyr. Based on UBV CCD data, Kjeldsen & Frandsen (1991) determined a reddening of $E(B-V) = 0.46 \pm 0.03$ mag, $(m-M)_0 = 9.80$ mag and an age of 0.9 Gyr. Claria & Mermilliod (1992), using UBV and Washington photometry, obtained a reddening of $E(B-V) = 0.35 \pm 0.02$ mag and a distance of about 760 pc; from the UV excesses they derived a metallicity [Fe/H] $= -0.05 \pm 0.12$ dex. Bruntt et al. (1999) analysed Strömgren photometry and determined an interstellar reddening $E(b-y) = 0.263 \pm 0.004$ mag (which translates to $E(B-V) = 0.365$ mag, according to Cousins & Caldwell (1985)), [Fe/H] $= 0.28 \pm 0.02$ dex, and an age of 0.69 ± 0.10 Gyr from isochrone fitting. Ahumada (2002), from $BVRI$ CCD observations determined a color excess in the range $0.29 \leqslant E(B-V) \leqslant 0.37$ mag, an age of 1.25 Gyr, and a distance of about 1080 ± 50 pc. In a more recent study Ahumada et al. (2013) (hereafter Ahu13), using $UBVI$ photometry, found an age between 0.82 and 0.95 Gyr and a dereddened distance modulus of 10.5 mag. Rasmussen et al. (2002) carried out an abundance analysis of the δScuti stars and confirm the high metal content of this cluster: [Fe/H] $= 0.38 \pm 0.05$ dex. From high-resolution spectra, Carretta et al. (2004) derived an iron abundance of [Fe/H]

$= 0.15 \pm 0.03$ dex and a color excess $E(B-V) = 0.355 \pm 0.005$ mag.

3.1.3 NGC 2243

NGC 2243 is an old OC located in the third quadrant, in the direction of the galactic anticenter (l $= 239°.478$; b $= -18°.014$) at R_G = 10.76 kpc. Like most of the old OCs it is located at high altitude on the galactic plane (|z| = 1.1 kpc). It is one of the most metal-poor OCs known, with a metallicity almost as sub-solar as that of 47 Tucanae, which, with a metallicity of [Fe/H] $= -0.76 \pm 0.04$ dex, is considered a metal rich GC (Koch & McWilliam, 2008).

For this reason NGC 2243 is a widely studied object. The first study of the cluster was performed by Hawarden (1975), using photoelectric UBV and photographic BV photometry. He pointed out for first time the peculiar sub-solar metallicty of the cluster, finding a value of [Fe/H] = -0.5. In addition he found an age of 5 ± 0.8 Gyr, a distance modulus of $(m-M)_0$ = 12.8 and a reddening of $E(B-V)$ = 0.006. This result was partially confirmed soon after by van den Bergh (1977). Using UBV photometry he found an age of 5 Gyr, $(m-M)_0$ = 13.3, and a reddening of $E(B-V)$ = 0.006.

The first study with CCD photometry was performed by Bonifazi et al. (1990) in BV bands. They delimited the age in a range between 3-5 Gyr and the metallicity in one between Z = 0.003 and Z = 0.006. They found $(m-M)_0$ = 12.8-12.8 and $E(B-V) = 0.006 - 0.008$. Bergbusch et al. (1991) (hereafter Berg91)found an age of 5 ± 1 Gyr and a distance modulus of $(m-M)_V$ = 13.05 (assuming $E(B-V) = 0.006$). They found a metallicity of [Fe/H] = -0.47 and an oxygen overabundance of [O/Fe] = 0.23. Gratton & Contarini (1994) analysing the high resolution spectra of two red giants of the cluster found [Fe/H] = -0.48 ± 0.15 and [Ca/Fe] =0.18 ± 0.17. Using VI bands Kaluzny et al. (1996) (hereafter Kal96) obtain a reddening value of $E(V-I) = 0.10 \pm 0.04$. Moreover they identified two W UMa-type system and three detached eclipsing binaries. With the intermediate-bands system $uvbyCaH\beta$, Anthony-Twarog et al. (2005) found a metallicity of [Fe/H] = -0.57 ± 0.03, an age of 3.8 ± 0.2 Gyr, an apparent modulus of $m - M = 13.5 \pm 0.1$ and a reddening of $E(b-y) = 0.039 \pm 0.003$, corresponding to $E(B-V) = 0.055 \pm 0.004$. Kaluzny et al. (2006) analysed the spectra of the five binary systems and two red giants. They obtained a distance modulus of $(m-M)_V = 13.24 \pm 0.08$. Furthermore using age-radius and age-luminosity relations they derived from one of the binary system an age of

4.35 ± 0.25, assuming [Fe/H] = -0.525. VandenBerg et al. (2006) re-analysed the BV photometry by Bergbusch et al. (1991) and obtained an age of 3.1 Gyr, a metallicity [Fe/H] = -0.61, an α-elements enhancement [α/Fe] = 0.3 and a distance modulus $(m - M)_V$ = 13.15 (assuming $E(B - V)$ = 0.062). Finally François et al. (2013) investigate the star mass value at which disappearance of Li occurs in this metal-poor cluster. They analysed the FLAMES+GIRAFFE spectra of 100 stars, obtaining [Fe/H] =-0.54 ± 0.10 and [Ca/Fe] =0.00 ± 0.14.

3.2 The data

In this section we present the observations, the data reduction procedures and the photometric calibration.

3.2.1 Observations: NGC 2225

NGC 2225 was observed with the the Large Binocular Camera (LBC) mounted at the Large Binocular Telescope (LBT, Mount Graham, Arizona) on Oct. 23 2011, see Sect. 3.2.4. The LBC is composed by two different cameras, one optimized for the UV-blue filters and one for the red-IR ones, mounted at each prime focus of LBT. Each LBC uses four EEV chips (2048×4608 pixels) placed three in a row, and the fourth above them and rotated by $90°$. The FoV of LBC is equivalent to 22×25 arcmin^2, with a pixel scale of 0.23 arcsec/pixel.

The cluster center was positioned in the central chip (chip #2) of the mosaic. We observed in the B filter with LBC-Blue camera and in V and I with LBC-Red. No dithering pattern was adopted. The data-set consists of 21 exposures, 7 for each filter. The exposures times are reported in Table 3.1. Short, medium, and long exposures where performed to cover a large magnitude range from the brightest sequence of giants down to main sequence (MS) dwarfs five magnitude fainter than the turn-off (TO).

filter	exposures	date	airmass
B	$1 \times$ 1s, $3 \times$ 5s, $3 \times$ 90s	2011 October 23	1.36
V, I	$1 \times$ 1s, $3 \times$ 5s, $3 \times$ 60s	2011 October 23	1.36

Table 3.1: Logbook of the observations for NGC 2225.

3.2.2 Observations: NGC 6134

NGC 6134 images in the B, V bands were retrieved from the ESO archive [1]. The data were taken with the WFI mounted at the Cassegrain focus of the 2.2-m MPG/ESO telescope at La Silla (ESO, Chile). WFI is composed by a mosaic of 8 CCDs (2150×4130 pixels), 2 row of 4 chips, with a FoV of 33×34 arcmin^2 and a pixel scale of 0.238 arcsec/pixel. The cluster center was positioned in the center of the mosaic, i.e. in the corners of 4 chips (CCDs #2, #3, #6, and #7), and a dithered pattern strategy was adopted to cover the mosaic gaps. The exposure time strategy is reported in Table 3.2.

filter	exposures	date	airmass
B	$8 \times$ 3s, $7 \times$ 120s	2000 June 10	1.25 - 1.74
V	$7 \times$ 2s, $7 \times$ 90s	2000 June 10	1.38 - 1.86

Table 3.2: Logbook of the observations for NGC 6134.

3.2.3 Observations: NGC 2243

WFI B, V, I images of NGC 2243 were retrieved from the ESO archive. The cluster is totally contained in the chip #2 of the CCD mosaic. We reduced chip #2 for the cluster photometry and chip #3 to evaluate the field contribution. The exposure time strategy is reported in Table 3.3.

3.2.4 The data reduction

In this section we briefly summarize the data reduction procedures and the calibration.

[1] http://archive.eso.org

filter	exposures	date	airmass
B	1×10s, 3×300s	2012 January 22	1.085-1.112
	2×30s	2012 December 10	1.349-1.462
V	2×15s, 3×600s	2012 January 22	1.031-1.064
	2×60s	2012 December 10	1.333-1.443
I	1×20s, 3×900s	2012 January 24	1.001-1.017
	2×90s	2012 December 10	1.317-1.442

Table 3.3: Logbook of the observations for NGC 2243.

From images to catalogs

The raw LBC images are processed by a pipeline developed by the Large Survey Center team at the Rome Astronomical Observatory[2]. The source detection and instrumental photometry are performed independently on each image, using the point spread function (PSF)-fitting code `DAOPHOTH/ALLSTAR` (Stetson 1987, Stetson 1994). We sample the PSF using the highest degree of spatial variability allowed by the program because the LBC images are affected by spatial distortions.
We use `DAOMASTER/DAOMATCH` programs (Stetson 1987, Stetson 1994) to obtain an average instrumental photometry for each chip in each photometric band. Then the catalogs with same band but different exposure time are cross-matched. After this the three catalogs (short, medium and long exposure time) are selected in different magnitude ranges, in order to obtain the faintest stars from long exposures and to recover the brightest ones, saturated in the long and medium exposures, from the short exposure.
We then use the `CATAPACK`[3] software (developed by Paolo Montegriffo at the INAF - Osservatorio Astronomico di Bologna) to obtain a unique photometric catalogue.

Pre-reduction of the WFI images was done by means of the Iraf[4] software `zerocombine`, `flatcombine` and `ccdproc` to correct for bias and flatfield and to trim the overscan region. `CATAPACK` is used to to align and merge the photometric catalogs.

[2]http://www.oa-roma.inaf.it/

[3]http://www. bo.astro.it/∼paolo/Main/CataPack.html

[4]http://iraf.noao.edu/

Artificial stars test

We derived the completeness level of the photometry by means of extensive artificial stars tests (AST) following the recipe described in Bellazzini et al. (2002). The procedure consists of adding stars of known magnitude and color in the FITS images, and then re-doing exactly the same photometric reduction. The AST allows to estimate the completeness and the photometric errors in a robust way (see e.g. Gallart et al. 1999; Harris & Zaritsky 2001; Cignoni et al. 2011). The artificial stars were created following the observed luminosity distribution in the frames, intentionally adding a large fraction of faint artificial stars to better test the completeness at faint magnitudes. For this reason, we performed the ASTs only on the long exposure frames. In order to avoid effects due to artificial crowding and blending, we imposed that the artificial stars should not be more than 3% of the observed stars in the frames and not closer than about three times the measured FWHM of the PSF. We repeated the procedure 100 times in each filter in order to have at least 10^5 stars, which guarantees a statistically significant estimate of the completeness level and photometric error.

3.2.5 The photometric calibration

NGC 2225

For the photometric calibration we used Landolt's stars (see Landolt 1992) to tie our instrumental magnitudes to the Johnson-Cousins photometric system. Landolt fields L92, L98, L101 and L113 were observed at two different airmasses (1.2 and 1.55) encompassing the cluster airmass (1.36). The limited number of observations did not allow us to obtain an accurate estimate of the extinction coefficients. We use the standard values suggested for the LBC instrument.

filter	zero point	color term
B	2.749 $\pm$0.027	-0.154 $\pm$0.033
V	2.625 $\pm$0.016	-0.072 $\pm$0.019
I	2.363 $\pm$0.022	0.028 $\pm$0.029
V	2.628 $\pm$0.017	-0.073 $\pm$0.021

Table 3.4: Coefficients of the calibration equation for zero points and color terms for NGC 2225.

The adopted calibration equation is:

$$M_i = m_i + ct(m_i - m_j) + zp_i + K_i X \tag{3.1}$$

where M_i indicates the calibrated magnitude i (either B or V or I), m_i the instrumental one, ct the color term, zp_i the zero point, K_i the atmospheric extinction coefficient, and X the airmass. The calibration value for zero points and color terms are reported in Table 3.4, the calibration relations are shown in Fig. 3.1.

Since our calibration was of insufficient quality, we refine it aligning our photometry to Carraro et al. (2005). However Car05 invoke a non-standard extinction law to explain the $V - I$ observational colors. For this reason we make use only of the $B - V$ color.

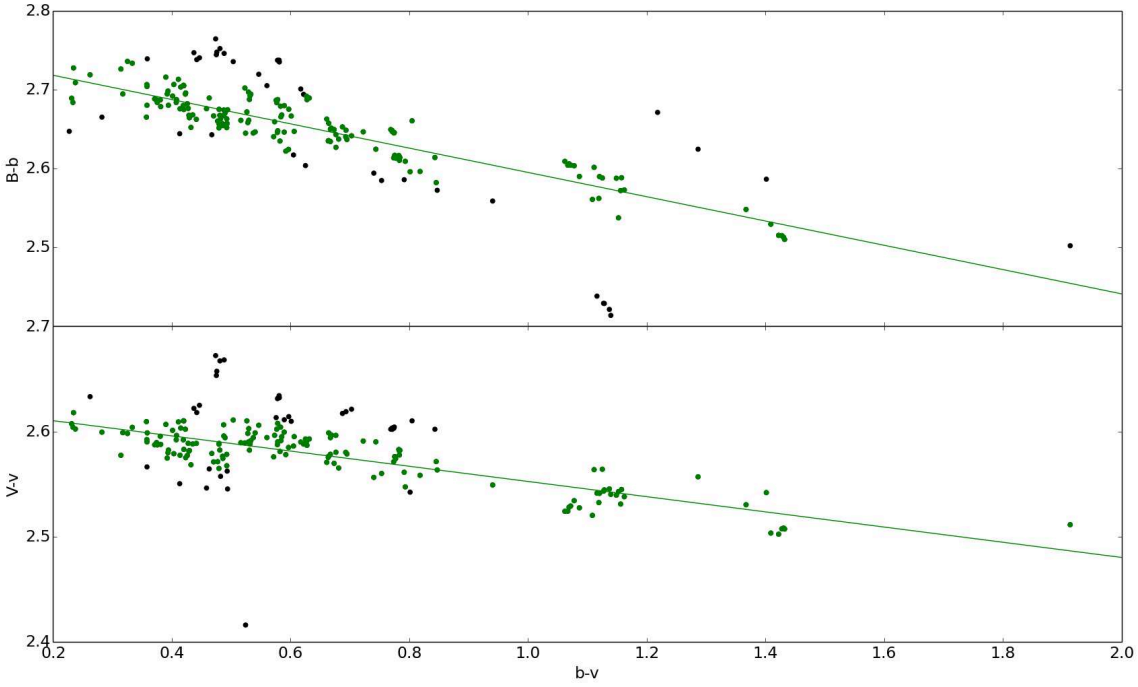

Figure 3.1: Calibration relations for NGC 2225. The lines are computed using only the green dots, retained after a 1σ clipping.

NGC 6134

In this case there were no observations of standard stars and we calibrated our catalog using Ahu13 photometry. In Table 3.6 are reported the coefficients of the used calibration equation:

$$M_i = m_i + ct(m_i - m_j) + zp_i \tag{3.2}$$

filter	zero point	color term
B	4.861 $\pm$0.015	0.326 $\pm$0.056
V	3.922 $\pm$0.016	-0.166 $\pm$0.058

Table 3.5: Coefficients of the calibration equation for zero points and color terms for NGC 6134.

Here M_i indicates the Ahu13 magnitude, whereas ct and zp_i have the same meaning as that in Eq. 3.1. In this case the calibrated magnitude is already airmass corrected by the authors and then the term $K_i X$ it should not be considered.

The calibration relations are shown in Fig. 3.2.

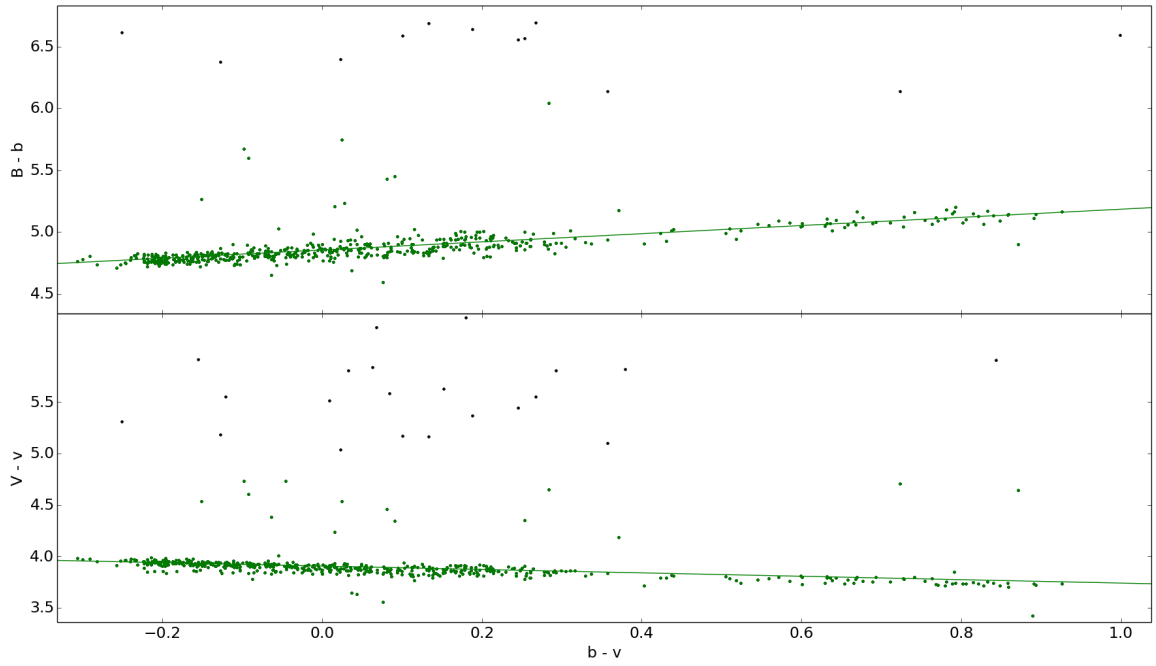

Figure 3.2: Calibration relations for NGC 6134. The lines are computed using only the green dots, retained after a 1σ clipping.

NGC 2243

ESO archive standard fields observations of photometric standards for NGC 2243 were available. However the weather reports indicated the presence of thin clouds during the

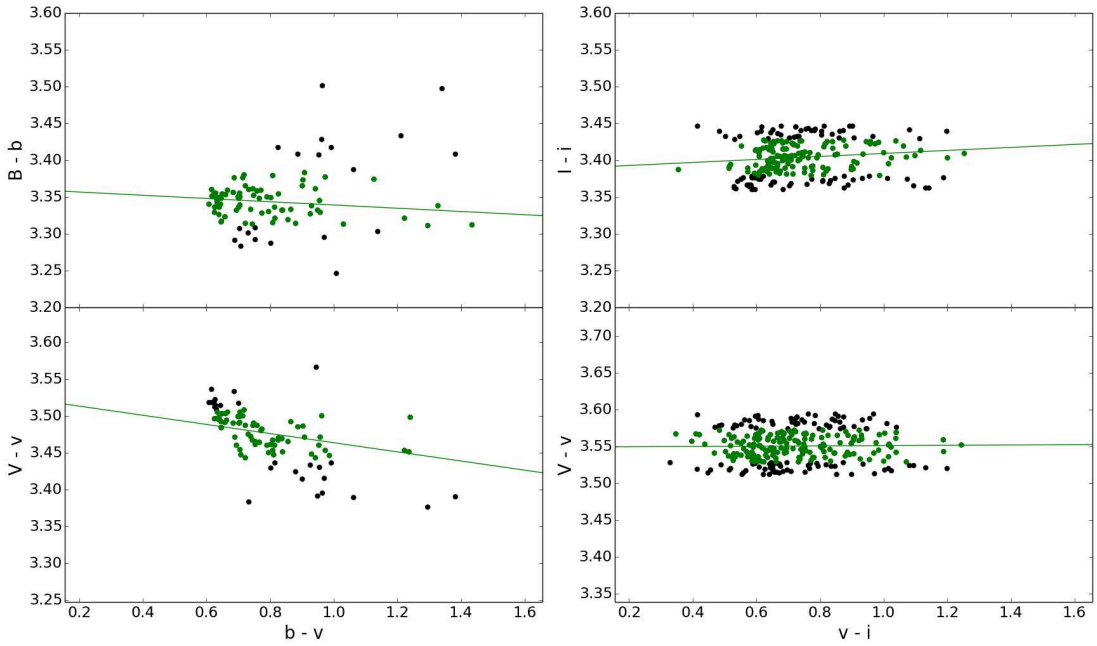

Figure 3.3: Calibration relation for NGC 2243. The lines are computed using only the green dots, retained after a 1σ clipping.

observation, that could compromise the photometric quality of the night. We preferred to align our catalog to literature photometries, using eq. 3.2. We aligned BV with Bergbusch et al. (1991) and VI with Kaluzny et al. (1996). The zero points and color terms for the calibrations are reported in 3.6, the calibration relations are shown in Fig. 3.3. The V band calibration versus both colors show a good agreement.

filter	zero point	color term
B	3.361 $\pm$0.131	-0.022 $\pm$0.09
V	3.526 $\pm$0.043	-0.062 $\pm$0.002
I	3.241 $\pm$0.117	0.063 $\pm$0.045
V	3.5 $\pm$0.078	0.015 $\pm$0.003

Table 3.6: Coefficients of the calibration equation for zero points and color terms for NGC 2243.

3.3 The methods

In this section we present the methods we use to determine the OCs properties, such as age, distance, extension, metallicity, reddening and membership. We also describe the main assumptions concerning stellar isochrones

CMDs analysis allows us to derive information about OCs parameters, such as age, metallicity, distance and reddening. CMDs contain information about cluster evolutionary stage, physical parameters, binary fraction and presence of anomalous stars. Understanding their features might not be straightforward in many cases. The majority of OCs have few hundred members and that makes it difficult to distinguish them from field stars. At bright magnitudes the field contamination is less important but the cluster stars are more massive and then fewer in number. The identification of cluster member candidates and the determination of the prominent evolutionary phases (like TO and RC) are two fundamental aspect in CMDs analysis.
Having at our disposal a large FoV permit to get information both on the cluster and on the field, i.e. it is useful to estimate up to what magnitude the field stars contamination is dominant. This in turn can help in the membership determination.

3.3.1 Radial profile

OCs have a variety of appearance, from highly concentrated to sparse irregular distribution. It is then not simple to define a unique method to determine OCs structural properties from observations. Poorly populated clusters show the surface brightness of an isothermal sphere distorted by the action of tidal fields, see for examples King (1966) or Mathieu (1984). Typical value r_{core} and r_{tidal}. are 1-2 pc and 10-25 pc, respectively. Furthermore, OCs lie generally in very crowed regions of disc, then the determination of r_{tidal} suffers very much from uncertainty. To identify the regions where the cluster population is dominant, we derive the radial surface density profile and the radial surface brightness profile.
The first step is to identify the center of gravity (C_{grav}) of the OCs. To calculate C_{grav} we follow the procedure described by Montegriffo et al. (1995). First a sample of clusters stars as much as possible cleaned up from field contamination is selected. To take into account only cluster members, we select a small circular area (1 arcmin radius) centered on literature OCs center. Inside this area are taken in account only the stars that lie in

the color interval delimited by the turnoff and RC. Then we define five different samples delimited by an inferior bright limit around the magnitude at which the field population become predominant, and scaled from each other by 0.5 mag.

The center for each of the five samples is determined simply averaging the α and δ coordinates of stars in them. C_{grav} is given by the average of these five estimated centers. In this way we reduce further the possibility that the C_{grav} determination is affected by field stars contribution. In Fig. 3.4 we show an example of the method applied to NGC 2243, one of the clusters studied in this work (see next chapter).

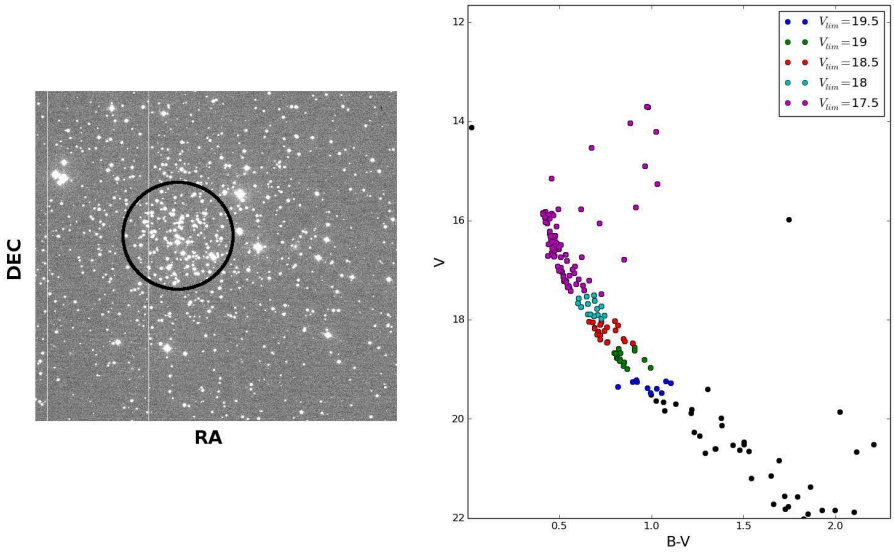

Figure 3.4: *Left panel:* Image of NGC 2234 with highlighted (black circle) the region used to derive C_{grav}. *Right panel:* CMD of the stars contained in the black circle. Colored dots define the five range of stars used in the estimation of C_{grav} (respectively brighter than V 19.5, 19, 18.5, 18 and 17.5), black dots represent stars rejected.

Once C_{grav} is derived, we calculate the radial surface density and the radial surface brightness profiles following the method illustrated by Lanzoni et al. (2010). The C_{grav} is used as center of a set of concentric annuli in which the cluster catalog is divided, from 0 up to a radius which visually delimits a region that contains the whole cluster. Each annulus is then divided in four quadrants and the surface density and brightness are calculated for each one of them, down to a limiting magnitude. The total surface density and brightness of each annulus is obtained as the mean of the density of the four quadrants. Lastly, in order

to remove the background contribution, the smallest density value among all the annuli is subtracted from the others.
This procedure is repeated for different magnitude bins. In this way the density profiles of single evolutionary phase stars (such TO and RC stars) as well as the total cluster stars can be examined.
The radial surface density and brightness profiles decrease at larger radii, until they reach a constant value. We define the cluster radial extent as the radius at which this occurs.

3.3.2 OC parameter derivation

Isochrones

Once the prominent features of OCs are identified on the CMDs, the determination of parameters can be done. We perform as first step a comparison between observed CMDs and a set of isochrones, to derive the preliminary range of parameters. Isochrones are the representation on H-R diagrams of an instant of the life of a stellar population. Isochrones vary as a function of two main parameters, age and metallicity. This means that finding the best fit isochrone consists in finding which combination of intrinsic parameters (age and metallicity) and of parameters such as distance and reddening, better mimic the feature of the OC on the CMDs.
The best clock of OCs age is the intrinsic luminosity of its TO. The TO is the bluest point of the MS and corresponds to the end of fuel for H-burning in the center of star's core. A star spends about 90% of its lifetime on the MS and then the position of the TO has a much greater sensitivity to age variations respect to the other evolutionary phases. Furthermore having a good definition of the TO permits to measure the difference in magnitude and color with the RC, which in turn depends on the combination of age and metallicity, see Stetson et al. (1996).

However we do not work with intrinsic luminosities and temperatures but with apparent magnitudes. Then, as mentioned before, also distance and reddening are involved in this kind of analysis and play a role in the position of the isochrones on the CMDs. This can bring degeneration into the CMS fit, because the effect of these parameters is not identified on CMDs independently from age and metallicity. Thus, it is often useful to use a differential method, tying age to the difference in magnitude between two features in the CMD. For example both age and distance modulus (DM) fix the magnitude of the MS tip, but the age

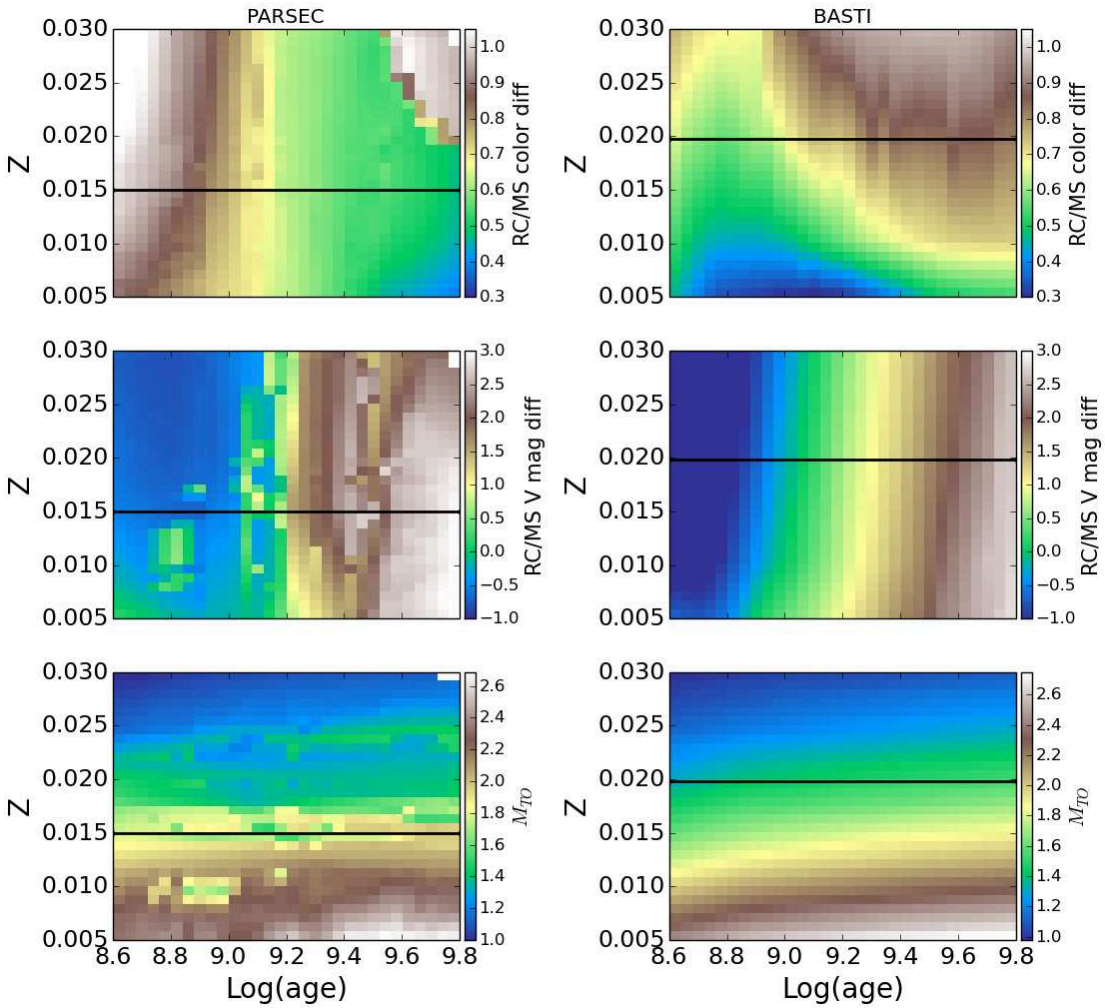

Figure 3.5: Color maps as a function of Z and Log(age). *Upper panels:* $B - V$ color differences between the RC and the TO . *Middle panels:* magnitude differences between RC and TO in V band. *Lower panels:* Mass of TO stars. The left column is obtained from PARSEC isochrones the right column from BASTI ones. The black lines indicate the solar metallicity model in the two different cases.

influences also the mutual position of TO and RC and then the effect of the two parameters can be distinguished. A different matter is the degeneration between the age, reddening and the metallicity, specially in the visible bands where the absorption have a stronger impact with respect to IR-bands. To reduce the impact of these degenerations, when possible it can be useful to have at our disposal at least two different colors. In the cases where only one color is available for the analysis, is difficult to find a unique solution without a previous

spectroscopic study that constrain the metallicity. We are able to define at most a possible range of parameters.
In the work presented in these pages we use as isochrones, the PARSEC Bressan et al. (2012) and the Bag of Stellar Tracks and Isochrones (BaSTI, Pietrinferni et al. (2004)). Different sets of isochrone produce slightly different results (see Fig. 3.5), due to different assumptions about opacities and treatment of convection, rotation, and transformation from theoretical to observational plane. Then in some cases it is useful to compare the results obtained by different sets in order to find which of them better reproduce the data.

Synthetic populations

After the isochrones analysis a more fine determination of parameters can be achieved performing a comparison between observed OC CMDs and LFs and a set of synthetic ones. The synthetic populations are built via Monte Carlo simulations starting from a set of isochrones. In this kind of analysis other parameters are involved, such binary fraction (f_b) and differential reddening (DR). Furthermore also the number of stars (N_*) of the cluster play an important role. Indeed the advantage to perform the analysis with synthetic populations instead of doing it with isochrones is the possibility to search not only a model that well reproduce the cluster shape on CMDs but also to compare the star counts at different magnitudes. The procedure to populate the isochrones and obtain a set of synthetic populations is described in section 3.3.2.
The observational number of stars in the cluster are imposed as input of Monte Carlo simulation. The completeness correction and the field star contamination are taken into account. Background/foreground star contamination as estimated in the external comparison field is added to the synthetic CMDs.
The f_b and the DR can be estimated independently. The DR is estimated from the width of the brighter part of the MS (where the photometric errors are negligible) and then fine-tuned together with f_b in order to reproduce all the MS width in the cluster central region.
When all these parameters (N_*, f_b and DR) are fixed, we can evaluate age, metallicity, distance and reddening. We subdivide the CMDs in magnitude bin and search for the synthetic CMD that best reproduce the count of stars in each bin. This allows us to put stronger constraints on the parameter determination.
We estimate the errors on the cluster's parameters considering both the instrumental photo-

metric errors and the uncertainties of the fit analysis, as done in Donati et al. (2012). The net effect of the former is an uncertainty on the luminosity and color of the cluster's stars and consequently on the evolutionary indicators used in our analysis. Concerning the uncertainties involved in the analysis, we noticed that the low number statistics typical of the OCs, like NGC 2225 (see section 3.1.1), makes evolutionary phases like the RC poorly defined and difficult to be clearly distinguished. With this in mind, we define the range of possible solutions as the ones that delimit the TO and fit the RC both in magnitude and color.
The uncertainties are assumed to be of the form:

$$\sigma^2_{E(B-V)} \sim \sigma^2_{(B-V)} + \sigma^2_{fit} \tag{3.3}$$

$$\sigma^2_{(m-M)_0} \sim \sigma^2_V + \sigma^2_{fit} + R^2_V \sigma^2_{E(B-V)} \tag{3.4}$$

$$\sigma^2_{age} \sim \sigma^2_{fit} \tag{3.5}$$

where R_V is $\frac{A_V}{E(B-V)}$.
To evaluate σ^2_{age} we use the two isochrones that bound respectively the blue and red edge of the TO. Their age difference gives us an estimate of the uncertainty on the age. Using the $\sigma^2_{(B-V)}$ and σ^2_V achieved from the ASTs, we obtain $\sigma^2_{E(B-V)}$ and $\sigma^2_{(m-M)_0}$.

FILLTHETEMPO

With the aim to perform a comparison between the observational CMDs and a set of artificial populations we have implemented a python code called `FILLTHETEMPO`.
The structure of the code is the following:

- uses isochrones from the desired set;
- applies a distance modulus and an extinction value given in input;
- applies a random extra value of reddening taken from a range given in input. In this way it reproduces the differential reddening (DR) effect;
- populates the isochrone with the desired number of stars by applying an Initial Mass Function (IMF, the Salpeter law Salpeter 1955 is used). The function is applied by extracting a number of random mass values equal to the number of stars chosen, in the

mass range of the isochrone (cut at a chosen value) following a probability function given by the IMF;

- assigns a magnitude and a color to each star using a mass-weighted interpolation of the magnitude and colors of the chosen isochrone;

- applies a random photometric errors from a range appropriate for the available photometry, as obtained from the AST;

- takes into account the completeness factor, as obtained from the AST;

- adds the desired percentage of photometric binary systems. Binaries are created adding the flux of a companion star created ad-hoc to the flux of a random synthetic star;

- adds the field stars contribution by using a given input catalogue. The appropriate choice of the external field is important to obtain an accurate synthetic CMD.

The code allows a preliminary investigation of the cluster's parameters. It uses a set of isochrones, only scaled in distance modulus and reddening, to be plotted against the cluster in order to study which combination of parameters better fits the observational CMD. This step is done to decrease the range of parameters to be used for the analysis with the synthetic CMD. This possibility is particularly convenient in cases such as NGC 2225 where the interpretation of the cluster evolutionary sequences is severely jeopardized by field contamination and by the low number of cluster stars, see 3.1.1.
When the preliminary isochrones fit is done, the code builds the synthetic CMDs and allows a visual and quantitative comparison with the observational one. In this phase other parameters are involved in the study, like binary fraction, the number of stars, the DR, the photometric error, the completeness level of the photometric reduction, and the field contamination. The comparison can be performed in several ways: 1) visually, by looking at the position on the CMDs of the relevant evolutionary features, 2) by comparison between the luminosity functions (LFs) of the observational and synthetic CMDs, checking if and where the difference in star counts is significant.

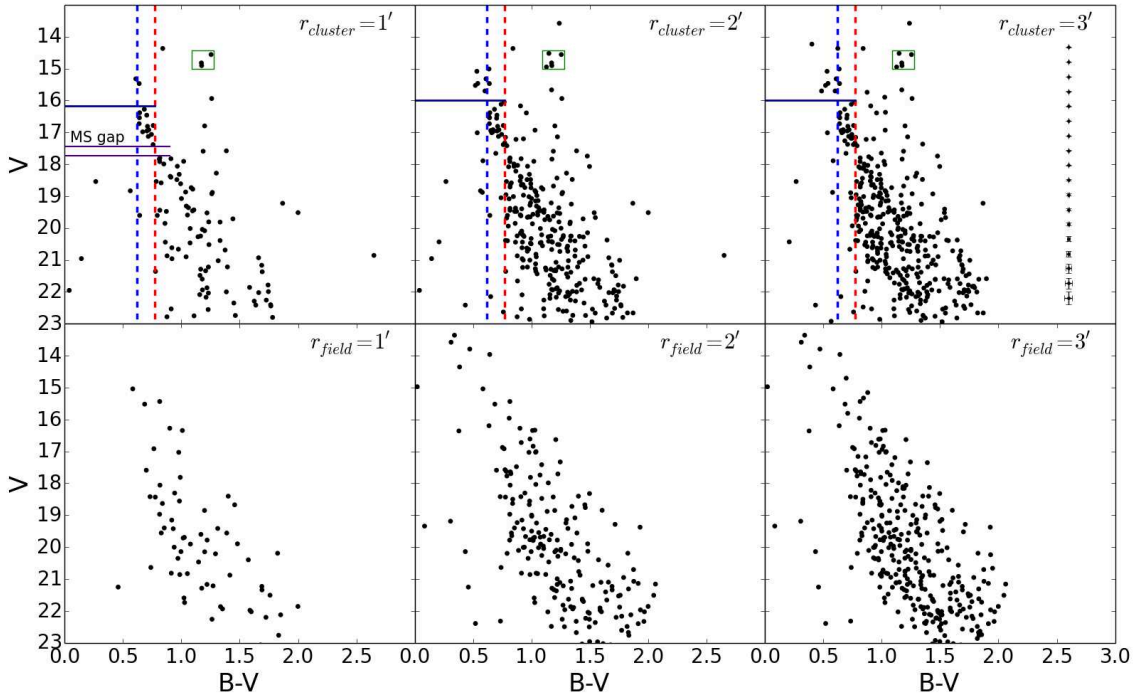

Figure 3.6: CMDs of NGC 2225 in the $B-V$ vs V plane at different distances from the cluster center (from left to right: $r < 1$ arcmin, $r < 2$ arcmin, and $r < 3$ arcmin). The upper panels show the CMDs centered on the cluster while the lower panels present the CMDs of the external field taken from chip #2. We highlight the main evolutionary features: the blue edge of the TO (in *blue*) and the red edge of the TO (in *red*) with dashed lines; the MS tip (in *dark blue*), the RC (in *green*) and the MS gap (*violet*) with solid lines.

3.4 Results

3.4.1 NGC 2225

The observational CMDs of the cluster at different distances from the center are shown in Fig. 3.6. In addition a background field is presented. The external field is taken at a radius > 3 arcmin in chip #2. As it is evident from the analysis of the luminosity and density profiles (see Sect. 3.4.2), this region samples the background and foreground population. NGC 2225 is a poorly populated cluster. The MS barely stands out from the field contamination, as it is evident from the figure.

The number of stars within 3 arcmin from the center is just about twice the number of stars in the background area of the same size. We identified the TO at $V \sim 16$ mag and the

red-clump (RC), composed by few stars, at $V \sim 14.5$ mag. There are bright stars above the TO. These stars are also present in the very central part of the cluster, and may tempting to identify the TO phase at brighter magnitudes, as in Car05. To better define the TO phase in NGC 2225 we take advantage of the membership probability in the DAML14 catalogue. We perform a cross-match between our catalog and the DAML14 one with the same area. We found 38 stars in common but we consider as member of the cluster only the 13 stars with a probability higher than 50%. The result is shown in the CMD in Fig. 3.7.
With this membership selection, only one blue star brighter than the TO is likely a cluster's member, with a P = 80%, whereas the others are in the probability range $0\% \leqslant$ P $\leqslant 25\%$. We than argue that the group of bright blue stars above the TO are field interlopers belonging to the the MS of the Galactic Disc population. A further evidence is provided by the external field shown in in Fig. 3.6. If we compare the CMD of the cluster with the external background field it is evident that the field contamination is significant at all magnitudes. Thus we did not consider the stars at $V \sim 15$ mag and $B - V \sim 0.6$ mag as part of the cluster in our analysis.

As a final remark, we note the presence of a gap along the MS of about 0.3 mag at $V \sim 17.5$ mag and $B - V$ in the range 0.72-0.8 mag. The gap is evident also in the CMD of the central part of the cluster. This points in favor of the the fact that the gap is a real features and not due to statistical effects. Similar gaps along the MS have also been found in other clusters, see e.g. de Bruijne et al. (2000) for the Hyades, Subramaniam & Bhatt (2007) for NGC 7245, Giorgi et al. (2002) for NGC 2571, and Balaguer-Núñez et al. (2005) for others. There is no clear correlation with age and/or metallicity. A possible explanation for this gap is provided by Kovtyukh et al. (2004), which determined precise Teff for a sample of 248 field F, G and K stars with accurate Hipparcos parallaxes and near-solar metallicity. They pointed out that this gap possibly coincides with the Li depression seen in OCs and field stars, due to the sudden change in the properties of atmospheric convection in stars slightly less massive than the Sun.

The completeness level is above 95% for $V < 17.5$ mag and lower than 80% for $V > 19$ mag (see Fig. 3.8).

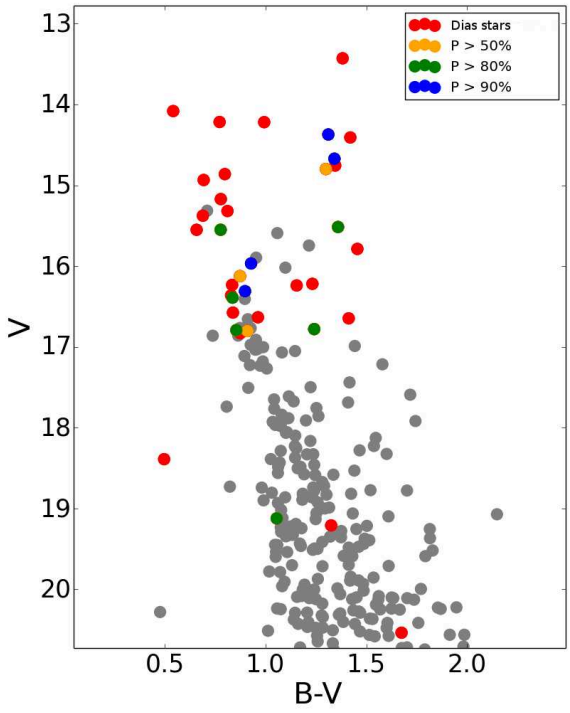

Figure 3.7: CMD of NGC 2225. The gray points are all the stars within 3' from the center, the colored ones are the stars in common with DAML14. The orange stars have a probability membership higher than 50%, the green higher than 80% and the blue higher than 90%. The red stars can be considered as non members.

3.4.2 Radial profile

The center of NGC 2225 indicated on the WEBDA is $\alpha = 96.6542°$ and $\delta = -9.6408°$. With the method explained in section 3.3.1, we find the same value for α but a value of δ 7" away in the direction of the Galactic center, with an uncertain of 0.7" in α and 1.4" in δ.
The radial surface density and brightness profiles are shown in Fig. 3.9.
To obtain these profiles we use only stars brighter than $V = 19$ mag, in order to limit as much as possible field stars contamination. The central panel of Fig. 3.9 shows the radial density profiles at different magnitude bins. The flattening of the profiles at r$> 3'$ indicates that the level of the background is reached.

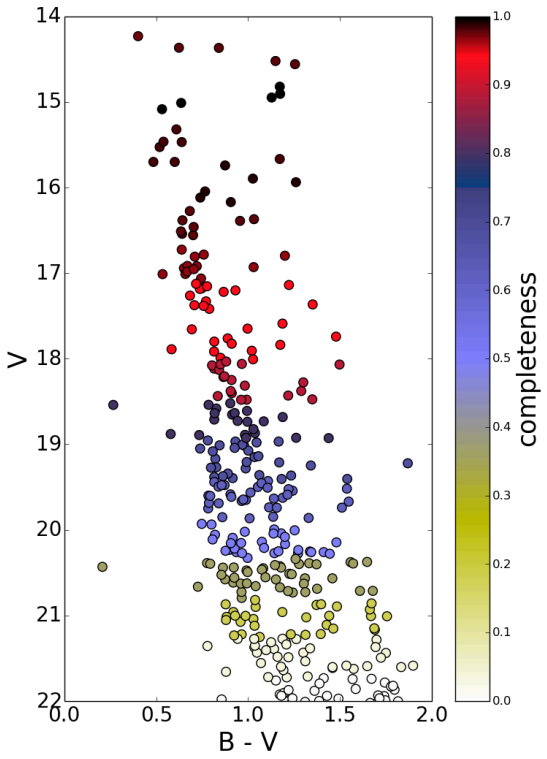

Figure 3.8: Completeness map for NGC 2225, derived from the complete set of ATSs.

Cluster Parameter determination

We first compare the CMDs with a set of PARSEC isochrones in the age range of $8.6 \leq$ Log$(t/yr) \leq 9.8$ with a step of Log$(t/yr) = 0.05$ and a metallicity range of $0.004 \leq$ Z ≤ 0.03 with a step of Z $= 0.001$.

None of models that we consider is able to well reproduce both the color and magnitude differences between the TO and the RC. In Fig. 3.10 we show the differences in color and magnitude between the TO and the RC as a function of age and metallicity using the PARSEC set. The cluster has a TO-RC color separation of ~ 0.5 mag and a magnitude separation of ~ 1.6 mag. Looking at Fig. 3.10, it is clear that none of the models is able to reproduce both color and magnitude separation at once. The same conclusion holds when BaSTI models with and without overshooting are used.

The reasons of the discrepancy might be that first, some inconsistencies in our calibration cannot be excluded, and second that the transformations from the theoretical plane to the observational one are more uncertain for cold stars (see discussion in Bragaglia & Tosi 2006). Starting with the best isochrone fit (Log $t = 9.25$ and Z = 0.015) we simulate the synthetic

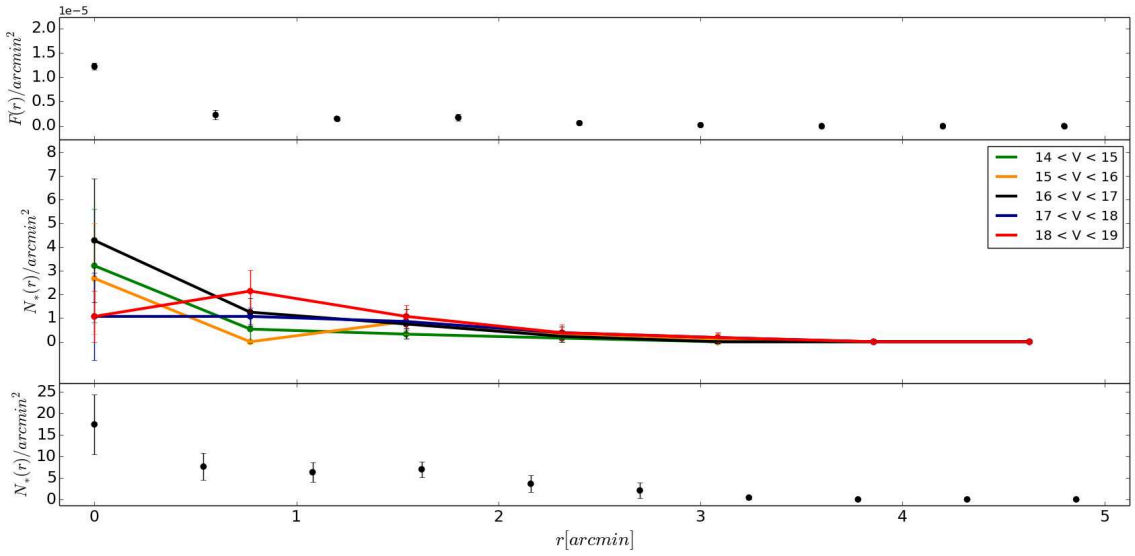

Figure 3.9: Radial surface density and brightness profiles for NGC 2225. *Upper panel:* radial brightness profile obtained from stars brighter than $V = 19$. *Middle panel*: radial density profile calculated in different magnitude bins. *Lower panel*: radial density profile calculated in different magnitude bins from all stars brighter than $V = 19$ mag.

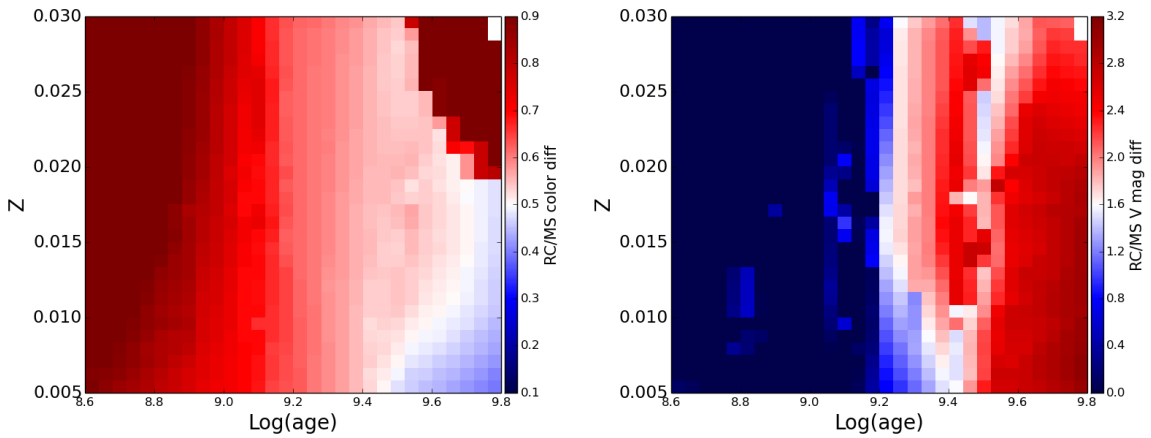

Figure 3.10: Color maps of the differences between the RC and the TO in $B-V$ *(left panel)* and V *(right panel)*. The color scheme is centered on the observed values in both cases.

CMD taking into account the photometric errors and completeness level as derived from AST, the DR effect, and the binary fraction (see Fig. 3.11). In comparison to literature, we decrease the reddening value to $E(B-V) = 0.32$ mag and estimate a observed distance modulus of 13.1 mag. To be able to reproduce the MS broadening we consider, in addition to photometric errors, a DR of $\Delta E(B-V) \sim 0.02$ mag. Finally, we found that a binary fraction of $f_b = 20\%$ well reproduces the observed CMD features.
We compare the observational LF with the synthetic one in Fig. 3.12. The two distributions are in good agreement at all magnitudes. The greatest discrepancy is located in the range $17 \leqslant V \leqslant 18$ mag where we have an over-abundance in our synthetic CMD. This magnitude range coincides whit the region of the MS gap that our models are not able to reproduce.
Our results are not in agreement with Car05. This is due to the different interpretation of the TO location. The brightest stars that we identified as Galactic disc MS-stars on the basis of proper motions, were considered by Car05 as the cluster's TO. This fact explains why they found a younger age and consequently a smaller distance modulus.
We derive the uncertainties on parameters estimate using eq. 3.3, 3.4 and 3.5. Fig. 3.13 show the age range. We find an age uncertainty of about ± 200 Myr, a reddening error of about ± 0.04 mag and an error of $\sim \pm 0.1$ mag for the distance modulus.

3.4.3 NGC 6134

The CMD shows that the principal evolutionary phases are well defined and well populated (Fig. 3.14). Within an area of 9' radius we find an overabundance of stars of $\sim 15\%$ in the cluster field with respect to the external field. Both the TO and the RC are evident at $V \sim 12.3$ mag and $V \sim 11.5$ mag respectively. For magnitudes fainter that $V \sim 16$ mag the field contamination starts to play a prominent role in the CMD. Also NGC 6134 presents a gap along the MS of about 0.4 mag at $V \sim 15.3$ and $B-V$ in the range 0.77-0.85 mag. This gas is particularly evident in the central part of the cluster (r_c = 3'). This gap is also discussed in Ahumada et al. (2013). They analyze the radial profiles of MS stars at different ranges of magnitude. The radial profile for the magnitude range containing the gap is comparable to the others for $r_c > 3$ arcmin, but in the inner region it is significantly different. This suggests that the gap is a natural cluster feature, hidden by field contamination at larger radii.

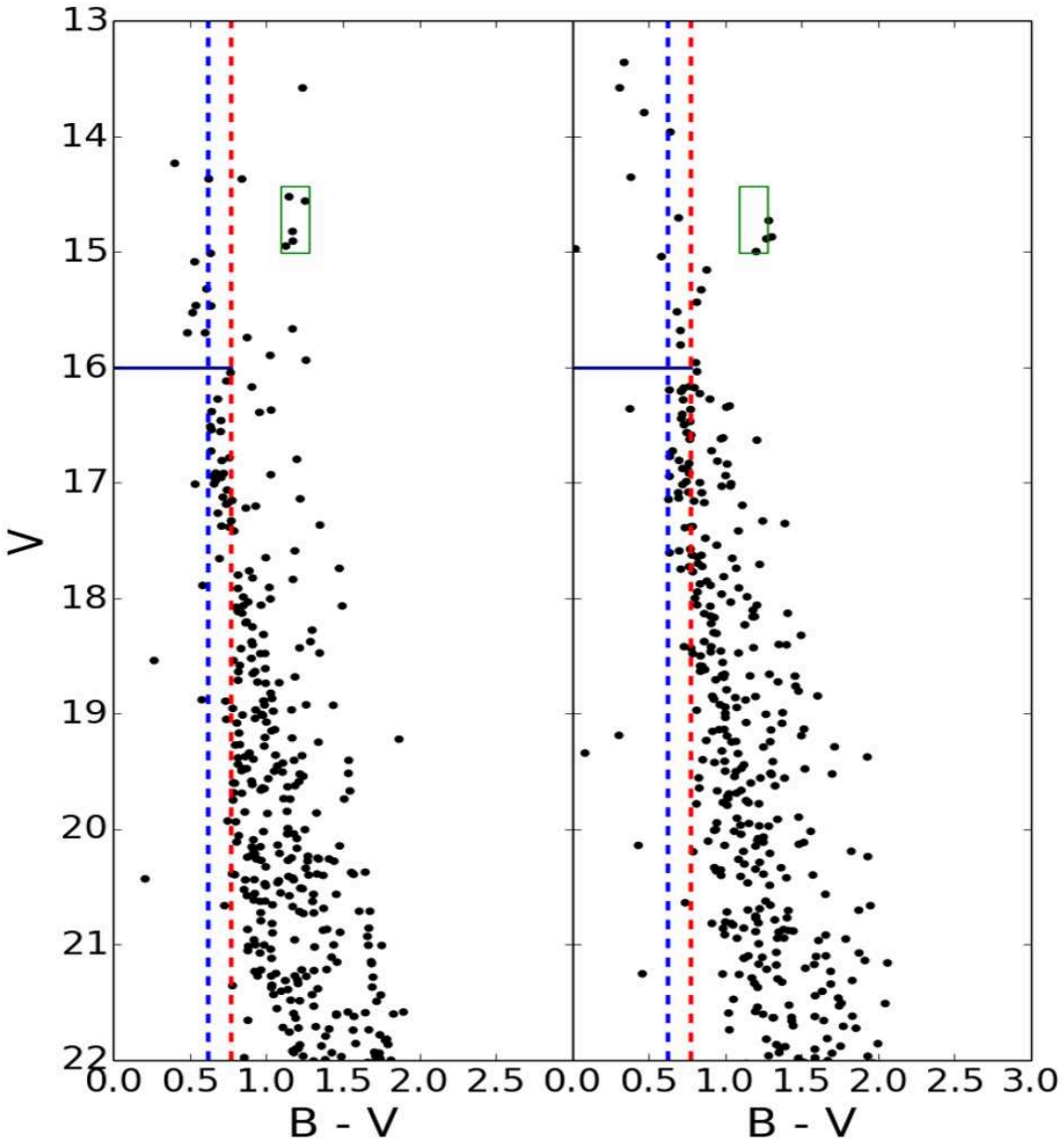

Figure 3.11: NGC 2225 observational CMD against the best-fitting synthetic CMD obtained from PARSEC models for the following parameters: Log $t = 9.25$, Z = 0.015, $(m - M)_0 = 13.1$ mag, and $E(B - V) = 0.32$ mag.

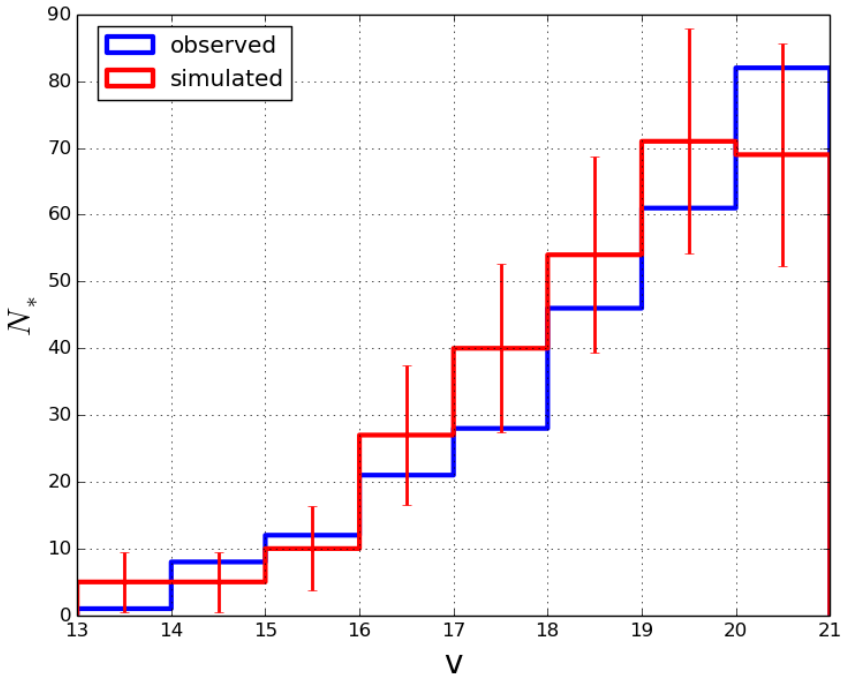

Figure 3.12: Comparison between the observational luminosity function of NGC 2225 *(blue)* and its best-fit synthetic LF *(red)*. The uncertainties on counts of the observed stars are of the same order as those shown in figure for simulated stars.

The completeness, obtained via AST, is shown in Fig. 3.15. For NGC 6134, the completeness remains greater than 95% for $V < 18$ mag and falls below 80% for $V > 19.7$ mag.

Radial and profiles

The center of NGC 6134 indicated on the WEBDA is $\alpha = 246.9417°$ and $\delta = -49.1517°$. We derive the center C_{grav} 2'28" easter and 4" souther with a $\sigma \approx 1.7''$ both in α and δ. The large discrepancy in α probably depends on the different methods used. Indeed, as already pointed out, the use of the luminosity center C_{lum} instead of density center C_{grav} can produce slightly different results.
The radial surface density and brightness profiles are shown in Fig. 3.16. Also in this case we set the lower brightness limit for stars selection at $V \sim 19$ mag.

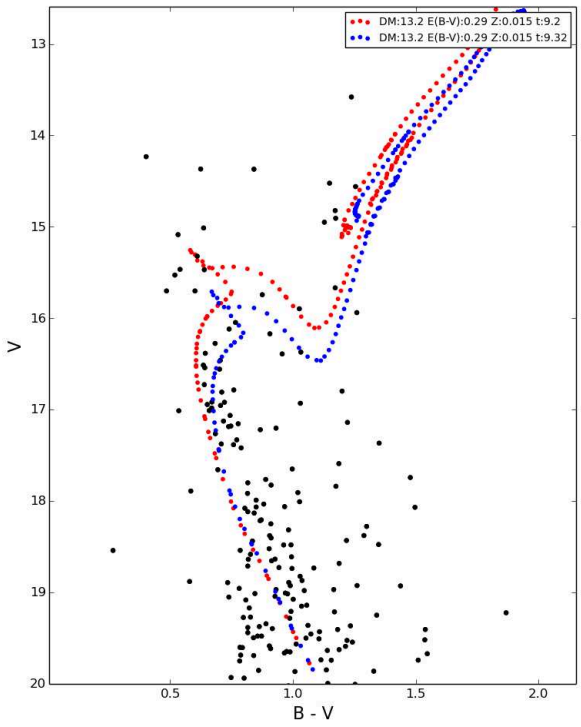

Figure 3.13: NGC 2225 observational CMD is compared with two isochrones of different age. In the age range Log(age)= 9.2 (in red) and Log(age)= 9.32 (in blue) all the solutions that well fit the cluster are contained.

The background level is reached at 5' from C_{grav}. The central panel clearly shows that the dominant stars at all radii are the low MS stars in the range $17 \leqslant$ V $\leqslant 18$. The yellow line represents the surface density profile of the stars in the magnitude bin that contain the MS gap. The profile is quite constant at all radii, except for a little increase between 2' and 3'.

Cluster Parameters derivation

Starting from the same set of isochrones used for NGC 2225, we search for a subset of models that well reproduce the $\Delta(B-V) \sim 0.6$ and the $\Delta V \sim 0.45$ between TO and RC, see Fig. 3.17. The plots show that the correct solution is around Log $t = 9.1$ at a solar metallicity or higher. The synthetic CMD that best reproduces the cluster is shown in Fig 3.18. The parameters that we found for this cluster are the following: Log $t = 9.1$; Z = 0.02; $(m-M)_0 = 10.2$ mag; $E(B-V)$ = 0.29 mag. The age we found is the same obtained by Ahumada (2002) with an analysis performed through the comparison between the observed

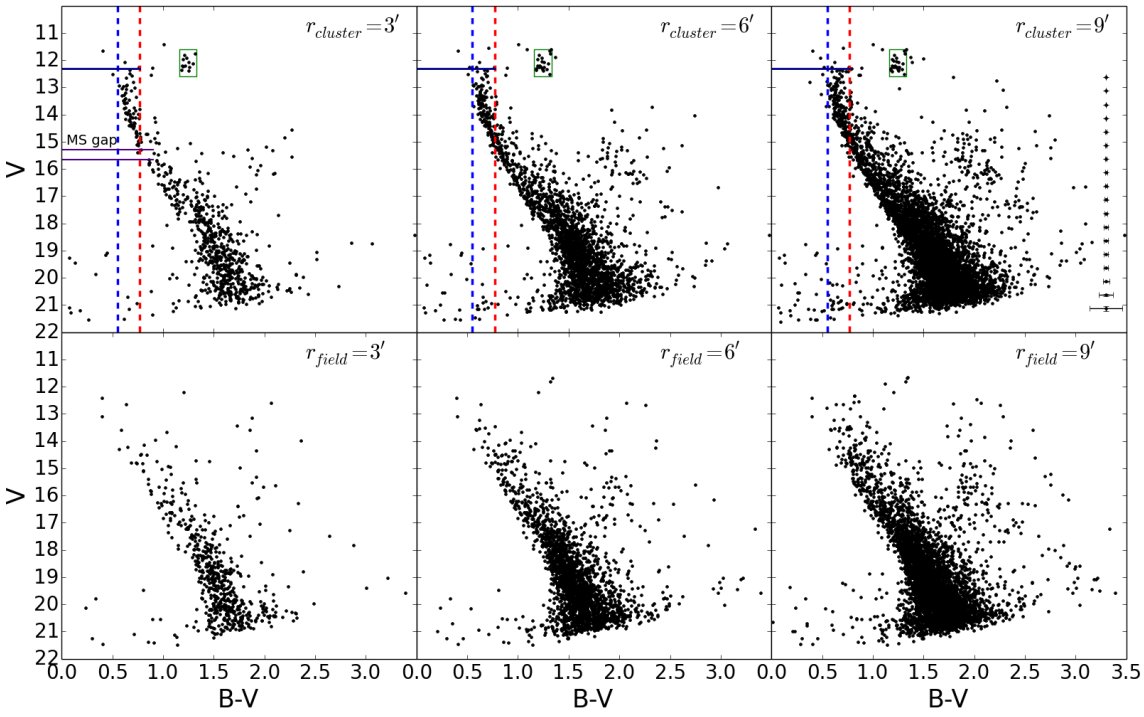

Figure 3.14: CMDs of NGC 6134 in the $B-V$ vs V plane for different distances from the cluster center (from left to right: $r < 3'$, $r < 6'$, and $r < 9'$). In the upper panels we plot the CMDs centered on the cluster and in the lower panel the CMDs of the external field. The magnitude and colors of the identified main evolutionary features follow the same scheme of Fig. 3.6.

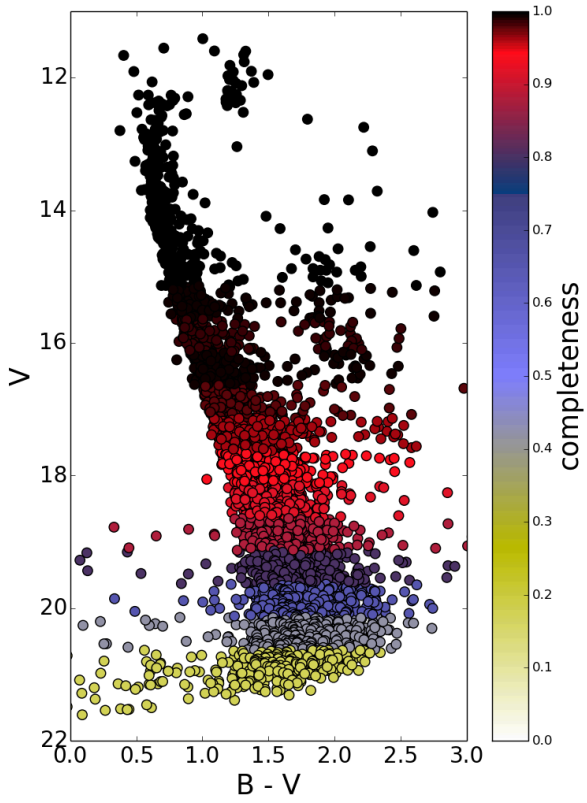

Figure 3.15: Completeness map for NGC 6134, derived from the ATSs.

sequences with different colors and the models by Schaller et al. (1992), Bertelli et al. (1994) and Girardi et al. (2000). However, we are in disagreement with the age quoted in Ahumada et al. (2013). By using the old Padova models (Bressan et al. (1993) and Fagotto et al. (1994)), they pointed out a Log t of 8.98, against our Log $t = 9.1$. Such difference is mainly the result of the different stellar models that are adopted, since we have the same calibration and identified the same features.

The synthetic CMD is in good agreement with the observational data. In this case we derive a DR of $\Delta E(B-V) = 0.01$ mag and a $f_b = 20\%$.

Also in this case the comparison of the LF shows a good agreement between the observed data and the simulations (see Fig. 3.19).

For what concerns the metallicity, it is difficult to evaluate a precise value via photometry, since we are using only one color. We are only able to define a solar metallicity solution as a lower limit.

As pointed out in the introduction, Carretta et al. (2004) obtain a metallicity of [Fe/H]

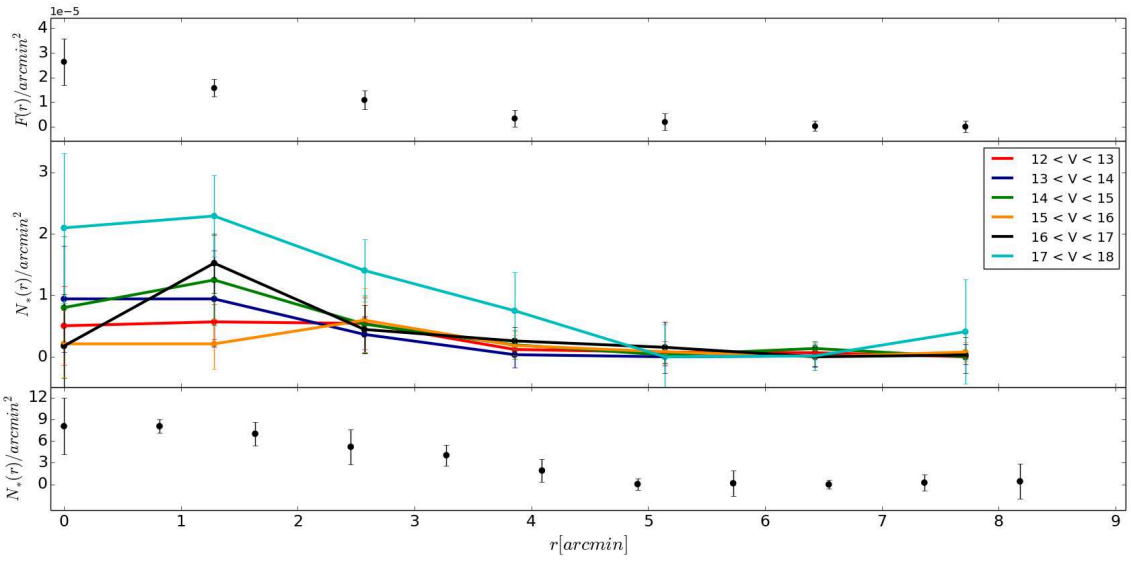

Figure 3.16: Radial surface density and brightness profiles for NGC 6134 with respect to the calculated C_{grav}. *Upper panel:* radial brightness profile obtained from stars brighter than $V = 19$. *Middle panel*: radial density profile calculated in different magnitude bins. *Lower panel*: radial density profile calculated in different magnitude bins from all stars brighter than $V = 19$ mag.

$= 0.15 \pm 0.03$ dex from high-resolution spectra. We fit also a super-solar metallicity solution, which implies a lower value for the reddening and produces a fit almost identical with only a slightly worse reproduction of the tip of the MS (see Fig. 3.20).
We obtained an uncertainty of ± 150 Myr (see Fig. 3.21) for the age and the same error for

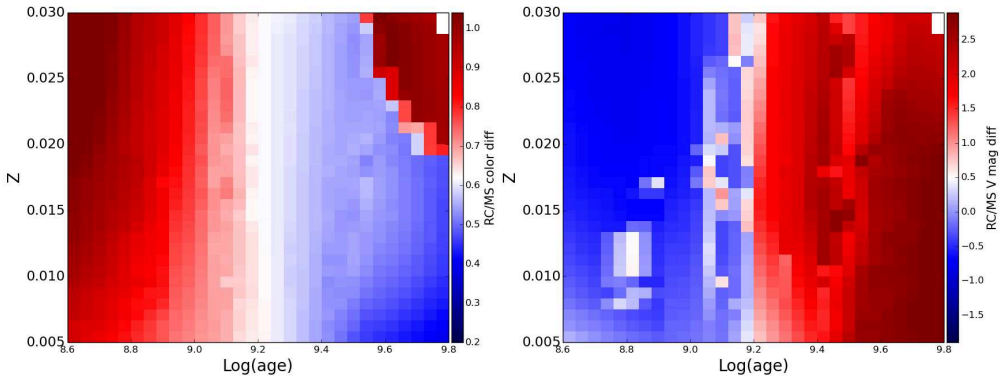

Figure 3.17: Color maps of the differences between the RC and the TO in $B-V$ *(left panel)* and V *(right panel)*. The color-scheme is centered in the observational values.

reddening and distance modulus as obtained for NGC 2225.

3.4.4 NGC 2243

The CMDs of NGC 2243 in different pass-bands are shown in Fig. 3.22. The TO is located at $V \sim 15.65 - 15.7$ and the RC between $V \sim$ 13.7-14.2. We found an overabundance of stars in the cluster inner 4', in comparison to the external field of $\sim 74\%$ in $B - V$ and of $\sim 64\%$ in $V - I$.
In the cluster CMD, a binary star sequence is clearly visible in both colors, down to faint magnitudes. The presence of a relatively large fraction of binaries may explain the scatter in the Sub-Giants Branch, particularly visible in $B - V$. However field star contamination cannot be excluded.
The field population CMD show a large spread in color, but seems to have a blue cut-off at $B - V$ and $V - I \sim 0.5$. As already noted by Kal96 this cut-off could represents the color of the TO of the halo population stars.

The completeness, as obtained via AST experiments, is shown in Fig. 3.23. The completeness remains greater than 90% until $V \sim 21.5$ in $B - V$ and $V \sim 22$ in $V - I$.

3.4.5 Radial profiles

For NGC 2243 WEBDA reports a center position of $\alpha = 97.3917°$ and $\delta = -31.2833°$. We estimate a C_{grav} 10" Est and 0.5" South of the WEBDA value, with an uncertain of about 0.5" both in α and δ.
Starting from our center we define the radial surface density and brightness profiles, see Fig. 3.24. Due to the high completeness level down to the faint MS, we analyze the stars brighter than $V \sim 20$ mag. We fix the cluster radial extension between 3 and 4 arcmin. In comparison to NGC 2225 and NGC 6134, NGC 2243 shows a higher concentration in its the central part. Indeed the surface density and brightness from 2' toward the center have higher values compared to the other two cluster. Furthermore in the inner arcmin a sudden

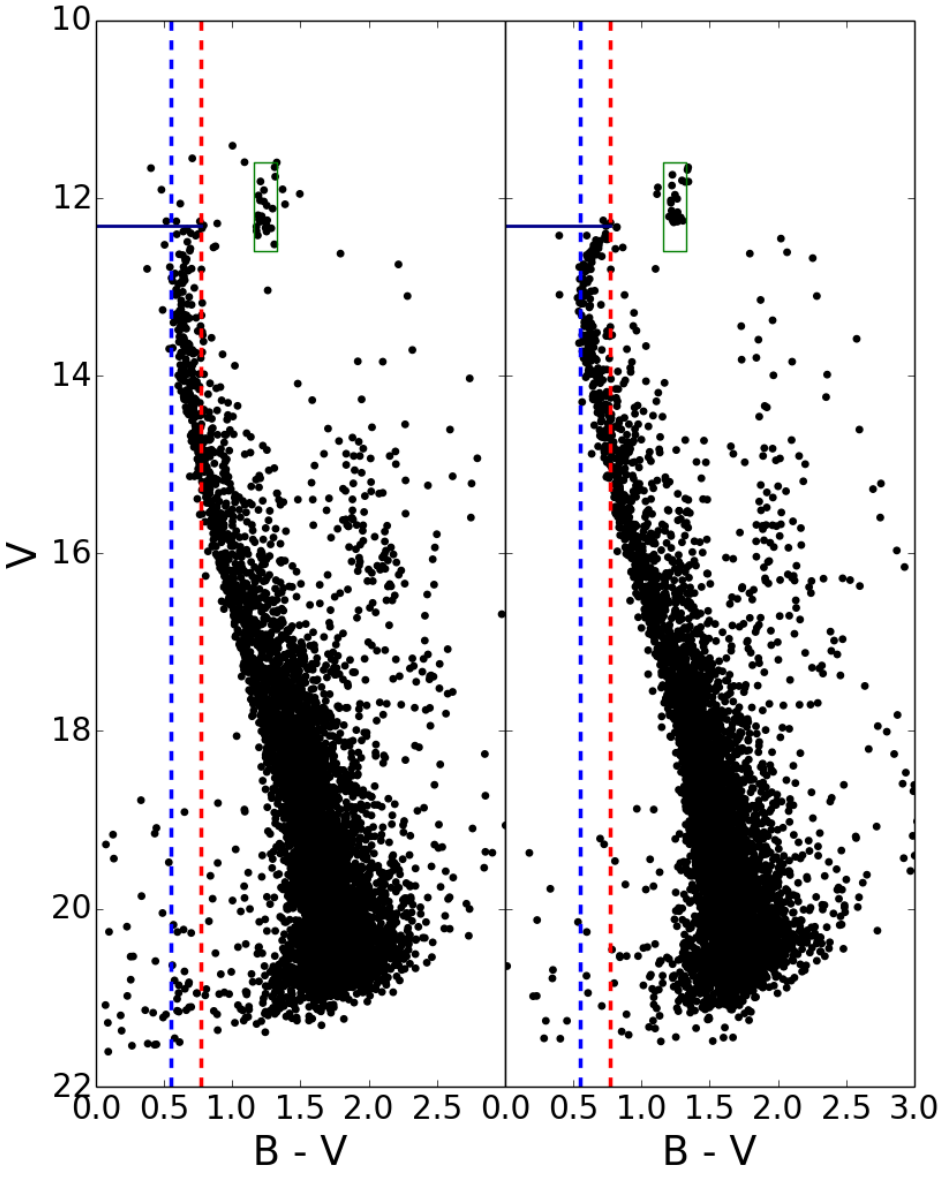

Figure 3.18: NGC 6134 observational CMD with the best-fitting synthetic CMD obtained from PARSEC models for the following parameters: Log $t = 9.1$, $Z = 0.02$, $(m - M)_0 = 10.2$ mag and $E(B - V) = 0.29$ mag.

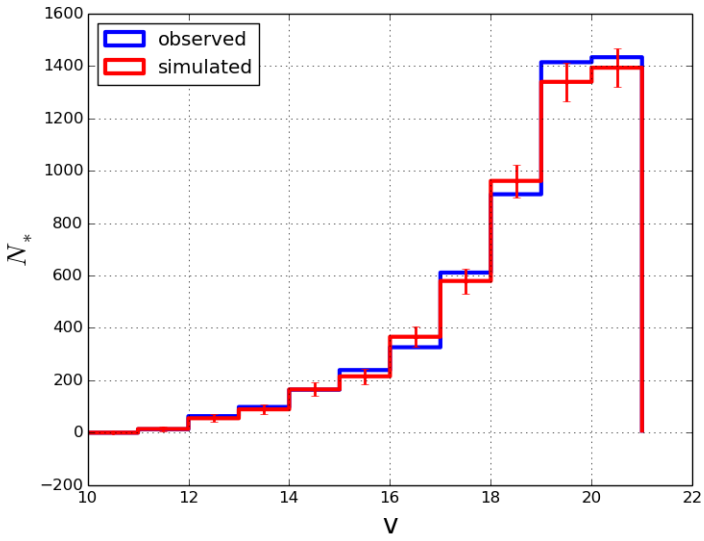

Figure 3.19: Comparison between the observational luminosity function of NGC 6134 *(blue)* and its best-fit synthetic LF *(red)*. The uncertainties on counts of the observed stars are of the same order as those shown in figure for simulated stars.

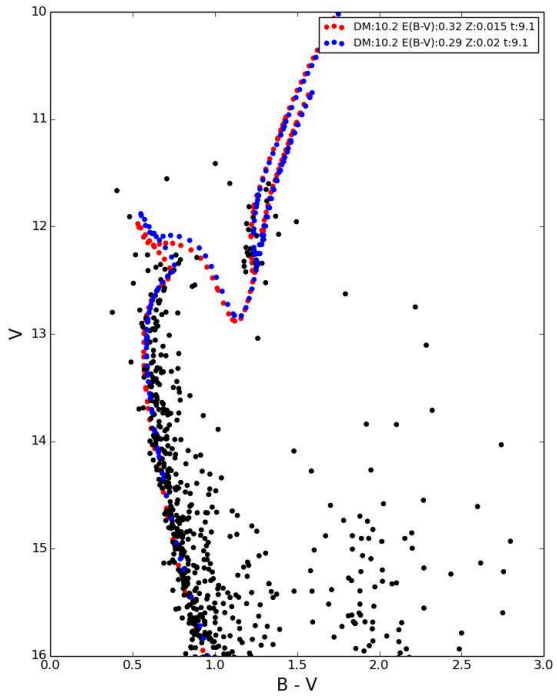

Figure 3.20: NGC 6134 observational CMD compared with two isochrones of the same age and different metallicity: $Z = 0.015$ *(i.e. solar, in red)* and Z = 0.02 *(in blue)*.

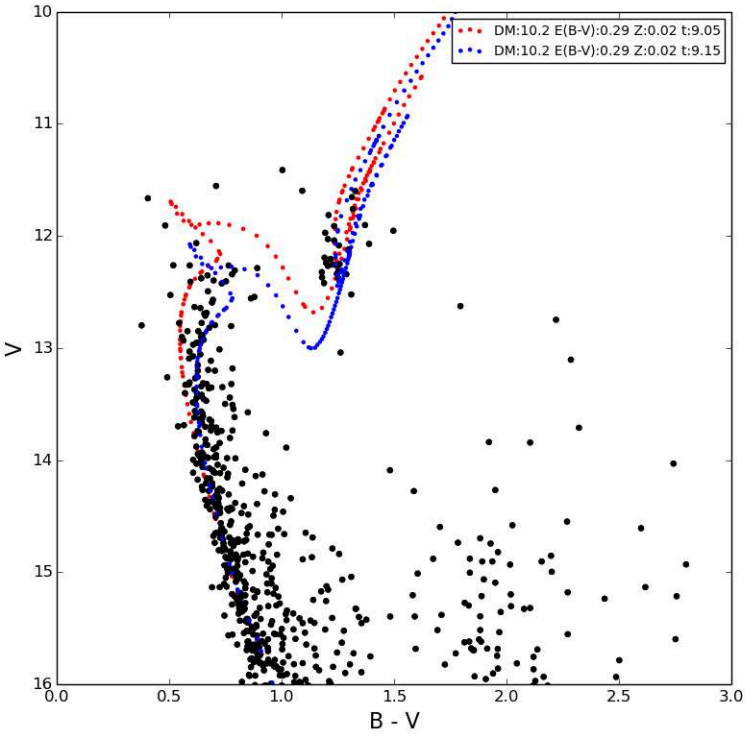

Figure 3.21: NGC 6134 observational CMD compared with two isochrones with different age. In the age range between Log $t = 9.05$ *(in red)* and Log $t = 9.15$ *(in blue)* all the solution that well-fit the TO and also match the RC are contained.

increase both of numerical density and surface brightness is visible. In particular the TO, sub-GB and RC stars (yellow, blue and green lines) maintain low density values up to 1' and then increase toward the center.

Fig. 3.24 uses the $B - V$ catalog, in which the photometric errors are slightly lower. However, the results shown using the $V - I$ catalog are in excellent agreement with those reported.

Parameters derivation

The separation in magnitude and color between TO and RC in the observational CMD are $\Delta V \sim 1.7$ mag and $\Delta B - V \sim 0.5$ in $B - V$ and $\Delta V \sim 1.7$ mag and $\Delta V - I \sim 0.55$ in $V - I$. As expected sub-solar isochrones turn out to be the best to reproduce these separations, in the age range of Log $t \approx 9.4 - 9.5$, see Fig 3.25.

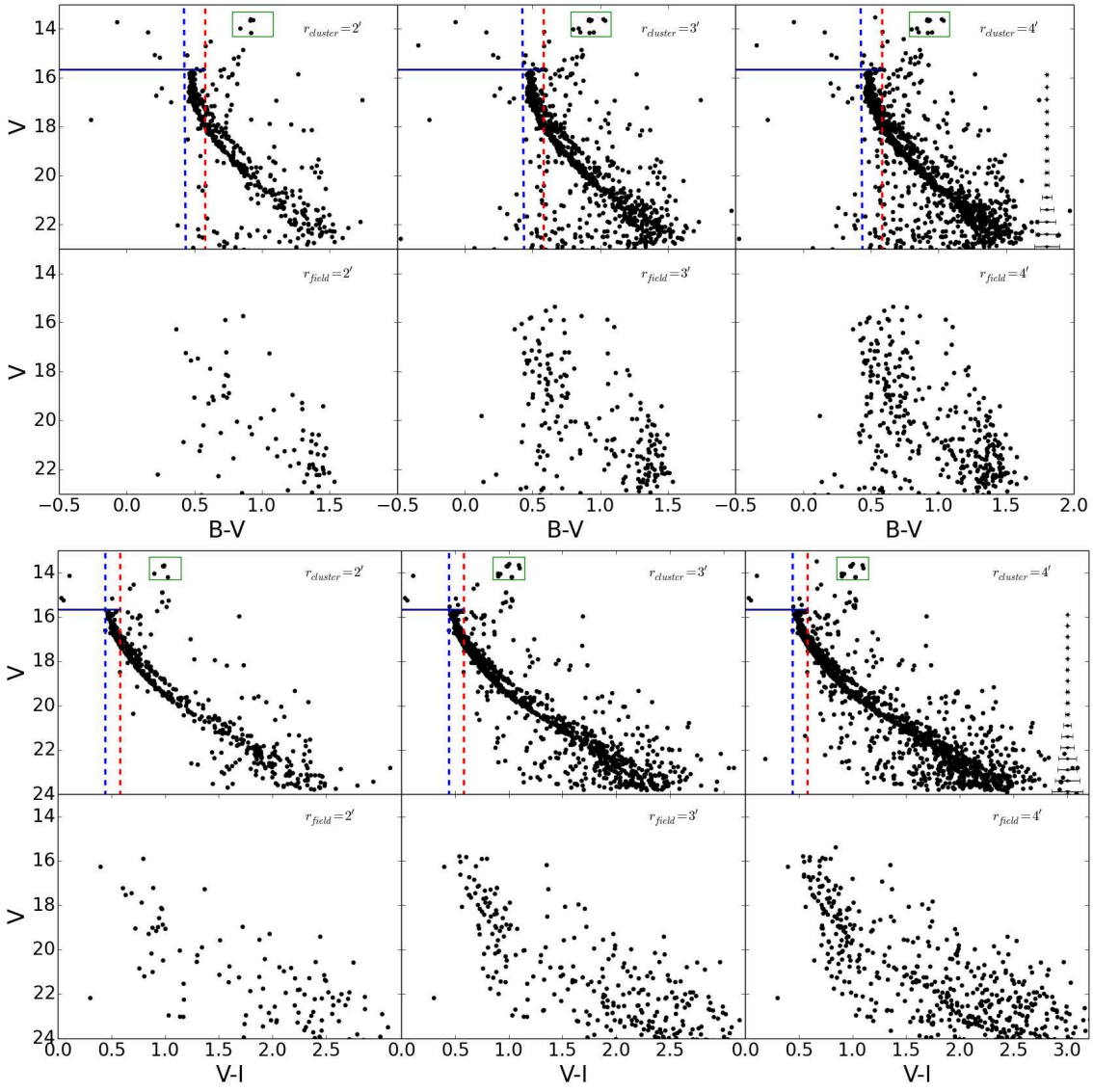

Figure 3.22: CMDs of NGC 2243 in the $B-V$ vs V *(upper panels)* and in the $V-I$ vs V *(lower panels)*, for different distances from the cluster center (from left to right: $r < 2'$, $r < 3'$ and $r < 4'$). In the upper panels we plot the CMDs centered on the cluster and in the lower panel the CMDs of the external field. The magnitude and colors of the main CMD features follow the same scheme of Fig. 3.6.

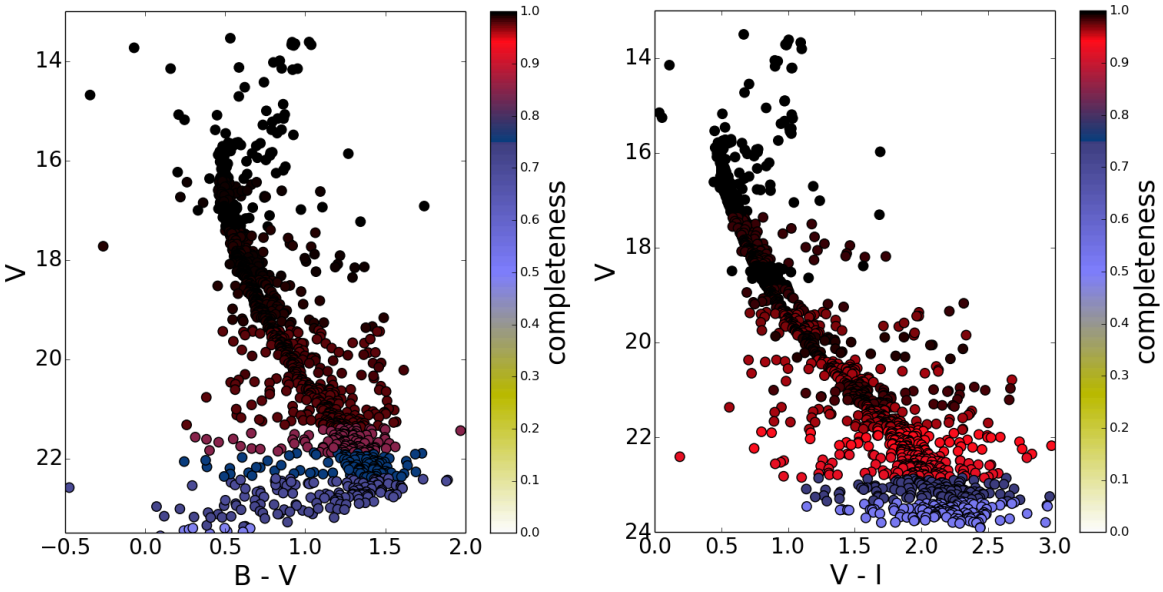

Figure 3.23: Completeness map for NGC 2243, derived from the complete set of ATSs.

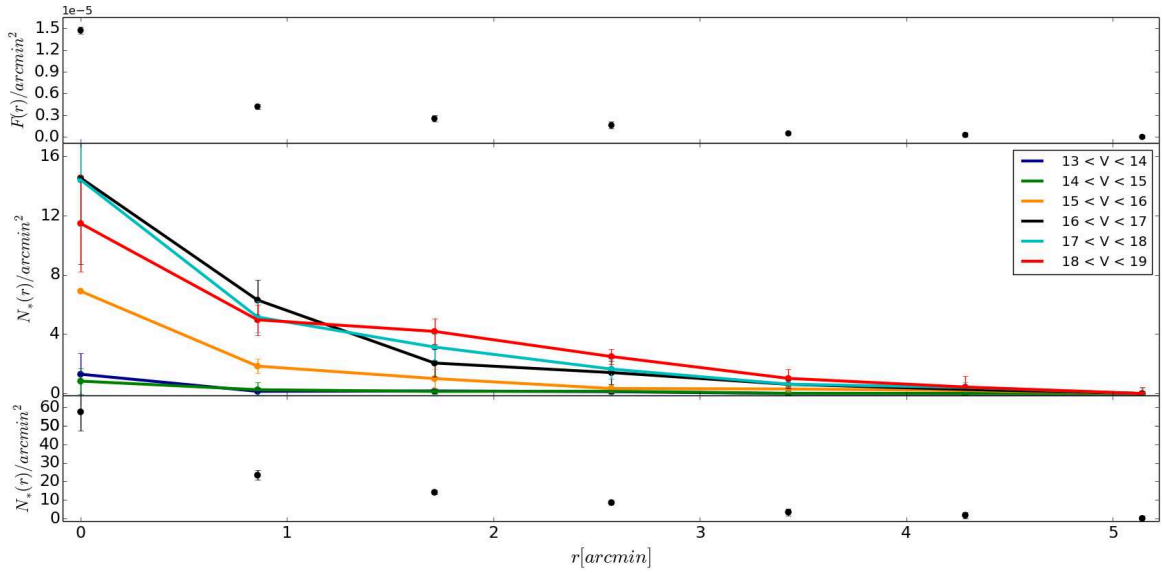

Figure 3.24: Radial surface density and brightness profiles for NGC 2243 with respect to the calculated C_{grav}. *Upper panel:* radial brightness profile obtained from stars brighter than $V = 20$. *Middle panel*: radial density profile calculated in different magnitude bins. *Lower panel*: radial density profile calculated in different magnitude bins from all stars brighter than $V = 20$ mag.

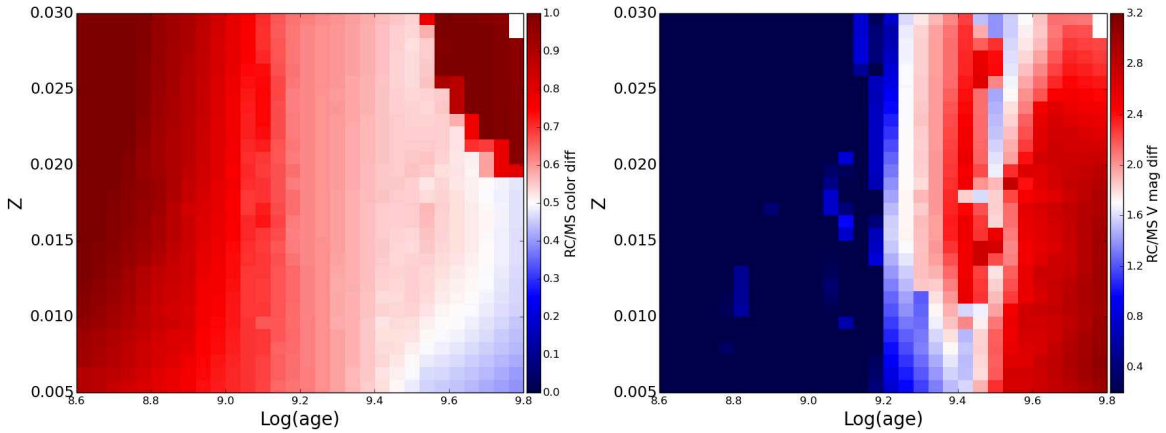

Figure 3.25: Color maps of the differences between the RC and the TO in $B-V$ *(left panels)* and V *(right panels)*. The color-scheme is centered on the value observed for the two differences.

Starting from this range of age and metallicity we searched for the synthetic population that better reproduce the cluster features on CMDs in both colors. In $B-V$ the best fit parameters are: a distance modulus of $(m-M)_0 = 13$, an age of Log $t = 9.5$, a metallicity of Z = 0.007 and a reddening of $E(B-V)$ = 0.07 mag, see Fig. 3.26. In $V-I$ we find the same age but a slightly higher distance modulus, $(m-M)_0 = 13.1$ and a lower metallicity value, Z = 0.004. For the reddening we obtain $E(V-I)$ = 0.08, see Fig. 3.27.
In both cases the binary fraction that best reproduce the data is $f_b = 20\%$, while for the DR we use $\Delta E(B-V)$ = 0.03 and $\Delta E(V-I)$ = 0.04.
The age that we found is in agreement with the more recent photometric study of the cluster, VandenBerg et al. (2006). The distance modulus and reddening we obtain are consistent with those present in literature. The possibility to perform this analysis in two different colors allowed us to better confine the metallicity in the range Z = 0.004 - 0.007, which transposed in terms of iron abundance becomes $-0.668 \leqslant$ [Fe/H] $\leqslant -0.425$, in good agreement with previous spectroscopic studies.

Fig. 3.28 and Fig. 3.29 compare the observational and the synthetic luminosity functions. The simulated LFs well reproduce the observational one, but at $V \sim 20$, where the cluster exhibits a reduction in the number of stars. However, the two distributions are marginally compatible inside the errors.

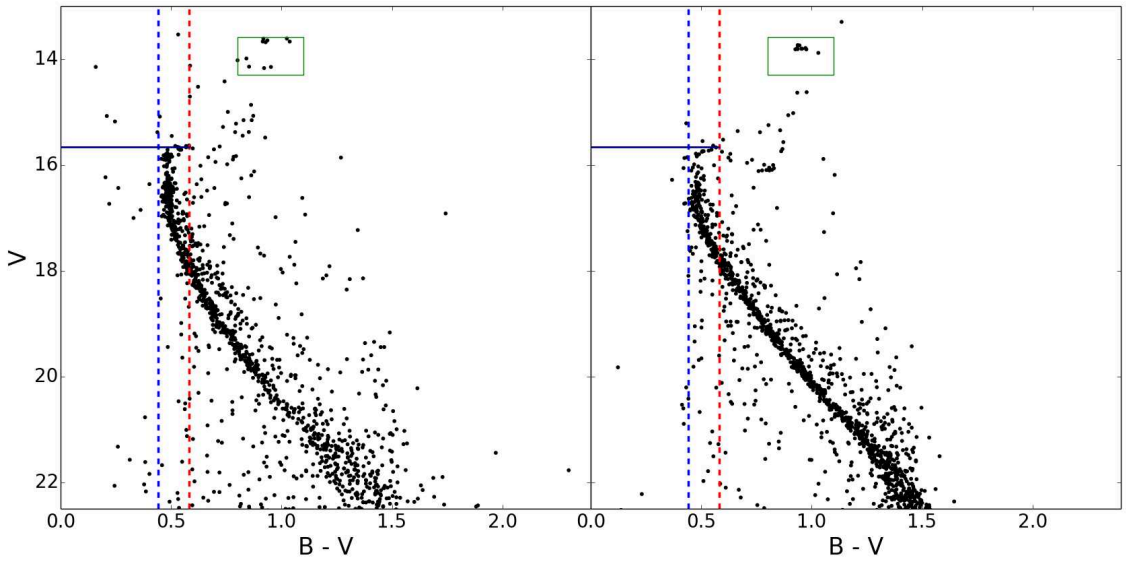

Figure 3.26: NGC 2243 observational CMD(left) and the best-fitting synthetic CMD in the $B-V$ vs. V plane (right). From PARSEC models we obtain the following parameters: Log $t = 9.5$, Z = 0.007, $(m-M)_0 = 13$ mag and $E(B-V)$ = 0.08 mag.

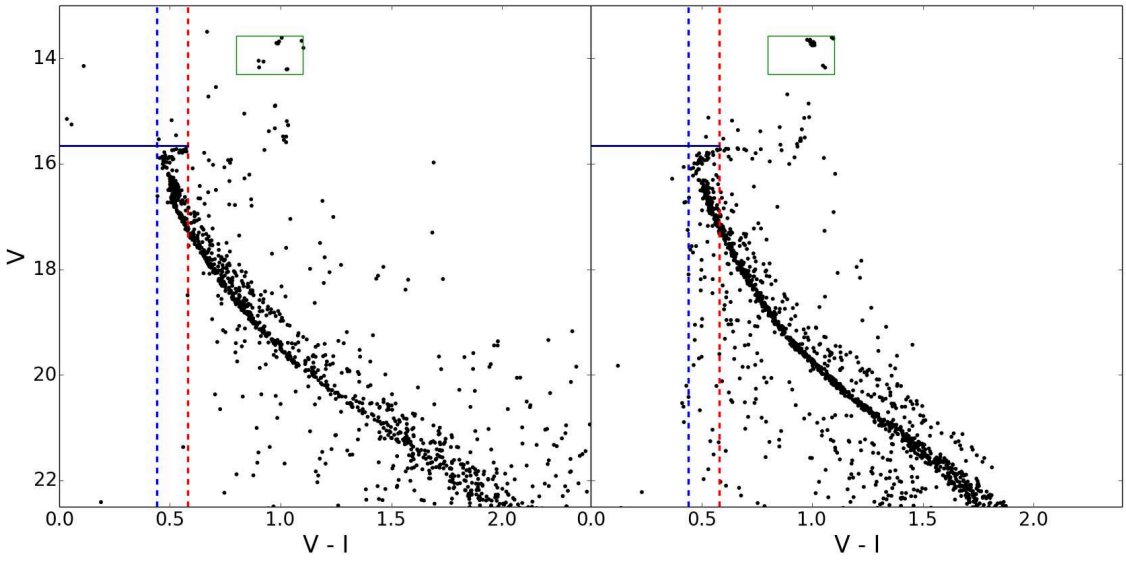

Figure 3.27: NGC 2243 observational CMD and the best-fitting synthetic CMD in the $V-I$ vs. V plane. From PARSEC models we obtain the following parameters: Log $t = 9.5$, Z = 0.004, $(m-M)_0 = 13.1$ mag and $E(V-I) = 0.08$ mag.

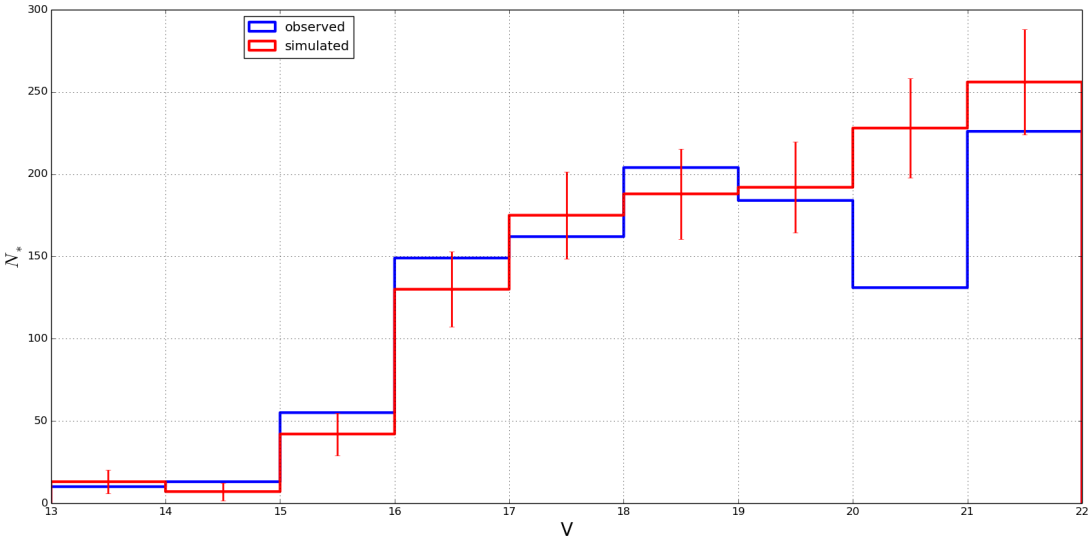

Figure 3.28: Comparison between the luminosity function of the observational CMD of NGC 2243 *(blue)* and its best-fit synthetic CMD in the $B - V$ vs V plane *(red)*. The uncertainties on counts of the observed stars are of the same order as those shown in figure for simulated stars.

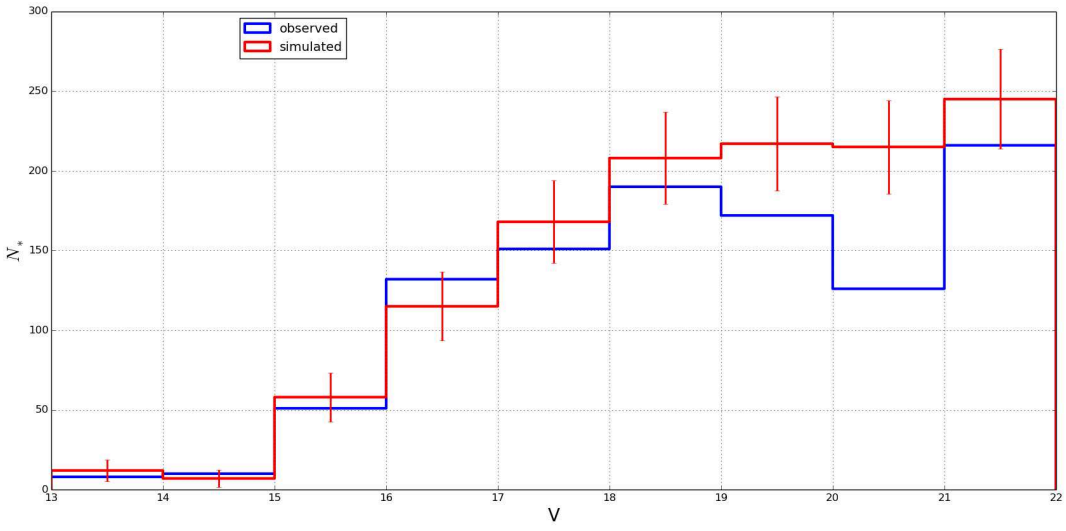

Figure 3.29: Comparison between the luminosity function of the observational CMD of NGC 2243 *(blue)* and its best-fit synthetic CMD in the $V - I$ vs V plane *(red)*. The uncertainties on counts of the observed stars are of the same order as those shown in figure for simulated stars.

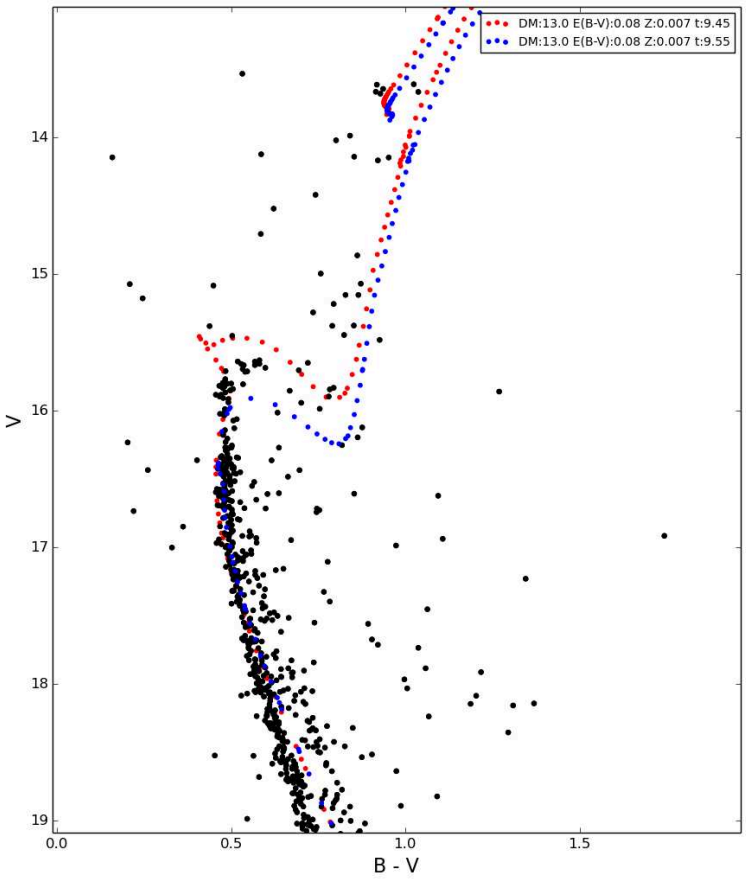

Figure 3.30: NGC 2243 observational CMD compared with two isochrones with at different ages. All the solution that well-fit the TO and the RC are confined in the age range between Log $t = 9.45$ *(in red)* and Log $t = 9.55$ *(in blue)*.

The uncertain in age is ± 350 Myr, (see Fig 3.30). We derive an uncertain of ± 0.125 mag for reddening and ± 0.15 for distance modulus.

3.5 Bayesian analysis with near infrared photometry

We use the results of this study to test the reliability of BASE-9, a Bayesian analysis tool for parameters determination of stellar clusters. For a detailed discussion of the properties and implementation see Sect. 4.7.

In Chapters 4-5 we use BASE-9 to analyze large samples of OCs taking advantage of its automatic pipeline. We implement the BASE-9 library with PARSEC isochrones, in order to work with the 2MASS JHK_S photometry of those clusters. Here we reproduce the same

OC	log t	[Fe/H]	A_V	dist.mod.
NGC 2225	9.20 ± 0.07	0.05 ± 0.02	1.05 ± 0.1	12.65 ± 0.15
NGC 6134	9.15 ± 0.04	0.18 ± 0.02	1 ± 0.05	10.0 ± 0.15
NGC 2243	9.55 ± 0.1	-0.45 ± 0.05	0.2 ± 0.07	13.0 ± 0.2

Table 3.7: Clusters parameters derived from JHK_S photometry for the OCs analysed in this study.

procedure, to verify the method. We perform, as a control step, an analysis of NGC 2225, NGC 6134, NGC 2243 in JHK_S bands using BASE-9.

We start cross-matching our OCs catalogs with the HSOY ones, see Sect. 5.2. In this way we obtain both the 2MASS photometry and the proper motions for the stars in common between the two catalogs. We select only the stars in our sample within r~ 3 arcmin from the center of the cluster in order to avoid as much as possible the field contamination. Then we discard the stars with outlier proper motions and with photometric uncertainties higher than 0.1 mag. This choice reduces our samples of NGC 2243 and NGC 2225 to just the TO and RC stars, while for the brighter NGC 6134 we can use all the upper part of the MS.

The analysis method is the same described in Sect. 4.7. We use the values of age, metallicity, distance modulus and extinction, obtained from the previous analysis, as the mean of the Gaussian distributions of the priors, while we take as Gaussian dispersions twice the associated uncertainties. Finally we perform five different runs of BASE-9 shifting separately for each run the age and the distance modulus of respectively ± 0.2 and ± 0.3.

The results for the three clusters are shown in Fig. 3.31-3.32-3.33 and summarized in Table 3.7. BASE-9 converges to two different solutions for NGC 2243, one is well constrained in a narrow range of values and one is very spread in all the dimensions of the parameter space. We take into account the solution with narrower dispersion. The results are in good agreement with those inferred from synthetic populations comparison. The ages, distance moduli and extinctions obtained from BASE-9 are comparable to those of the previous study within 1σ, where σ are from Eq. 3.3-3.4-3.5. Only the distance modulus of NGC 2225 shows a higher discrepancy. This disagreement probably depends on the lack of models able to reproduce both the color and the magnitude differences between TO and RC, see Sect. 3.4.1. The metallicities found by BASE-9 are in agreement with the ones listed in literature.

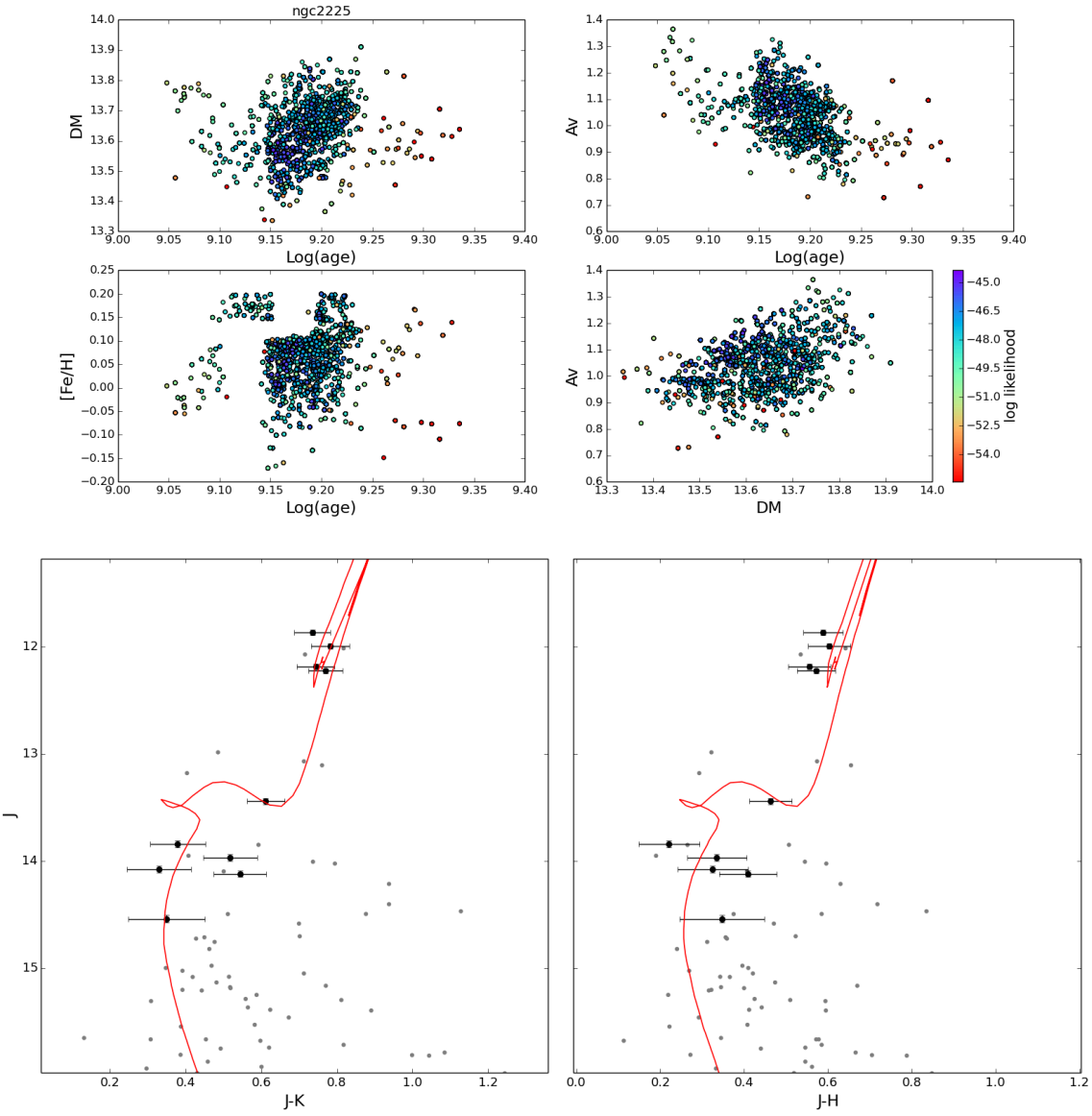

Figure 3.31: BASE-9 results for NGC 2225. Upper panels: Posterior distribution maps, combining the outputs of five runs of BASE-9. Lower panels: CMDs in the $J - K$ vs J and $J - H$ vs J planes. Grey dots represents the stars in common between our catalog and the HSOY one, black dots are the stars used as BASE-9 input. PARSEC isochrones with parameters defined by the BASE-9 best fit solution, see Table 3.7, are plotted in red.

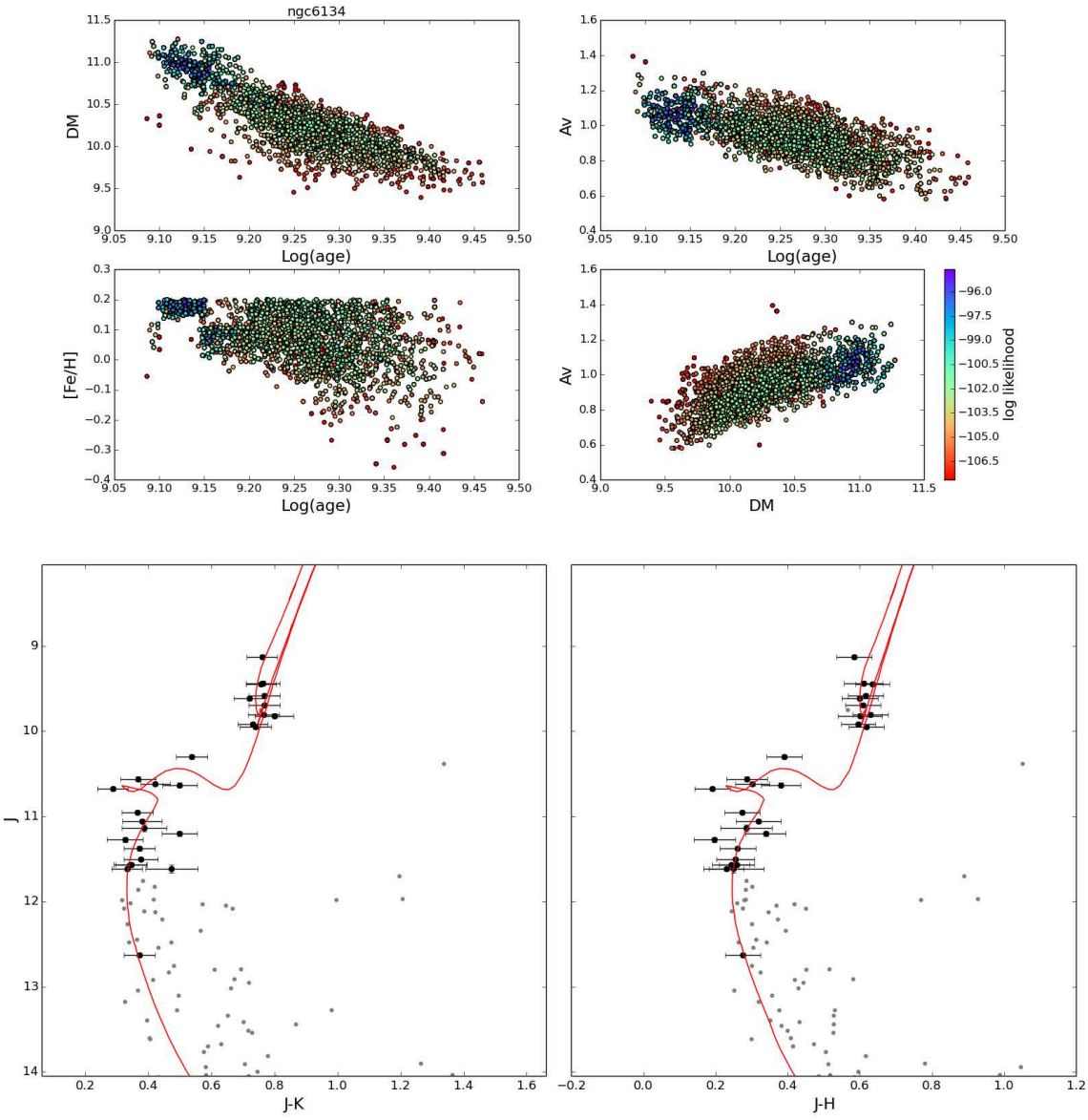

Figure 3.32: BASE-9 results for NGC 6134. For the description of the panels see Fig. 3.31.

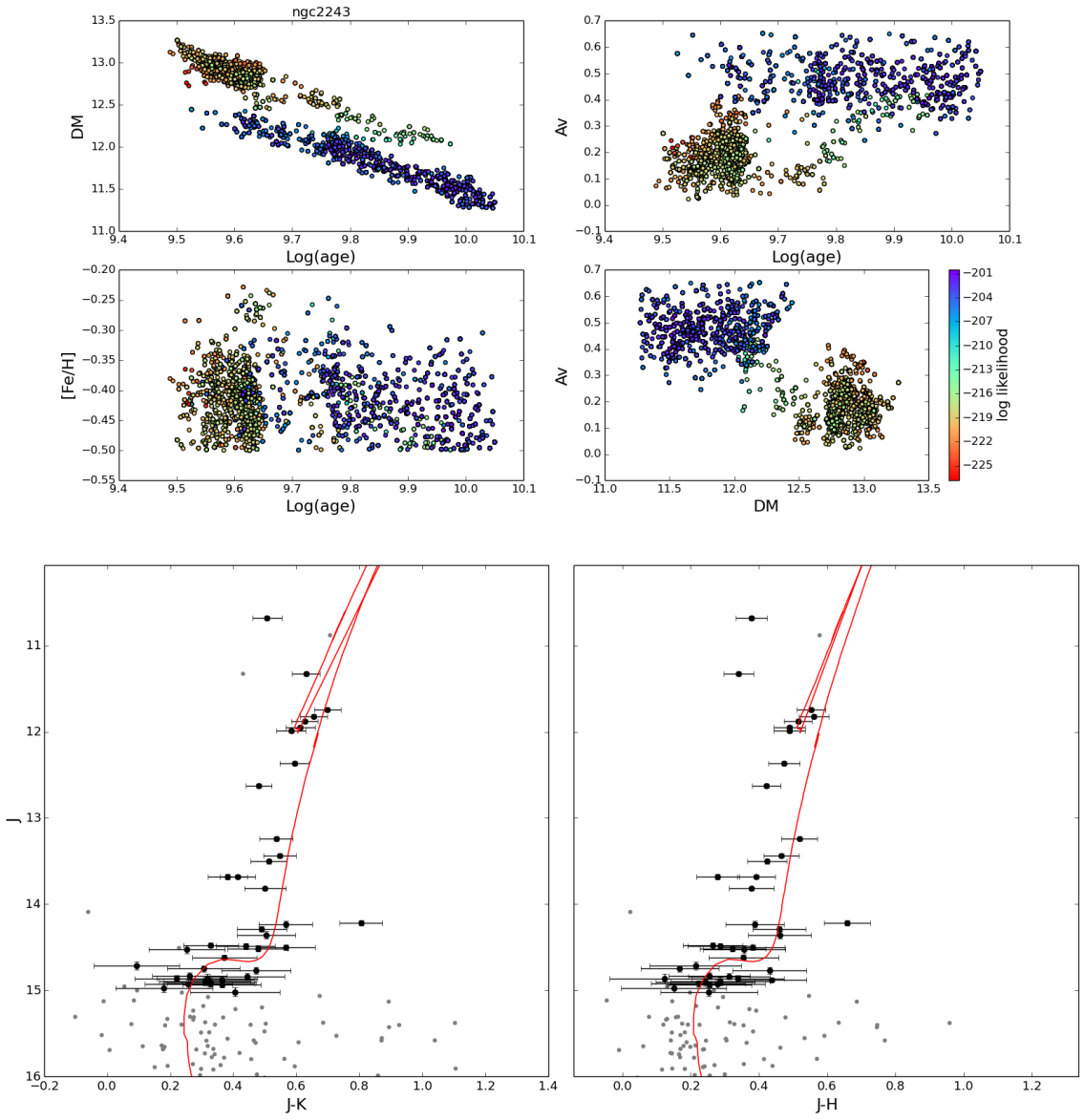

Figure 3.33: BASE-9 results for NGC 2243. For the description of the panels see Fig. 3.31.

3.6 Conclusions

In this Chapter we analyze the properties of three open clusters, namely NGC 2225, NGC 2243, NGC 6134. These clusters are specially interesting because of their location in the Galactic disk. Two of them are located in the anti-center direction, while the other is in the inner disk. These clusters have already been studied in literature. However, a larger field of view allows us to perform a better field contamination correction and to evaluate the radial extension of the clusters.
From a comparison of the observational CMDs and LFs with synthetic ones, we derive the following best fitting parameters:

- For NGC 2225, we used the DAML14 data available to identify the likely members of the cluster in upper part of the MS. In this way, we were able to confidently define the cluster TO by discarding field interlopers that could have hampered our interpretation of the CMD morphology.
  From the comparison between models and data we obtained that: the age of the cluster is 1.7 ± 0.2 Gyr, its distance modulus is $(m-M)_0 = 13.1 \pm 0.1$ mag, and its reddening $E(B-V)$ in the range 0.32-0.35. With the data at our disposal we found that the solar metallicity solution is a lower limit to the metallicity of the object.
  Examining the radial density profile of the cluster we determine a radial extension of r $\sim$3 arcmin.

- NGC 6134 is a well studied cluster. The age estimation obtained by other authors vary between 0.7 to 1.3 Gyr, in good agreement with our estimation of 1.3 ± 0.15 Gyr. We found $(m - M)_0 = 10.2 \pm 0.1$ mag and $E(B - V)$ in the range 0.29-0.32 mag. Also in this case we found a solar-metallicity solution as a lower limit.
  Examining the radial density profile of the cluster we determine a radial extension of r $\sim$5 arcmin.

- NGC 2243 is also a well studied cluster. Spectroscopic study pointed out a metallicity far below the typical values of the OCs. In this case we have at disposal both $B-V$ and $V - I$ colors and then we are able to better constrain the cluster metallicity for which we found a values between Z = 0.004 and Z = 0.007, in agreement with literature. For the age we found 3.15 Gyr $\pm$0.35. The distance modulus values have slightly differences in the two colors, respectively we found $(m - M)_0 = 13 \pm 0.15$ mag for $B - V$ and $(m - M)_0 = 13.1 \pm 0.15$ mag for $V - I$. For the reddening we found

$E(B-V)$ = 0.007 and $E(V-I)$ = 0.008.

Examining the radial density profile of the cluster we determine a radial extension of r $\sim$3-4 arcmin.

Both NGC 2225 and NGC 6134 CMDs show a MS gap respectively at $V \sim 17.5$ mag and $B-V$ within 1-1.3 mag and $V \sim 15.3$ mag and $B-V$ within 0.77-0.85 mag, already identified in past studies. Similar gaps have been observed in other OCs. There is no evident correlation neither with age nor with metallicity while arguments about internal convection may offer an explanation for some of them (see Kovtyukh et al. (2004)). This peculiar aspects deserves further investigation both in terms of observational constraints and theoretical modeling.

Furthermore we take advantage of our parameters determinations for the three clusters to validate the reliability of BASE-9 in working with 2MASS JHK_S photometry and small numbers of members. We redo an analysis of NGC 2225, NGC 6134 and NGC 2243 in JHK_S bands using BASE-9 and compare the obtained results with the previous ones. The good agreement between the solutions obtained from the two different methods indicate that BASE-9 is able to performs a trustworthy OCs parameters determination using near infrared data.

4 Characterization of OCs in the solar vicinity with Gaia first data release

4.1 Introduction

As mentioned in Chapter 1 the majority of known OCs are located within 2 kpc from the Sun. This census is far from being complete, in particular for the fainter objects, that are small and sparse or remnants of disrupted clusters. Those OCs can escape detection (Bica & Bonatto, 2011), even when their stars are visible, because they do not stand out as significant over-densities. Furthermore detected OCs can actually be only asterisms.

In order to be able to distinguish between those and a genuine cluster, astrometric information are necessary. The ongoing *Gaia* space mission will provide those astrometric data (proper motions and parallaxes) for a billion sources, see e.g. Perryman et al. (1997) and Gaia Collaboration et al. (2016b). In the first *Gaia* Data Release (GDR1) a full astrometric solution is provided for 2 million of sources in the TGAS data set, see Sect. 2.3.

The aims of the work presented in this chapter are two-fold: i) to update the cluster census in the solar neighborhood, deriving memberships, mean distance modulus and proper motions from the GDR1 and ii) to validate the use of tools which will be applied to the second Gaia data release, whose high quality will allow for a deeper study of a much larger sample of clusters. Handling such large, multi-dimensional datasets (whose applications extend well beyond cluster science) requires automated methods in order to identify and select cluster members, and to characterize stellar clusters (see e.g. Robichon et al. (1999), with Hipparcos data).

This present study focuses on objects located within 2 kpc of the Sun, for which the number of stars and quality of the astrometry present in GDR1 is sufficient.

4.2 Proper motion in the TGAS dataset

The quality of TGAS data is not constant across the sky. Indeed, because of the *Gaia* scanning law, the sky coverage is not homogeneous in the GDR1, based on 14 months of data (Gaia Collaboration et al., 2016a). This produce significant inhomogeneities of the TGAS data quality.

These inhomogeneities become apparent when we compare the TGAS uncertainties on proper motions with those of UCAC4 catalog (Zacharias et al., 2012). The uncertainties on proper motions of TGAS stars are in the range 0.5–2.6 mas yr^{-1} , with a median value of 1.1 mas yr^{-1} (Lindegren et al., 2016b). UCAC4 proper motion formal uncertainties are in the range 1–10 mas yr^{-1} , with possible systematics of the order of 1–4 mas yr^{-1} (Zacharias et al., 2013), on average higher than TGAS uncertainties. However, the effect of the Gaia scanning law is that in some regions TGAS uncertainties can be higher than in UCAC4. Fig 4.1, give a clear picture of what we said.

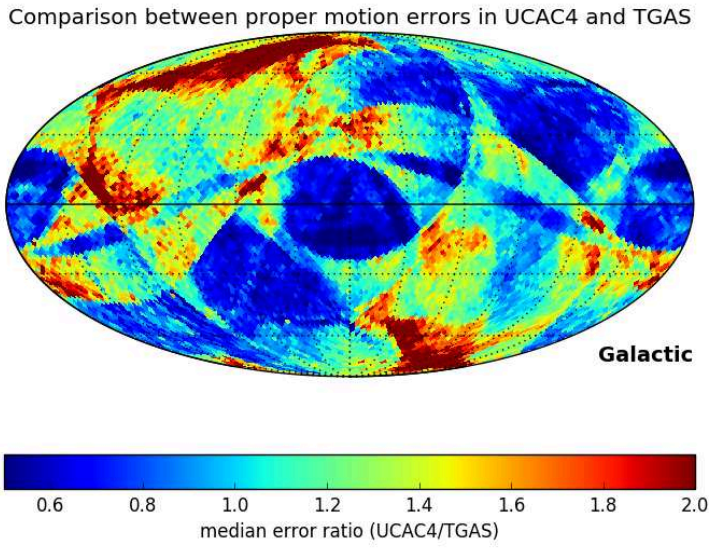

Figure 4.1: Median proper motion error ratio between UCAC4 and TGAS for stars present in both catalogs, in HEALPix level 5 pixels, in Galactic coordinates (North to the top, increasing longitude to the left, Galactic center at the center).

The plot shows a comparison between the proper motion uncertainties in UCAC4 and TGAS for the stars present in both catalogs. The mean proper motion difference between TGAS and UCAC4 for those stars is plotted in Fig 4.2. Local systematic differences of the order of 1 to 3 mas yr^{-1} are present all across the sky.
In each field under analysis we used the proper motion catalog which provided the smallest median uncertainty, thus using TGAS proper motions in the regions where the ratio shown in Fig 4.1 is above 1. For the parallaxes we always refer to TGAS value.

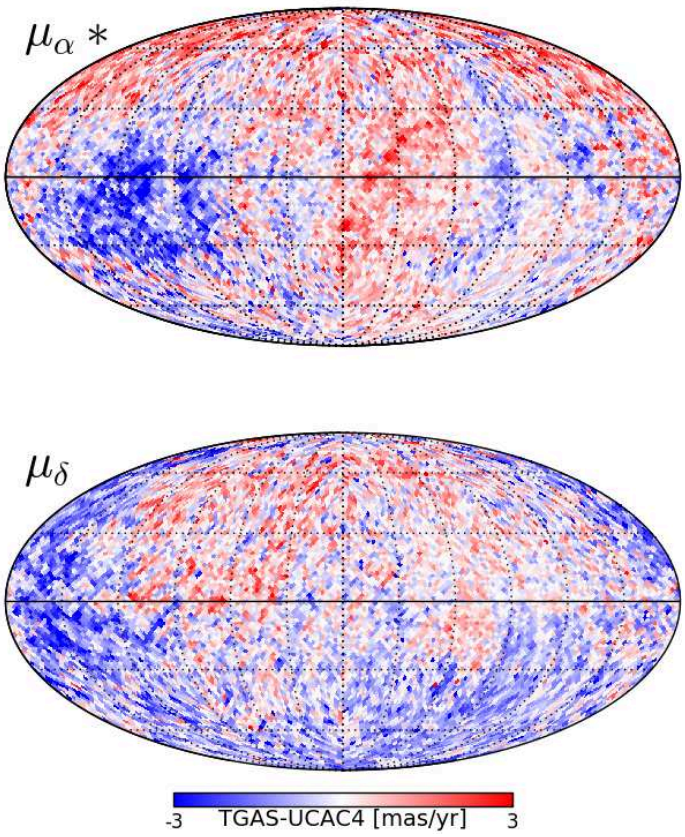

Figure 4.2: *Upper panel*: Mean $\mu_{\alpha*}$ difference between UCAC4 and TGAS for stars present in both catalogs, in HEALPix level 5 pixels, in Galactic coordinates (North to the top, increasing longitude to the left, Galactic center at the center). *Upper panel*: same for the μ_δ component of the proper motion.

4.3 Target selection

To select the targets for this study we start with cluster coordinates and parameters provided by MWSC catalog. In order to use the TGAS information we discard all the cluster more distant of 2000 pc, i.e. with a parallax value less than 0.5 mas. For clusters more distant than this limit the distance estimation is strongly affected by parallax uncertainty, with a relative errors σ_{ϖ}/ϖ larger than 50%. Another discrimination factor is if clusters have or not stars brighter than V = 11.5, which is the completeness limit of TGAS catalog. Using PARSEC isochrones we evaluate which clusters are visible in TGAS according to their listed age, distance, and extinction.
Finally, we exclude from this study the 19 nearby OCs studied in Gaia Collaboration et al. (2017), namely: the Hyades, the Pleiades, Coma Berenices, Praesepe, Alpha Perseus, Blanco 1, Collinder 140, IC 2391, IC 2602, IC 4665, NGC 2451A, NGC 6475, NGC 6633, NGC 7092, NGC 2516, NGC 2232, NGC 2422, NGC 3532, and NGC 2547. This left us with a list of 694 OCs to investigate. Possible members are investigated inside a wide radius of the order of 20 pc at the reference distance of the cluster.

4.4 Methods: Membership determination with UPMASK

Our determination of cluster membership relies on proper motions and parallaxes. To eliminate obvious field stars we first performed a broad selection, rejecting all stars with proper motions more distant than 10 mas yr^{-1} from the cluster literature value. For clusters closer than 500 pc we also rejected stars with parallaxes under 1 mas. Although the field of view of some pairs of OCs overlap (e.g. NGC 2451 with NGC 2477), the difference in proper motions allowed us to tell the two clusters apart. On the remaining star sample, our approach to membership determination is based on the principles of unsupervised membership assignment method UPMASK (Krone-Martins & Moitinho, 2014).

4.4.1 Conceptual approach

The UPMASK method starts from the definition of star clusters as spatial over-densities of stars with a common origin, whereas field stars as spatially sparse objects which don't share a single origin. The basic assumption of the method is that member of stellar clusters

share common properties owing to their common origin. Statistically they will be clustered together in most parameter spaces. This approach does not rely on strong physical assumptions on the nature of clusters (no assumptions on a density profile modeling nor on the structure in photometric space), except that their stars share common properties, and that the spatial distributions of cluster stars is concentrated, while the distribution of field stars is random. The core idea of UPMASK is to apply a simple clustering algorithm (for instance, k-means clustering) to identify small groups[1] of stars with similar properties, then check all these small groups individually and determine whether their spatial distribution is more tightly concentrated than a random distribution (this is referred to as the "veto" step).
However, several observable are correlated, and the provided information could be redundant. To avoid redundancy is necessary to reduce the parameter space in a space of independent variables. This kind of operation can be done through principal component analysis (PCA). PCA is a statistical procedure that uses a linear transformation to convert a set correlated variables into a set of uncorrelated latent variables called principal components (PCs). This is done projecting the data onto an orthogonal coordinate system encoding most of the information content of original observables (see Pearson (1901) and Hotelling (1933)).

4.4.2 The UPMASK method with astrometric data

The authors use photometry and position to built the parameter space for searching cluster members aggregation, but the same procedure can be easily applied to other types of quantities, as its only strong assumption is to consider that cluster members must be, in any observable space, more tightly distributed than field stars. This assumption happens to hold not only for photometry and positions, but also for astrometry, since all stars within a cluster are expected to be located at the same distance from us and moving in the same direction, regardless of their colour and luminosity. In this study, rather than applying the k-means clustering to a set of magnitudes in different photometric filters, we applied it to the three-dimensional astrometric space of proper motions and parallaxes ($\mu_{\alpha*}$, μ_δ , ϖ). The code, that we develop in python language, permit also to increase the number of observables adding also photometric data. In this case PCA is applied in order to avoid redundancy. In order to avoid that observables with large variance dominate the determination of PCs, we

[1] In machine learning and data mining it is common to refer to a group of objects as a cluster. We tried to refer to the output of k- means clustering (abstract grouping of data points with similar observed properties) as groups, to avoid any possible confusion with stellar clusters (astronomical objects).

scale each of these observables to unit variance.
Then a k-means clustering method is conducted on the selected parameter space in order to divide data in k groups. The number k can not be set directly by the user, instead the user have to set the number of stars per group. The test performed by Krone-Martins & Moitinho (2014) had best results using values between 10 and 25 stars per group. In this study since we expect several clusters to have very few members in the TGAS data, we set this mean number to 10.
The next step is to determine if those identified groups are spatially more concentrated than a random distribution. To do this we adopt the method described by Allison et al. (2009). Originally the method was developed by the authors to detect and quantify mass segregation in star clusters. The method consist in comparing the minimum spanning three (MST) of stars groups with that of random distribution. Defining l_{obs} as branch length of the MST of a group and l the expected value in a random distribution containing the same number of stars, we set as condition, for stars in the group to be possible cluster members, that l_{obs} have to be smaller than the tabulated l by at least σ_l.

$$\Lambda = \frac{l - l_{obs}}{\sigma_l} > 1 \tag{4.1}$$

To save computation time, for sample sizes from 3 to 80 we pre-computed and tabulated the expected l and associated standard deviations σ_l by generating 2000 random circular distributions.
Figure 4.3 shows an example of k-means clustering applied to the stellar cluster NGC 752, and the sky distribution of three selected groups. In that example, two of the shown groups are considered as containing potential cluster members.

After the veto step the star flagged as cluster members is retained for subsequent iteration, whereas the stars classified as field are discarded. These steps are repeated until the number of selected stars is equal to the previous iteration (no more field stars selected) or the number of selected stars is 0 (no cluster members).
What described until now is considered the core UPMASK kernel, see Fig. 4.4. The kernel routine, due to its random nature, could discard some cluster members and catalog them as field stars. To minimize this possibility the UPMASK kernel is insert in an outer loop, with a prefixed number of iterations, we choose 100. At each iteration, instead of using the catalogue value we add to each data point a random offset in proper motion and parallax, corresponding to the uncertainties. After a total of 100 iterations, the frequency with which

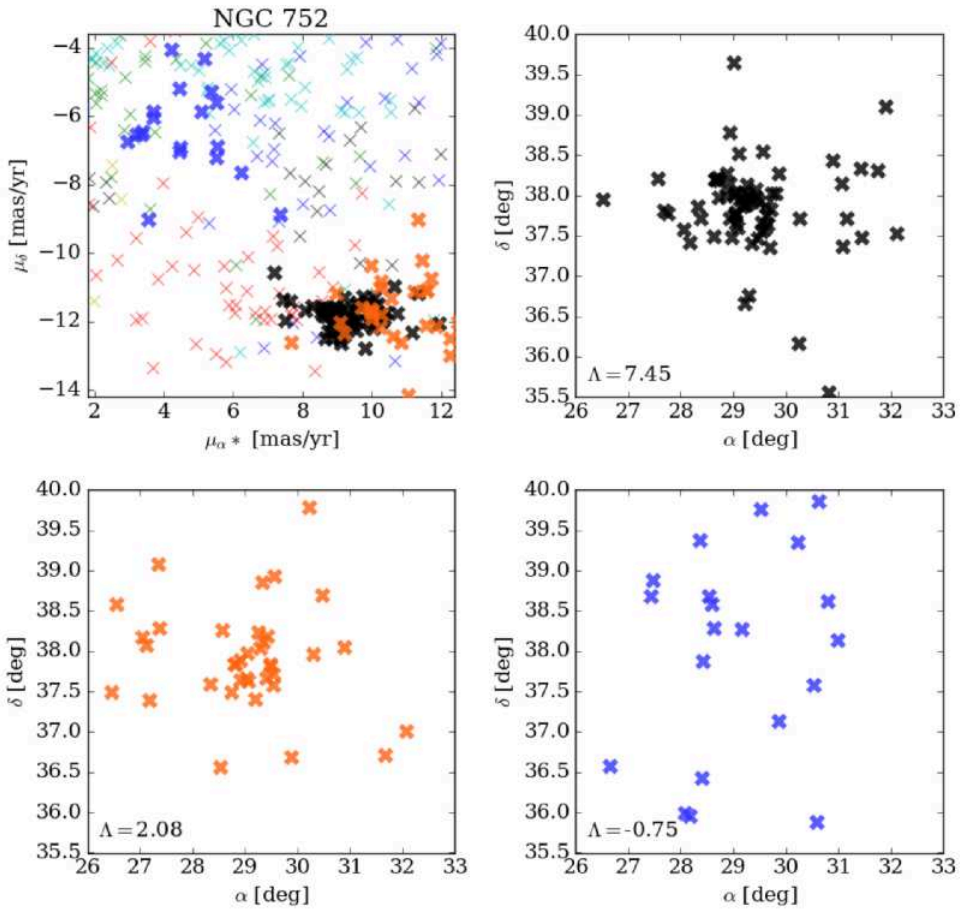

Figure 4.3: The top left panel shows the proper motions of stars in the field of NGC 752. The colour-code corresponds to the groups identified by k-means clustering in the ($\mu_{\alpha*}$, μ_δ , ϖ) space. The sky distribution of the three highlighted groups is shown in the other panels. Λ is a measurement of spatial clustering, as defined in Eq. 4.1. Stars are considered potential cluster members when $\Lambda > 1$.

a star was flagged as part of a clustered group is interpreted as its membership probability, see Fig. 4.5.

The random nature of the grouping step performed in the heuristic of UPMASK means that small groups of field stars might sometimes be flagged as clustered (in other words, even purely random distribution are expected to satisfy Eq. 4.1), and these stars end up with non-zero membership probabilities of a few percent, which can be considered noise level. To obtain cleaner results and a better contrast between field and cluster stars, we applied the procedure a second time for all OCs, after discarding stars for which the first run yielded

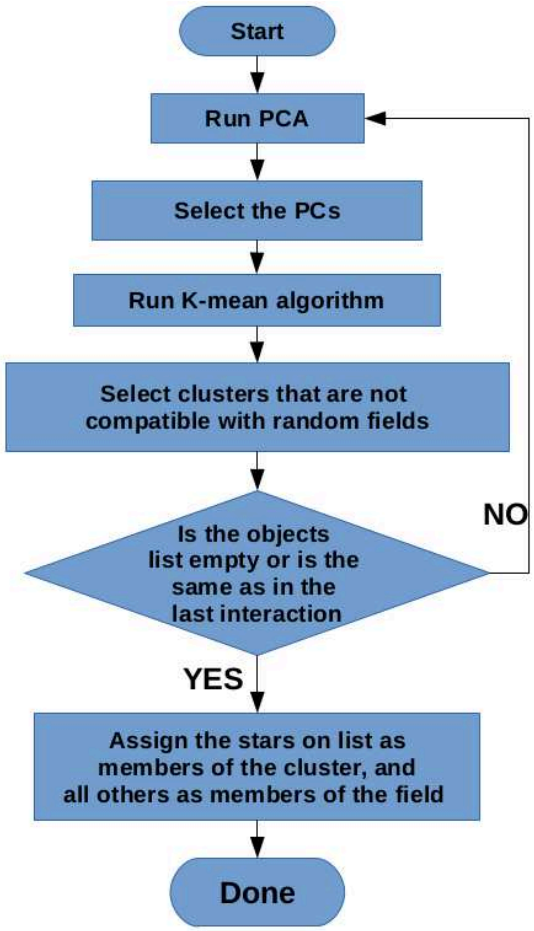

Figure 4.4: Flowchart of the UPMASK kernel.

probabilities lower than 10%. We consider the final membership probability to be the result of this second run.

In this work we analyze the probability membership of stars in the field of view of 134 clusters, finding a total of 5844 potential member (probability $> 50\%$) and 1322 high probability members (probability $>90\%$).

The results of the member selection procedure is shown for 10 clusters (ASCC 16, ASCC 21, IC 4756, NGC 752, NGC 1647, NGC 1750, NGC 2287, NGC 2423, NGC2437 and NGC3532) as examples, see Fig. 4.6, Fig. 4.7, Fig. 4.8, Fig. 4.9 and Fig. 4.10.

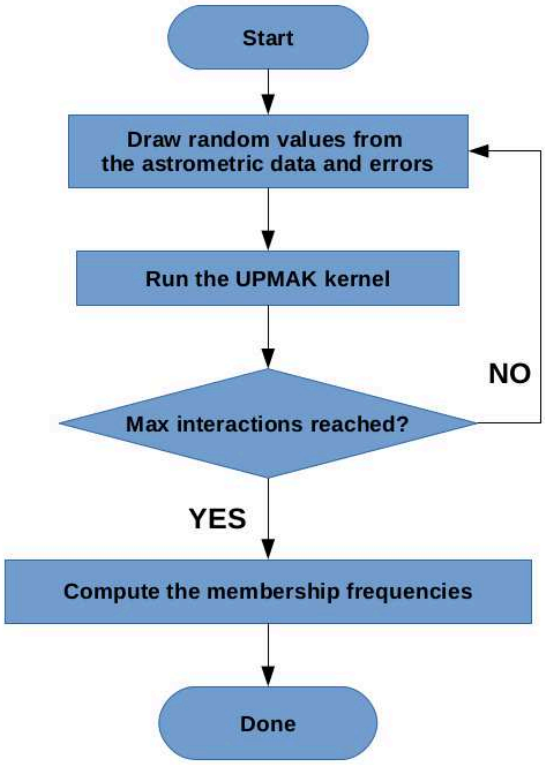

Figure 4.5: Flowchart of the UPMASK kernel.

4.4.3 TGAS parameter correlations

As mentioned in the previous section at each iteration of the UPMASK outer loop, a different point in the astrometric space is taken for each star. The value is chosen randomly between all the possible value contained in the range fixed by the uncertainties of the sources. When we use TGAS astrometric value we have to take in account the fact that the parameters uncertainties are correlated, see Sect. 2.3.3. Furthermore this correlations are not constant in the different regions of the sky, see Lindegren et al. (2016b).

For each star, the covariance matrix is:

$$Cov = \begin{bmatrix} \sigma^2_{\alpha*} & \sigma_{\alpha*}\sigma_{\delta}\rho_{\mu_{\alpha*}\mu_{\delta}} & \sigma_{\alpha*}\sigma_{\varpi}\rho_{\mu_{\alpha*}\mu_{\varpi}} \\ \sigma_{\alpha*}\sigma_{\delta}\rho_{\mu_{\alpha*}\mu_{\delta}} & \sigma^2_{\delta} & \sigma_{\delta}\sigma_{\varpi}\rho_{\mu_{\delta}\mu_{\varpi}} \\ \sigma_{\alpha*}\sigma_{\varpi}\rho_{\mu_{\alpha*}\mu_{\varpi}} & \sigma_{\delta}\sigma_{\varpi}\rho_{\mu_{\delta}\mu_{\varpi}} & \sigma^2_{\varpi} \end{bmatrix}$$

Non-diagonal terms represent the correlation coefficients between the corresponding parameters on the main diagonal. To regard the errors as independent means neglecting the non-diagonal terms, i.e. fix $\rho = 0$, which in general is a wrong assumption. This is illus-

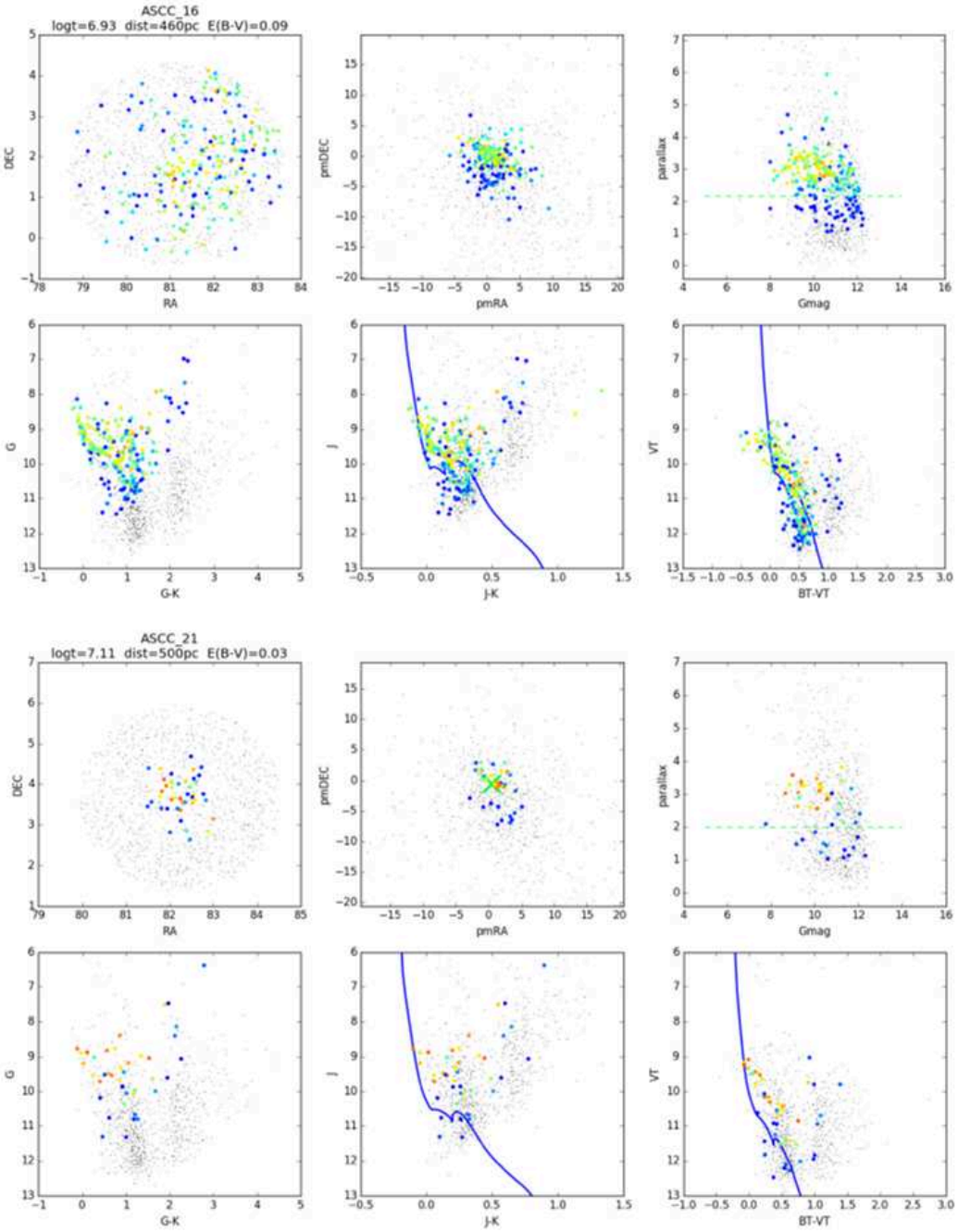

Figure 4.6: Membership for ASCC 16 *(top panels)* and ASCC 21 *(bottom panels)*. Black dots are all stars within 20 pc. Coloured dots are stars with probability membership over 10% (blue=10%, red=%100). The green line shows the expected parallax from literature distance. The plotted isochrones are PARSEC models with literature value.

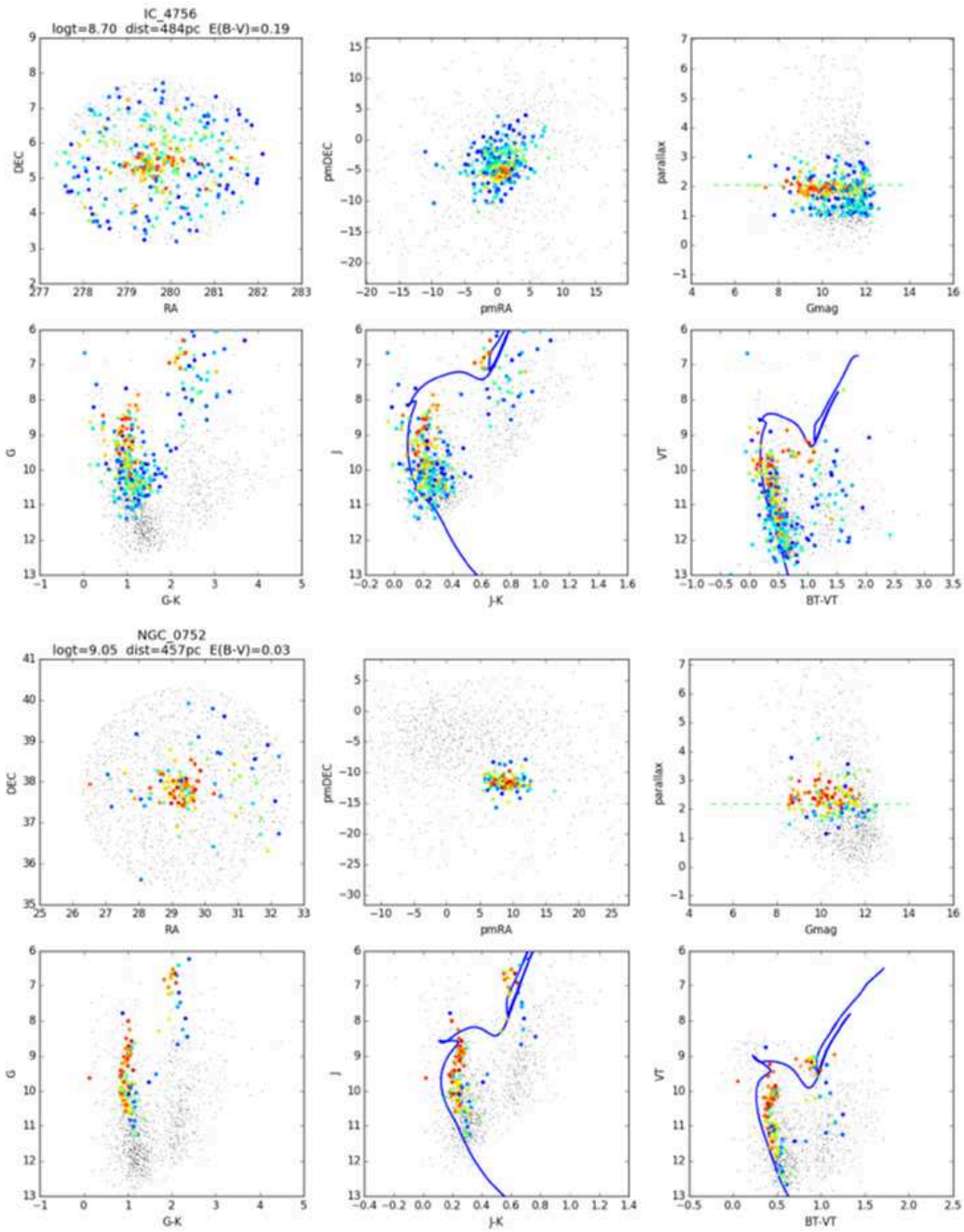

Figure 4.7: Membership for IC 4756 *(top panels)* and NGC 752 *(bottom panels)*. Black dots are all stars within 20 pc. Colored dots are stars with probability membership over 10% (blue=10%, red=%100). The green line shows the expected parallax from literature distance. The plotted isochrones are PARSEC models with literature value.

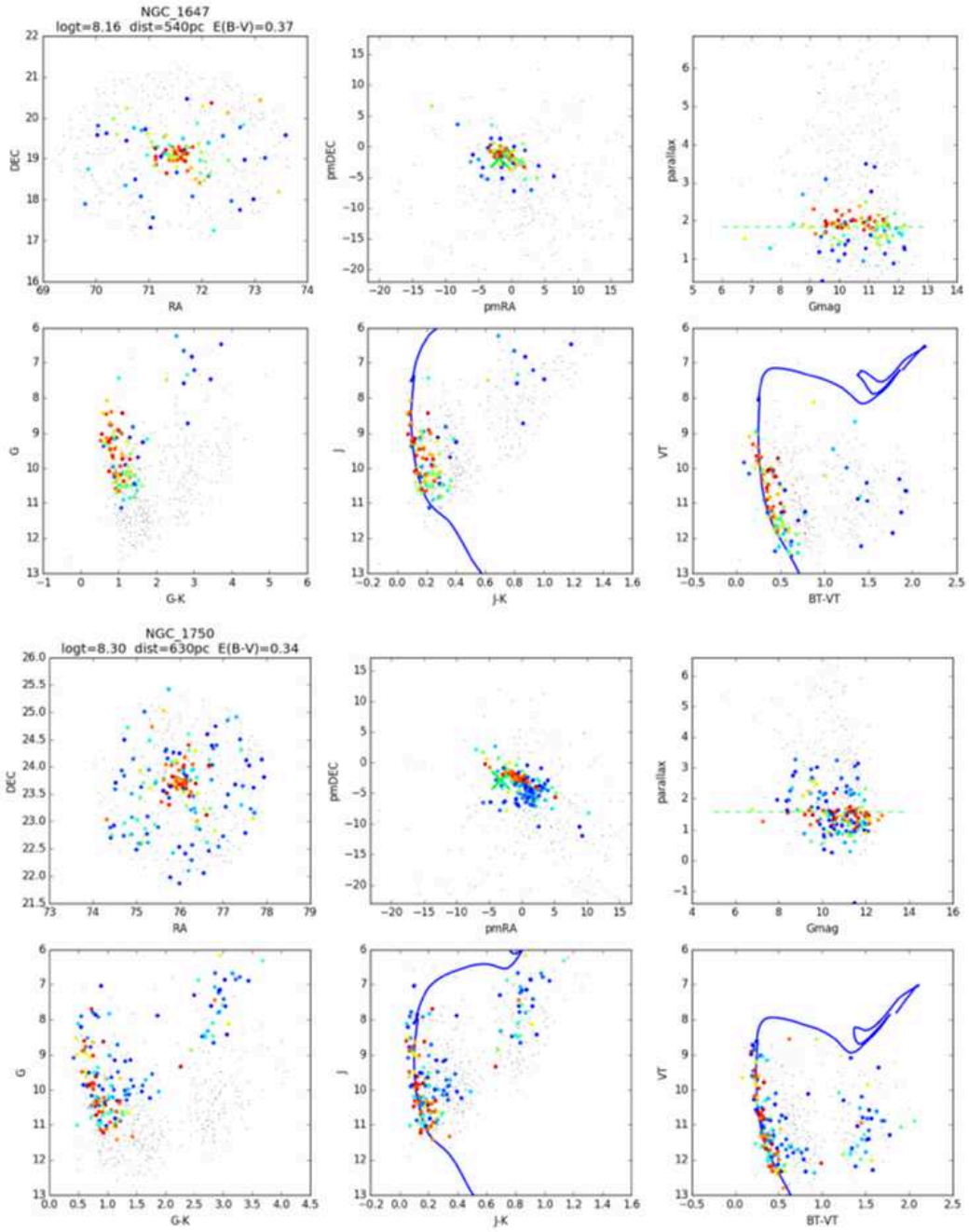

Figure 4.8: Membership for NGC 1647 *(top panels)* and NGC 1750 *(bottom panels)*. Black dots are all stars within 20 pc. Colored dots are stars with probability membership over 10% (blue=10%, red=%100). The green line shows the expected parallax from literature distance. The plotted isochrones are PARSEC models with literature value.

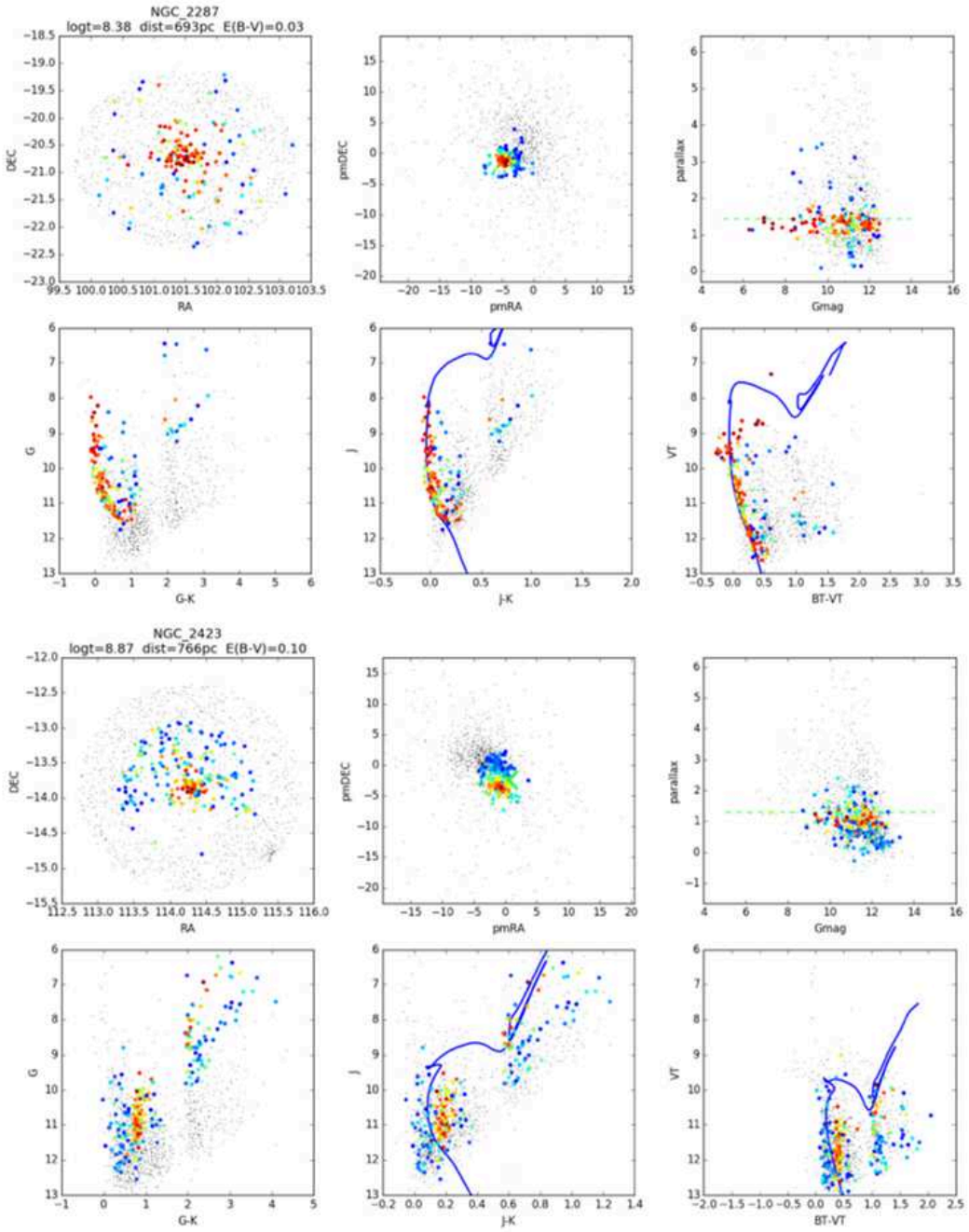

Figure 4.9: Membership for NGC 2287 *(top panels)* and NGC 2423 *(bottom panels)*. Black dots are all stars within 20 pc. Colored dots are stars with probability membership over 10% (blue=10%, red=%100). The green line shows the expected parallax from literature distance. The plotted isochrones are PARSEC models with literature value.

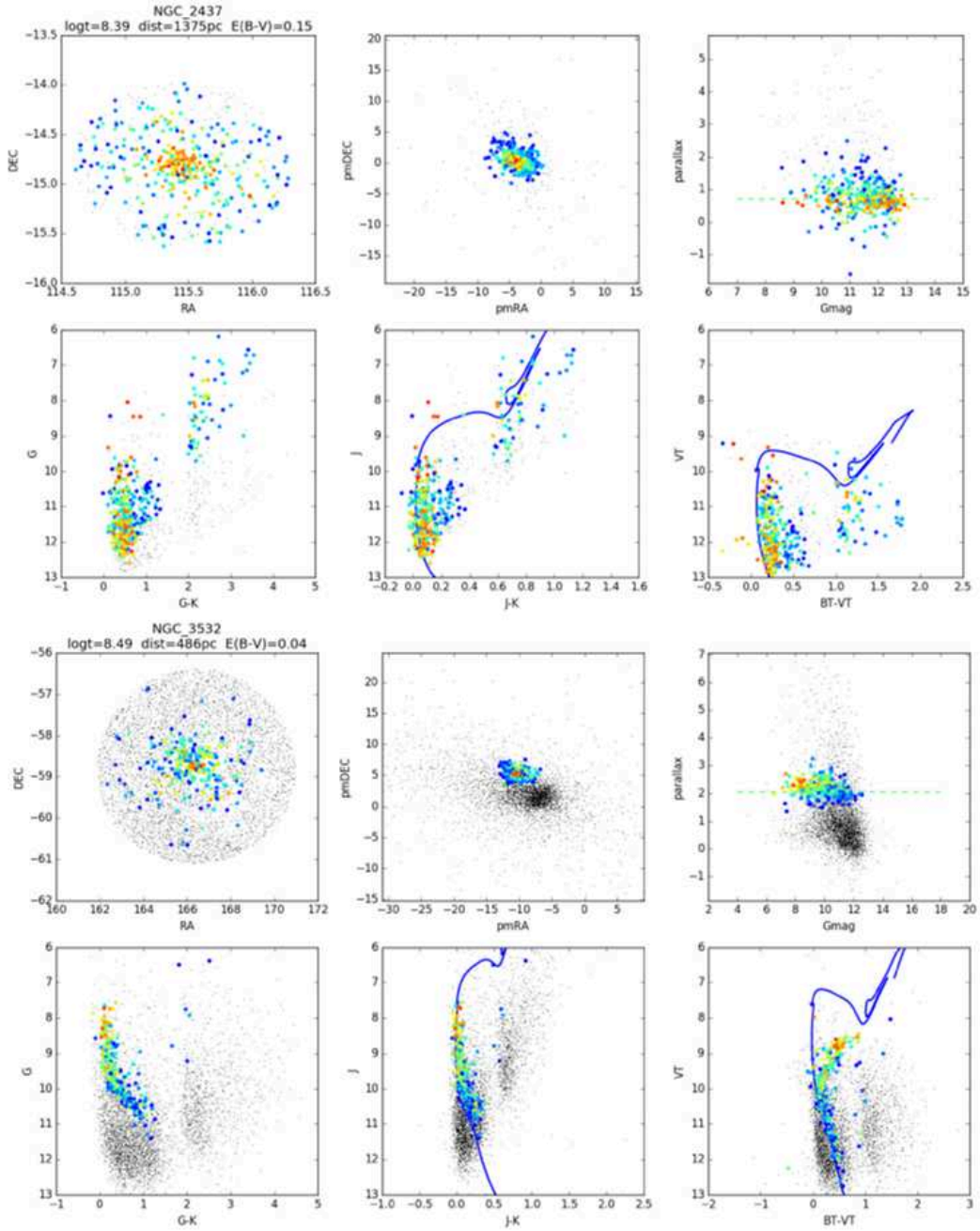

Figure 4.10: Membership for NGC 2437 *(top panels)* and NGC 3532 *(bottom panels)*. Black dots are all stars within 20 pc. Colored dots are stars with probability membership over 10% (blue=10%, red=%100). The green line shows the expected parallax from literature distance. The plotted isochrones are PARSEC models with literature value.

trated in Fig. 4.11, where ρ for proper motions and parallaxes are shown to be significantly different from zero for a large number of stars used in this study.

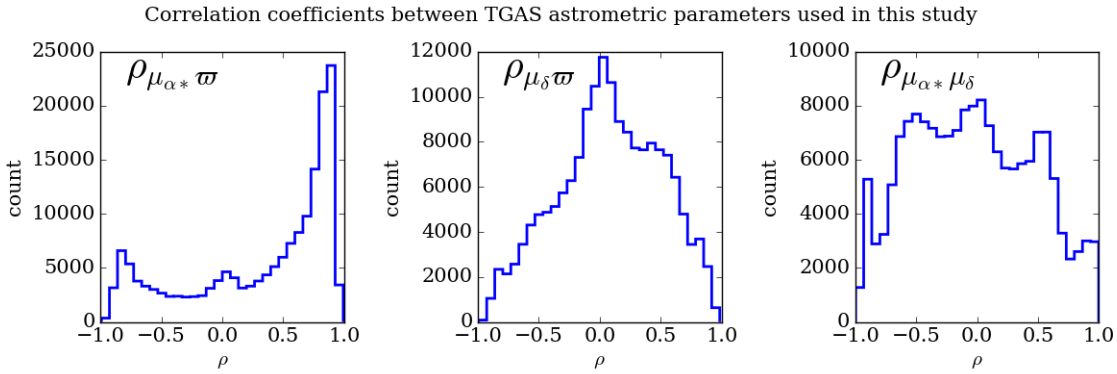

Figure 4.11: Histograms for the value of the correlation coefficient ρ between the three astrometric parameters $\mu_{\alpha*}$, μ_δ and ϖ for the stars used in this study in the field where TGAS proper motions uncertainties are smaller that the UCAC4 uncertainties.

A visual example of how much parameter correlations influence the membership probability analysis, is given in Fig. 4.12. The panels show a comparison between UCAC4 and TGAS proper motions uncertainties for NGC 2360. For TGAS the uncertainties are represented as error bars, or ellipses in the non-covariant representation (respectively left and central panel), and as tilted ellipses when the correlations are taken into account, which are always narrower than the non-covariant representation. Obviously the identification of clustered features are clearer with the TGAS data.

For this cluster, TGAS uncertainties are significantly smaller than UCAC4 ones. It is also clearly visible that some stars that appear as marginally compatible with cluster membership in the non-covariant representation, are easily identifiable as outliers when correlations are considered.

4.5 Mean proper motions and parallaxes

We computed the mean astrometric parameters of high probability cluster members after applying a two-sigma clipping on the proper motions, parallaxes, and sky distribution of the member stars. In order to determine a mean proper motion and mean parallax for each cluster taking into account both the membership probability and the uncertainty on the parameters of each star, we performed thousand random drawings where we picked stars ac-

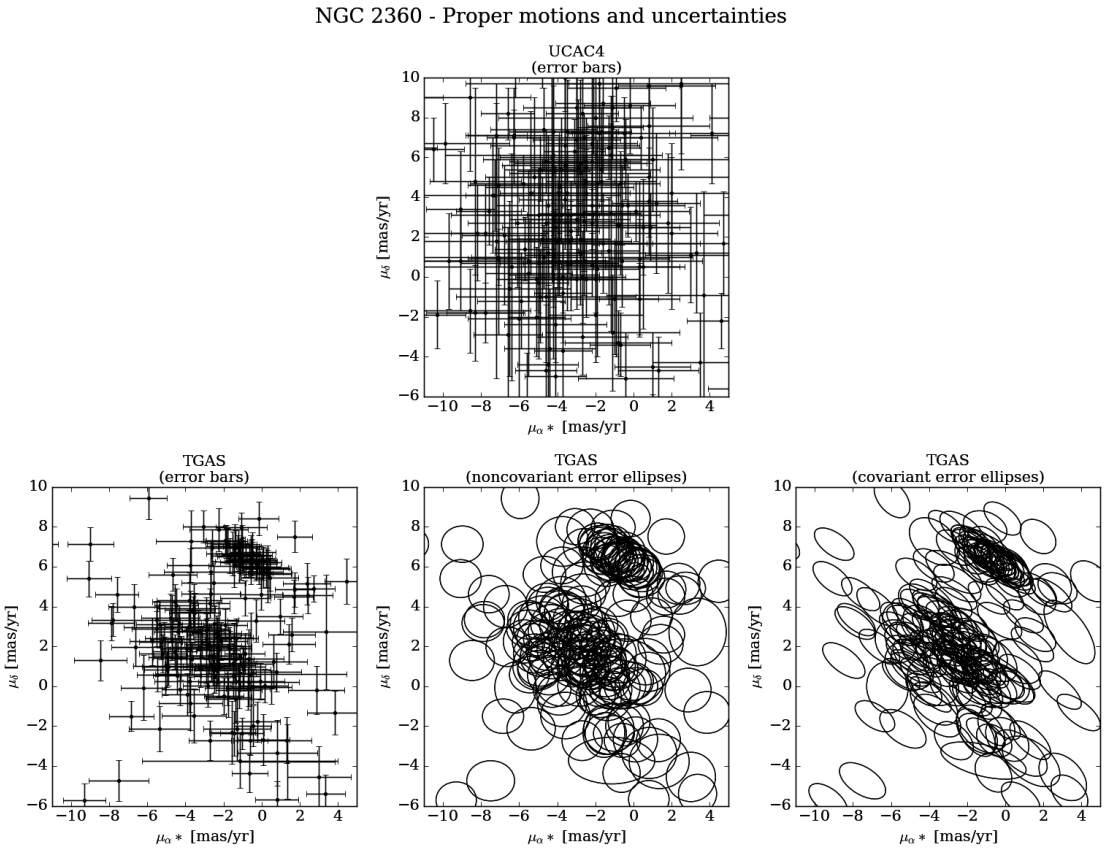

Figure 4.12: *Top*: UCAC4 proper motions for NGC 2360. *Bottom left*: TGAS proper motions for the same set of stars, with nominal uncertainties represented as error bars. *Bottom middle*: same as bottom left panel, but the uncertainties represented as non-covariant error ellipses. *Bottom right*: same data as bottom middle panel, with uncertainties represented as tilted error ellipses, showing the correlations between μ_{alpha} and μ_{delta} errors (here of the order of -0.8).

cording to their probability of being cluster members. For each redrawing, the mean proper motion and mean parallax was computed as a weighted mean, where the weight for each star corresponds to the inverse variance (inverse uncertainty, squared), and the uncertainty on this mean value is the standard deviation divided by the square root of the number of selected stars. The final value is the average over all re-drawings, and the final uncertainty is the average the uncertainties over all re-drawings.

As pointed out by Arenou et al. (2017), the TGAS parallax zero-point show local systematic biases, see Sect. 2.3.4. This effect anyway does not affect our ability to distinguish between

background and foreground stars within a small field of view.
We derive the distance modulus from the parallax as $5log(\varpi) - 5$ for the 134 OCs that converged in our analysis. The results are shown in Table 4.1, 4.2 and 4.3.
Out of the 134 OCs for which we derived mean astrometric parameters, 72 have mean proper motions obtained from TGAS data (with a median proper motion error of 0.23 mas yr^{-1}), while UCAC4 data was used for 61 of them (these OCs have a median proper motion error of 0.32 mas yr^{-1}).
The TGAS permit to enlarge the distance in which OCs membership and parallaxes can be identified. For comparison we remind that with Hipparcos data(e.g. Robichon et al. (1999) or Bouy & Alves (2015)) relative parallax error reach 50% at 350 pc.

Finally we remark that the MWSC and DAML catalogs sometimes list different distance moduli for the same object. In Fig. 4.13 we show 42 objects for which our distance modulus estimate disagrees with either MWSC or DAML (and with both in the case of Collinder 350 and Haffner 13) by more than one unit of uncertainty.

4.6 Preliminary photometric analysis

To determine the physical parameters for such a large number of clusters we use an automated approach based on Bayesian statistic. The advantage of this choice is to obtain an uniform parameters determination for the whole sample. The purpose is to obtain a set of results free from inhomogeneities that can be generated in a classic isochrone eye-fitted analysis performed separately for every single cluster.
Before starting the Bayesian analysis of the OCs photometric data, we perform a preliminary analysis to insure that our parallaxes are a good prior. This analysis consist in a classical isochrones fit analysis performed on OCs CMD. The idea is to verify if the distances estimated in previous section, combined with the literature value for age, extinction and metallicity, produce a plausible isochrone fit with data. When metallicity values are not provided by literature we use a solar metallicity solution.
With each cluster we associate three parallaxes values, i.e., the average value obtained by parallax and the upper and lower limits of the parallax range fixed by the uncertainties. The isochrones fit is performed on the candidate members in the B-V vs V and J-K vs K planes, with PARSEC models (Bressan et al., 2012), using a `FILLTHETEMPO` routine, see

OC	α [deg]	δ [deg]	$<\varpi>$ [mas]	dist.mod.	$<\mu_{\alpha*}>$ [mass yr^{-1}]	$<\mu_{\delta}>$ [mass yr^{-1}]	PM	nb
ASCC 10	51.750	35.040	1.65 ± 0.13	8.92 ± 0.17	-3.11 ± 0.26	-1.19 ± 0.21	U	19
ASCC 112	304.108	52.100	1.46 ± 0.12	9.17 ± 0.17	-0.83 ± 0.32	-0.13 ± 0.34	U	15
ASCC 113	318.000	38.600	1.72 ± 0.05	8.83 ± 0.06	0.78 ± 0.14	-3.86 ± 0.09	T	43
ASCC 123	340.646	54.260	4.49 ± 0.11	6.74 ± 0.05	10.90 ± 0.35	-1.77 ± 0.47	U	5
ASCC 124	342.029	46.250	1.32 ± 0.09	9.40 ± 0.15	0.31 ± 0.10	-1.79 ± 0.08	T	8
ASCC 16	81.146	1.800	2.95 ± 0.08	7.65 ± 0.06	1.94 ± 0.30	0.53 ± 0.21	U	20
ASCC 18	81.537	0.820	2.94 ± 0.06	7.66 ± 0.04	0.56 ± 0.23	0.60 ± 0.15	U	71
ASCC 19	81.942	-1.980	2.63 ± 0.10	7.90 ± 0.08	1.13 ± 0.21	-1.29 ± 0.16	T	22
ASCC 21	82.242	3.650	2.97 ± 0.10	7.63 ± 0.08	0.59 ± 0.25	0.93 ± 0.31	U	17
ASCC 23	95.083	46.670	1.61 ± 0.10	8.96 ± 0.13	0.29 ± 0.22	-0.41 ± 0.14	U	18
ASCC 32	105.492	-26.500	1.20 ± 0.04	9.60 ± 0.07	-3.22 ± 0.09	3.50 ± 0.07	T	44
ASCC 41	116.758	0.020	3.40 ± 0.09	7.34 ± 0.05	1.25 ± 0.22	-4.33 ± 0.39	U	14
ASCC 51	139.500	-69.690	2.01 ± 0.17	8.48 ± 0.18	-7.48 ± 0.45	9.01 ± 0.44	T	9
ASCC 99	282.267	-18.730	3.37 ± 0.11	7.36 ± 0.07	5.63 ± 0.42	-0.63 ± 0.34	U	30
Alessi 10	301.183	-10.480	1.97 ± 0.11	8.53 ± 0.12	1.68 ± 0.30	-7.15 ± 0.21	T	16
Alessi 12	310.875	23.780	1.84 ± 0.15	8.68 ± 0.17	3.83 ± 0.15	-5.30 ± 0.13	U	23
Alessi 13	52.050	-35.900	9.94 ± 0.16	5.01 ± 0.04	36.69 ± 0.35	-4.25 ± 0.30	T	10
Alessi 21	107.696	-9.340	1.77 ± 0.08	8.76 ± 0.10	-5.62 ± 0.16	2.70 ± 0.18	T	22
Alessi 2	71.562	55.230	1.73 ± 0.05	8.82 ± 0.07	-1.09 ± 0.26	-0.91 ± 0.15	U	24
Alessi 3	109.079	-46.610	3.71 ± 0.05	7.15 ± 0.03	-9.70 ± 0.11	12.22 ± 0.12	T	37
Alessi 5	160.783	-61.170	2.52 ± 0.04	7.99 ± 0.03	-15.50 ± 0.08	2.61 ± 0.10	T	16
Alessi 6	220.062	-66.120	1.23 ± 0.03	9.55 ± 0.05	-10.38 ± 0.11	-5.78 ± 0.10	T	8
Alessi 9	265.979	-47.180	4.87 ± 0.11	6.56 ± 0.05	10.84 ± 0.30	-8.16 ± 0.38	U	19
BH 99	159.475	-59.183	2.43 ± 0.10	8.07 ± 0.09	-14.48 ± 0.09	1.30 ± 0.10	T	12
Chereul 1	217.267	55.392	10.05 ± 0.18	4.99 ± 0.04	-16.71 ± 0.44	-2.82 ± 0.29	T	8
Collinder 135	109.321	-36.817	3.41 ± 0.08	7.33 ± 0.05	-9.11 ± 0.22	5.57 ± 0.24	U	39
Collinder 140	110.800	-32.033	2.78 ± 0.09	7.78 ± 0.07	-8.08 ± 0.10	4.77 ± 0.11	T	7
Collinder 350	267.029	1.350	2.78 ± 0.05	7.78 ± 0.04	-3.85 ± 0.21	0.23 ± 0.22	U	24
Collinder 359	270.275	2.900	1.84 ± 0.07	8.68 ± 0.09	1.89 ± 0.20	-8.30 ± 0.25	U	46
Collinder 394	283.117	-20.317	1.28 ± 0.08	9.46 ± 0.13	-0.68 ± 0.34	-4.73 ± 0.32	U	23
Collinder 463	27.100	71.950	1.28 ± 0.08	9.47 ± 0.13	-1.82 ± 0.12	-0.22 ± 0.17	T	56
Haffner 13	115.125	-30.080	2.15 ± 0.02	8.33 ± 0.02	-5.74 ± 0.23	6.39 ± 0.17	T	10
IC 4725	277.946	-19.117	1.59 ± 0.07	9.00 ± 0.09	-3.20 ± 0.29	-5.51 ± 0.33	U	46
IC 4756	279.750	5.450	1.94 ± 0.02	8.56 ± 0.02	0.57 ± 0.13	-2.64 ± 0.15	U	117
King 6	52.025	56.450	1.55 ± 0.36	9.04 ± 0.52	-0.55 ± 2.04	-2.21 ± 0.90	T	10
Lynga 2	216.146	-61.333	1.04 ± 0.05	9.92 ± 0.10	-6.73 ± 0.16	-4.90 ± 0.20	T	7
Melotte 101	160.550	-65.100	0.29 ± 0.07	12.68 ± 0.52	-6.94 ± 0.18	2.48 ± 0.08	T	10
NGC 0752	29.421	37.785	2.34 ± 0.04	8.16 ± 0.04	8.13 ± 0.08	-12.13 ± 0.07	U	76
NGC 1027	40.667	61.595	0.71 ± 0.07	10.74 ± 0.21	-3.59 ± 0.17	2.45 ± 0.16	U	11
NGC 1039	40.521	42.762	1.97 ± 0.07	8.53 ± 0.08	-0.56 ± 0.12	-6.43 ± 0.10	U	33
NGC 1342	52.908	37.377	1.49 ± 0.05	9.13 ± 0.07	0.09 ± 0.20	-1.55 ± 0.10	T	25
NGC 1528	63.846	51.215	0.93 ± 0.04	10.16 ± 0.10	2.06 ± 0.12	-1.92 ± 0.14	U	26
NGC 1545	65.237	50.253	1.30 ± 0.10	9.43 ± 0.16	-2.24 ± 0.18	0.54 ± 0.18	U	9
NGC 1647	71.479	19.115	1.87 ± 0.03	8.65 ± 0.04	-0.95 ± 0.10	-1.73 ± 0.11	U	65
NGC 1662	72.112	10.937	2.56 ± 0.05	7.96 ± 0.04	-1.02 ± 0.13	-2.04 ± 0.12	T	48

Table 4.1: Mean astrometric parameters computed for 134 OCs. U indicates the UCAC4 proper motions were used, T indicates TGAS proper motions.

OC	α [deg]	δ [deg]	$<\varpi>$ [mas]	dist.mod.	$<\mu_{\alpha*}>$ [mass yr^{-1}]	$<\mu_{\delta}>$ [mass yr^{-1}]	PM	nb
NGC 1750	75.979	23.658	1.49 ± 0.05	9.13 ± 0.07	-3.58 ± 0.13	-3.67 ± 0.12	U	58
NGC 1778	77.017	37.023	0.53 ± 0.04	11.38 ± 0.18	-0.57 ± 0.26	-4.70 ± 0.26	U	9
NGC 1901	79.562	-68.437	2.63 ± 0.09	7.90 ± 0.08	1.45 ± 0.37	12.59 ± 0.29	T	18
NGC 1912	82.167	35.848	0.86 ± 0.05	10.32 ± 0.11	-0.07 ± 0.26	-4.73 ± 0.26	U	54
NGC 1960	84.075	34.140	1.01 ± 0.04	9.98 ± 0.09	-0.38 ± 0.15	-5.40 ± 0.11	U	25
NGC 1977	83.850	-4.820	2.34 ± 0.10	8.16 ± 0.09	0.41 ± 0.20	0.14 ± 0.25	T	21
NGC 2099	88.075	32.553	0.77 ± 0.06	10.58 ± 0.17	2.12 ± 0.23	-7.20 ± 0.21	U	52
NGC 2168	92.250	24.350	1.12 ± 0.04	9.76 ± 0.07	0.75 ± 0.09	-4.18 ± 0.08	U	102
NGC 2215	95.204	-7.283	1.22 ± 0.12	9.57 ± 0.21	0.36 ± 0.27	-2.99 ± 0.24	T	23
NGC 2244	97.979	4.942	0.82 ± 0.03	10.43 ± 0.08	-0.40 ± 0.46	0.35 ± 0.38	U	8
NGC 2264	100.242	9.895	1.38 ± 0.05	9.31 ± 0.08	-0.18 ± 0.24	-3.17 ± 0.24	U	12
NGC 2281	102.071	41.078	2.14 ± 0.07	8.35 ± 0.08	-3.96 ± 0.18	-8.11 ± 0.13	U	53
NGC 2287	101.504	-20.757	1.28 ± 0.02	9.46 ± 0.04	-4.40 ± 0.06	-1.39 ± 0.05	T	84
NGC 2323	105.675	-8.383	1.03 ± 0.03	9.94 ± 0.06	-0.59 ± 0.10	-0.61 ± 0.10	T	110
NGC 2353	108.625	-10.267	0.65 ± 0.09	10.94 ± 0.31	-0.98 ± 0.20	0.80 ± 0.27	T	21
NGC 2360	109.429	-15.642	0.74 ± 0.03	10.66 ± 0.09	-0.12 ± 0.13	5.99 ± 0.11	T	35
NGC 2423	114.275	-13.872	1.04 ± 0.04	9.92 ± 0.07	-0.79 ± 0.09	-3.57 ± 0.07	T	69
NGC 2437	115.442	-14.810	0.64 ± 0.02	10.97 ± 0.06	-3.78 ± 0.07	0.33 ± 0.06	T	123
NGC 2447	116.125	-23.857	1.12 ± 0.04	9.74 ± 0.07	-3.55 ± 0.12	5.08 ± 0.07	T	61
NGC 2451B	116.112	-37.667	2.86 ± 0.05	7.72 ± 0.04	-9.74 ± 0.17	4.31 ± 0.15	T	22
NGC 2477	118.042	-38.530	0.53 ± 0.10	11.38 ± 0.41	0.27 ± 0.60	2.06 ± 0.73	U	13
NGC 2482	118.800	-24.258	0.73 ± 0.07	10.69 ± 0.21	-4.53 ± 0.23	2.29 ± 0.11	T	31
NGC 2527	121.242	-28.147	1.73 ± 0.03	8.81 ± 0.03	-5.37 ± 0.07	7.36 ± 0.07	T	79
NGC 2539	122.654	-12.818	0.99 ± 0.25	10.03 ± 0.57	-2.35 ± 0.26	-1.80 ± 0.35	U	19
NGC 2546	123.062	-37.595	0.94 ± 0.07	10.13 ± 0.16	-3.66 ± 0.09	4.20 ± 0.06	T	25
NGC 2547	122.537	-49.215	2.72 ± 0.07	7.83 ± 0.05	-8.77 ± 0.11	4.51 ± 0.09	T	14
NGC 2548	123.429	-5.750	1.45 ± 0.06	9.20 ± 0.10	-0.82 ± 0.18	2.07 ± 0.20	U	67
NGC 2567	124.633	-30.640	0.55 ± 0.03	11.29 ± 0.11	-2.98 ± 0.06	2.42 ± 0.07	T	26
NGC 2571	124.733	-29.750	0.98 ± 0.08	10.05 ± 0.17	-4.60 ± 0.13	4.42 ± 0.08	T	15
NGC 2669	131.592	-52.948	1.15 ± 0.12	9.70 ± 0.22	-4.17 ± 0.30	4.64 ± 0.31	T	7
NGC 2670	131.375	-48.800	0.57 ± 0.05	11.21 ± 0.19	-5.67 ± 0.23	3.68 ± 0.11	T	13
NGC 2682	132.825	11.800	1.40 ± 0.14	9.28 ± 0.21	-9.34 ± 0.33	-4.70 ± 0.35	U	18
NGC 3228	155.342	-51.728	2.19 ± 0.07	8.29 ± 0.07	-13.92 ± 0.28	-1.40 ± 0.51	T	5
NGC 3330	159.692	-54.123	0.61 ± 0.04	11.08 ± 0.14	-6.92 ± 0.12	0.93 ± 0.08	T	5
NGC 3680	171.408	-43.243	1.17 ± 0.06	9.67 ± 0.12	-7.16 ± 0.17	0.85 ± 0.19	T	17
NGC 4103	181.667	-61.250	0.40 ± 0.09	11.99 ± 0.51	-6.56 ± 0.21	-0.18 ± 0.19	T	25
NGC 4609	190.575	-62.995	0.68 ± 0.10	10.85 ± 0.33	-4.87 ± 0.16	-1.06 ± 0.19	T	15
NGC 4852	195.037	-59.613	0.64 ± 0.08	10.96 ± 0.27	-7.92 ± 0.15	-2.07 ± 0.22	T	22
NGC 5138	201.817	-59.033	0.60 ± 0.10	11.11 ± 0.36	-3.58 ± 0.14	-1.75 ± 0.21	T	17
NGC 5281	206.646	-62.917	0.67 ± 0.11	10.86 ± 0.35	-4.40 ± 0.29	-2.79 ± 0.22	T	20
NGC 5316	208.488	-61.868	0.70 ± 0.04	10.78 ± 0.13	-6.32 ± 0.06	-1.53 ± 0.07	T	25
NGC 5460	211.863	-48.343	1.45 ± 0.11	9.20 ± 0.17	-2.92 ± 0.32	-1.23 ± 0.27	U	14
NGC 5593	216.404	-54.800	1.23 ± 0.07	9.56 ± 0.13	-5.19 ± 0.16	-2.37 ± 0.14	T	9
NGC 5617	217.433	-60.712	0.28 ± 0.06	12.74 ± 0.47	-5.85 ± 0.13	-3.44 ± 0.10	T	18
NGC 5662	218.904	-56.618	1.34 ± 0.03	9.37 ± 0.05	-6.56 ± 0.09	-7.19 ± 0.07	T	53
NGC 5822	226.092	-54.400	1.18 ± 0.02	9.64 ± 0.04	-7.45 ± 0.08	-5.26 ± 0.05	T	77
NGC 6025	240.821	-60.432	1.17 ± 0.05	9.67 ± 0.09	-3.05 ± 0.10	-3.01 ± 0.11	T	34
NGC 6067	243.296	-54.218	0.35 ± 0.04	12.26 ± 0.25	-1.97 ± 0.09	-2.70 ± 0.08	T	37
NGC 6087	244.708	-57.935	1.00 ± 0.04	10.01 ± 0.09	-1.67 ± 0.06	-2.47 ± 0.07	T	13

Table 4.2: Continue.

OC	α [deg]	δ [deg]	$<\varpi>$ [mas]	dist.mod.	$<\mu_{\alpha*}>$ [mass yr^{-1}]	$<\mu_{\delta}>$ [mass yr^{-1}]	PM	nb
NGC 6124	246.333	-40.653	1.67 ± 0.08	8.89 ± 0.10	-0.60 ± 0.20	-0.50 ± 0.20	U	46
NGC 6134	246.942	-49.152	0.91 ± 0.10	10.20 ± 0.25	1.83 ± 0.35	-4.50 ± 0.23	T	6
NGC 6152	248.175	-52.640	0.63 ± 0.04	11.02 ± 0.15	-2.78 ± 0.16	-4.88 ± 0.16	T	24
NGC 6281	256.171	-37.985	1.73 ± 0.04	8.81 ± 0.06	-2.07 ± 0.20	-3.10 ± 0.22	U	63
NGC 6405	265.083	-32.253	2.20 ± 0.09	8.29 ± 0.08	-1.50 ± 0.26	-4.92 ± 0.32	U	43
NGC 6416	266.079	-32.362	0.92 ± 0.08	10.18 ± 0.20	-1.16 ± 0.36	-0.01 ± 0.29	U	26
NGC 6494	269.267	-18.985	1.25 ± 0.04	9.52 ± 0.08	1.15 ± 0.20	-0.07 ± 0.20	U	61
NGC 6604	274.512	-12.242	0.36 ± 0.12	12.22 ± 0.77	-0.77 ± 0.23	-1.74 ± 0.34	U	19
NGC 6694	281.325	-9.383	0.51 ± 0.04	11.47 ± 0.16	0.22 ± 0.22	-1.12 ± 0.25	T	14
NGC 6705	282.771	-6.270	0.57 ± 0.04	11.21 ± 0.17	-1.95 ± 0.39	-4.90 ± 0.42	T	8
NGC 6716	283.642	-19.902	1.40 ± 0.07	9.26 ± 0.11	-0.52 ± 0.28	-4.64 ± 0.31	U	60
NGC 6793	290.804	22.140	1.67 ± 0.10	8.89 ± 0.13	3.63 ± 0.23	3.44 ± 0.25	T	28
NGC 6811	294.321	46.388	0.96 ± 0.07	10.08 ± 0.16	-4.48 ± 0.11	-7.62 ± 0.12	U	29
NGC 6866	300.979	44.158	0.78 ± 0.14	10.53 ± 0.38	-1.62 ± 0.47	-4.79 ± 0.22	U	7
NGC 6913	305.988	38.508	0.49 ± 0.05	11.56 ± 0.22	-4.11 ± 0.16	-5.42 ± 0.12	U	32
NGC 6940	308.608	28.283	0.91 ± 0.04	10.21 ± 0.08	-2.09 ± 0.10	-9.54 ± 0.12	T	98
NGC 6991	313.633	47.450	1.82 ± 0.06	8.70 ± 0.07	5.16 ± 0.13	8.79 ± 0.09	U	45
NGC 7209	331.279	46.483	1.08 ± 0.05	9.84 ± 0.11	2.17 ± 0.14	0.28 ± 0.11	T	37
NGC 7243	333.783	49.898	1.28 ± 0.05	9.47 ± 0.09	0.16 ± 0.07	-2.40 ± 0.07	U	28
Platais 10	205.421	-59.210	3.99 ± 0.07	7.00 ± 0.04	-30.33 ± 0.21	-10.53 ± 0.20	T	9
Platais 3	68.850	71.580	5.56 ± 0.06	6.27 ± 0.02	3.50 ± 0.22	-21.10 ± 0.17	T	13
Platais 8	136.950	-59.140	7.57 ± 0.06	5.60 ± 0.02	-15.38 ± 0.22	14.98 ± 0.26	T	11
Platais 9	138.537	-44.140	5.69 ± 0.14	6.23 ± 0.05	-24.85 ± 0.29	12.76 ± 0.23	T	14
Roslund 3	299.675	20.483	0.81 ± 0.12	10.47 ± 0.32	-1.28 ± 0.26	-4.08 ± 0.30	U	24
Roslund 6	307.196	39.260	2.66 ± 0.06	7.87 ± 0.05	5.12 ± 0.16	1.58 ± 0.15	U	50
Ruprecht 145	282.642	-18.220	1.31 ± 0.08	9.41 ± 0.14	7.38 ± 0.29	-2.59 ± 0.29	U	15
Ruprecht 147	289.167	-16.300	3.26 ± 0.07	7.43 ± 0.05	-1.42 ± 0.22	-27.00 ± 0.18	U	59
Ruprecht 1	99.104	-14.180	0.81 ± 0.08	10.46 ± 0.22	-1.11 ± 0.28	0.07 ± 0.19	T	17
Ruprecht 98	179.667	-64.583	2.10 ± 0.08	8.39 ± 0.08	-4.30 ± 0.16	-8.65 ± 0.10	T	22
Stock 10	84.750	37.930	2.97 ± 0.13	7.64 ± 0.09	-4.20 ± 0.21	-0.80 ± 0.22	U	12
Stock 12	353.892	52.690	2.01 ± 0.07	8.48 ± 0.07	8.31 ± 0.17	-2.13 ± 0.16	U	7
Stock 1	293.950	25.217	2.30 ± 0.03	8.19 ± 0.03	6.04 ± 0.08	0.32 ± 0.11	T	49
Stock 2	33.750	59.267	2.79 ± 0.03	7.77 ± 0.02	16.22 ± 0.05	-13.76 ± 0.05	U	122
Stock 7	37.400	60.650	1.42 ± 0.09	9.23 ± 0.14	-4.51 ± 0.26	1.16 ± 0.19	U	10
Trumpler 10	131.975	-42.450	2.30 ± 0.05	8.19 ± 0.05	-12.38 ± 0.14	6.84 ± 0.12	T	52
Trumpler 2	39.325	55.983	1.51 ± 0.07	9.11 ± 0.10	0.36 ± 0.13	-6.14 ± 0.08	U	18
Trumpler 33	276.175	-19.717	0.60 ± 0.08	11.10 ± 0.28	-1.47 ± 0.89	-0.75 ± 1.56	U	8
Trumpler 3	47.954	63.190	1.38 ± 0.08	9.31 ± 0.12	-3.99 ± 0.15	-0.23 ± 0.12	U	27
Turner 5	143.129	-36.470	2.44 ± 0.06	8.07 ± 0.05	0.19 ± 0.28	-2.66 ± 0.33	T	21
vdBergh 92	105.975	-11.490	0.76 ± 0.07	10.60 ± 0.21	-5.43 ± 0.28	2.55 ± 0.27	T	12

Table 4.3: Continue.

Sect. 3.3.2.

As explained the scope of this step is not the determination of cluster parameters by isochrones fit, but to check if our distance values and membership probabilities for cluster stars bring to a reasonable determination of them. In some case this check is possible and provide a good feedback, in Fig 4.14-4.15-4.16 some OCs are plotted as examples. In other cases the check can not be done because the high scatter of cluster member or the weak determination of cluster member, see respectively the upper and the lower panel in Fig 4.17.

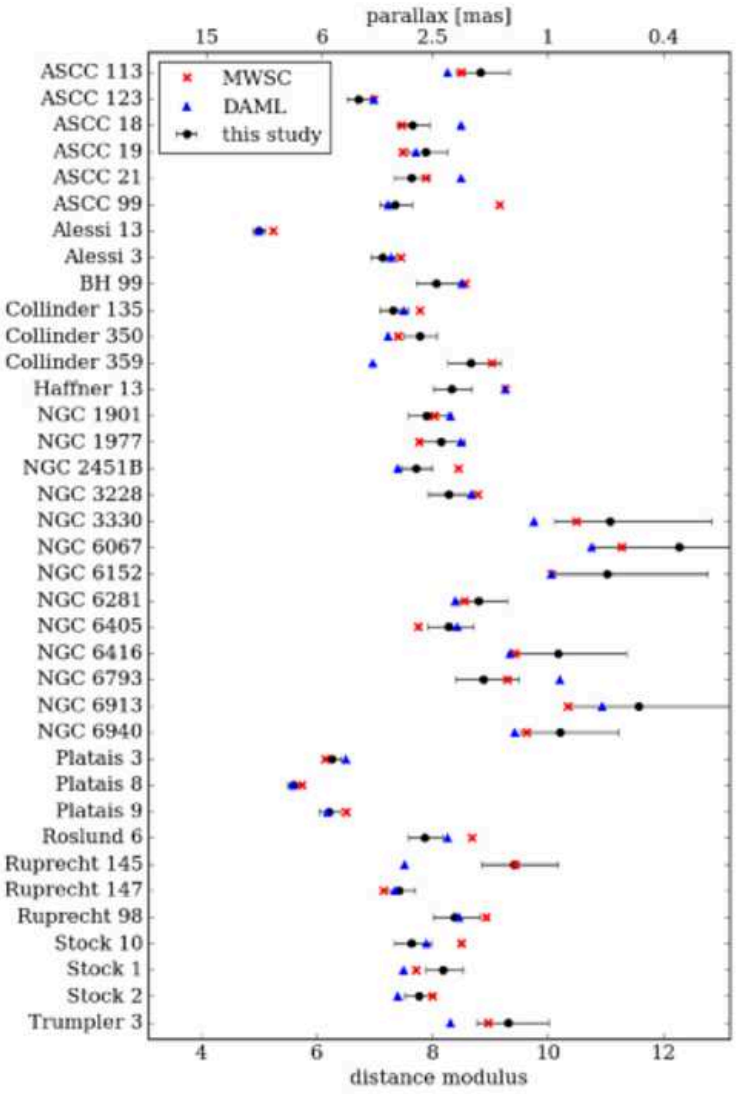

Figure 4.13: Distance modulus for the OCs for which TGAS parallaxes yield values discrepant with the values listed in either MWSC or DAML.

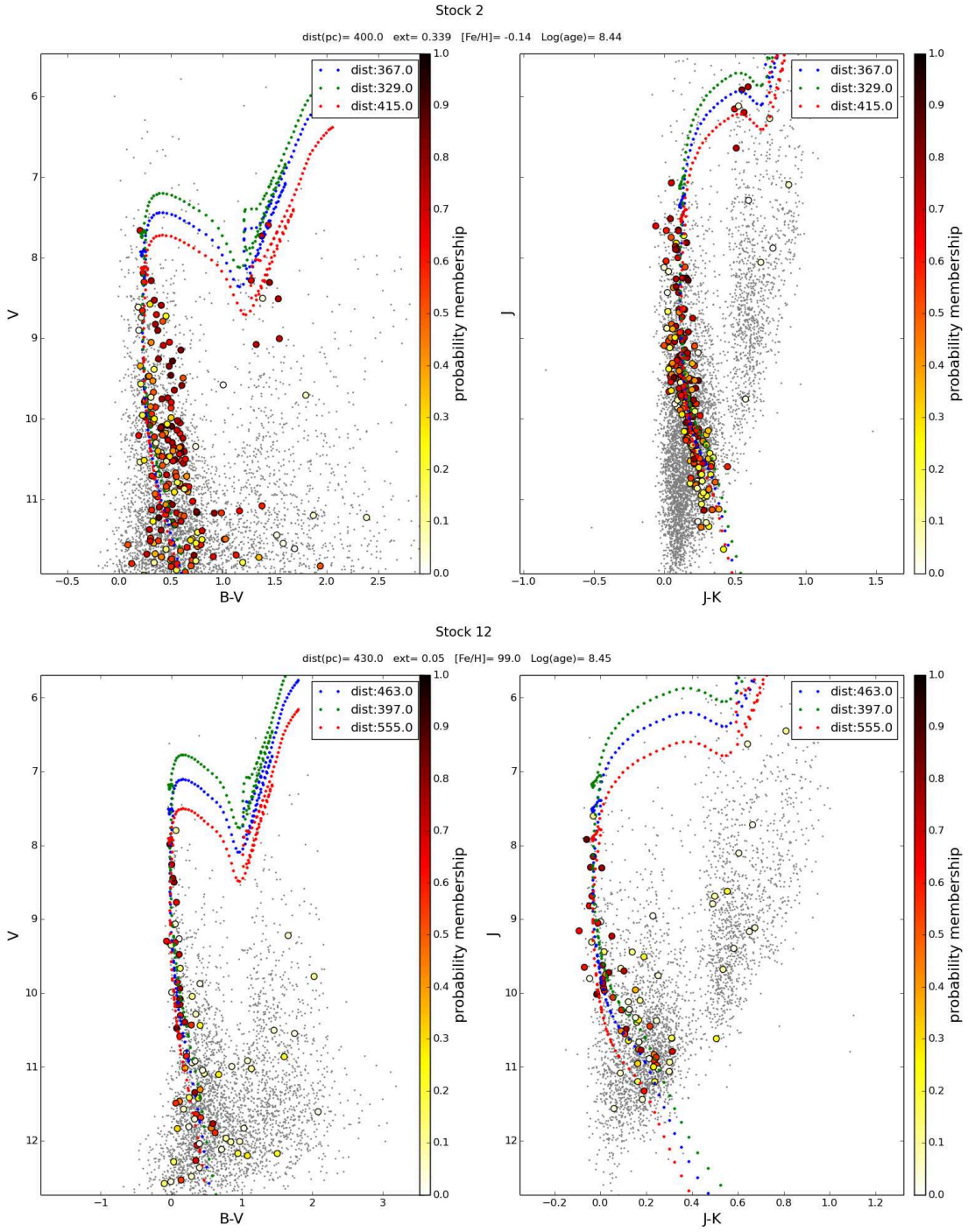

Figure 4.14: CMDs in B-V vs V and J-K vs K planes for Stock 2 and Stock 12. The literature values for distance, extinction, metallicity and age are reported upon the plots. The isochrones are scaled with the three distance value obtained by calculated parallax and its uncertainties.

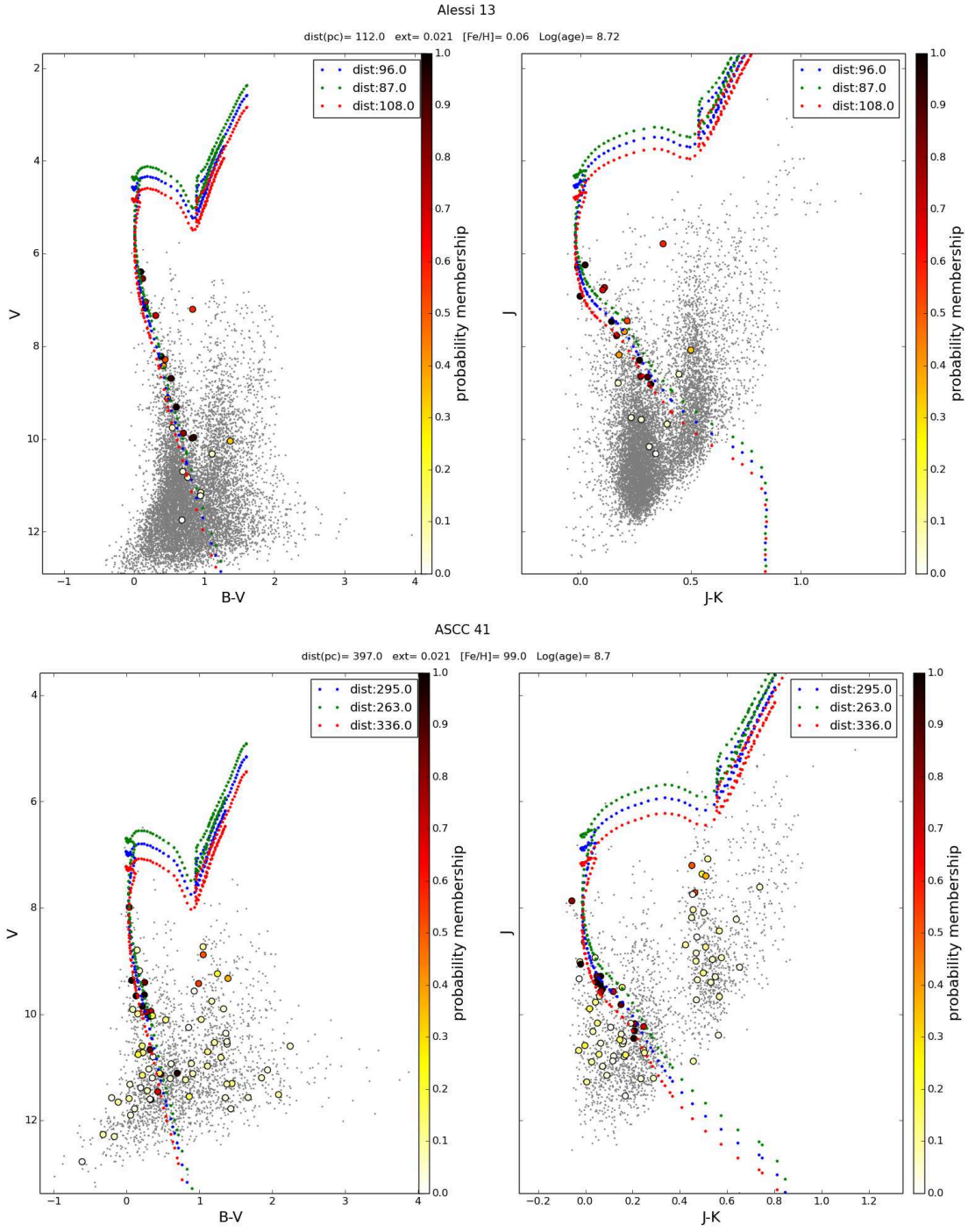

Figure 4.15: CMDs in B-V vs V and J-K vs K planes for Alessi 13 and ASCC 41. The literature values for distance, extinction, metallicity and age are reported upon the plots. The isochrones are scaled with the three distance value obtained by calculated parallax and its uncertainties.

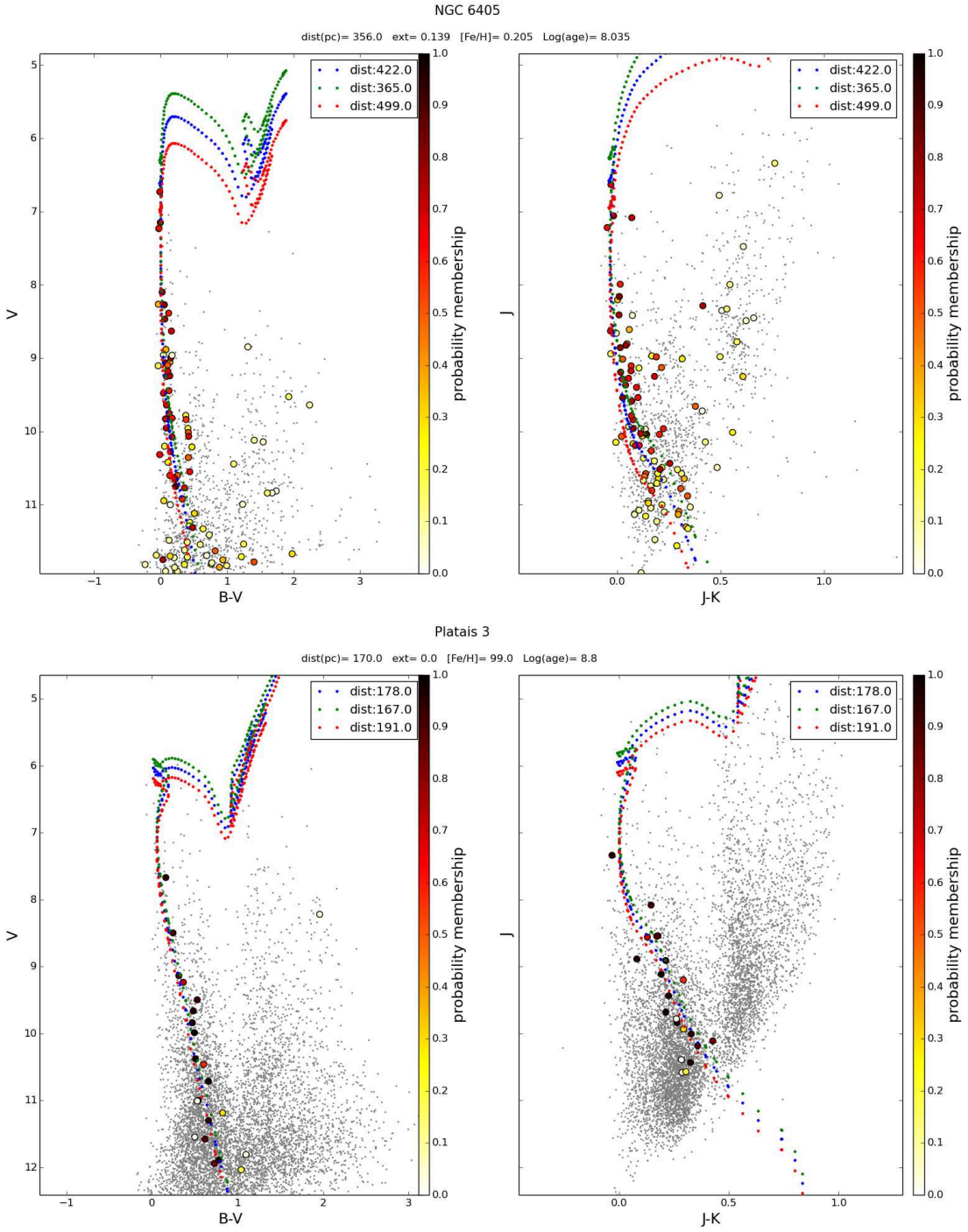

Figure 4.16: CMDs in B-V vs V and J-K vs K planes for NGC 6405 and Platais 3. The literature values for distance, extinction, metallicity and age are reported upon the plots. The isochrones are scaled with the three distance value obtained by calculated parallax and its uncertainties.

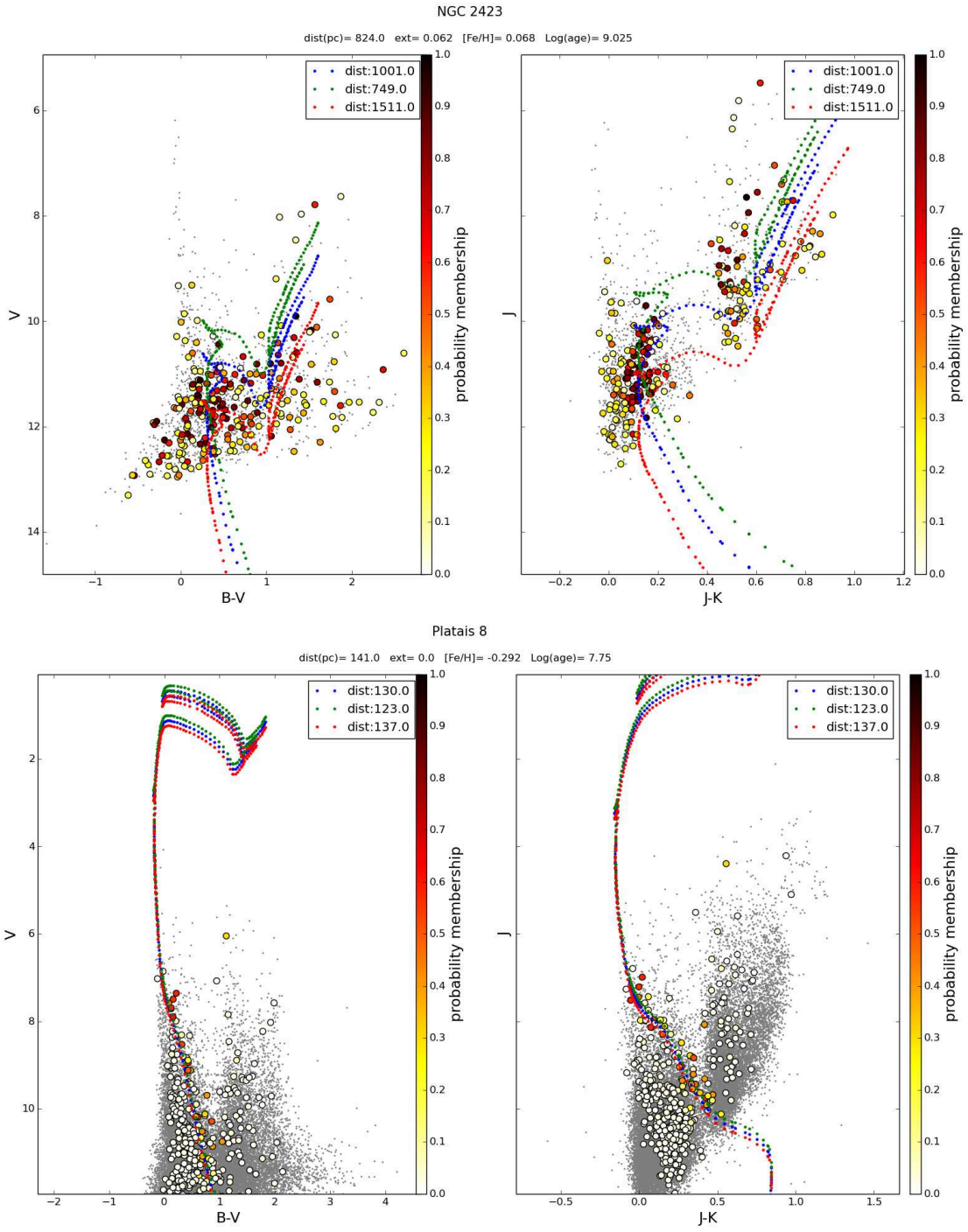

Figure 4.17: CMDs in B-V vs V and J-K vs K planes for NGC 2423 and Platais 8. The literature values for distance, extinction, metallicity and age are reported upon the plots. The isochrones are scaled with the three distance value obtained by calculated parallax and its uncertainties.

4.7 Parameters determination by Bayesian classification

We determined cluster parameters for our clusters with the freely available code Bayesian Analysis for Stellar Evolution with Nine Parameters (BASE-9, von Hippel et al. (2006)).

4.7.1 BASE9: Method

The concept of the code is to invert simulated CMDs to obtain the underlying cluster properties of age, distance, metallicity, and line-of-sight absorption, as well as individual stellar masses. The Bayesian approach require a prior, that is a set of initial parameters for the cluster. This set is encoded in term of Gaussian distribution for age, metallicity, distance modulus and extinction. Those distributions are used to create synthetic populations from isochrones. In order to obtain the synthetic population, the isochrones are populated via random addition of stars following an IMF and adding reasonable photometric errors. During this procedure also the WD contribution, the presence of unresolved binary stars and probability membership for each stars are taken into account. The CMDs of simulated clusters are then compared with the observed ones, searching for the most likelihood solution. This step is performed searching the convergent solution for a Markov chain Monte Carlo (MCMC).This solution provides the posterior distribution for each parameter of the cluster. We set BASE-9 to provide posterior distribution for four parameters: age (Log t), metallicity ([Fe/H]), distance modulus ($(m-M)_V$) and V-band extinction (A_V = 3.1 $\times$ $E(B-V)$). We made use of PARSEC isochrones (Bressan et al., 2012), which are not shipped with BASE-9 but were straightforward to implement.

The photometric bands chosen for this analysis are the 2MASS JHK_S bands, using the pre-computed cross-match between *Gaia* and 2MASS catalogs provided with the *Gaia* DR1 (Marrese et al., 2017). We have at our disposal also the high quality G-magnitude provided by DR1, but we prefer not to use it. The reason is that the common approximation that all stars are affected equally by interstellar extinction does not hold for these precise photometric measurements. In the presence of interstellar extinction, it is common to assume that all stars are affected in the same way regardless of their spectral type, and that absorption produces an identical, rigid shift in color and magnitude for all stars in a cluster. In reality, stars of different spectral types are affected differently by extinction, with variations of up to 10–15 mmag in G-band, even in cases of moderate extinction with $A_V \sim 0.5$ (Sordo et al., in prep.). This effect must be accounted for when working with *Gaia* photometry, which

for the subset of TGAS stars (brighter than G = 13) have a median photometric error of 1.3 mmag.

As prior, we adopt the distance modulus found via parallax (Sect. 4.5) as center of the Gaussian and the correlated uncertainty as σ. We set rather loose Gaussian priors on the other three parameters. For log t and A_V the MWSC values are used as center of Gaussian distributions, with dispersions of 0.5, and 0.2 respectively. Concerning the metallicity, [Fe/H] both prior and dispersion of distribution are fixed by literature spectroscopic studies, when possible. If no values are present in literature we adopt -0.1 for [Fe/H] and 0.2 for the dispersion.

Following the approach of Jeffery et al. (2016), for every OC we performed five runs of BASE-9 sampling 3000 points each, using slightly different starting points. The first run started from the literature value for age, extinction, and metallicity, and the distance modulus used was the one determined in Sec. 4.5. The starting points for the additional four runs were identical, but shifting either the initial distance modulus by ± 0.3 or the age by ± 0.2 in logarithmic scale. These values correspond to the average accuracy in the MWSC Catalog. In most cases the output of BASE-9 has proved to be sensitive to the starting values, which we attribute to the low number of member stars in most of our clusters. Indeed if the weight of single stars are high in the choice of the best fit model the Markov chain assume a chaotic path. In those cases the choice of the initial prior distribution have a strong influence on the final results. For 26 OCs the five realization converge into similar posterior solution that provides a satisfactory fit to the observed CMD. Unsurprisingly, these clusters tend to be those with the larger number of members, or featuring red clump stars which provide good constrains on the cluster parameters. For those 26 OCs, we combined the results of all five runs to compute the final cluster parameters and their uncertainty (effectively using a total of 15,000 samplings). The posterior distributions are generally non-symmetrical, and show correlations between parameters. In Fig. 4.18 - 4.19 we report two examples (NGC 2281 and NGC 3532) of the obtained posterior distribution. In Fig. 4.20 we show the posterior parameter distributions for NGC 2567 and the isochrones fits obtained from them. As pointed out by Jeffery et al. (2016), the uncertainties on the cluster parameters reflect the internal precision of the procedure (the certainty with which a certain PARSEC isochrone represents the data better than a different PARSEC isochrone), rather than an absolute accuracy.

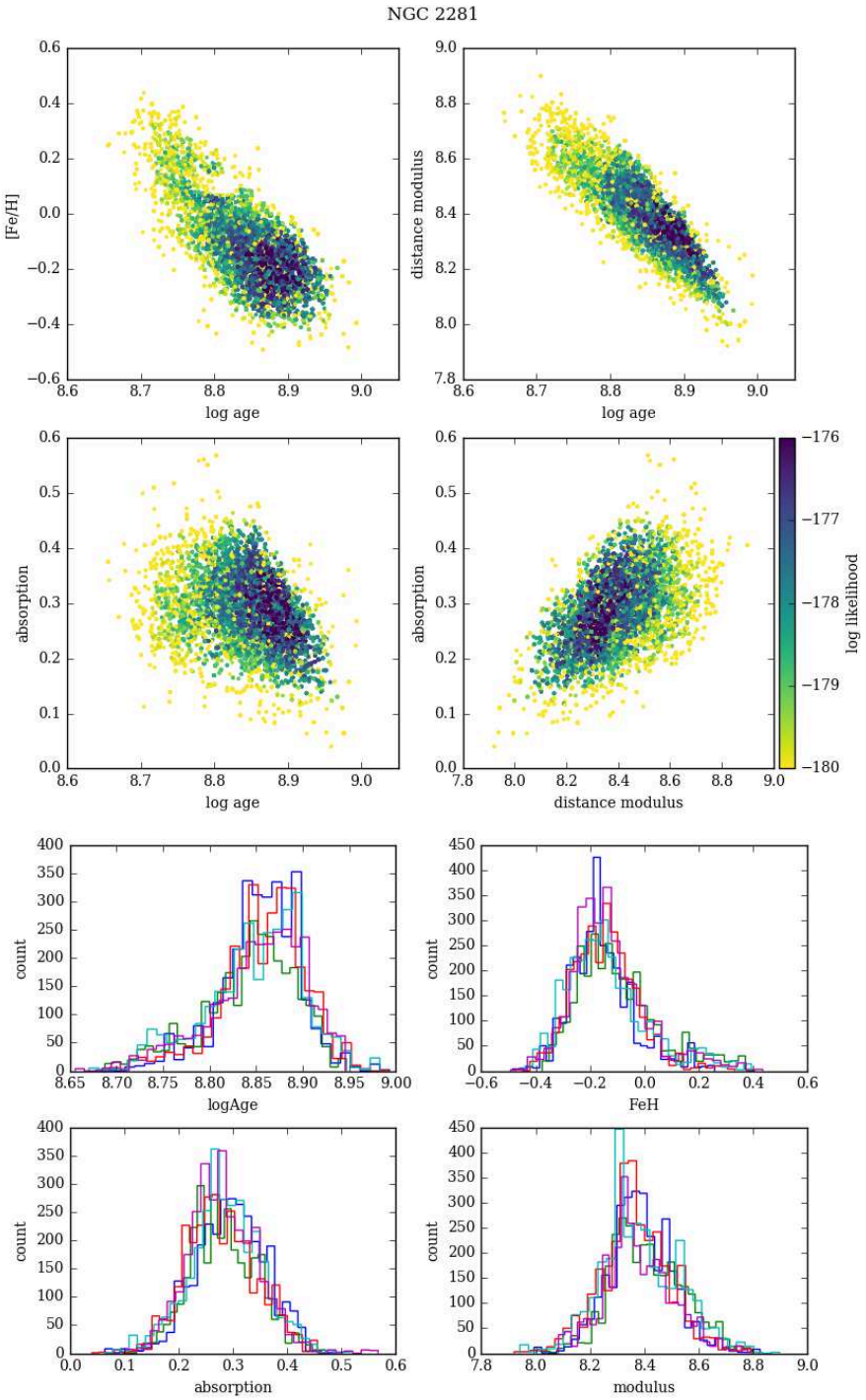

Figure 4.18: Posterior distribution maps for NGC 2281, combining the outputs of five BASE-9 runs.

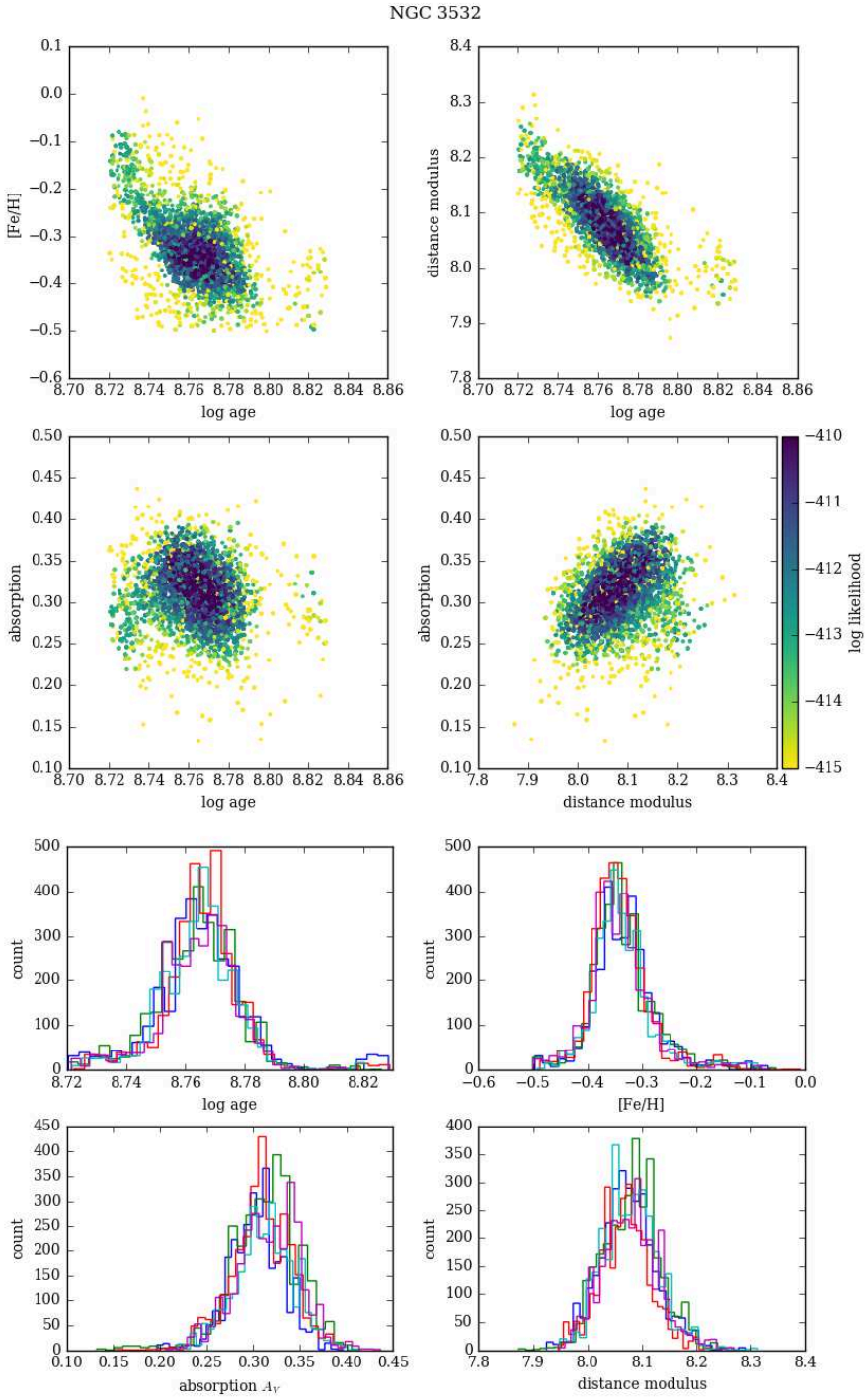

Figure 4.19: Posterior distribution maps for NGC 3532, combining the outputs of five BASE-9 runs.

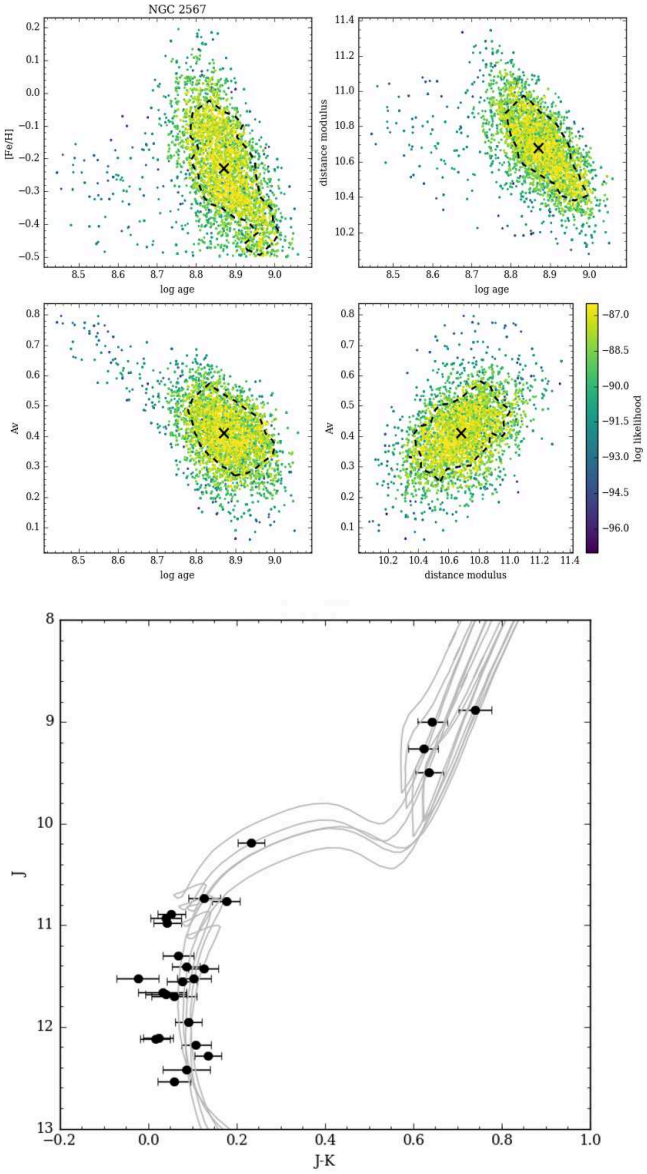

Figure 4.20: *Upper panel:* Posterior distribution maps for NGC 2567, combining the outputs of five BASE-9 runs. The dashed contour encircles 68% of the total likelihood, and the crossed symbol shows the mean value. *Lower panel:* Colour-magnitude diagram for NGC 2567. The grey lines are 5 PARSEC isochrones randomly chosen from the posterior distribution returned by BASE-9.

4.7.2 Results

The results for the 26 OCs for which BASE-9 produce a convergent solution are reported in Table 4.4.

OC	log t	[Fe/H]	A_V	dist.mod.
Alessi 2	8.96 ±0.08	-0.27 ±0.17	0.45 ±0.13	8.52 ±0.20
IC 4756	9.09 ±0.01	-0.09 ±0.03	0.31 ±0.04	8.24 ±0.05
NGC 0752	9.17 ±0.02	0.03 ±0.05	0.11 ±0.05	8.19 ±0.07
NGC 1528	8.94 ±0.04	-0.09 ±0.11	0.30 ±0.10	9.49 ±0.14
NGC 1662	9.03 ±0.03	-0.41 ±0.07	0.66 ±0.06	7.60 ±0.08
NGC 1750	8.58 ±0.09	-0.43 ±0.05	0.94 ±0.07	9.09 ±0.09
NGC 1912	8.85 ±0.10	-0.36 ±0.10	0.69 ±0.10	9.77 ±0.13
NGC 2099	8.95 ±0.05	-0.19 ±0.08	0.50 ±0.08	9.69 ±0.14
NGC 2281	8.85 ±0.04	-0.14 ±0.11	0.29 ±0.06	8.40 ±0.12
NGC 2482	8.88 ±0.06	-0.20 ±0.15	0.15 ±0.08	9.76 ±0.16
NGC 2527	9.03 ±0.04	-0.26 ±0.11	0.24 ±0.05	8.73 ±0.10
NGC 2539	8.96 ±0.15	-0.18 ±0.16	0.29 ±0.15	9.97 ±0.22
NGC 2548	8.90 ±0.04	-0.38 ±0.09	0.28 ±0.05	9.07 ±0.08
NGC 2567	8.87 ±0.07	-0.23 ±0.13	0.41 ±0.09	10.68 ±0.18
NGC 4852	8.89 ±0.08	-0.13 ±0.15	0.26 ±0.12	9.37 ±0.19
NGC 5822	9.15 ±0.02	-0.24 ±0.08	0.41 ±0.10	9.32 ±0.09
NGC 6152	8.75 ±0.09	-0.03 ±0.15	0.69 ±0.14	10.34 ±0.27
NGC 6281	8.80 ±0.09	-0.38 ±0.07	0.63 ±0.07	8.19 ±0.11
NGC 6793	9.07 ±0.11	-0.27 ±0.19	0.47 ±0.10	8.56 ±0.20
NGC 6811	9.16 ±0.03	-0.38 ±0.06	0.36 ±0.07	9.75 ±0.10
NGC 6991	9.15 ±0.02	-0.00 ±0.06	0.25 ±0.06	8.82 ±0.11
NGC 7209	9.01 ±0.06	-0.41 ±0.07	0.34 ±0.10	9.45 ±0.15
Platais 3	8.90 ±0.15	-0.22 ±0.14	0.17 ±0.08	6.23 ±0.11
Ruprecht 98	8.96 ±0.05	-0.29 ±0.11	0.53 ±0.09	8.01 ±0.12
Stock 1	8.77 ±0.04	-0.12 ±0.11	0.27 ±0.07	7.76 ±0.10
Turner 5	8.80 ±0.08	-0.19 ±0.15	0.11 ±0.08	7.58 ±0.17

Table 4.4: Cluster parameters derived from JHK_S photometry for 26 OCs.

Fig 4.21 summarize the results compared with the literature value given by MWSC. The age listed MWSC catalog indeed are obtained from old PADOVA isochrones, while we use PARSEC ones. This different choice produce a systematic shift toward older age in our determination with log t higher by on average 0.26. In particular, it is known that a different solar metallicity reference value and the choice of mixing-length parameter lead to slightly different RC stars brightness prediction, which result in a different age determination (see e.g. Cantat-Gaudin et al. (2014)).

The central and lower panels of Fig 4.21 show the result for the metallicity. This is the parameter that is less constrained by isochrone fitting. We find a mean metallicity value of [Fe/H] = -0.23, although large uncertainties has to be considered. Also in this case the comparison between our results and MWSC ones produce a quite rigid shift, whit a value of Δ[Fe/H] = 0.19. Despite the large uncertainties of our metallicity estimation, our sample traces a negative Galactocentric metallicity gradient, whit a slope of -0.04±0.04 dex kpc^{-1}. The uncertainty on the gradient slope was computed as the standard deviation among 1000

redrawing, performed by picking a metallicity and a mean parallax from a Gaussian distribution representing the values found in this study and their associated errors.
Similar value for the metallicity gradient was recently found by Netopil et al. (2016), -0.085±0.017 dex kpc^{-1}, which derive metallicities for 172 OCs. Jacobson et al. (2016) use the Gaia-ESO Survey (GES) [Fe/H] values and stellar parameters for stars in 12 open clusters in the inner disk from GES-UVES data and derive a gradient slope of -0.1±0.02 dex kpc^{-1}. However, in addition to the rather small number of OCs (26) in our sample, we stress the fact that for metallicity spectroscopic study produce more accurate results.

4.8 3D velocities and full orbits

To obtain a three dimensional picture of cluster motion it is necessary to add at our proper motion information on the radial velocities of the clusters. To do that we combined the proper motions determined in this study with the radial velocities listed in Mermilliod et al. (2008) and Mermilliod et al. (2009). After excluding the non-members and the stars flagged as either variables or binaries, we found that 36 of the OCs in our sample have radial velocities that can be computed from at least two stars.
In Table 4.5 we provide the current distance (|z|), the maximum altitude above the Galactic plane (z_{max}) and the eccentricity for cluster orbits. In order to obtain this value we compute the orbits, from three dimensional positions and velocities for each cluster, using *galpy* and the static, axisymmetric *MWPotential2014* (Bovy, 2015). As expected both |z| and z_{max} are correlated with age. Younger OCs are nearer to the galactic plane, with all clusters with an age of 300 Myr or less being all contained within 180 pc of the plane, while half the older clusters have orbits that extend beyond this limit. With an age of $\sim$ 3 Gyr, NGC 2682 is the oldest cluster in our sample, and also one of the oldest known clusters, and from its orbit we estimate a distance of more than 400 pc from the Galactic plane.
We computed the eccentricity of each orbit ($e = \frac{r_a - r_p}{r_a + r_p}$ where r_p and r_a are the perigalacticon and apogalacticon of the orbit), and found no apparent correlation of eccentricity with age. The results for |z|, z_{max} and e are plotted as a function of age in Fig. 4.22.
In Fig. 4.23 is shown the position of our OCs sample along with the schematic location of the spiral arms of the Milky Way in the model of Reid et al. (2014). As can be seen from the plot our sample cover mainly the interarm region. As explained in Sect. 1.4, to trace the spiral arms structure is necessary to analyze the young clusters (age < 20 Myr) that have

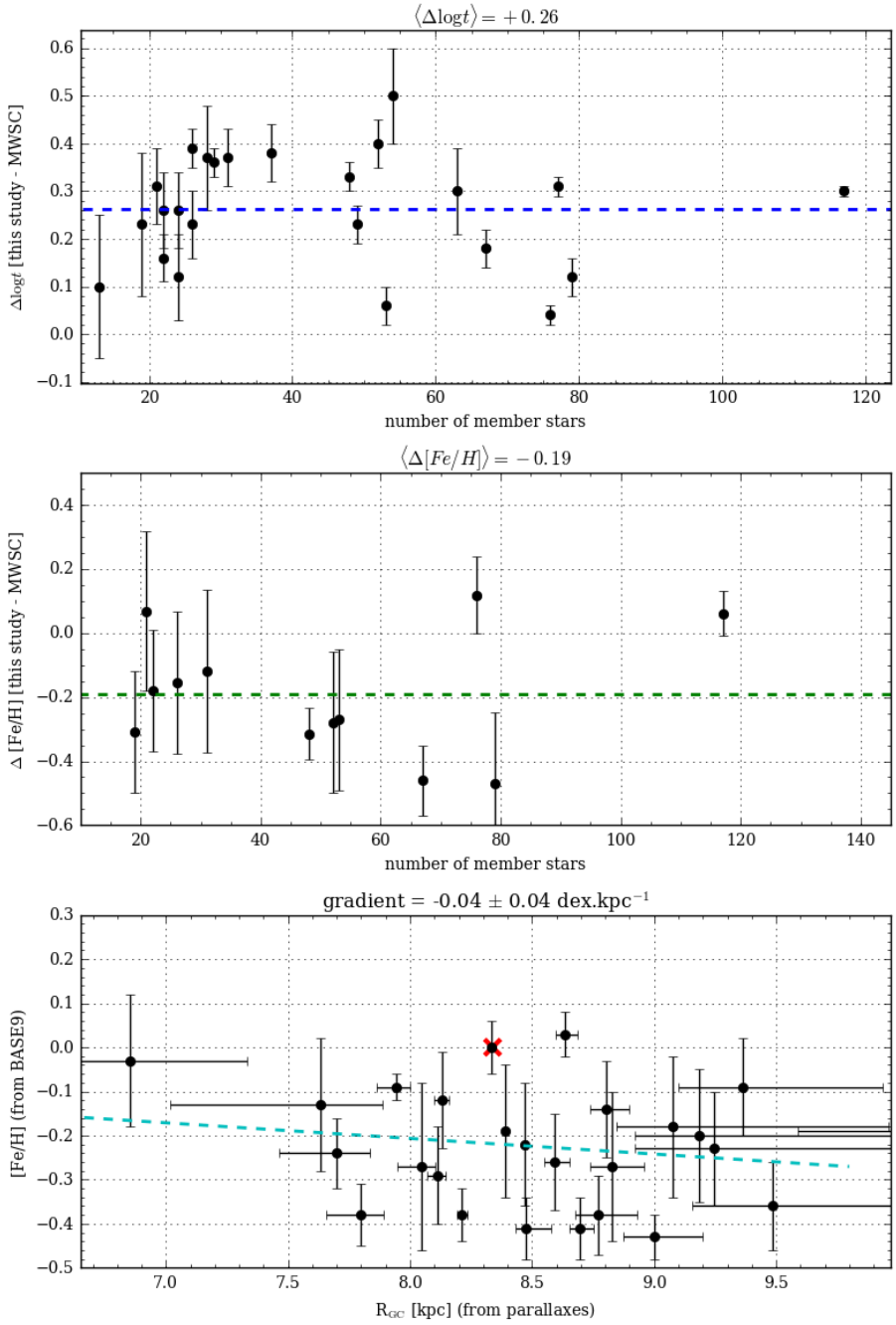

Figure 4.21: *Upper panel*: difference in log t between the ages found in this study and those quoted in the MWSC catalogue. The dashed line indicates the mean value. *Middle panel*: difference between the [Fe/H] found in this study and those quoted in the MWSC catalogue (for the OCs with metallicity estimates). The dashed blue line indicates the mean value. *Lower panel*: metallicity ([Fe/H]) obtained in this study based on JHK_S photometry, against Galactocentric radius. The red cross indicates the solar metallicity and Galactocentric radius (8.34 kpc, Reid et al. (2014)).

not yet enough time to leave the spiral arm. These young clusters and associations are often sparsely populated and/or embedded in their progenitor molecular cloud (thus requiring the use of infrared photometry). Another problem is at the magnitude limits of TGAS solution no young clusters could be seen or only a number of stars too small to establish secure membership could be detected.

OC	log t	z [pc]	z_{max}	e
IC 4725	7.97	-23±8	94±8	0.081±0.012
IC 4756	9.09	70±3	71±2	0.087±0.003
NGC 0752	9.17	-137±17	224±20	0.067±0.009
NGC 1342	8.6	-150±42	178±15	0.037±0.003
NGC 1647	8.3	-129±18	151±13	0.06±0.001
NGC 1662	9.03	-118±14	175±6	0.084±0.001
NGC 2099	8.95	88±11	105±24	0.165±0.046
NGC 2168	8.26	61±8	64±2	0.086±0.012
NGC 2281	8.85	157±12	161±13	0.053±0.005
NGC 2360	8.8	-9±13	416±97	0.058±0.034
NGC 2423	9.03	86±10	102±22	0.12±0.018
NGC 2447	8.68	27±0	67±9	0.018±0.007
NGC 2477	8.91	-158±124	348±129	0.137±0.05
NGC 2527	9.03	44±2	95±1	0.103±0.006
NGC 2539	8.96	212±55	225±53	0.105±0.011
NGC 2546	8.13	-10±12	41±7	0.028±0.003
NGC 2548	8.9	207±27	271±31	0.047±0.006
NGC 2567	8.87	116±23	117±20	0.088±0.016
NGC 2682	9.54	403±77	427±98	0.116±0.009
NGC 3680	9.2	270±37	271±34	0.037±0.004
NGC 5138	7.55	130±36	159±53	0.098±0.048
NGC 5316	8.23	27±0	83±4	0.069±0.036
NGC 5617	8.25	20±3	82±48	0.119±0.062
NGC 5662	8.28	70±7	136±27	0.043±0.012
NGC 5822	9.15	76±6	79±4	0.064±0.008
NGC 6067	7.97	-61±56	95±32	0.083±0.058
NGC 6124	8.29	89±9	116±8	0.04±0.003
NGC 6134	9.02	21±1	177±45	0.028±0.012
NGC 6281	8.8	44±2	83±4	0.034±0.006
NGC 6494	8.52	64±5	72±2	0.014±0.002
NGC 6705	8.51	-44±39	67±21	0.123±0.01
NGC 6811	8.8	246±40	319±42	0.083±0.009
NGC 6866	8.64	169±41	197±38	0.077±0.002
NGC 6940	8.98	-108±45	221±50	0.077±0.009
NGC 7209	9.01	-99±19	117±13	0.101±0.014
Trumpler 3	8.01	81±8	90±13	0.056±0.006

Table 4.5: Selected parameters for 36 integrated orbits.

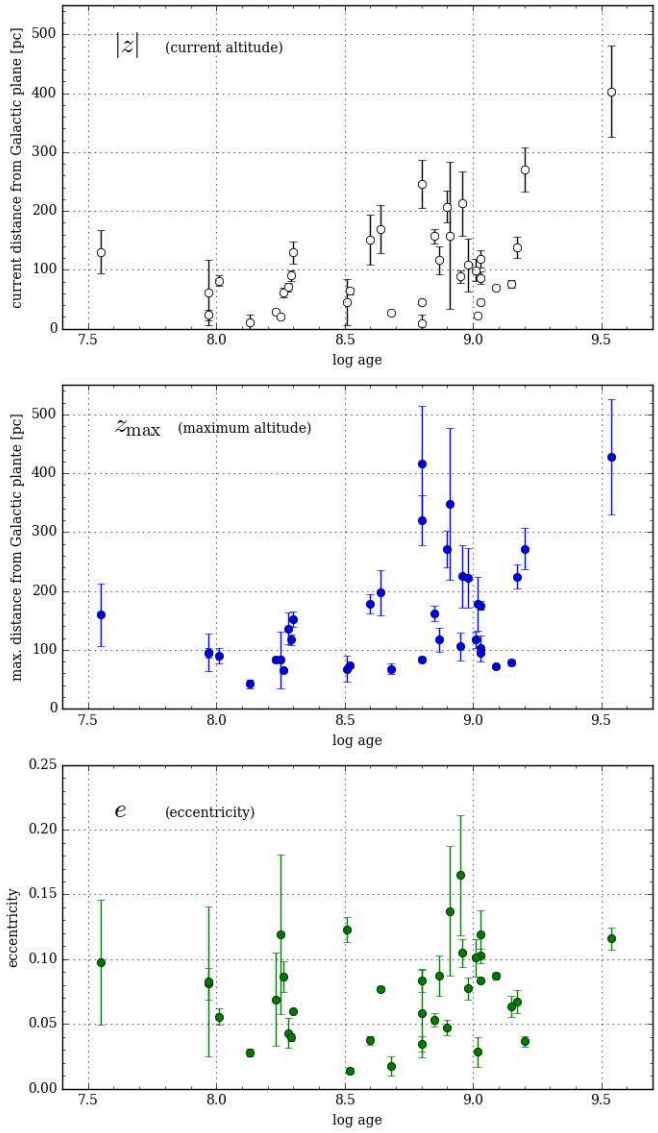

Figure 4.22: *Upper panel:* current distance |z| from the Galactic plane as a function of age for the 36 OCs for which we computed full orbits. *Middle panel:* maximum altitude above the Galactic plane for the integrated orbits of those OCs. *Lower panel:* eccentricity of the integrated orbits against age of the cluster.

4.9 Conclusions

In the work presented in this chapter, we make use of a suitable combination of *Gaia* DR1 TGAS parallaxes and proper motions and UCAC4 proper motions to derive a list of high probability cluster members for 134 OCs. For those objects, we compute mean proper mo-

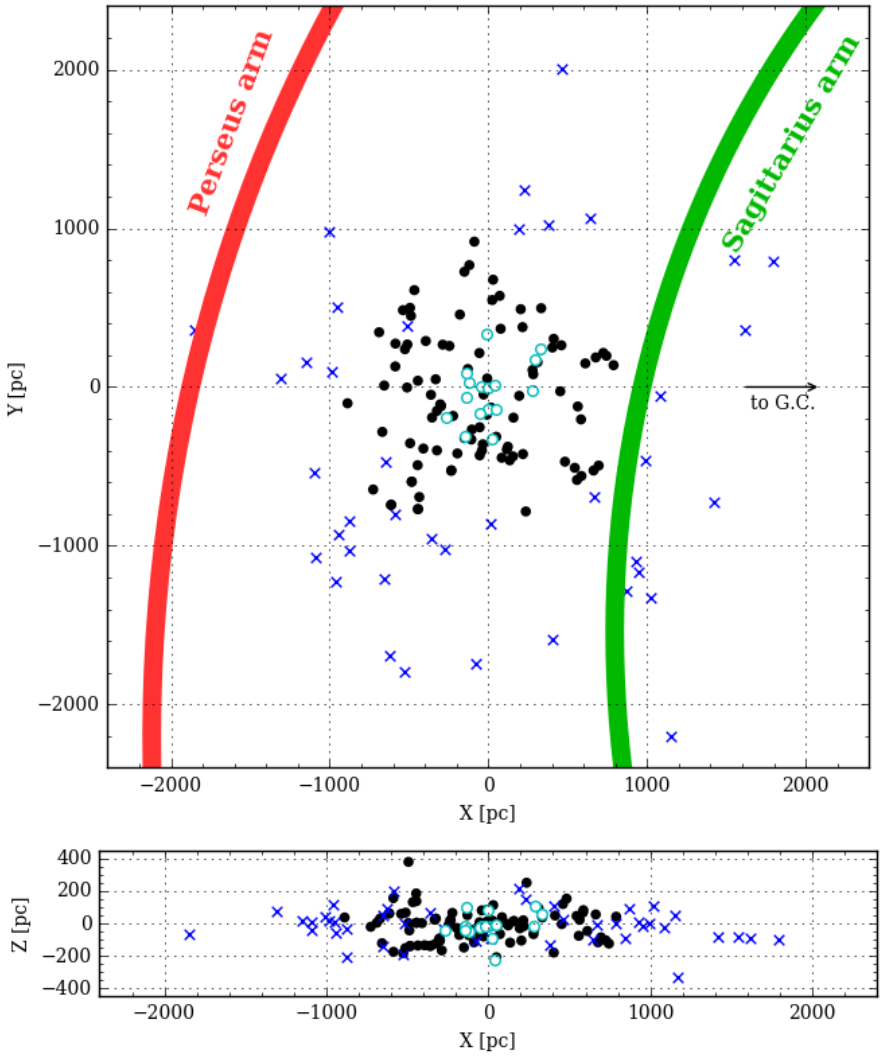

Figure 4.23: Position of the OCs studied in this paper in Galactic rectangular XYZ coordinates. Black dots: OCs from this study with relative distance errors under 50%. Crosses: OCs from this study with relative error distance over 50%. Open symbols: OCs from Gaia Collaboration et al. (2017). The spiral arms are traced according to the model of Reid et al. (2014).

tions and parallaxes. For 26 clusters, we obtain parameters such as age, extinction, [Fe/H], distance modulus from comparison with isochrones using BASE-9, a Bayesian/MCMC method. What we done shows the strength of automatic approaches when dealing with large datasets. In particular our UPMASK adaptation to make it work with astrometric data produce good results. We also add PARSEC isochrones in the BASE-9 library, and use them to analyse the OCs in the 2MASS JHK_S bands. These determinations should be performed for as many clusters as possible in order to build large homogeneous samples and avoid the additional dispersion in results introduced by compiling ages determinations originating from various studies making use of various sets of models. Automated tools provide an objective estimate of the cluster parameters, a convenient alternative to fitting CMDs by eye (which yields non-reproducible results and is completely impractical when dealing with samples of hundreds of objects), and allows us to consider independent measurements such as distance estimates obtained from trigonometric parallaxes.

Furthermore we compute the full orbits of 36 OCs. The difference in scale height observed between young and old objects is traditionally attributed to disk heating, see Sect. 1.4. The z_{max} obtained for our sample indicate that the disc heating in average start to produce significant shift from the formal disc plane (> 100 pc) for clusters older than 300 Myr. Instead the absence of an apparent correlation between age and eccentricity seems to indicate that radial deviations from a flat circular orbit have a longer timescale with respect to vertical deviations for the objects in our sample.

5

Characterization of OCs in the near Third Quadrant with Hot Stuff for One Years catalog

5.1 Introduction

In the previous Chapter, we present a characterization of about 400 OCs using the first Gaia Data release data contained in the TGAS subset. Nevertheless TGAS represent only 0.2% of the entire *Gaia* DR1. For the other sources DR1 provide only the positions and the magnitudes in *Gaia* G band. With no color nor astrometric information, at least proper motions, a characterization of OCs properties became impossible. To overcome this problem we take advantage of the astrometric catalog, the Hot Stuff for One Year catalog (hereafter HSOY) Altmann et al. (2017) built combining Gaia DR1 with PPMXL positions. This catalog, presented in the next section, provides proper motions for about half of the Gaia DR1 sources albeit with a coarse precision in comparison with TGAS. In this way we are able to exceed the limit of brightness imposed by TGAS and characterize clusters down to fainter magnitudes. HSOY contains also informations on magnitudes and colors provided by a crossmatch with 2MASS catalog. HSOY do not contains parallaxes. When possible, information about cluster parallaxes are derived using TGAS data for the stars in common. We select our sample looking at the clusters closer to 1.5 kpc from us, in the region of sky in the third galactic quadrant. The third quadrant ($180 < l < 300$ deg) is a very interesting region to characterize the spiral structure (see Carraro & Costa (2009), Carraro et al. (2017), Moitinho et al. (2006), Vázquez et al. (2008)), in particular the Local Arm, the Carina-Sagittarius, the Perseus and the Outer arm. In addition, at large distances from us, the disk

present a bending that is clearly visible in the open cluster distribution , see Vázquez et al. (2008) and Vázquez et al. (2010). The peculiar morphology of the third galactic quadrant and in particular of the warp have remained so far not well understood. The high accurate astrometric data that Gaia will provide will for sure improve our comprehension of the features of this interesting region. What we present in this chapter has to be considered as a preliminary study since the more distant arms and the disk warp cannot be reached with the present data. Waiting to be able to reach greater distance with better accuracy thanks to *Gaia* DR2 we begin to analyze all the clusters that are visible with HSOY, in order to get their physical properties.

The methods used to analyze the clusters, are described in Chapter. 4. However, since parallaxes are not available for these stars, we can not employ the full astrometric solution of the stars as UPMASK input. In the present analysis we combine the photometric and the available astrometric information (positions and proper motions) to define the parameter space in which UPMASK searches evidences of clustering. As in the previous Chapter, the cluster physical parameters are always obtained via a Bayesian analysis performed on JHK_S 2MASS photometry with BASE9.

In Sect. 5.2 we summarize the main properties of the HSOY Catalog; in Sect.5.3 we describe the target selection; in Sect. 5.4 we derive the proper motions of the clusters; in section 5.5 we derive a prior on the cluster parallaxes based on the limited number of data available in TGAS; in section 5.6 we perform a Bayesian analysis of the OCs to derive age, metallicity, and distance; in section 5.7 we discuss the disk properties on the basis of OC our sample; finally in Sect. 5.8 we draw some conclusions.

5.2 The Hot Stuff for One Year catalog

HSOY is a catalog released in February 2017. The aim of this catalog is to derive proper motions for a number of sources of *Gaia* DR1 that are not part of the TGAS subset. In comparison to the 2 million of sources contained in TGAS, HSOY provides proper motions for more than 580 million of stars. As its name suggests, the goal of HSOY is to provide an intermediate catalog before the *Gaia* DR2 full 5 parameter astrometry. We make use of this Catalog to study a subset of OCs which are too faint to show a significant number of members in TGAS data.

HSOY is obtained by combining *Gaia* DR1 and the PPMXL positions (Roeser et al., 2010).

PPMXL is a catalog obtained matching 2MASS and USNO-B1.0 (Monet et al., 2003) positions. In addition to proper motions, 2MASS JHK$_s$ and USNO-B1.0 BRI photometry is provided. The method to derive the HSOY astrometry is the same used to build the PPMXL catalog itself. It consists of a cross-matches between the datasets, and a weighted least-squares fit to derive positions and proper motions, for details see Roeser et al. (2010). HSOY contains the sources in common between the two catalogs. DR1 have 1.1 billions of sources while PPMXL 900 millions. HSOY only contains 583,001,653 entries, i.e. about 50-60% of the objects of the input catalogs. This is mainly due to non-stellar objects and failed matches originating in the USNO-B1, and in smaller part to the inhomogeneous sky coverage of *Gaia* DR1 (Gaia Collaboration et al., 2016b). A number of sources contained in HSOY are not related to physical objects. This fraction of false sources come out because spurious objects contained in PPMXL could accidentally match a real (or spurious) *Gaia* object. Furthermore in both catalogs, a couple of hundred sources fainter than G$\sim$21 mag can be found. These have to be considered spurious sources.

The accuracy of the photometric data is given by the original accuracy of parents catalogs. For positions and proper motions the accuracy depends on the results of the catalog building step. The mean epoch of the objects in HSOY is 2014.8, near to 2015 mean epochs of DR1. In the catalog the position are given at J2000.0 by applying a propagation based on proper motions. This step produce some additional uncertainties on positions because of the not negligible uncertainties on proper motion, in particular for fainter stars (see Fig. 5.1). The rms-errors at J2000.0 on the position are well below 0.1 arcsec on average, while on proper motions they can reach 5 mas/yr for fainter stars. Furthermore the errors reflect the systematics in both catalogs. In Fig. 5.1 the errors North and South of $\delta = -30°$are presented. The reason is that the errors down to this declination reflects the shorter baseline for proper motions in the Southern quarter of the sky.

5.3 Targets selection

In this section we focus in one of the region more interesting of the Galactic disc, the Third Quadrant (TQ, $180° \leqslant l \leqslant 270°$). This region have a very complicated structure, still not completely understood, including spiral arms and Galactic warp.
Gaia mission, with its high precision astrometry and photometry, in the coming years will

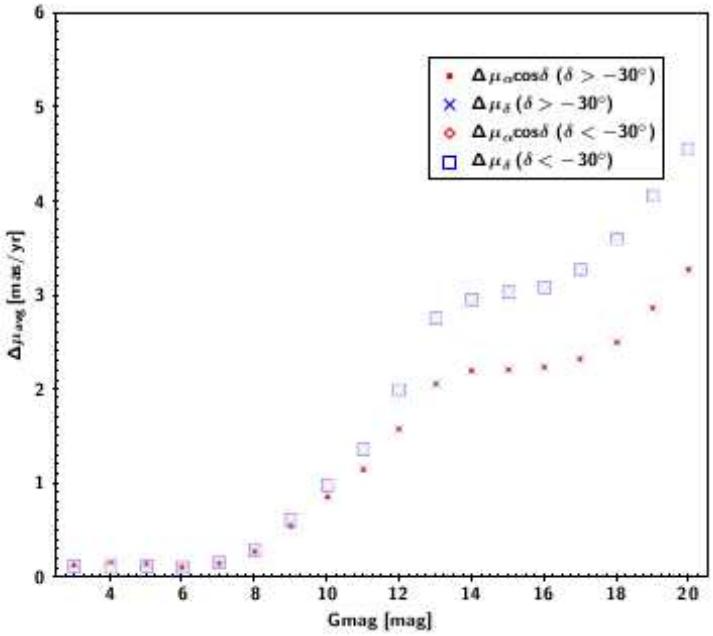

Figure 5.1: HSOY mean standard errors for proper motions as a function of *Gaia* G magnitude. The data are divided between $\delta \lessgtr 30°$, see the text for explanation. Image from Altmann et al. (2017).

be a powerful tool to describe the warp, better defining its features both in the outed disc, in which detection of new OCs is expected, and in solar neighborhood. This study is to be considered as a first step in this direction. Even if we have to wait the next data releases to be able to study OCs at the distances in which the warp is more evident ($R_{GC} > 12$ kpc) and to better define the spiral structure, it is of interest to study the distribution of OCs in the Local environment.

In DAML14, we select all clusters located in the region ($230° \leqslant l \leqslant 255°$) confined in negative latitude part of the disc $b \leqslant$ -2°). We limit our research to OCs closer to 1.5 kpc from us (see Fig. 5.2. This choice is motivated by the request that $\frac{\sigma_\varpi}{\varpi} \leqslant 35\%$. This guarantees a better precision in parallax estimate in particular for the clusters for which TGAS provides only few tens of stars. This left us with a list of 30 OCs to investigate, listed in Table 5.1.

We select a circular fields of 10 arcmin of radius for each cluster, applying a magnitude cut-off in order to take only stars with associated uncertainties on proper motions less than 2.5 mas yr^{-1}.

OC	α [deg]	δ [deg]	dist [pc]	age [Log(yr)]
ASCC 32	105.4958	-26.5033	750	8.18
ASCC 36	108.6292	-21.12	750	8.51
ASCC 33	105.7958	-25.05	800	7.26
Collinder 121	104.0833	-24.7294	1100	7.08
Collinder 132	108.8333	-30.6833	472	7.08
Collinder 135	109.3208	-36.8167	316	7.407
Collinder 140	111.1125	-31.85	405	7.548
ESO 368-11	116.0917	-34.6186	1490	9.0
ESO 493-03	114.9375	-27.2933	1400	8.6
FSR 1255	110.2208	-19.6475	1023	8.495
Haffner 13	115.125	-30.0833	714	NaN
Haffner 23	107.35	-16.95	1000	8.84
Ivanov 6	111.0583	-24.6333	442	7.2
NGC 2287	101.5042	-20.7567	710	8.4
NGC 2358	109.2333	-17.1167	630	8.72
NGC 2362	109.6708	-24.955	480	6.7
NGC 2367	110.025	-21.8817	1400	6.7
NGC 2439	115.1875	-31.6933	1300	7.0
NGC 2451A	115.8	-38.4	189	7.78
NGC 2451B	116.1125	-37.6667	302	7.648
NGC 2477	118.0417	-38.53	1341	8.85
Ruprecht 12	106.7917	-28.2	900	7.56
Ruprecht 13	106.9625	-25.8697	1300	9.0
Ruprecht 17	110.9	-23.1833	1263	8.325
Ruprecht 18	111.1625	-26.2167	1056	7.648
Ruprecht 20	111.6792	-28.8167	1208	8.5
Ruprecht 27	114.4208	-26.5294	1490	8.95
Ruprecht 31	115.7417	-35.5972	930	9.0
SAI 82	118.0583	-33.0408	1150	8.65
Trumpler 7	111.8417	-23.95	1474	7.43

Table 5.1: Position, distance and age of the 30 OCs studied in this work. The value are taken from DAML14.

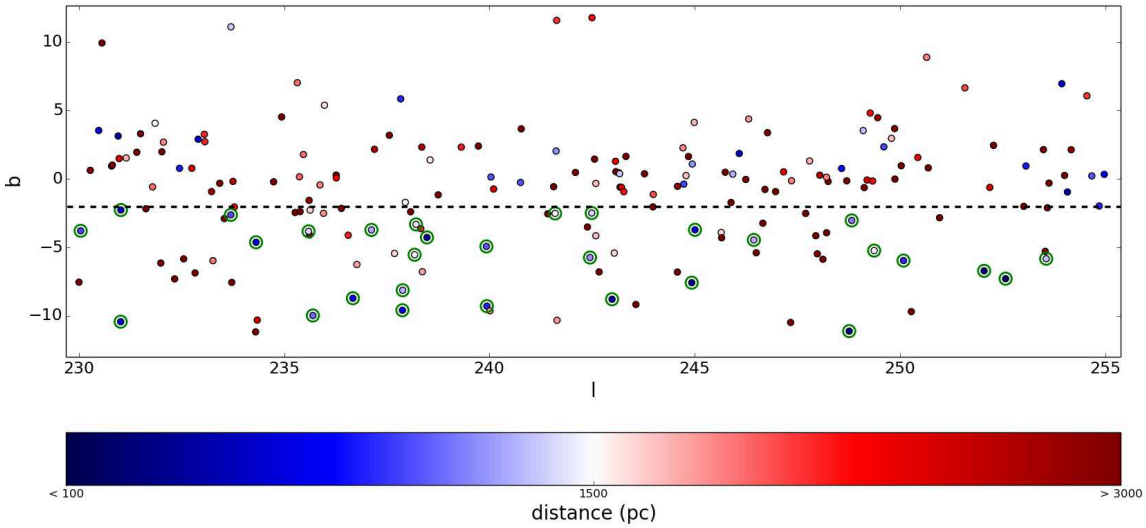

Figure 5.2: The warp region of the TQ (230°$\leqslant l \leqslant$ 255°). The point correspond to OCs, colored following a dichotomic color scale to highlight the distance. The green circles indicate the cluster selected in this work, the dashed line indicate b = -2°, the latitude at which we start to consider clusters.

5.4 Cluster proper motions determination

To derive proper motions, parallaxes and membership probability for the clusters we use the UPMASK code already presented in previous Chapter. In comparison to what we did in previous Chapter, we take advantage of the versatility of UPMASK looking for clustering in a parameter space that includes astrometry and photometry, i.e. $\mu_{\alpha*}$, μ_δ and photometry in the J, H, K_S and G bands. Redundancy caused by similar information carried by different photometric bands is avoided thanks to the PCA step, see Sect. 4.4. Since we are dealing with crowded fields, we adopt a value between 12 and 15 for the mean number of groups. UPMASK runs twice, the first with all the stars in the field; the second with only stars with an associated membership probability greater than 10%. The stars in the second run are then used, in agreement with their membership probability, to calculate the proper motions of the clusters by means of a weighted mean as done in the previous Chapter.

Via PCA, we project our six-dimensional parameter space in a four-dimensional space. In our sample, only the brighter stars have uncertainties less than 1 mas yr^{-1}, the majority of stars in our samples have uncertainties around $\sim$ 2 mas yr^{-1}. We remind that the aver-

age uncertainties on proper motions in TGAS is around 1.1 mas yr^{-1}, see Lindegren et al. (2016a). These uncertainties lead to a loose determination of OC members based on proper motions. In order to better constrain our solution, we apply some preliminary selection, based on CMD inspection.

We first select the stars inside a rectangular box that we define in the $J-K$ versus J plane. The rectangle is chosen in order to isolate as much as possible the stars of the clusters from field population. The brighter part of the CMD is the most efficient region to perform this kind of analysis, in particular the brighter end of the MS. In comparison with the RC, the higher number of stars in the upper part of the MS produces better constrains on the proper motion estimate. These stars are then used to derive an independent estimate of the cluster proper motion $\mu_{\alpha*}$ and μ_δ, fitting two Gaussians on the data. The peak of the cluster Gaussian, μ_G represents the value of the proper motion and the σ the error associated to it. In Fig. 5.3 we present the results of this method for NGC 2287 and NGC 2362. This method works quite well when the OC MS is well separated from the disk population. In some cases it is difficult to separate cluster and field stars. For young populations statistical effects due to the low number of stars can hamper the determination. For old clusters it is not always simple to distinguish between the MS of the cluster and the one of the disc population, since they are often superimposed. In those cases we base our pre-selection of the region of interest following the upper MS traced by isochrones chosen in agreement with age, metallicity, distance modulus and reddening listed in DAML14. Two examples of this are Collinder 121 and NGC 2247, respectively a young and an old OC, as Fig. 5.4 shows. In three cases (Collinder 140, NGC 2541A and Ruprecht 17) it is impossible to find a clear evidence of a single pick in $\mu_{\alpha*}$ and/or μ_δ. We discard these OCs from the sample.

Finally, we compare the results obtained with UPMASK and with the photometric method, retaining only the clusters for which the two values obtained for $\mu_{\alpha*}$ and/or μ_δ are in agreement within 1 mas yr^{-1}, see Fig. 5.5. This is the case for 13 OCs. We finally perform a weighted mean between the two results to derive the final proper motion values and related uncertainties. As it is clear from Fig. 5.5, the derived proper motions are in agreement with DAML14, but for a few cases, namely Coll 121, Ho23, NGC 2287 for $\mu_{\alpha*}$, and FSR1255 and NGC2367 for μ_δ.

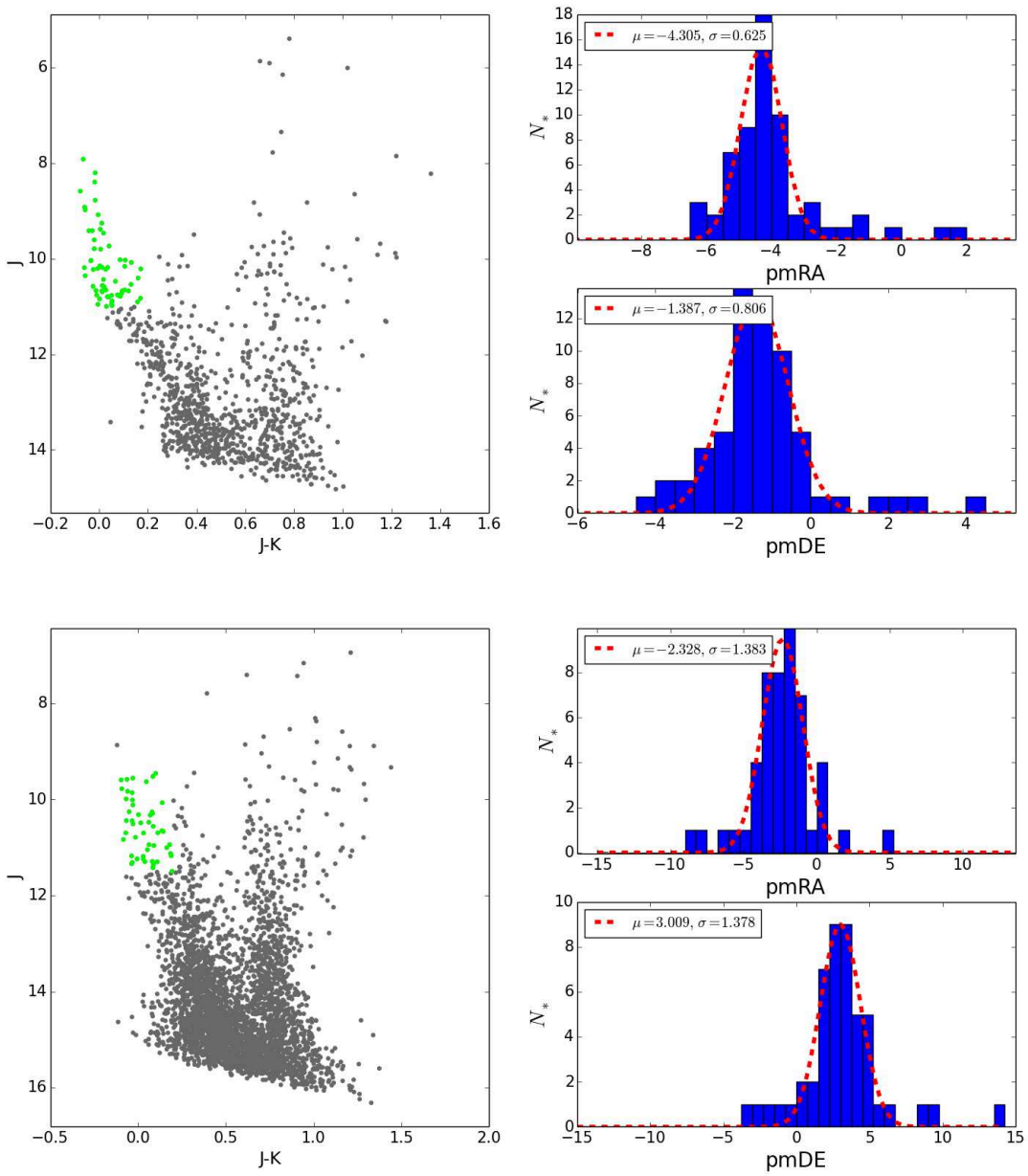

Figure 5.3: Proper motions determination with photometric selection for NGC 2287 (upper panels) and NGC 2362 (lower panels). On the left we plot the CMDs of the clusters. The green dots represent the selected stars. On the right the stars count as a function of $\mu_{\alpha*}$ and μ_δ with the best fitting Gaussian distribution over-plotted in red.

5.5 Parallaxes determination

We estimate the parallaxes of the 13 OCs in a similar way. We perform a weighted mean of TGAS parallaxes for the stars of the clusters that have the proper motions falling in the

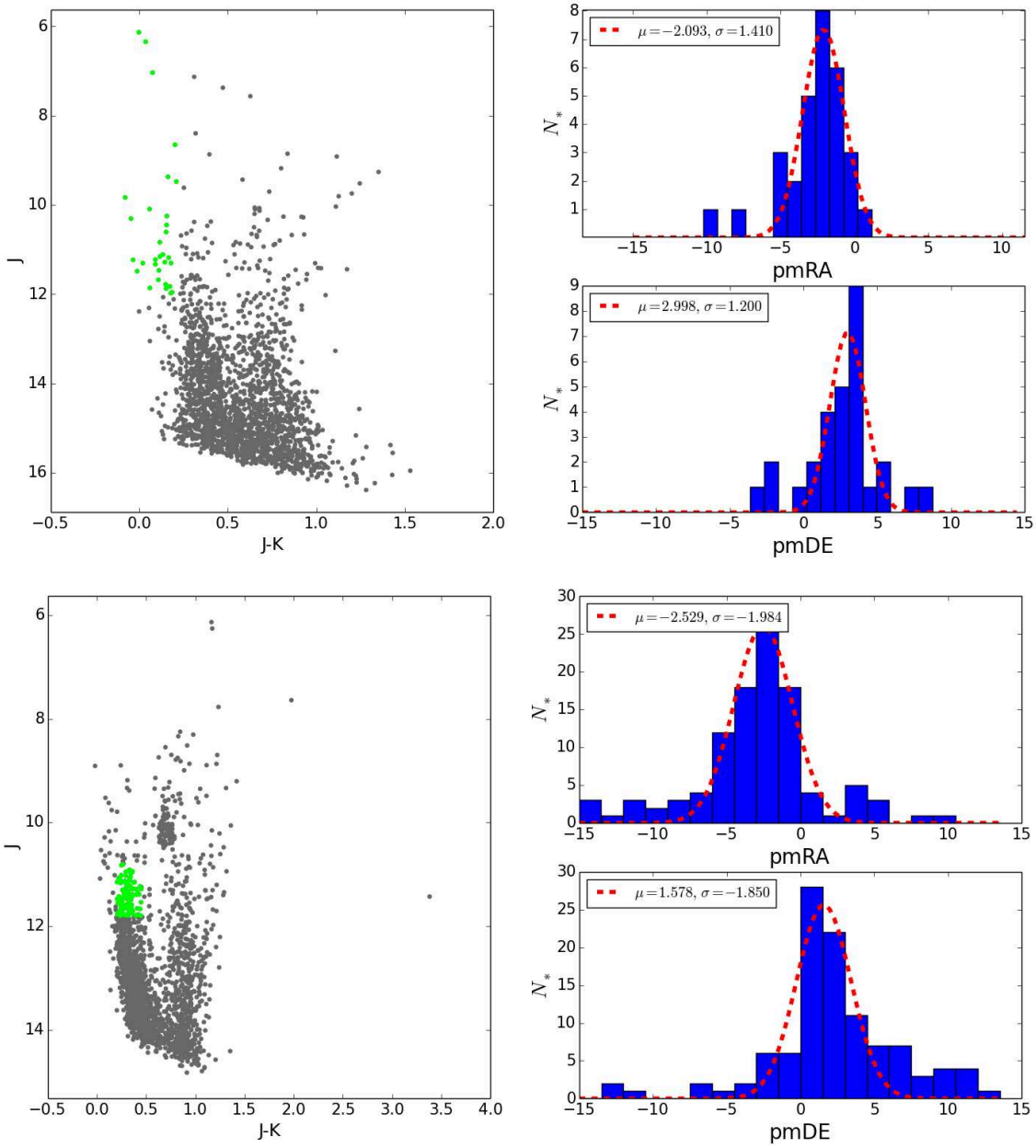

Figure 5.4: Proper motions determination with photometric selection for Collinder 121 (upper panels) and NGC 2477 (lower panels). The scheme is the same of 5.3.

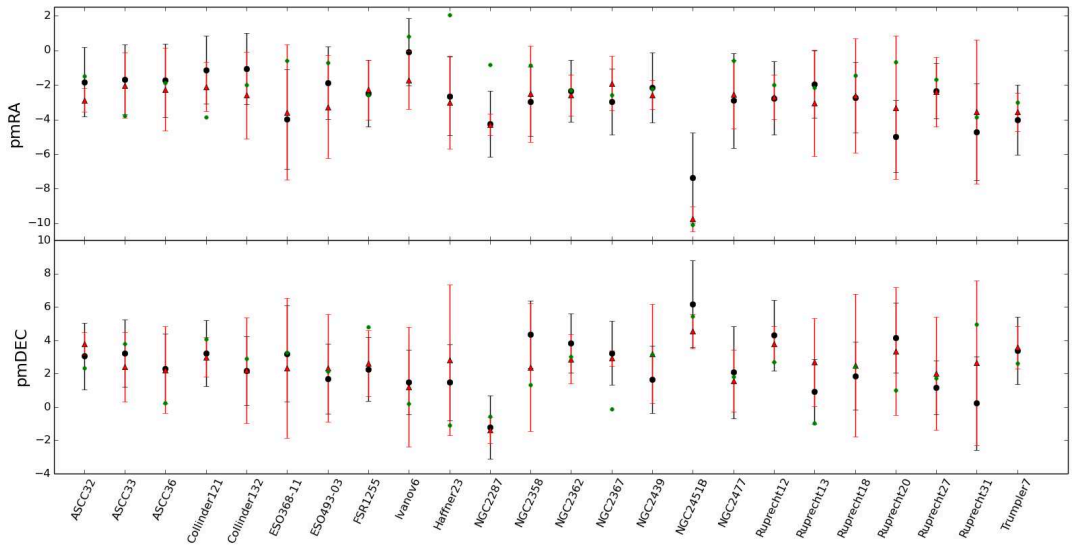

Figure 5.5: Comparison between different proper motion determinations. The black dots and the red triangles represents respectively the results obtained from UPMASK method and photometric selection. The green diamonds are the values listed in DAML14.

OC	ϖ [mas]	$\mu_{\alpha*}$ [mas yr^{-1}]	μ_{δ} [mas yr^{-1}]
ASCC 32	1.26 ±0.08	-3.05 ±0.4	3.68 ±0.31
ASCC 33	0.78 ±0.19	-2.02 ±1.88	2.41 ±2.08
ASCC 36	0.82 ±0.22	-2.25 ±2.38	2.23 ±2.59
Collinder 121	0.78 ±0.28	-2.1 ±1.41	3.05 ±1.2
ESO 368-11	0.97 ±0.18	-3.58 ±3.92	2.34 ±4.21
FSR 1255	0.75 ±0.41	-2.28 ±1.73	2.63 ±1.98
NGC 2287	1.26 ±0.11	-4.30 ±0.62	-1.39 ±0.8
NGC 2362	0.95 ±0.13	-2.33 ±1.38	3.01 ±1.39
NGC 2477	0.65 ±0.26	-2.53 ±1.98	1.58 ±1.85
Ruprecht 12	1.71 ±0.20	-2.68 ±1.28	3.77 ±1.07
Ruprecht 18	0.85 ±0.16	-2.62 ±3.31	2.52 ±4.28
Ruprecht 27	0.71 ±0.11	-2.40 ±2.00	2.03 ±3.39
Trumpler 7	0.42 ±0.12	-3.57 ±1.12	3.57 ±1.26

Table 5.2: Mean astrometric parameters computed for the 13 OCs selected.

range defined before. To perform this step we took into account the TGAS correlations between proper motions and parallaxes as in previous Chapter (see top panels of Fig. 5.6-5.7). A sigma clipping is used to discard outliers. The final parallax values are then re-calculated (see lower panels of Fig. 5.6-5.7).
The typical uncertainties obtained are of the order of $\sim$0.2 mas yr^{-1}. These parallax values are used as priors for the cluster CMD Bayesian analysis that we perform in the next Section.
The astrometric solutions obtained for the 13 OCs selected are reported in Table 5.2.

5.6 Bayesian analysis of the clusters

To determine the OCs parameters (age, metallicity, distance modulus and extinction) we make use of BASE-9 as done for the TGAS sample. To set the prior of the Gaussian distribution of age, metallicity, and extinction we use the values reported in MWSC, obtained using 2MASS photometry. When the metallicity values are not reported in MWSC, we adopt a solar metallicity with $\pm$0.2 dex of dispersion. For the distance modulus we use the values obtained from the parallaxes computed in the previous Section. The adopted Gaussian dispersions is the one derived in previous Section.
To built the input cluster catalogs for BASE-9 we use again JHK_S photometry, taking into account only stars with associated photometric errors $\leqslant$0.15 in each photometric band. We consider only those with proper motions inside the range computed in the previous Section. In this way we decrease the noise caused by the large amount of stars present in the FoV of our OCs. The method is the same adopted in previous Chapter. We use PARSEC isochrones (Bressan et al., 2012),we perform 5 different runs, sampling 3000 points each. Since the uncertainties on parallaxes are larger than those obtained from TGAS data, we enlarge the shift on distance modulus from $\pm$0.3 to $\pm$0.4. Consequently we chose to enlarge also the shift on the log t mean value from $\pm$0.2 to $\pm$0.3. In previous Chapter we see that for the TGAS OCs, BASE-9 converges only for $\sim$25% of the total sample. This is due to the magnitude limit of TGAS, that allows us to use only the brighter part of the OCs in the majority of the cases. This makes it difficult for BASE-9 to find a single solution. Here instead we are able to use the whole CMD for all the clusters and BASE-9 provides a consistent result for all, concerning age, distance modulus and reddening.

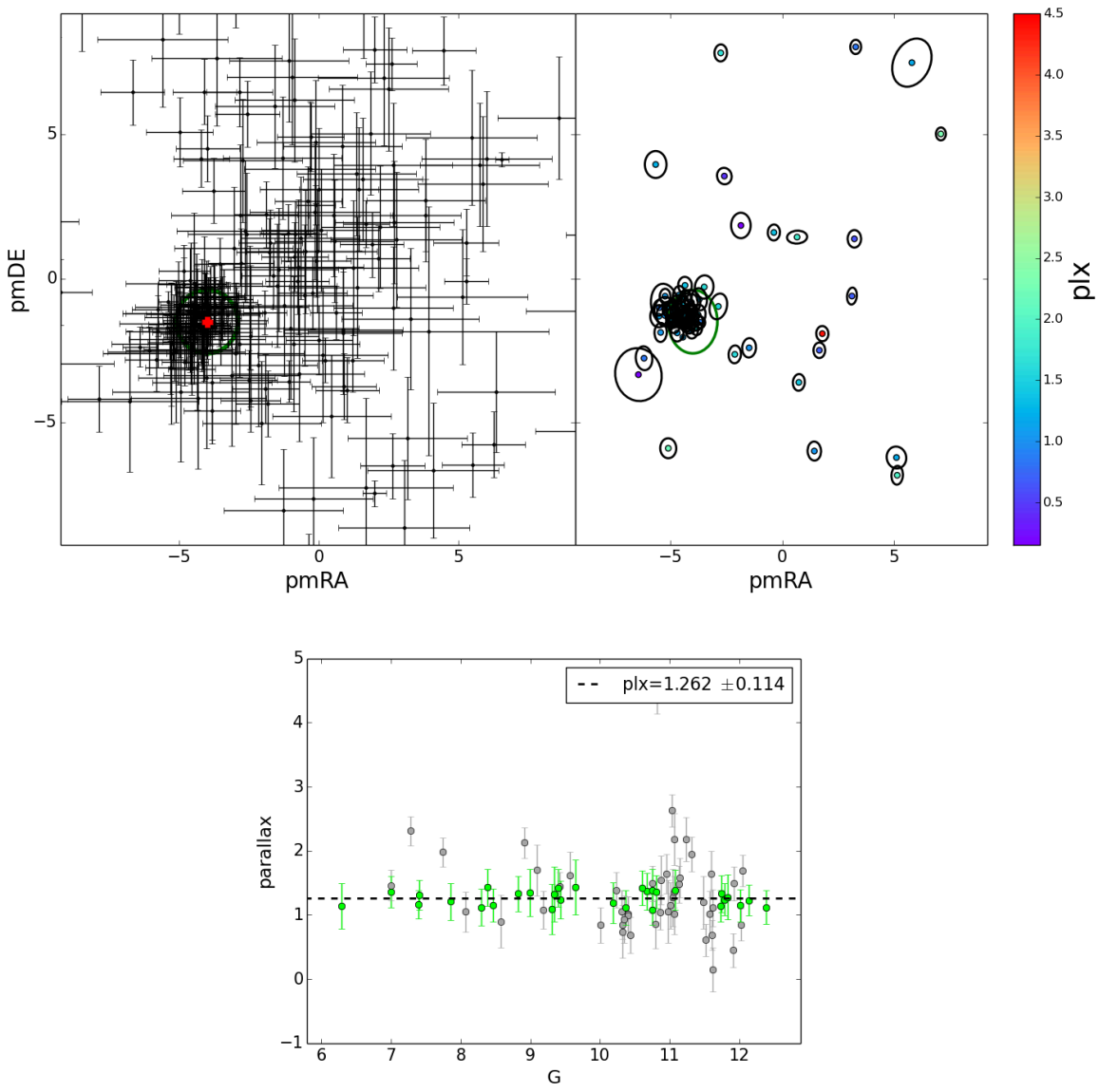

Figure 5.6: Estimated parallax for NGC 2287. In the upper panels we show the proper motions of stars brighter than $J = 12$ mag for HSOY (right) and those for TGAS (left). For TGAS we represent the errors as ellipse, defined by the correlated proper motion errors, see section 4.4.3, and the stars are different colored according with their associated parallaxes. The lower panel shows the star parallaxes as a function of *Gaia* G band. The dashed line represents the mean value, the green dots the stars selected after the 1 sigma clipping.

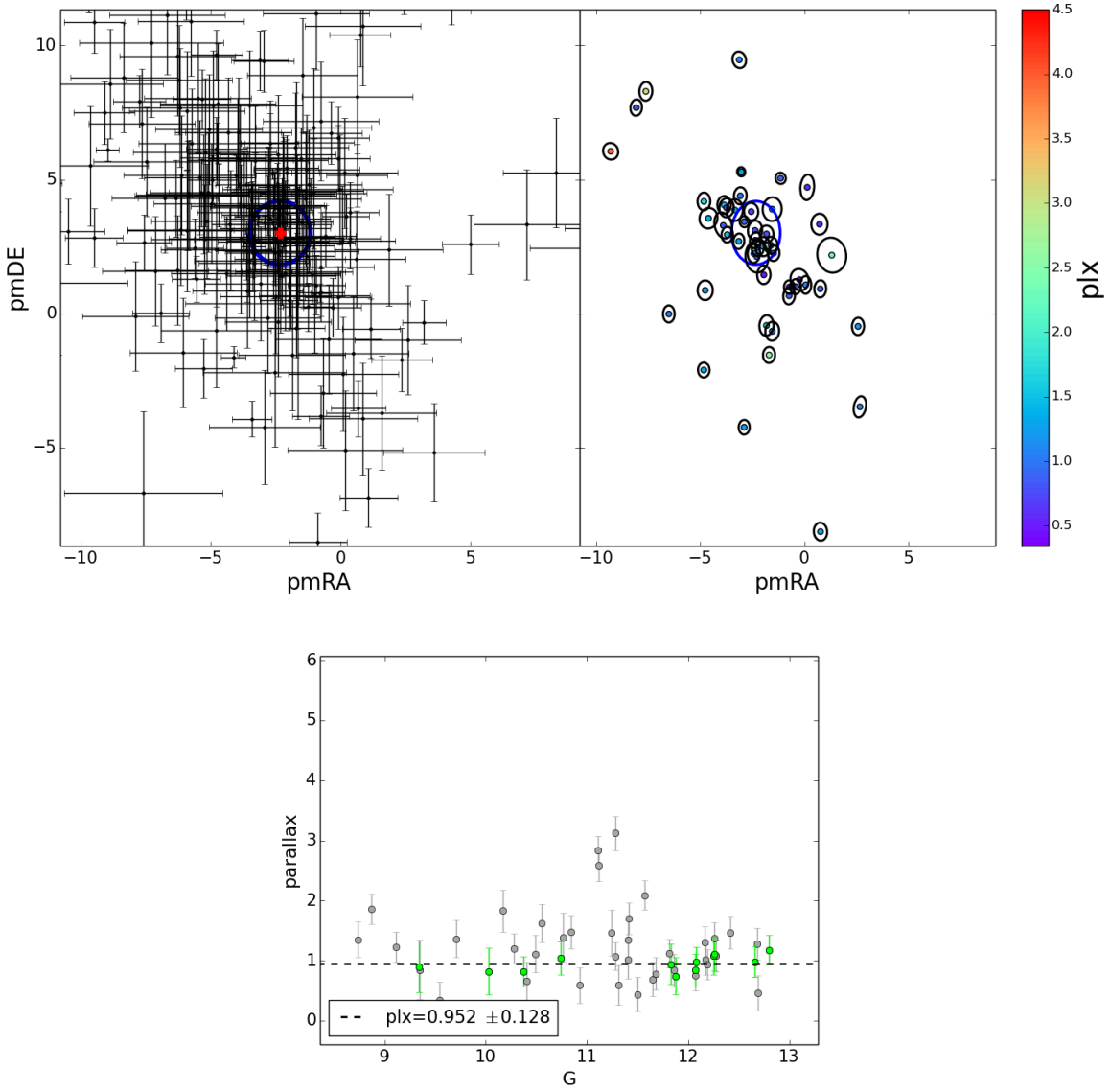

Figure 5.7: Parallax estimate for NGC 2362. The scheme is the same of 5.6.

OC	log t	[Fe/H]	A_V	dist.mod.
ASCC 32	7.50 ± 0.03		0.06 ± 0.01	8.50 ± 0.05
ASCC 33	8.60 ± 0.29	-0.17 ± 0.04	0.22 ± 0.05	9.30 ± 0.09
ASCC 36	8.50 ± 0.25	-0.06 ± 0.16	0.03 ± 0.01	9.45 ± 0.27
Collinder 121	7.65 ± 0.15		0.12 ± 0.05	9.80 ± 0.09
ESO 368-11	8.90 ± 0.2	-0.1 ± 0.16	0.25 ± 0.04	9.10 ± 0.24
FSR 1255	9.05 ± 0.07		0.13 ± 0.04	10.3 ± 0.05
NGC 2287	8.60 ± 0.05	-0.23 ± 0.02	0.03 ± 0.01	8.87 ± 0.03
NGC 2362	6.90 ± 0.09		0.35 ± 0.04	9.65 ± 0.25
NGC 2477	9.10 ± 0.04	0.04 ± 0.03	0.6 ± 0.07	10.65 ± 0.19
Ruprecht 12	7.65 ± 0.02	-0.21 ± 0.08	0.25 ± 0.04	10.2 ± 0.13
Ruprecht 18	8.95 ± 0.06	-0.03 ± 0.03	0.4 ± 0.11	10.4 ± 0.18
Ruprecht 27	9.00 ± 0.03	-0.03 ± 0.03	0.28 ± 0.06	10.6 ± 0.12
Trumpler 7	7.65 ± 0.11		0.9 ± 0.08	11.0 ± 0.23

Table 5.3: Cluster parameters derived from JHK_S photometry for 13 OCs.

For five OCs we are not able to define a solution for [Fe/H]. For those objects, no metallicity value is reported in MWSC. It is possible that the solar metallicity adopted as prior, is not really appropriate. This is not always the case. Indeed, in the case of ASCC 36, ESO 368-11, Ruprecht 12 and Ruprecht 27, even if the initial value of the metallicity is missing, we are able to derive a well defined solution for [Fe/H]. We should consider that working on average with few RC stars, the evolutionary phase of interest in our analysis is the upper part of the MS, in particular the TO. Its magnitude is fixed mainly by the right combination of distance modulus and age. At low/moderate extinction, the effect of reddening is less relevant in JHK_S bands. Then the color of the TO is mainly dependent on age and metallicity. In Fig. 5.8 we show the variation of TO color in the optical $(B-V)$ and in the near infrared ($J-K$ and $J-H$) as a function of age and metallicity, as obtained from the PARSEC isochrones. As expected $(J-K)$ and $(J-H)$ are less sensible to age variation in comparison to $(B-V)$, and have similar response to metallicity in particular at older ages. Breaking the age-metallicity degeneracy on TO color using only near-infrared bands, without combining them with optical bands, is then not always possible.

The obtained results are listed in Table 5.3. In Fig. 5.11-5.12-5.13-5.14 we show, as exam-

ple, the output of BASE-9 and the fits, obtained with the maximum likelihood solutions, for ASCC 36, NGC 2287, NGC 2477 and Ruprecht 27.

Finally we compare our results with the literature values listed in MWSC, see Fig. 5.9. As already noticed in Sect. 4.7.2, the different choice of the models adopted for the analysis produce a shift toward older age in our determination, with log t higher by on average 0.28. As a consequence the distance moduli that we found are usually lower, with a mean difference of -0.31. We find also lower values in average for the extinction factor, with ΔA_V =-0.11.

5.7 Vertical dispersion determination

For the 13 OCs having the full parameter determination, we compute the present vertical altitude on the Galactic plane, to search for significant deviations from the scale height typical of OCs in the same age range. We remind that the disk scale height defined by young clusters (ages $<$ 200 Myr) is of the order of 60 $\pm$14 pc, while at ages $<$ 1 Gyr the scale height is of the order of 100 $\pm$24 pc, see Buckner & Froebrich (2014).

The results are shown in Fig. 5.10 in which z is plotted against the distance from the galactic center. We divide the whole sample between OCs younger and older than 400 Gyr. We highlight on the plots the mean scale height defined by the older clusters in each sub-sample. Collinder 121 and Ruprecht 12, whit an height of respectively z=-158 pc and z=-177 pc and with an age of 45 Myr for both, represent two significant deviations from the expected height.

A possible explanation is that during their relatively short life the two OCs have experienced encounters with giant molecular clouds and/or interaction with non-axisymmetric features of the disk (spiral arms) that have distorted their initial orbits. Currently there are not radial velocities listed in Mermilliod et al. (2008) and Mermilliod et al. (2008) for any star of the two clusters. Then it is not possible to compute their full orbits to search for significant deviations from flat and circular orbits.

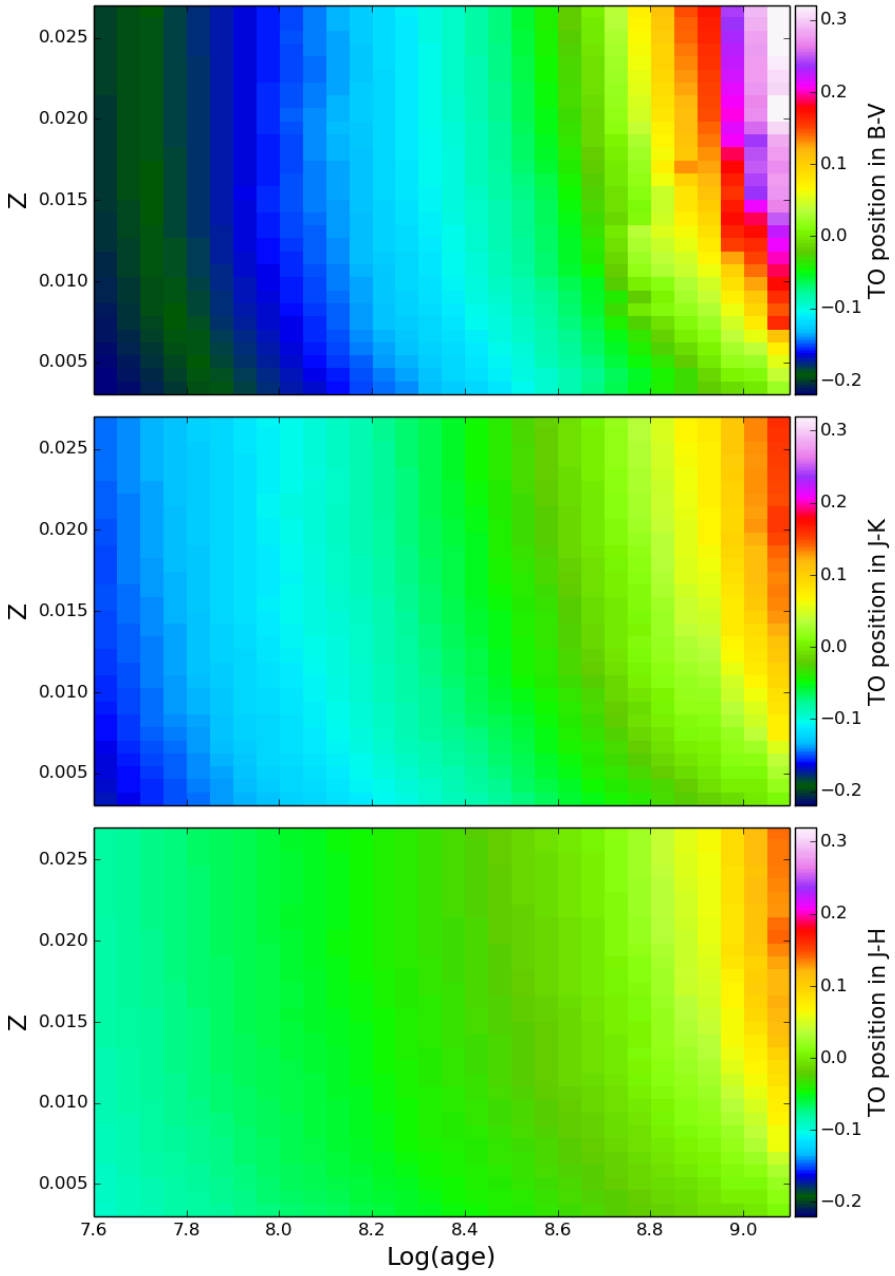

Figure 5.8: TO color variation as a function of age and metallicity. The color scheme represents the variation in color for $B-V$ *(upper panel)*, $J-K$ *(middle panel)* and $J-H$ *(lower panel)*.

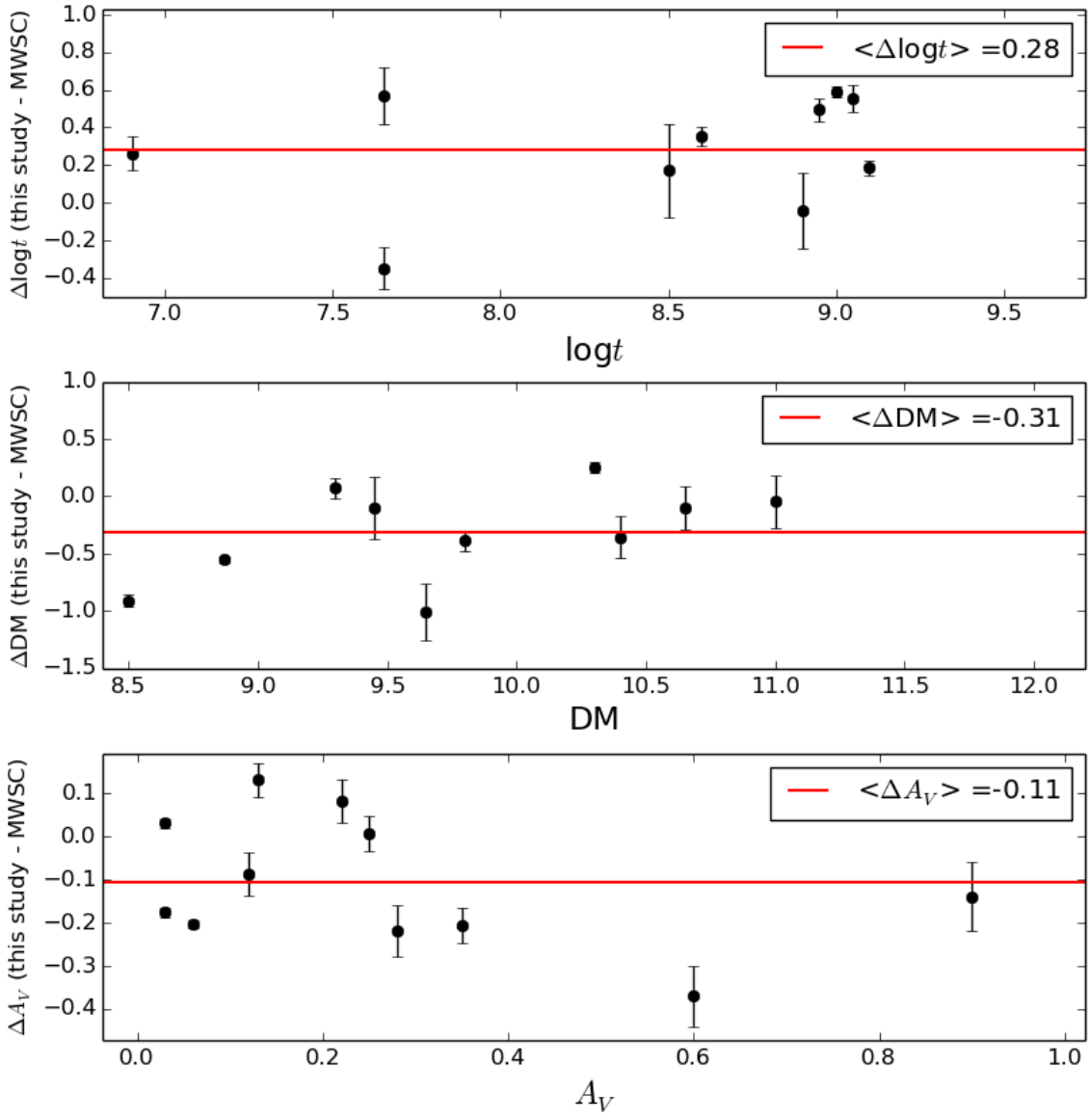

Figure 5.9: Difference in log t *(upper panel)*, in distance modulus *(middle panel)* and in extinction *(lower panel)* between the values found in this study and those quoted in the MWSC catalog. The red lines indicate the mean values.

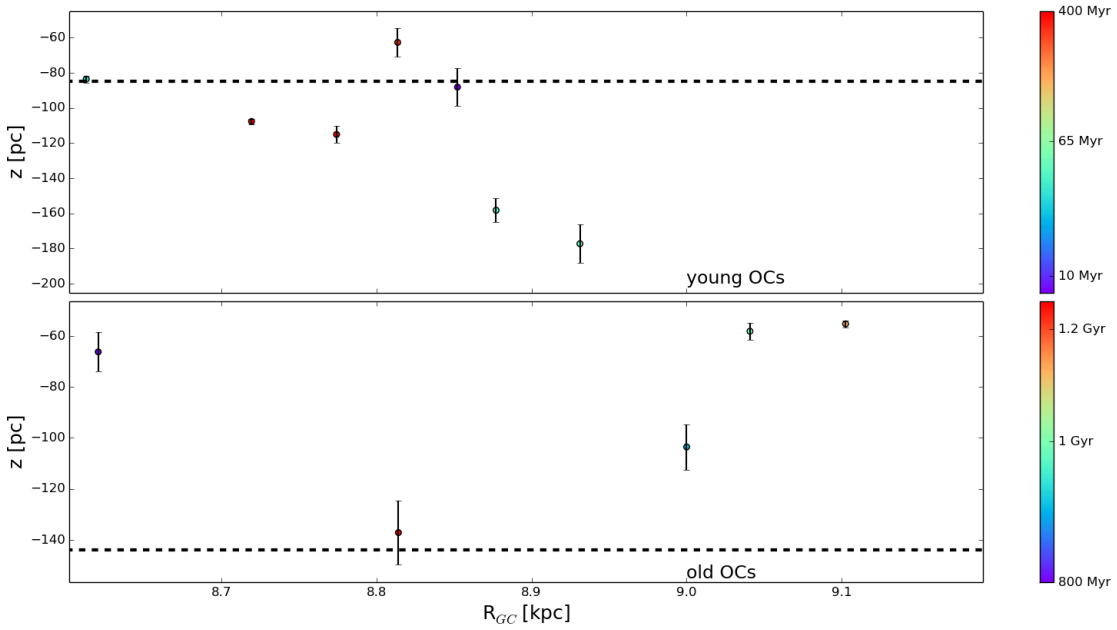

Figure 5.10: Young OCs (upper panel) and old OCs (lower panel) in the R_{GC}-Z plane. The dashed lines represent the mean scale height for OCs with an age of ∼400 Myr *(upper panel)* and ∼1.2 Gyr *(lower panel)*, respectively 85 pc and 145 pc (Buckner & Froebrich, 2014).

5.8 Conclusions

In this work we analyze a sample of 30 OCs taking advantage of the proper motions and the near infrared photometry provided by HSOY and the parallaxes provided by TGAS. The sample contains all the OCs in the solar neighborhood with galactic latitude less than b=-2°, that lie in the region of the TQ warp. The aims of the work is to perform a preliminary study of an interesting region of the disc waiting for *Gaia* GDR2 to reach clusters more distant from us, where the bend of the disc starts to be effective.

To obtain proper motions, distances and physical parameters of the selected OCs we use an automated approach. This allows for an homogeneous determination of those parameters. We perform a cluster membership selection on HSOY data using UPMASK. We combine astrometric and photometric data in order to overcome the problem of the absence of a full astrometric solution for the stars in HSOY. Due to the larger uncertainties on proper motions in comparison to TGAS, we perform a parallel analysis retrieving the cluster proper motions from a photometric selection, and considering as reliable only the values in agreement between the two methods. In this way we determine $\mu_{\alpha*}$ and μ_δ for 13 OCs.

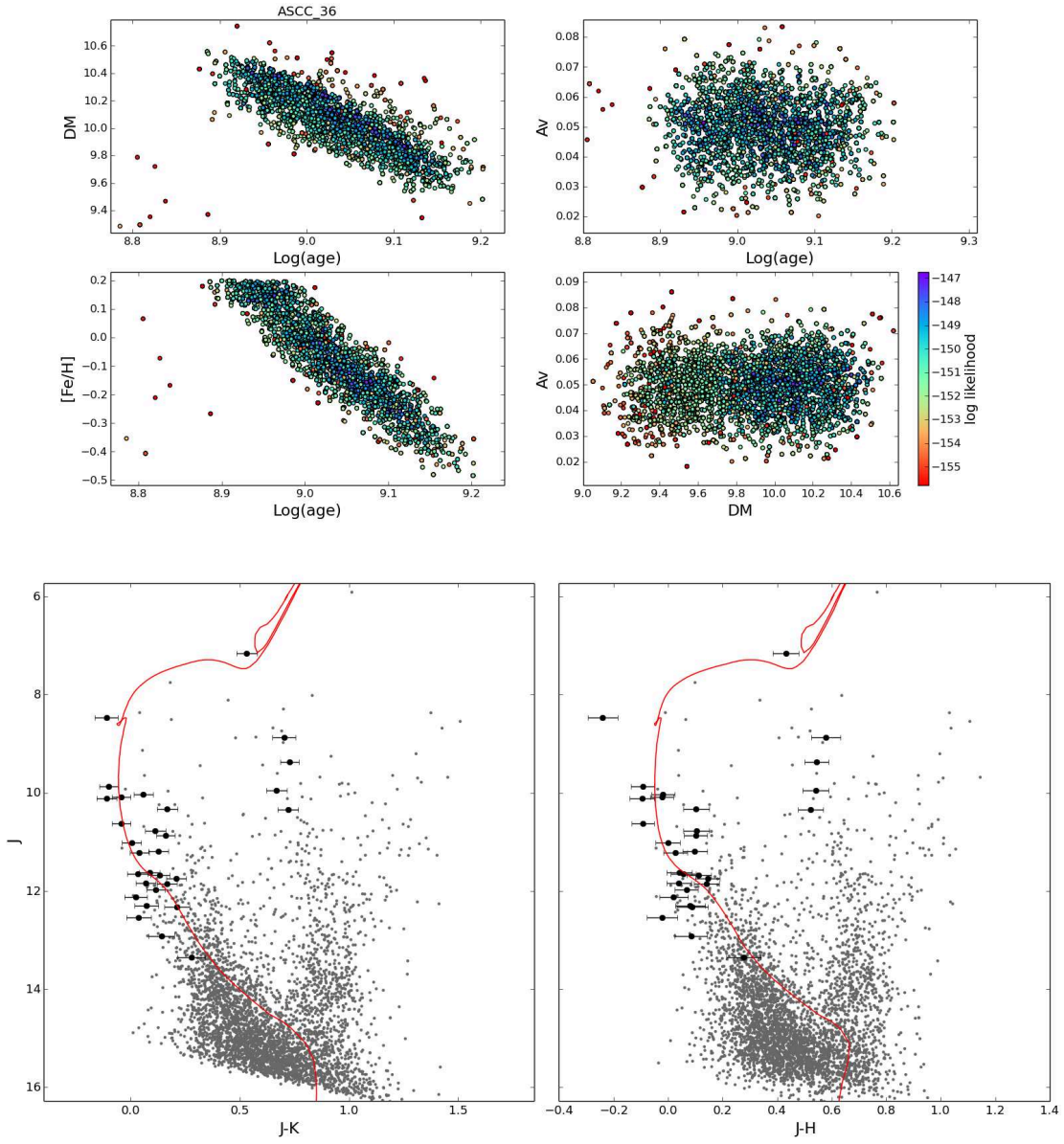

Figure 5.11: BASE-9 results for ASCC 36. *Upper panels*: Posterior distribution maps, combining the outputs of five runs of BASE-9. *Lower panels*: CMDs in the $J - K$ vs J and $J - H$ vs J planes. Grey dots represents all the HSOY stars, black dots are the stars used as BASE-9 input. PARSEC isochrones with parameters defined by the BASE-9 best fit solution, see Table 5.3, are plotted in red.

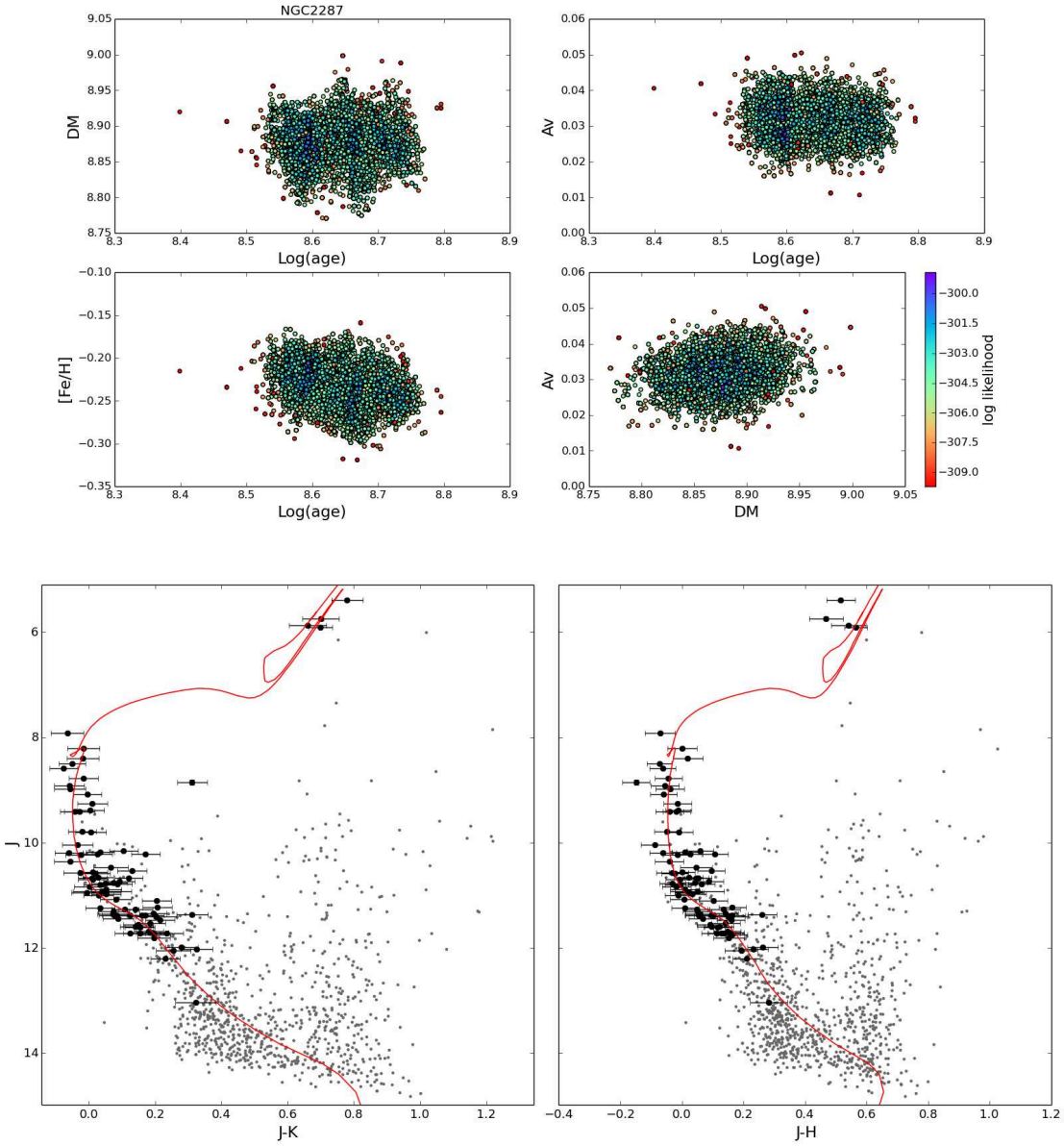

Figure 5.12: BASE-9 results for NGC 2287. For the description of the panels see Fig. 5.11.

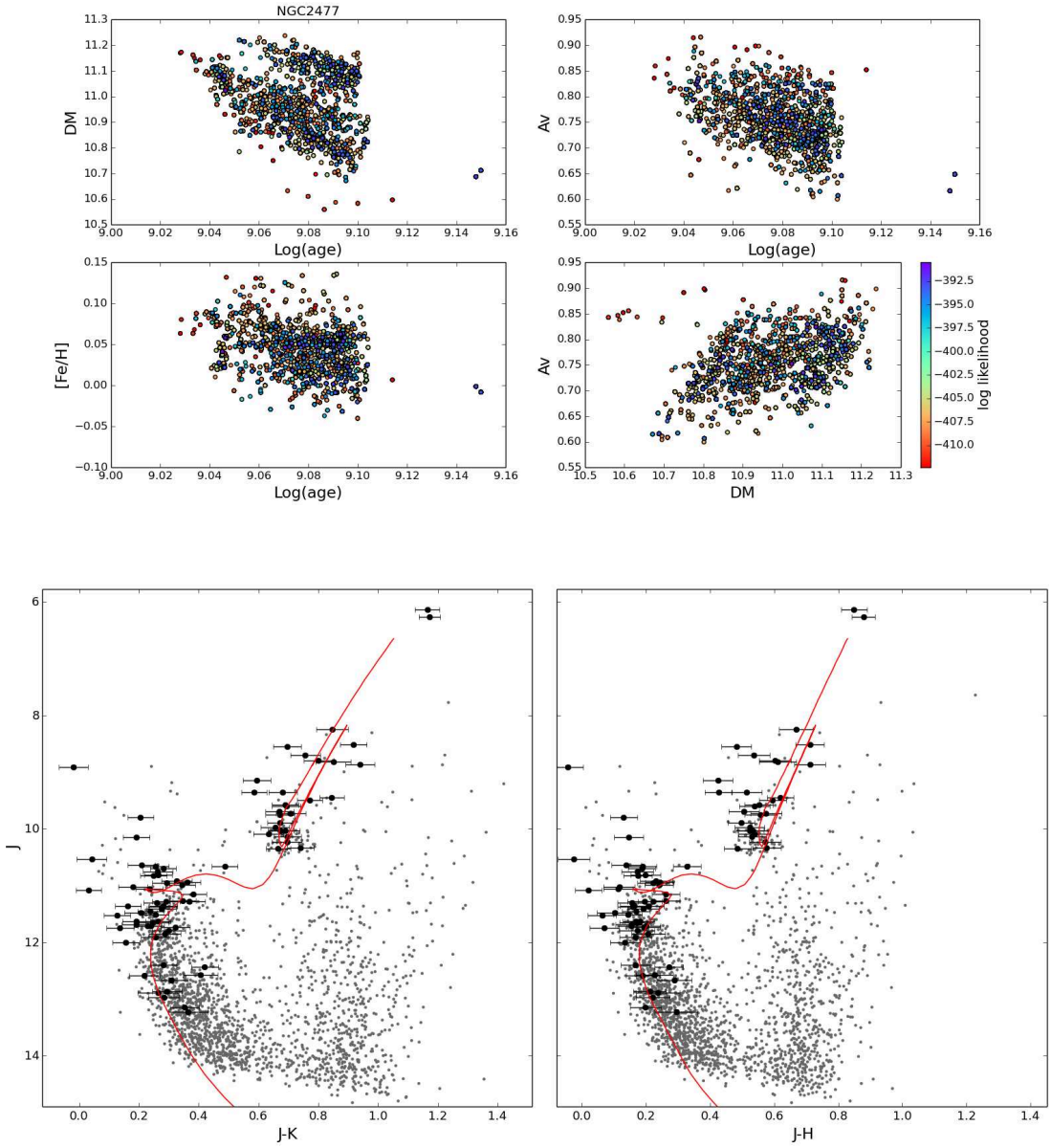

Figure 5.13: BASE-9 results for NGC 2477. For the description of the panels see Fig. 5.11.

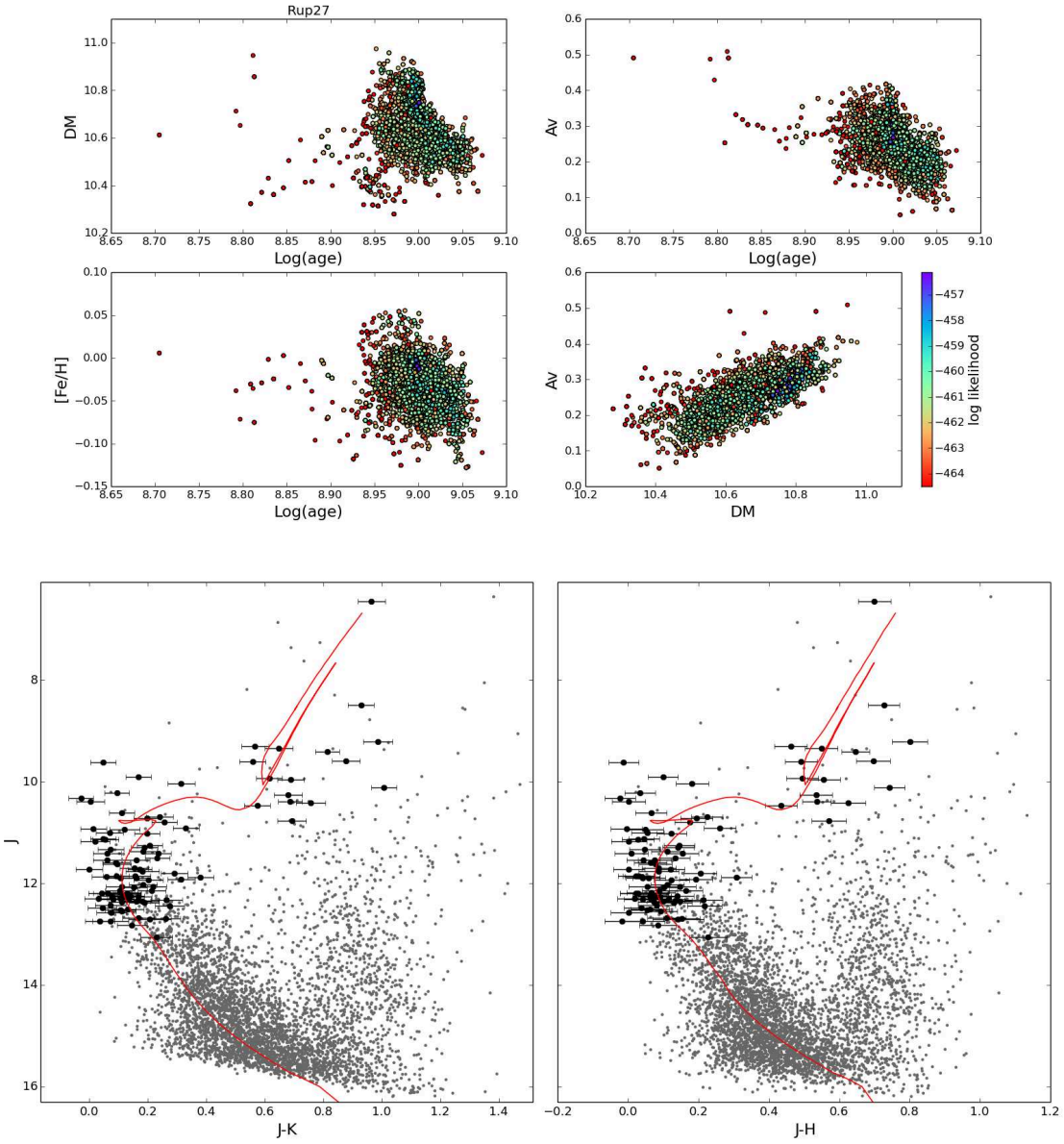

Figure 5.14: BASE-9 results for Ruprecht 27. For the description of the panels see Fig. 5.11.

For those clusters we are also able to define a mean value for the parallaxes, considering the parallax values of the stars in common with TGAS that fall in the proper motion range defined by $\mu_{\alpha*}$ and μ_δ and their uncertainties. But for a few cases, the new determinations of proper motions are in agreement with literature values.

Then with BASE-9 we find the age, distance modulus and extinction factor for all the 13 OCs and the metallicity for 8 of them. Finally we calculate the value of |z| and discuss the trend with age. We find that two very young clusters, Collinder 121 and Ruprecht 12, have values of |z| larger than the scale height of OCs in this age range. Radial velocity determination are needed to understand how their altitude has to be interpreted.

6 Summary and conclusions

OCs are ideal tracers of Galactic disk physical properties and morphology. However to infer disc properties from OCs, we need a consistent and homogeneous data base. Over the years OCs have been studied with a large variety of methods producing very inhomogeneous sets of their parameters. In the last decades the releases of whole sky surveys, such as 2MASS, and of large dataset of OCs parameters, such as DALM14 and MWSC, have improved this situations as well as have enlarged the clusters census, but have not really solved the problem.
In the coming years the very precise data provided by *Gaia* mission (see Chapter 2 for a detailed description) will substantially improve both the number of known clusters and the precision on their parameters determination. The main goal of this Thesis is to derive a homogeneous catalog of OC properties. Here we make use of the first *Gaia* data release, and we validate the tools that will led to the scientific exploitation of the second and upcoming data releases. We study a sample of 150 OCs.

We first analyze three clusters from ESO-archive, NGC 2225, NGC 134 and NGC 2243. The performed photometric analysis is reported in Chapter 3. For these clusters we have at our disposal optical photometry on a large Field of View, that permits to evaluate the field stars contamination and the radial extension of the clusters. We reduce the archive data with classical methods, infer photometric uncertainties and completeness via artificial stars test and analyze them first comparing with synthetic populations. To this purpose, we develop `FILLTHETEMPO` a python code to create synthetic stellar populations and compare them with the observed data. The code starts from an isochrones library, populates isochrones

according to a chosen IMF and taking into account completeness, assigns to each star a random photometric errors from a range appropriate for the available photometry and adds the field contribution evaluated from an external area of the clusters FoVs. The code permits both a visual comparison between the observed and simulated CMDs and a comparisons between the two luminosity functions. Finally a freely available automated tool for Bayesian analysis, BASE-9 is validated and used to derive cluster properties (see Sect. 3.5). We upgrade the BASE-9 models library in order to work in 2MASS JHK_S photometric bands using PARSEC isochrones (Bressan et al., 2012).
The parameters derived are summarized in Sect. 3.6. For NGC 6134 and NGC 2243 the results obtained for age, distance modulus and reddening are in agreement with the literature, with slight differences due to the different choice of models adopted for the analysis. For NGC 2225 our results are not in agreement with those obtained in the only one study present in literature, in reason of the different interpretation of the TO location. We are able to obtain a well constrained determination of the metallicity only for NGC 2243, the only one of the three clusters for which we have at disposal both $B - V$ and $V - I$ colors. Our result is in agreement with previous spectroscopic studies.
The good agreement in the results inferred by the two methods validate the reliability of the automated procedure.

Then we derive the properties of a sample of 134 OCs located within 2 kpc from us (see Chapter 4).
We use the proper motions provided by TGAS combined to the ones of UCAC4, to minimize the uncertainties, and the parallaxes from TGAS to calculate the probability membership of the OCs stars with the UPMASK method, see Sect. 4.4. UPMASK works with the TGAS astrometry, determining the clusters proper motions and parallaxes from their stars according to the determined probability memberships. BASE-9 output converges on a single solution for 26 OCs, for which we determine ages, extinctions, distance moduli and metallicities. Furthermore for 36 OCs we are able to retrieve the radial velocities and to compute the full 3D orbits, z_{max}, |z| and the eccentricity. We find evidences of vertical heating already effective on the time defined by the age of our clusters ($\sim$1 Gyr). No evident sign of radial heating is detected.

In order to overcome the problem of the TGAS completeness limit (G = 11-12) we take advantage of the HSOY catalog. We perform an analysis, (discussed in Chapter 5) of 30

OCs located in the region of the Third Galactic Quadrant. This is a very interesting region for the presence of the spiral structure and of the disc warp. The present data allows us to study OCs within 1.5 kpc distance, not sufficient to discuss these structures. The work has the aim to be a preliminary study, waiting for the next *Gaia* releases to go deeper in the disc. In order to determine the proper motions of the OCs we use a dual approach:

- we use UPMASK combining HSOY astrometry and 2MASS photometry to derive the membership probability.
- we perform a photometric selection on the OC CMDs with the near infrared colors to select the regions where the cluster population is prominent.

We accept only the solutions where the two methods converge at the same result. This choice leaves us with 13 OCs to be analyzed with BASE-9. For all of them we have determined ages, extinctions and distance moduli, while for 8 of them we have determined also the metallicity. No radial velocity is available in literature for these cluster. This prevent us to reconstruct the full orbits. Studying the present vertical dispersion of the clusters we have found that two of them, Collinder 121 and Ruprecht 12, have a high negative latitude despite their young age ($\sim$ 45 Myr). A study of the orbits of those clusters has to be performed in order to understand the nature of these features.

In summary, in this work we estimate in a homogeneous way:

- proper motions and parallaxes of 147 OCs
- age, distance moduli and extinction of 42 OCs
- metallicities of 37 OCs
- 3D orbits of 36 OCs.

We stress the fact that tools such as BASE-9 provide an objective estimate of the cluster parameters, a convenient alternative to fitting colour-magnitude diagrams by eye. Furthermore in the next years scientific missions like *Gaia* will provide us with larger and larger OCs samples, and automated tools able to handle large amount of data will become indispensable in this field of research.

We develop and validate an automatic pipeline that can be used on the astrometric and photometric data of the second *Gaia* data release. This release will contain a full astrometric solution and BP and RP magnitudes for one billion stars, allowing us to perform studies like those reported in this Thesis using *Gaia* data alone. We will be also able to identify more distant and new OCs, thanks to the higher astrometric precision and the deeper magnitude limit (G $\sim$20.7).

Eventually this will result in an improved cluster census combined with an homogeneous parameters determination. This will represent a crucial step toward understanding the structure, and the evolution of the Milky Way disc.

Bibliography

Ahumada, A. V., Cignoni, M., Bragaglia, A., et al.: 2013, MNRAS **430**, 221

Ahumada, J. A.: 2002, in T. Lejeune and J. Fernandes (eds.), *Observed HR Diagrams and Stellar Evolution*, Vol. 274 of *Astronomical Society of the Pacific Conference Series*, p. 307

Allison, R. J., Goodwin, S. P., Parker, R. J., et al.: 2009, MNRAS **395**, 1449

Altmann, M., Roeser, S., Demleitner, M., et al.: 2017, A&A **600**, L4

Andreuzzi, G., Bragaglia, A., Tosi, M., et al.: 2011, MNRAS **412**, 1265

Anthony-Twarog, B. J., Atwell, J., Twarog, B. A.: 2005, AJ **129**, 872

Arenou, F., Luri, X., Babusiaux, C., et al.: 2017, A&A **599**, A50

Balaguer-Núñez, L., Jordi, C., Galadí-Enríquez, D.: 2005, A&A **437**, 457

Bastian, N.: 2011, in *Stellar Clusters and Associations: A RIA Workshop on Gaia*, pp 85–97

Bastian, N., Goodwin, S. P.: 2006, MNRAS **369**, L9

Baumgardt, H., Kroupa, P.: 2007, MNRAS **380**, 1589

Becker, W., Fenkart, R. B.: 1970, in W. Becker and G. I. Kontopoulos (eds.), *The Spiral Structure of our Galaxy*, Vol. 38 of *IAU Symposium*, p. 205

Bellazzini, M., Fusi Pecci, F., Messineo, M., et al.: 2002, AJ **123**, 1509

Bergbusch, P. A., Vandenberg, D. A., Infante, L.: 1991, AJ **101**, 2102

Bertelli, G., Bressan, A., Chiosi, C., et al.: 1994, A&AS 106

Bessel, F. W.: 1838, *Astronomische Nachrichten* **16**, 65

Bica, E., Bonatto, C.: 2011, A&A **530**, A32

Bonifazi, A., Tosi, M., Fusi Pecci, F., et al.: 1990, MNRAS **245**, 15

Borissova, J., Chené, A.-N., Ramírez Alegría, S., et al.: 2014, A&A **569**, A24

Bouvier, J., Kendall, T., Meeus, G., et al.: 2008, A&A **481**, 661

Bouy, H., Alves, J.: 2015, A&A **584**, A26

Bovy, J.: 2015, ApJS **216**, 29

Bragaglia, A., Gratton, R. G., Carretta, E., et al.: 2012, A&A **548**, A122

Bragaglia, A., Tosi, M.: 2006, AJ **131**, 1544

Bragaglia, A., Tosi, M., Andreuzzi, G., et al.: 2006, MNRAS **368**, 1971

Bressan, A., Fagotto, F., Bertelli, G., et al.: 1993, A&AS **100**, 647

Bressan, A., Marigo, P., Girardi, L., et al.: 2012, MNRAS **427**, 127

Brogaard, K., VandenBerg, D. A., Bruntt, H., et al.: 2012, A&A **543**, A106

Bruntt, H., Frandsen, S., Kjeldsen, H., et al.: 1999, A&AS **140**, 135

Buckner, A. S. M., Froebrich, D.: 2014, MNRAS **444**, 290

Bukowiecki, Ł., Maciejewski, G., Konorski, P., et al.: 2011, Acta Astron. **61**, 231

Cantat-Gaudin, T., Donati, P., Vallenari, A., et al.: 2016, A&A **588**, A120

Cantat-Gaudin, T., Vallenari, A., Zaggia, S., et al.: 2014, A&A **569**, A17

Carraro, G., Baume, G., Vázquez, R. A., et al.: 2005, MNRAS **362**, 649

Carraro, G., Bresolin, F., Villanova, S., et al.: 2004, AJ **128**, 1676

Carraro, G., Costa, E.: 2009, A&A **493**, 71

Carraro, G., Geisler, D., Villanova, S., et al.: 2007, A&A **476**, 217

Carraro, G., Sales Silva, J. V., Moni Bidin, C., et al.: 2017, AJ **153**, 99

Carrasco, J. M., Weiler, M., Jordi, C., et al.: 2017, in S. Arribas, A. Alonso-Herrero, F. Figueras, C. Hernández-Monteagudo, A. Sánchez-Lavega, and S. Pérez-Hoyos (eds.), *Highlights on Spanish Astrophysics IX*, pp 622–627

Carretta, E., Bragaglia, A., Gratton, R. G., et al.: 2010, A&A **516**, A55

Carretta, E., Bragaglia, A., Gratton, R. G., et al.: 2004, A&A **422**, 951

Cedrés, B., Cepa, J., Bongiovanni, Á., et al.: 2013, A&A **560**, A59

Cignoni, M., Beccari, G., Bragaglia, A., et al.: 2011, MNRAS **416**, 1077

Claria, J. J., Mermilliod, J.-C.: 1992, A&AS **95**, 429

Cousins, A. W. J., Caldwell, J. A. R.: 1985, *The Observatory* **105**, 134

Crowley, C., Kohley, R., Hambly, N. C., et al.: 2016, A&A **595**, A6

de Bruijne, J. H. J., Hoogerwerf, R., de Zeeuw, P. T.: 2000, ApJ **544**, L65

de La Fuente Marcos, R.: 1997, A&A **322**, 764

Dias, W. S., Alessi, B. S., Moitinho, A., et al.: 2002, *aap* **389**, 871

Dias, W. S., Alessi, B. S., Moitinho, A., et al.: 2014, *VizieR Online Data Catalog* 1

Dias, W. S., Lépine, J. R. D.: 2005, ApJ **629**, 825

Donati, P., Bragaglia, A., Cignoni, M., et al.: 2012, MNRAS **424**, 1132

ESA (ed.): 1997, *The HIPPARCOS and TYCHO catalogues. Astrometric and photometric star catalogues derived from the ESA HIPPARCOS Space Astrometry Mission*, Vol. 1200 of *ESA Special Publication*

Evans, D. W., Riello, M., De Angeli, F., et al.: 2017, A&A **600**, A51

Eyer, L., Mowlavi, N., Evans, D. W., et al.: 2017, *ArXiv e-prints*

Fagotto, F., Bressan, A., Bertelli, G., et al.: 1994, A&AS 105

Finch, C. T., Zacharias, N.: 2016, *VizieR Online Data Catalog* 515

François, P., Pasquini, L., Biazzo, K., et al.: 2013, A&A **552**, A136

Friel, E. D.: 1995, ARA&A **33**, 381

Friel, E. D.: 2013, *Open Clusters and Their Role in the Galaxy*, p. 347

Friel, E. D., Janes, K. A.: 1993, A&A **267**, 75

Friel, E. D., Janes, K. A., Tavarez, M., et al.: 2002, AJ **124**, 2693

Frinchaboy, P. M., Thompson, B., Jackson, K. M., et al.: 2013, ApJ **777**, L1

Froebrich, D., Scholz, A., Raftery, C. L.: 2007, MNRAS **374**, 399

Gaia Collaboration, Brown, A. G. A., Vallenari, A., et al.: 2016a, A&A **595**, A2

Gaia Collaboration, Prusti, T., de Bruijne, J. H. J., et al.: 2016b, A&A **595**, A1

Gaia Collaboration, van Leeuwen, F., Vallenari, A., et al.: 2017, A&A **601**, A19

Gallart, C., Freedman, W. L., Aparicio, A., et al.: 1999, AJ **118**, 2245

Giorgi, E. E., Vàzquez, R. A., Baume, G., et al.: 2002, A&A **381**, 884

Girardi, L., Bertelli, G., Bressan, A., et al.: 2002, A&A **391**, 195

Girardi, L., Bressan, A., Bertelli, G., et al.: 2000, A&AS **141**, 371

Glushkova, E. V., Koposov, S. E., Zolotukhin, I. Y., et al.: 2010, *Astronomy Letters* **36**, 75

Goodwin, S. P.: 2009, Ap&SS **324**, 259

Gratton, R., Bragaglia, A., Carretta, E., et al.: 2006, ApJ **642**, 462

Gratton, R. G., Bonifacio, P., Bragaglia, A., et al.: 2001, A&A **369**, 87

Gratton, R. G., Carretta, E., Bragaglia, A.: 2012, A&A Rev. **20**, 50

Gratton, R. G., Contarini, G.: 1994, A&A **283**, 911

Haisch, Jr., K. E., Lada, E. A., Lada, C. J.: 2001, ApJ **553**, L153

Harris, J., Zaritsky, D.: 2001, ApJS **136**, 25

Hawarden, T. G.: 1975, MNRAS **173**, 801

Heiter, U., Soubiran, C., Netopil, M., et al.: 2014, A&A **561**, A93

Henderson, T.: 1840, MmRAS **11**, 61

Hills, J. G.: 1980, ApJ **235**, 986

Høg, E., Fabricius, C., Makarov, V. V., et al.: 2000, A&A **355**, L27

Høg, E., Knude, J.: 2014, *ArXiv e-prints*

Hotelling, H.: 1933, *Journal of Educational Psychology 24* pp 417–441, and 498–520

Hurley, J. R., Pols, O. R., Aarseth, S. J., et al.: 2005, MNRAS **363**, 293

Jacobson, H. R., Friel, E. D., Jílková, L., et al.: 2016, A&A **591**, A37

Jeans, J. H.: 1902, *Philosophical Transactions of the Royal Society of London Series A* **199**, 1

Jeffery, E. J., von Hippel, T., van Dyk, D. A., et al.: 2016, ApJ **828**, 79

Kaluzny, J., Krzeminski, W., Mazur, B.: 1996, A&AS **118**, 303

Kaluzny, J., Pych, W., Rucinski, S. M., et al.: 2006, Acta Astron. **56**, 237

Kennicutt, R. C., Evans, N. J.: 2012, ARA&A **50**, 531

Kharchenko, N. V., Piskunov, A. E., Röser, S., et al.: 2005a, A&A **440**, 403

Kharchenko, N. V., Piskunov, A. E., Röser, S., et al.: 2005b, A&A **438**, 1163

Kharchenko, N. V., Piskunov, A. E., Schilbach, E., et al.: 2013, A&A **558**, A53

King, I. R.: 1966, AJ **71**, 64

Kjeldsen, H., Frandsen, S.: 1991, A&AS **87**, 119

Klessen, R. S., Heitsch, F., Mac Low, M.-M.: 2000, ApJ **535**, 887

Koch, A., McWilliam, A.: 2008, AJ **135**, 1551

Kohley, R., Garé, P., Vétel, C., et al.: 2012, in *Space Telescopes and Instrumentation 2012: Optical, Infrared, and Millimeter Wave*, Vol. 8442 of Proc. SPIE, p. 84421P

Koposov, S. E., Glushkova, E. V., Zolotukhin, I. Y.: 2008, A&A **486**, 771

Kovtyukh, V. V., Soubiran, C., Belik, S. I.: 2004, A&A **427**, 933

Kraus, A. L., Hillenbrand, L. A.: 2007, AJ **134**, 2340

Krone-Martins, A., Moitinho, A.: 2014, A&A **561**, A57

Lada, C. J., Lada, E. A.: 2003, ARA&A **41**, 57

Lamers, H. J. G. L. M., Gieles, M.: 2006, A&A **455**, L17

Landolt, A. U.: 1992, AJ **104**, 340

Lanzoni, B., Ferraro, F. R., Dalessandro, E., et al.: 2010, ApJ **717**, 653

Lauberts, A.: 1982, *ESO/Uppsala survey of the ESO(B) atlas*

Lépine, J. R. D., Cruz, P., Scarano, Jr., S., et al.: 2011, MNRAS **417**, 698

Lindegren, L., Bastian, U.: 2011, *EAS Pub. Ser.* **45**, 109

Lindegren, L., Lammers, U., Bastian, U., et al.: 2016a, A&A **595**, A4

Lindegren, L., Lammers, U., Bastian, U., et al.: 2016b, A&A 595

Lindegren, L., Lammers, U., Hobbs, D., et al.: 2012, A&A **538**, A78

Lindoff, U.: 1972, A&AS **7**, 231

Loktin, A. V., Gerasimenko, T. P., Malysheva, L. K.: 2001, *Astronomical and Astrophysical Transactions* **20**, 607

Lynga, G.: 1981, *Astronomical Data Center Bulletin* **1**, 90

Lynga, G.: 1987, *Computer Based Catalogue of Open Cluster Data, 5th ed.*

Magrini, L., Randich, S., Donati, P., et al.: 2015, A&A **580**, A85

Marigo, P., Girardi, L., Bressan, A., et al.: 2008, A&A **482**, 883

Marrese, P. M., Marinoni, S., Fabrizio, M., et al.: 2017, *ArXiv e-prints*

Mathieu, R. D.: 1984, ApJ **284**, 643

Mermilliod, J.-C.: 1995, in D. Egret and M. A. Albrecht (eds.), *Information and On-Line Data in Astronomy*, Vol. 203 of *Astrophysics and Space Science Library*, pp 127–138

Mermilliod, J. C., Mayor, M., Udry, S.: 2008, A&A **485**, 303

Mermilliod, J.-C., Mayor, M., Udry, S.: 2009, A&A **498**, 949

Meylan, G.: 2000, in A. Lançon and C. M. Boily (eds.), *Massive Stellar Clusters*, Vol. 211 of *Astronomical Society of the Pacific Conference Series*, p. 215

Meynet, G., Mermilliod, J.-C., Maeder, A.: 1993, A&AS **98**, 477

Michalik, D., Lindegren, L., Hobbs, D.: 2015, A&A **574**, A115

Moitinho, A., Vázquez, R. A., Carraro, G., et al.: 2006, MNRAS **368**, L77

Monet, D. G., Levine, S. E., Canzian, B., et al.: 2003, AJ **125**, 984

Montegriffo, P., Ferraro, F. R., Fusi Pecci, F., et al.: 1995, MNRAS **276**, 739

Moraux, E., Kroupa, P., Bouvier, J.: 2004, A&A **426**, 75

Munari, U., Tomasella, L., Fiorucci, M., et al.: 2008, A&A **488**, 969

Netopil, M., Paunzen, E., Carraro, G.: 2015, A&A **582**, A19

Netopil, M., Paunzen, E., Heiter, U., et al.: 2016, A&A **585**, A150

Pancino, E., Carrera, R., Rossetti, E., et al.: 2010, A&A

Pearson, K.: 1901, *Philosophical Magazine 2* pp 559–572

Perryman, M.: 2009, *Astronomical Applications of Astrometry: Ten Years of Exploitation of the Hipparcos Satellite Data*, Cambridge University Press

Perryman, M.: 2012, *European Physical Journal H* **37**, 745

Perryman, M. A. C., Hassan, H., Batut, T., et al. (eds.): 1989, *The Hipparcos mission. Pre-launch status. Volume I: The Hipparcos satellite.*, Vol. 1

Perryman, M. A. C., Lindegren, L., Turon, C.: 1997, in R. M. Bonnet, E. Høg, P. L. Bernacca, L. Emiliani, A. Blaauw, C. Turon, J. Kovalevsky, L. Lindegren, H. Hassan, M. Bouffard, B. Strim, D. Heger, M. A. C. Perryman, and L. Woltjer (eds.), *Hipparcos - Venice '97*, Vol. 402 of *ESA Special Publication*, pp 743–748

Pietrinferni, A., Cassisi, S., Salaris, M., et al.: 2004, ApJ **612**, 168

Piotto, G., Villanova, S., Bedin, L. R., et al.: 2005, ApJ **621**, 777

Piskunov, A. E., Kharchenko, N. V., Röser, S., et al.: 2006, A&A **445**, 545

Portegies Zwart, S. F., Hut, P., McMillan, S. L. W., et al.: 2004, MNRAS **351**, 473

Rasmussen, M. B., Bruntt, H., Frandsen, S., et al.: 2002, A&A **390**, 109

Recio-Blanco, A., de Laverny, P., Allende Prieto, C., et al.: 2016, A&A **585**, A93

Reid, M. J., Menten, K. M., Brunthaler, A., et al.: 2014, ApJ **783**, 130

Roberts, W. W.: 1969, ApJ **158**, 123

Robichon, N., Arenou, F., Mermilliod, J.-C., et al.: 1999, A&A **345**, 471

Roeser, S., Demleitner, M., Schilbach, E.: 2010, AJ **139**, 2440

Salaris, M., Cassisi, S.: 2005, *Evolution of stars and stellar populations*

Salaris, M., Weiss, A.: 2002, A&A **388**, 492

Salaris, M., Weiss, A., Percival, S. M.: 2004, A&A **414**, 163

Salpeter, E. E.: 1955, ApJ **121**, 161

Schaller, G., Schaerer, D., Meynet, G., et al.: 1992, A&AS **96**, 269

Sestito, P., Bragaglia, A., Randich, S., et al.: 2008, A&A **488**, 943

Shu, F. H., Milione, V., Gebel, W., et al.: 1972, ApJ **173**, 557

Skrutskie, M. F., Cutri, R. M., Stiening, R., et al.: 2006, AJ **131**, 1163

Smith, R., Fellhauer, M., Goodwin, S., et al.: 2011, MNRAS **414**, 3036

Spitzer, Jr., L.: 1958, ApJ **127**, 17

Spitzer, Jr., L.: 1969, ApJ **158**, L139

Spitzer, Jr., L., Harm, R.: 1958, ApJ **127**, 544

Stetson, P. B.: 1987, PASP **99**, 191

Stetson, P. B.: 1994, in R. J. Hanisch and R. L. White (eds.), *The Restoration of HST Images and Spectra - II*, p. 308

Stetson, P. B., Vandenberg, D. A., Bolte, M.: 1996, PASP **108**, 560

Subramaniam, A., Bhatt, B. C.: 2007, MNRAS **377**, 829

Tadross, A. L.: 2001, New A **6**, 293

Tadross, A. L.: 2008a, MNRAS **389**, 285

Tadross, A. L.: 2008b, New A **13**, 370

Tadross, A. L.: 2009a, New A **14**, 200

Tadross, A. L.: 2009b, Ap&SS **323**, 383

Tadross, A. L.: 2011, *Journal of Korean Astronomical Society* **44**, 1

Tadross, A. L.: 2012, New A **17**, 198

Tadross, A. L., El-Bendary, R., Osman, A., et al.: 2012, *Research in Astronomy and Astrophysics* **12**, 75

Tadross, A. L., Nasser, M. A.: 2010, *ArXiv e-prints*

Terlevich, E.: 1987, MNRAS **224**, 193

Twarog, B. A., Ashman, K. M., Anthony-Twarog, B. J.: 1997, AJ **114**, 2556

van den Bergh, S.: 1977, ApJ **215**, 89

van Leeuwen, F. (ed.): 2007, *Hipparcos, the New Reduction of the Raw Data*, Vol. 350 of *Astrophysics and Space Science Library*

VandenBerg, D. A., Bergbusch, P. A., Dowler, P. D.: 2006, ApJS **162**, 375

Vázquez, R. A., May, J., Carraro, G., et al.: 2008, ApJ **672**, 930

Vázquez, R. A., Moitinho, A., Carraro, G., et al.: 2010, A&A **511**, A38

von Hippel, T., Jefferys, W. H., Scott, J., et al.: 2006, ApJ **645**, 1436

von Struve, O. W.: 1840, *Astronomische Nachrichten* **17**, 177

Yong, D., Carney, B. W., Friel, E. D.: 2012, AJ **144**, 95

Zacharias, N., Finch, C. T., Girard, T. M., et al.: 2012, *VizieR Online Data Catalog* 1322

Zacharias, N., Finch, C. T., Girard, T. M., et al.: 2013, AJ **145**, 44